NASA TECHNICAL MEMORANDUM

NASA TM X-1221

NASA TM X-1221

FACILITY FORM 602

N66-21101
(ACCESSION NUMBER)

(THRU)

209
(PAGES)

1
(CODE)

(NASA CR OR TMX OR AD NUMBER)

12
(CATEGORY)

DATA ON EFFECTS OF INCIDENT-REFLECTING SHOCKS ON THE TURBULENT BOUNDARY LAYER

by S. Z. Pinckney

Langley Research Center
Langley Station, Hampton, Va.

GPO PRICE $ ________

CFSTI PRICE(S) $ 2.30

Hard copy (HC) ________

Microfiche (MF) 1.25

ff 653 July 65

NATIONAL AERONAUTICS AND SPACE ADMINISTRATION • WASHINGTON, D. C. • MARCH 1966

NASA TM X-1221

DATA ON EFFECTS OF INCIDENT-REFLECTING SHOCKS ON THE TURBULENT BOUNDARY LAYER

By S. Z. Pinckney

Langley Research Center
Langley Station, Hampton, Va.

NATIONAL AERONAUTICS AND SPACE ADMINISTRATION

For sale by the Clearinghouse for Federal Scientific and Technical Information
Springfield, Virginia 22151 – Price $2.30

7

DATA ON EFFECTS OF INCIDENT-REFLECTING SHOCKS ON THE TURBULENT BOUNDARY LAYER

By S. Z. Pinckney
Langley Research Center

SUMMARY

21101

An experimental investigation has been conducted to study the effect of the impingement of an incident-reflecting shock on the development of a turbulent boundary layer. The data are presented in the form of shadowgraphs and schlieren photographs of the shock—boundary-layer interaction region, boundary-layer Mach number and velocity profiles, and static-pressure and wall-temperature gradients on the flat plate. The Mach number varied from 2.0 to 4.36 and the Reynolds number based on boundary-layer thickness varied from approximately 0.22×10^6 to 2.22×10^6. The incident shock-turning angles were 6°, 8°, and 10°. The data show that the impingement of a two-dimensional incident-reflecting shock on a turbulent boundary layer decreases the boundary-layer velocity profile.

Autho

INTRODUCTION

The successful design and performance of inlets for hypersonic air-breathing propulsion systems requires a knowledge of the development of the turbulent boundary layer as influenced by the intersection of incident-reflecting shocks. The available experimental data presented in references 1 to 3 are for Mach numbers 3.0 (refs. 1 and 2) and 3.85 (ref. 3) and Reynolds numbers based on boundary-layer thickness from 0.26×10^6 to 0.58×10^6. The purpose of the present investigation was to extend the data over a broader range of variables and to produce needed information on the changes in the parameters of the turbulent boundary layer intersected by an incident-reflecting shock. A contract (NAS1-3489) was negotiated by the Langley Research Center with General Dynamics/Astronautics for this purpose. The results as received from General Dynamics/Astronautics are presented herein in the form of boundary-layer velocity and Mach number profiles, flat-plate static-pressure distributions, flat-plate temperature distributions, and shadowgraphs and schlieren photographs of the shock-interaction region. The Mach number varies from 2.0 to 4.36 and the Reynolds number based on boundary-layer thickness ranges from 0.22×10^6 to 2.22×10^6. Shock-generator wedge angles are 6°, 8°, and 10°. The experimental data of the present paper have been used in the analysis presented in reference 4, where a semiempirical method is formulated for predicting the effects of incident-reflecting shocks on the turbulent boundary layer.

SYMBOLS

M	Mach number
N	exponent of an exponential velocity profile $\frac{V}{V_l} = \left(\frac{y}{\delta}\right)^{1/N}$; fits as much of the actual boundary-layer velocity profile as possible
p	pressure
$R_{\delta,1}$	Reynolds number based on boundary-layer thickness δ_1
T	temperature, °Rankine
V	velocity
y	perpendicular distance from wall, inches
α	shock-generator wedge angle, degrees
δ	boundary-layer thickness at point where $M/M_l = 0.99$

Subscripts:

l	local free stream
t	stagnation conditions
w	wall
1	upstream of shock—boundary-layer interaction
2	conditions after normal shock

APPARATUS AND PROCEDURE

Shock-Generator Model

Figure 1 shows the shock-generator model, which consists of a flat plate (both a 24-inch-long and a 48-inch-long plate were used) with a different sidewall for each of the design Mach number areas investigated. Glass inserts were incorporated in the model sidewalls for schlieren and shadowgraph viewing of the incident-reflecting shock—boundary-layer interaction region; reference lines were located on the glass inserts. (Fig. 2 gives reference line dimensions.) A boundary-layer trip was mounted on the flat-plate leading edge (fig. 1) for the test runs in which the 48-inch-long flat plate was used; however, test runs for the 24-inch-long flat plate were conducted without a

boundary-layer trip. Plate leading-edge radii were on the order of 0.003 to 0.005 inch. Photographs of the shock-generator model features for the 48-inch-long flat plate are shown in figures 3 to 5 for each of the general Mach number areas investigated.

The shock-generator wedges were secured to the shock-generator model sidewalls in predetermined fixed positions, which were changed manually between runs. The wedge positions and lengths are listed in figure 6 for each test Mach number and wedge orientation angle. For the test runs in which the 48-inch-long flat plate was used the shock-generator wedge lengths were designed so that the wedges could be oriented at an angle of approximately 13° without exceeding the limiting supersonic starting contraction ratio of the model. For the test runs for the 24-inch-long flat plate, wedge extensions (see dimension E in fig. 6) were installed. This modification lengthens the distance between the intersections of the incident shock and the expansion fan with the flat plate. The expansion fan originates at the trailing edge of the shock-generator wedge surface.

Instrumentation

The static-pressure and temperature distributions on the surface of the flat plate were measured by 90 wall static-pressure orifices and 4 thermocouples, respectively, located as indicated in figure 1. Pitot-pressure and total-temperature surveys were made of the boundary layer both upstream and downstream of the shock—boundary-layer interaction region. The combination pitot-pressure and total-temperature probe used for the boundary-layer surveys is shown in figure 7. There was a small hole in the bottom of the probe which allowed a continuous flow of air over the thermocouple as the probe traversed. The airflow Mach number was approximately 0.1 (area-ratio calculation) and thus was believed to have no significant effect on pitot-pressure measurements. The probe drive was designed so that the probe could be remotely actuated perpendicular to the flat plate; a manual adjustment could be made in the axial direction only when the tunnel was not in operation. The vertical probe speeds for boundary-layer surveys of the 24-inch and 48-inch plates were approximately 0.125 and 0.20 inch per second, respectively. The opening of an electrical ground-strip contact between the probe tip and the plate surface determined the instant that the probe left the surface of the plate (zero indication). At contact with the plate, the probe center line was 0.024 inch from the flat-plate surface. During each test run, shadowgraphs and schlieren photographs of the shock—boundary-layer interaction region were taken by using the single-pass, parallel-beam combination shadowgraph and schlieren system shown schematically in figure 8.

Plate static pressures and boundary-layer pitot pressures were measured by means of pressure transducers. Flat-plate surface temperatures and boundary-layer total temperatures were measured by using copper-constantan thermocouples. The survey probe position was geared to a ten-turn potentiometer. The output of these measuring devices was recorded on tape on an analog digital converter.

Tunnel Description

The shock-generator model was sting mounted in the test section of the General Dynamics High Speed Wind Tunnel discussed in reference 5. The tunnel is of the blowdown type with a 4- by 4-foot test section. The range in tunnel Mach number is from 1.0 to 5.0 with stagnation temperatures up to 710° R and a range of Reynolds number per foot from 1.5×10^6 to 25×10^6. Run lengths are normally between 20 and 30 seconds. Unpublished results indicate that the variation in tunnel center-line flow angle (relative to the center line) is less than 0.2° at an axial location near the center of the schlieren windows.

Accuracy

Backlash in the probe drive mechanism made the determination of exact probe position difficult. The resulting inaccuracy in probe position was investigated by running the probe in both directions relative to the flat plate (away and toward), and the results revealed as much as 0.075-inch backlash (for several test runs) in the probe mechanism. The inaccuracy in probe position created by the backlash was overcome by operating the probe in a constant direction (away from the flat plate) in each run and by using an electrical contact between the probe and the flat plate to determine the zero probe position (position of the probe when the probe broke electrical contact with the plate surface).

The time lag due to the settling out of the pressure measurements may cause a change in the indicated local Mach number values. The effect of this time lag on the local Mach number was investigated by introducing a brief pause in probe traverse at about the midposition of the survey (where boundary-layer total-pressure gradient is present). Less than a 1-percent change in local Mach number values was indicated for the cases investigated.

The plotting accuracy of the data presented in this report is limited to the capability of the automatic plotter. A check of the zero location of the probe position revealed inaccuracies due to backlash effects, as mentioned previously. The data points of the boundary-layer Mach number and velocity profile plots must therefore be corrected in the y-direction by the amounts presented in table I for each test run. Comparison of the data points made by the automatic plotter with tabulated results (furnished by General Dynamics/Astronautics) revealed inaccuracies of less than 0.5 percent in probe position, Mach number, and plate static pressure.

The pressure transducers used to measure flat-plate static pressures and boundary-layer pitot pressures are accurate to ±0.5 percent and ±1 percent of full scale, respectively. The error in pitot-pressure measurements gave a maximum inaccuracy in Mach number value of approximately ±0.5 percent.

Procedure

In addition to shadowgraphs and schlieren photographs of the shock interaction region, the present investigation includes boundary-layer pitot-pressure

and total-temperature surveys along with flat-plate static-pressure and surface-temperature distributions. Table II presents a list of test runs conducted and the types of data (identified by checkmarks) obtained for each run. No shock interaction region was present for the runs in table II for which no flat-plate surface static-pressure distributions are indicated. The abbreviation "Rep" and the question mark indicate repeat static-pressure runs and questionable plate static pressures, respectively. No data are presented for either of these cases. In general, for the runs for which neither boundary-layer Mach number nor velocity profiles are presented, the boundary-layer surveys were taken in a region in which the static pressure could not be assumed constant across the boundary layer.

The experimental data were recorded on an analog digital converter in five steps of electrical readout. Step 1 consisted of the electrical readout of the boundary-layer survey data, and in all except runs 1 to 10, step 1 was conducted before steps 2 to 5. This technique enabled the probe to be well clear of the flat-plate surface when the flat-plate surface static pressures and temperatures were recorded. In runs 1 to 10, step 1 was conducted after steps 2 to 5. Steps 2 to 5 consisted of the electrical readout of flat-plate static pressures, flat-plate surface temperatures, and tunnel operating conditions.

Data Reduction

The tape on which the experimental data of the tunnel and shock-generator model were recorded is introduced into an IBM 1401 electronic data-processing system along with the proper program to obtain the final data. The experimental data on the tape consist of probe height y, pitot pressures $p_{t,2}$, total temperatures T_t, and flat-plate surface temperatures and static pressures. In the computer calculations, the static pressure across the boundary layer is assumed constant and equal to the local wall value. Thus, the Mach number distribution for each boundary-layer survey is computed from the distribution of the ratio $p/p_{t,2}$. For each boundary-layer survey the local free-stream Mach number M_l and total temperature $T_{t,l}$ were chosen at the point in the boundary layer where the maximum Mach number was realized. Upon the introduction of these local free-stream parameters into the IBM 1401 electronic data-processing system, the velocity distribution of the corresponding boundary-layer survey is calculated by using the following equation:

$$\frac{V}{V_l} = \left(\frac{T_t}{T_{t,l}}\right)^{1/2} \frac{M}{M_l}\left(\frac{1 + 0.2M_l^2}{1 + 0.2M^2}\right)^{1/2}$$

RESULTS AND DISCUSSION

The results of the present experimental investigation are presented in the form of shadowgraphs and schlieren photographs (figs. 9 to 11), flat-plate

surface static-pressure distributions and wall-temperature gradients (figs. 12 to 48), boundary-layer Mach number profiles (figs. 49 to 117), and boundary-layer velocity profiles (figs. 118 to 185). Table III presents identifying conditions for each of the test runs, including the tunnel Mach number, stagnation pressure, and stagnation temperature along with the local free-stream values of Mach number M_l and total temperature $T_{t,l}$ corresponding to the boundary-layer survey of each run. Figures 12 to 185 were plotted by the automatic data plotter of General Dynamics/Astronautics.

The typical schlieren photographs presented in figures 9 to 11 show the shock—boundary-layer intersections for local free-stream Mach numbers upstream of the incident shock of 1.99, 3.03, and 4.27, respectively, at incident shock-turning angles of 6°, 8°, and 10°. In addition to schlieren photographs, figures 10 and 11 present shadowgraphs of the shock—boundary-layer intersection region. Examination of figures 9, 10, and 11 shows that the incident and reflected shocks intersect at progressively greater distances from the flat-plate surface as the incident shock-turning angle increases.

The boundary-layer buildup on the shock-generator wedge increases the effective wedge angle and the strength of the incident shock interacting with the flat-plate boundary layer. This increase in shock strength can be seen in figure 186 where the theoretical incident shock-turning angle is plotted against the increase in turning angle $(\alpha_{data} - \alpha_{wedge})$. The angle α_{data} corresponds to the experimental peak pressure rise on the flat plate. Figure 186 shows that the increase in incident shock-turning angle due to the boundary-layer buildup on the shock-generator wedge surface is generally less than 1° in magnitude.

The backlash in the probe mechanism is illustrated in the figures of the velocity and Mach number profiles of runs 1 to 10, 46, 81, and 83 for which the probe was allowed to traverse both toward and away from the flat plate. The effect of time lag on probe pitot-pressure measurements is illustrated in figures 59 and 127.

The curves of figure 187 show that the boundary-layer thickness δ in general decreases across an incident-reflecting shock; as shown in reference 4, the thickness does not decrease, however, when severe boundary-layer separation occurs (for example, see curves for $\alpha = 8^\circ$ and $\alpha = 10^\circ$ in fig. 187(a)). The boundary-layer thicknesses plotted in figure 187 were chosen at the point in the boundary layer where the ratio M/M_l has a value of 0.99. The curves of figure 187 also show that outside the pressure-gradient region the boundary-layer thickness increases in the streamwise direction. This increase in boundary-layer thickness is primarily caused by the turbulent mixing of free-stream flow into the boundary layer. This mixing causes a more uniform momentum distribution in the boundary layer. In figure 187(c), the data that show the boundary-layer thickness development downstream of the flat-plate surface-pressure gradient for $\alpha = 10^\circ$ are not considered reliable because the edge of the boundary layer is believed to be in a pressure-gradient region.

The curves of figure 188 show that the boundary-layer velocity profile index N in the constant-pressure region downstream of the flat-plate surface pressure gradient decreases as the incident shock-turning angle increases. The

profile index N of figure 188 is the exponent of the exponential velocity profile $\frac{V}{V_l} = \left(\frac{y}{\delta}\right)^{1/N}$. The exponent N determines the best fit of the actual boundary-layer velocity profile. The profile index downstream of the pressure-gradient region increases, however, with plate distance from the reference station.

CONCLUDING REMARKS

An experimental investigation has been conducted to study the effect of the impingement of an incident-reflecting shock on the development of a turbulent boundary layer. The Mach number varied from 2.0 to 4.36 and the Reynolds number based on boundary-layer thickness varied from approximately 0.22×10^6 to 2.22×10^6. In general, the experimental data show that the impingement of a two-dimensional incident-reflecting shock on a turbulent boundary layer reduces the boundary-layer thickness across the shock except when severe boundary-layer separation occurs. The impingement of a two-dimensional incident-reflecting shock on a turbulent boundary layer decreases the boundary-layer velocity profile.

Langley Research Center,
National Aeronautics and Space Administration,
Langley Station, Hampton, Va., November 24, 1965.

REFERENCES

1. Kepler, C. E.; and O'Brien, R. L.: Supersonic Turbulent Boundary Layer Growth Over Cooled Walls in Adverse Pressure Gradients. ASD-TDR-62-87, U.S. Air Force, Oct. 1962.

2. Bogdonoff, S. M.; Kepler, C. E.; and Sanlorenzo, E.: A Study of Shock Wave Turbulent Boundary Layer Interaction at M = 3. Rept. No. 222 (Contract No. N6-onr-270, Task Order No. 6, Project No. NR-061-049), Dept. Aeron. Eng., Princeton Univ., July 1953.

3. Vas, I. E.; and Bogdonoff, S. M.: Interaction of a Shock Wave With a Turbulent Boundary Layer at M = 3.85. Rept. No. 294 (AFOSR TN 55-199), Dept. Aeron. Eng., Princeton Univ., April 1955.

4. Pinckney, S. Z.: Semiempirical Method for Predicting Effects of Incident-Reflecting Shocks on the Turbulent Boundary Layer. NASA TN D-3029, 1965.

5. Anon.: Facility Manual - The General Dynamics High Speed Wind Tunnel. GD/C-64-182, Gen. Dyn./Convair, Apr. 1964.

TABLE I

PROBE-HEIGHT CORRECTION FACTORS[1]

Run	Correction, in.	Run	Correction, in.	Run	Correction, in.	Run	Correction, in.
1	-0.008	22	-0.005	43	-0.030	64	-0.012
2		23	.004	44	.008	65	-.027
3	-.008	24	.004	45	-.038	66	-.011
4		25	-.010	46		67	-.010
5		26	-.013	47	-.018	68	
6		27		48	-.006	69	
7		28	-.003	49		70	
8		29		50	-.030	71	
9		30	.005	51	-.010	72	
10		31	-.006	52		73	
11	.007	32		53		74	
12		33		54		75	
13		34	-.006	55	-.007	76	
14	-.009	35		56		77	
15	-.012	36		57		78	
16	.002	37		58		79	
17		38		59		80	
18		39		60		81	
19		40		61		82	
20		41		62	-.007	83	
21		42	-.032	63		84	

[1]No data were obtained for runs for which no correction is indicated.

TABLE II

TYPES OF EXPERIMENTAL DATA OBTAINED FOR EACH TEST RUN

Run	Pitot pressure surveys	Total temperature surveys	Flat-plate surface temperatures	Shadowgraphs and schlieren photographs (a)	Boundary-layer Mach number profiles, M	Boundary-layer velocity profiles, V/V_1	Flat-plate static pressures (b)	Run	Pitot pressure surveys	Total temperature surveys	Flat-plate surface temperatures	Shadowgraphs and schlieren photographs (a)	Boundary-layer Mach number profiles, M	Boundary-layer velocity profiles, V/V_1	Flat-plate static pressures (b)
1	✓	✓	✓	✓	✓		✓	43	✓	✓	✓	✓	✓	✓	
2	✓	✓	✓	✓	✓	✓		44	✓	✓	✓	✓	✓	✓	
3	✓	✓	✓	✓	✓	✓		45	✓	✓	✓	✓	✓	✓	
4	✓	✓	✓	✓	✓	✓		46	✓	✓	✓	✓	✓	✓	
5	✓	✓	✓	✓	✓	✓		47	✓	✓	✓	✓	✓	✓	
6	✓	✓	✓	✓	✓	✓		48	✓	✓	✓	✓	✓	✓	✓
7	✓	✓	✓	✓	✓	✓		49	✓	✓	✓	✓	✓	✓	✓
8	✓		✓		✓	✓		50	✓	✓	✓	✓	✓	✓	Rep
9	✓		✓	✓	✓	✓		51	✓	✓	✓	✓	✓	✓	Rep
10	✓		✓	✓	✓	✓		52	✓	✓	✓	✓	✓	✓	Rep
11	✓	✓	✓	✓	✓	✓	✓	53	✓	✓	✓	✓	✓	✓	✓
12	✓	✓	✓	✓	✓	✓	✓	54	✓	✓	✓	✓	✓	✓	✓
13	✓	✓	✓	✓	✓	✓	✓	55	✓	✓	✓	✓	✓	✓	Rep
14	✓	✓	✓	✓	✓	✓	✓	56	✓	✓	✓	✓	✓	✓	Rep
15	✓	✓	✓	✓	✓	✓	Rep	57	✓	✓	✓	✓	✓	✓	✓
16	✓	✓	✓	✓	✓	✓	Rep	58	✓	✓	✓	✓	✓	✓	✓
17	✓	✓	✓	✓	✓	✓	✓	59	✓	✓	✓	✓	✓	✓	Rep
18	✓	✓	✓	✓	✓	✓	✓	60	✓	✓	✓	✓	✓	✓	Rep
19	✓	✓	✓	✓	✓	✓	✓	61	✓	✓	✓	✓	✓	✓	✓
20	✓	✓	✓	✓	✓	✓	Rep	62	✓	✓	✓	✓	✓	✓	Rep
21	✓	✓	✓	✓	✓	✓	✓	63	✓	✓	✓	✓	✓	✓	✓
22	✓	✓	✓	✓	✓	✓	✓	64	✓	✓	✓	✓	✓	✓	Rep
23	✓	✓	✓	✓	✓	✓	✓	65	✓	✓	✓	✓	✓	✓	
24	✓	✓	✓	✓	✓	✓	Rep	66	✓	✓	✓	✓	✓	✓	
25	✓	✓	✓	✓	✓	✓		67	✓	✓	✓	✓	✓	✓	
26	✓	✓	✓	✓	✓	✓		68			✓	✓			✓
27	✓	✓	✓	✓	✓	✓		69	✓	✓	✓	✓	✓	✓	Rep
28	✓	✓	✓	✓	✓	✓	✓	70	✓	✓	✓	✓	✓	✓	✓
29	✓	✓	✓	✓	✓	✓	✓	71	✓	✓	✓	✓	✓	✓	Rep
30	✓	✓	✓	✓	✓	✓	✓	72	✓	✓	✓	✓	✓	✓	✓
31	✓	✓	✓	✓	✓	✓	Rep	73	✓	✓	✓	✓	✓	✓	✓
32	✓	✓	✓	✓			✓	74	✓	✓	✓	✓			Rep
33	✓	✓	✓	✓			✓	75	✓	✓	✓	✓			Rep
34	✓	✓	✓	✓			✓	76	✓	✓	✓	✓	✓	✓	✓
35	✓	✓	✓	✓			Rep	77	✓	✓	✓	✓	✓	✓	✓
36	✓	✓	✓	✓			✓?	78	✓	✓	✓	✓			Rep
37	✓	✓	✓	✓			✓?	79	✓	✓	✓	✓			Rep
38	✓	✓	✓	✓			✓?	80	✓	✓	✓	✓	✓	✓	
39	✓	✓	✓	✓			✓?	81	✓	✓	✓	✓	✓	✓	Rep
40	✓	✓	✓	✓			✓?	82	✓	✓	✓	✓	✓	✓	Rep
41	✓	✓	✓	✓			✓?	83	✓	✓	✓	✓	✓	✓	Rep
42	✓	✓	✓	✓	✓	✓		84	✓	✓	✓	✓	✓	✓	Rep

[a]No shadowgraphs were obtained for runs 46 to 84.

[b]Repeat runs are indicated by the abbreviation "Rep," and questionable plate pressures are indicated by a question mark. No data are presented for either of these conditions.

TABLE III

IDENTIFYING CONDITIONS FOR EXPERIMENTAL TEST RUNS

Run	Axial location of flat-plate surveys, in.	Plate length, in.	Tunnel Mach number	$T_{l,t}$, °R	M_l	Tunnel stagnation pressure, psia	Example shadowgraphs and schlieren photographs	Shock-generator wedge angle, deg	Tunnel stagnation temperature, °R	$M_{l,1}$	$R_{\delta,1}$
1	3.90	48	2.0			36.79		6	523	1.95	0.72 × 10^6
2	-.50	48	2.0	511	1.916	36.49		0	522	1.92	.72
3	-.50	48	2.0	527	1.952	24.65		0	538	1.95	.52
4	-.50	48	2.0	521	1.900	48.11		0	529	1.90	.97
5	-.50	48	2.99	534	2.885	55.25		0	547	2.89	.61
6	-.50	48	2.99	541	2.867	76.50		0	552	2.87	.96
7	-.50	48	2.99	545	2.821	99.34		0	554	2.82	1.18
8	-.50	48	4.36	495	4.165	235.0		0	536.5	4.19	1.64
9	-.50	48	4.36	495	4.266	193.2		0	545.2	4.27	1.26
10	-.50	48	4.36	495	4.103	314.4		0	557.6	4.10	2.22
11	4.0	48	2.99	531	2.267	55.19		6	540.7	2.84	.61
12	4.0	48	3.2	508	2.373	66.66	✓	6	520.7	3.03	.78
13	4.0	48	3.2	516	2.360	90.50		6	525.7	3.05	1.06
14	4.0	48	3.2	520	2.360	119.7		6	530.7	3.04	1.45
15	3.2	48	3.2	529	2.345	66.96		6	539.2	3.02	.78
16	3.2	48	3.2	532	2.323	90.50		6	541.2	3.05	1.06
17	4.0	48	3.2	531	2.204	66.66	✓	8	538.2	3.02	.78
18	4.0	48	3.2	537	2.203	90.50		8	542.2	3.05	1.06
19	4.0	48	3.2	518	2.200	120.6		8	525.2	3.04	1.45
20	3.5	48	3.2	530	2.072	90.80		10	536.7	3.05	1.06
21	4.0	48	3.2	506	2.079	66.96	✓	10	516.7	3.02	.78
22	4.0	48	3.2	511	2.056	90.50		10	520.7	3.05	1.06
23	4.0	48	3.2	520	2.050	120.2		10	529.2	3.04	1.45
24	3.8	48	3.2	524	2.054	120.8		10	537.2	3.04	1.45
25	-.50	48	3.2	518	3.024	66.81		0	531.7	3.02	.78
26	-.50	48	3.2	524	3.048	90.50		0	534.2	3.05	1.06
27	-.50	48	3.2	516	3.035	120.6		0	529.7	3.04	1.45
28	6.0	48	2.4	534	1.776	63.06		6	540.7	2.27	1.05
29	5.5	48	2.4	525	1.790	47.86		6	532.7	2.31	.81
30	5.5	48	2.4	538	1.810	33.65		6	545.2	2.33	.53
31	5.5	48	2.4	542	1.785	62.91		6	545.2	2.27	1.05
32	4.0	48	4.36	511	3.116	188		6	539.2	4.27	1.26
33	4.0	48	4.36	536	3.154	240.8		6	552.2	4.19	1.64
34	4.0	48	4.36	530	3.167	313.6		6	542.2	4.10	2.22
35	3.0	48	4.36	534	3.012	205.6	✓	6	550.7	4.27	1.26
36	5.0	48	4.36	545	2.873	242		8	556.7	4.19	1.64
37	5.0	48	4.36	538	2.874	188.8	✓	8	561.2	4.27	1.26
38	5.0	48	4.36	537	2.704	194.8	✓	10	559.7	4.27	1.26
39	5.0	48	4.36	530	2.727	242.4		10	546.7	4.19	1.64
40	5.0	48	4.36	535	2.721	313.2		10	550.7	4.10	2.22
41	5.0	48	4.36	546	2.855	311.6		8	558.7	4.10	2.22
42	-.50	48	4.36	539	4.176	242		0	559.7	4.19	1.64

Run	Axial location of flat-plate surveys, in.	Plate length, in.	Tunnel Mach number	$T_{l,t}$, °R	M_l	Tunnel stagnation pressure, psia	Example shadowgraphs and schlieren photographs	Shock-generator wedge angle, deg	Tunnel stagnation temperature, °R	$M_{l,1}$	$R_{\delta,1}$
43	-0.50	48	2.40	530	2.326	33.73		0	540.2	2.33	0.53 × 10^6
44	-.50	48	2.40	528	2.306	48.04		0	537.2	2.31	.81
45	-.50	48	2.40	539	2.273	65.21		0	547.7	2.27	1.05
46	-.50	24	2.0	535	1.969	24.40		0	538.2	1.97	.22
47	-.50	24	2.0	548	1.994	36.31		0	545.7	1.99	.27
48	7.5	24	2.0	539	1.529	24.64		6	540.7	1.97	.22
49	7.5	24	2.0	546	1.520	36.25		6	544.2	1.99	.27
50	4.2	24	2.0	556	1.521	25.06		6	555.7	1.97	.22
51	4.2	24	2.0	557	1.519	36.73		6	554.7	1.99	.27
52	4.2	24	2.0	565	1.518	25.06		6	565.2	1.97	.22
53	7.5	24	2.0	563	1.389	25.00		8	562.2	1.97	.22
54	7.5	24	2.0	564	1.402	37.27		6	559.2	1.99	.27
55	5.8	24	2.0	562	1.410	25.67		8	564.2	1.97	.22
56	5.8	24	2.0	565	1.411	37.33		8	561.2	1.99	.27
57	6.5	24	2.0	528	1.386	25.06		10	533.2	1.97	.22
58	6.5	24	2.0	531	1.356	48.27		10	532.2	1.99	.36
59	5.3	24	2.0	547	1.346	25.00		10	531.2	1.97	.22
60	5.3	24	2.0	550	1.331	48.33	✓	10	549.7	1.99	.36
61	7.5	24	2.0	557	1.416	48.21	✓	8	552.2	1.99	.36
62	5.8	24	2.0	543	1.416	48.21		8	541.7	1.99	.36
63	7.5	24	2.0	555	1.528	48.03	✓	6	550.7	1.99	.36
64	4.2	24	2.0	565	1.523	48.15		6	562.7	1.99	.36
65	-.50	24	2.0	570	1.989	48.03		0	561.7	1.99	.36
66	-.50	24	4.2	570	4.238	155.6		0	572.7	4.24	.38
67	-.50	24	4.2	564	4.161	267.9		0	568.7	4.16	.74
68	-.50	24	4.2			162.8		10	536.2	4.24	.38
69	6.0	24	4.2	537	2.706	162.8		10	538.2	4.24	.38
70	7.5	24	4.2	546	2.687	266.3		10	548.7	4.16	.74
71	6.0	24	4.2	549	2.721	265.1		10	548.2	4.16	.74
72	7.0	24	4.2	552	2.947	164.0		8	549.7	4.24	.38
73	7.0	24	4.2	560	2.944	266.7		8	559.7	4.16	.74
74	3.5	24	4.2			164.0		8	550.2	4.24	.38
75	3.3	24	4.2			265.9		8	562.7	4.16	.74
76	7.5	24	4.2	570	3.20	164.0		6	567.7	4.24	.38
77	7.5	24	4.2	577	3.182	266.3		6	573.2	4.16	.74
78	3.2	24	4.2			164.0		6	564.2	4.24	.38
79	3.1	24	4.2			265.5		6	571.7	4.16	.74
80	-.50	48	4.2	540	4.149	209.9		0	544.2	4.15	1.16
81	6.0	24	4.2	527	3.258	165.6		6	529.7	4.24	.38
82	6.0	24	4.2	545	3.267	265.1		6	546.2	4.16	.74
83	5.5	24	4.2	550	2.936	161.6		8	547.2	4.24	.38
84	5.5	24	4.2	556	2.963	263.9		8	555.2	4.16	.74

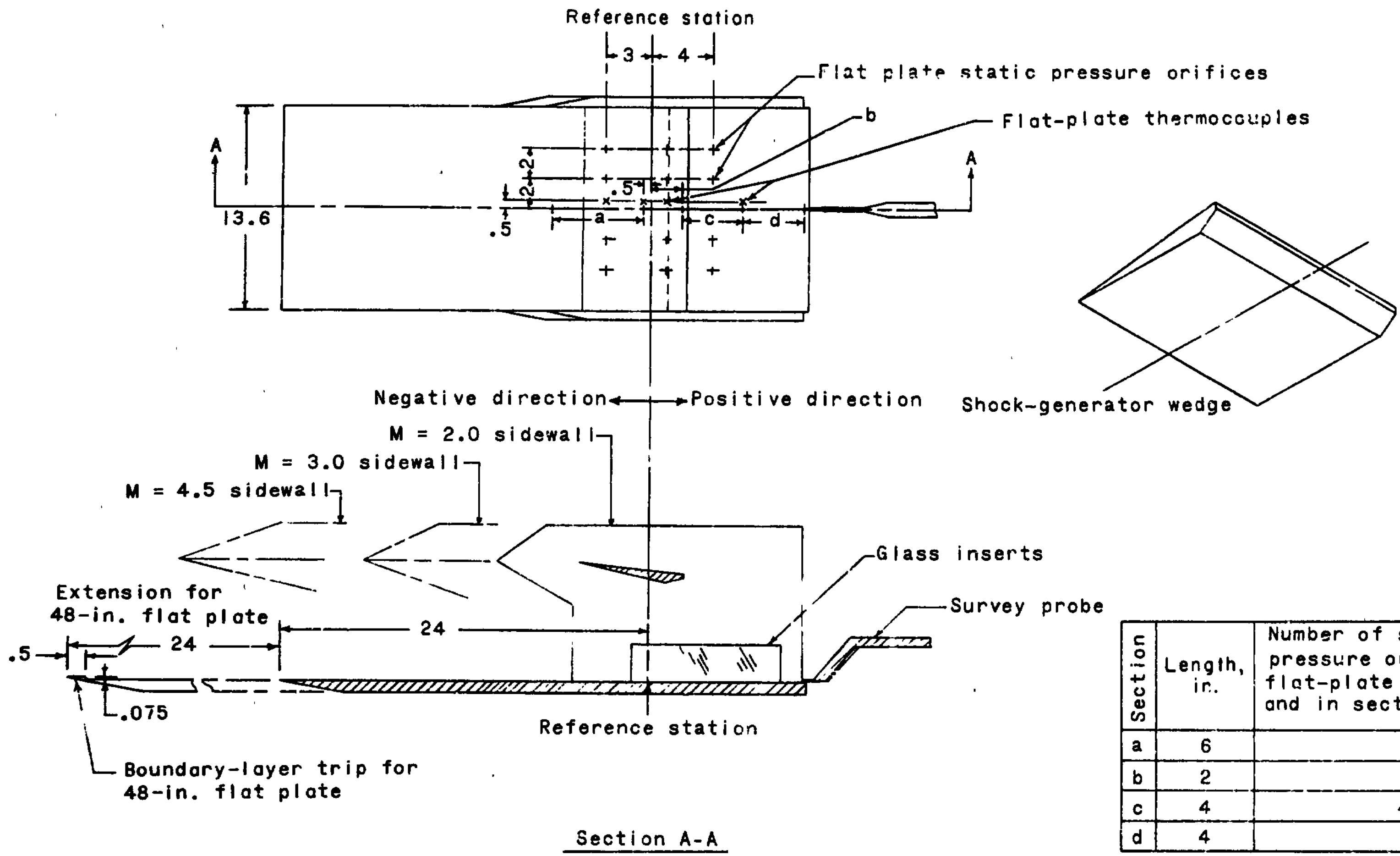

Section	Length, in.	Number of static pressure orifices on flat-plate center line and in section
a	6	13
b	2	9
c	4	40
d	4	16

Figure 1.- Schematic drawing of shock-generator model. All dimensions are in inches. Locations of pressure orifices indicated by + mark and locations of thermocouples indicated by × mark.

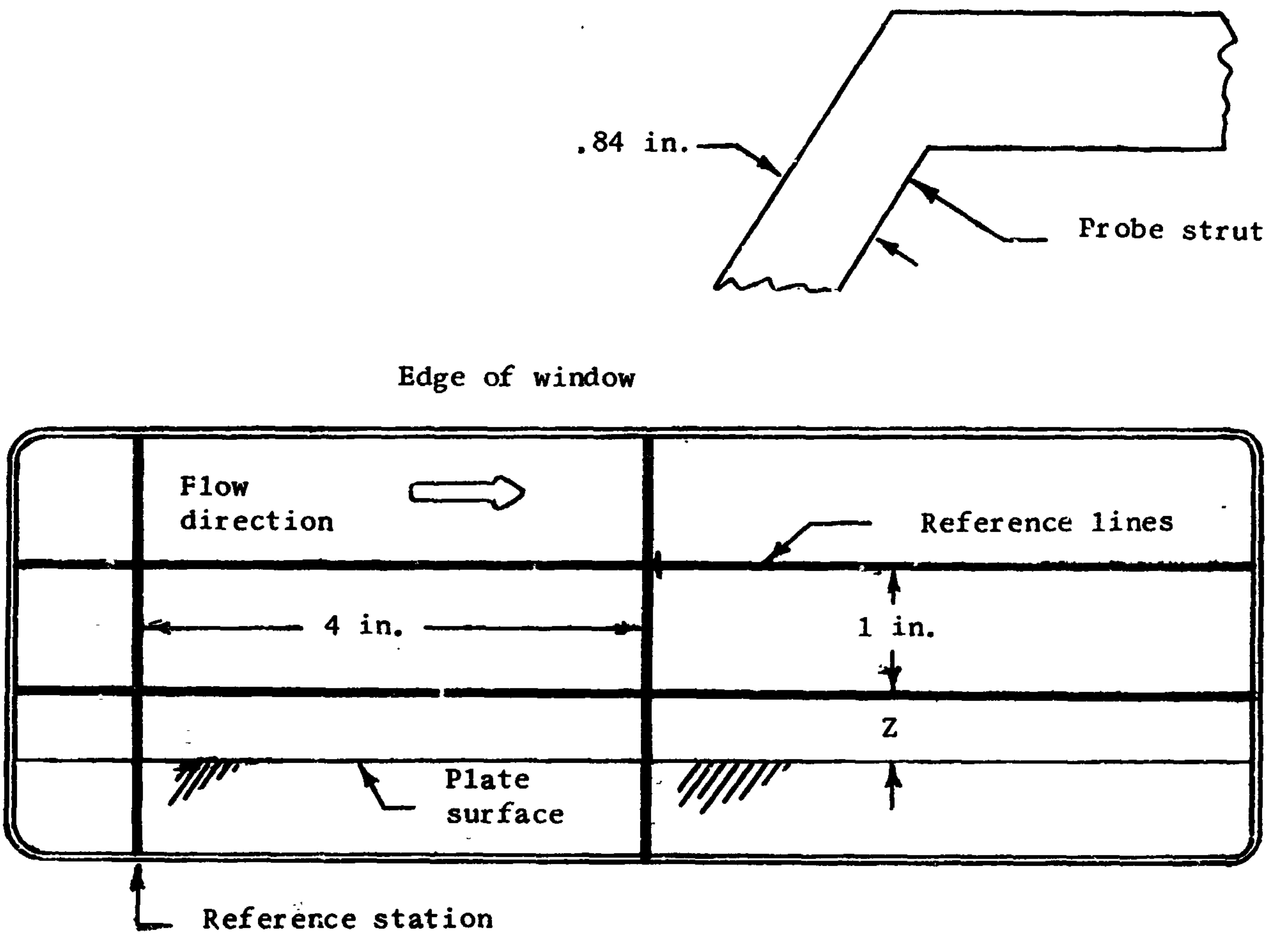

Configuration Mach number	Z, in.
2.0	0.49
3.0	.525
4.5	.55

Figure 2.- Sketch of optical viewing window with reference line dimensions.

L-65-9009

Figure 3.- Flat plate with Mach 2.0 sideplate and shock generator.

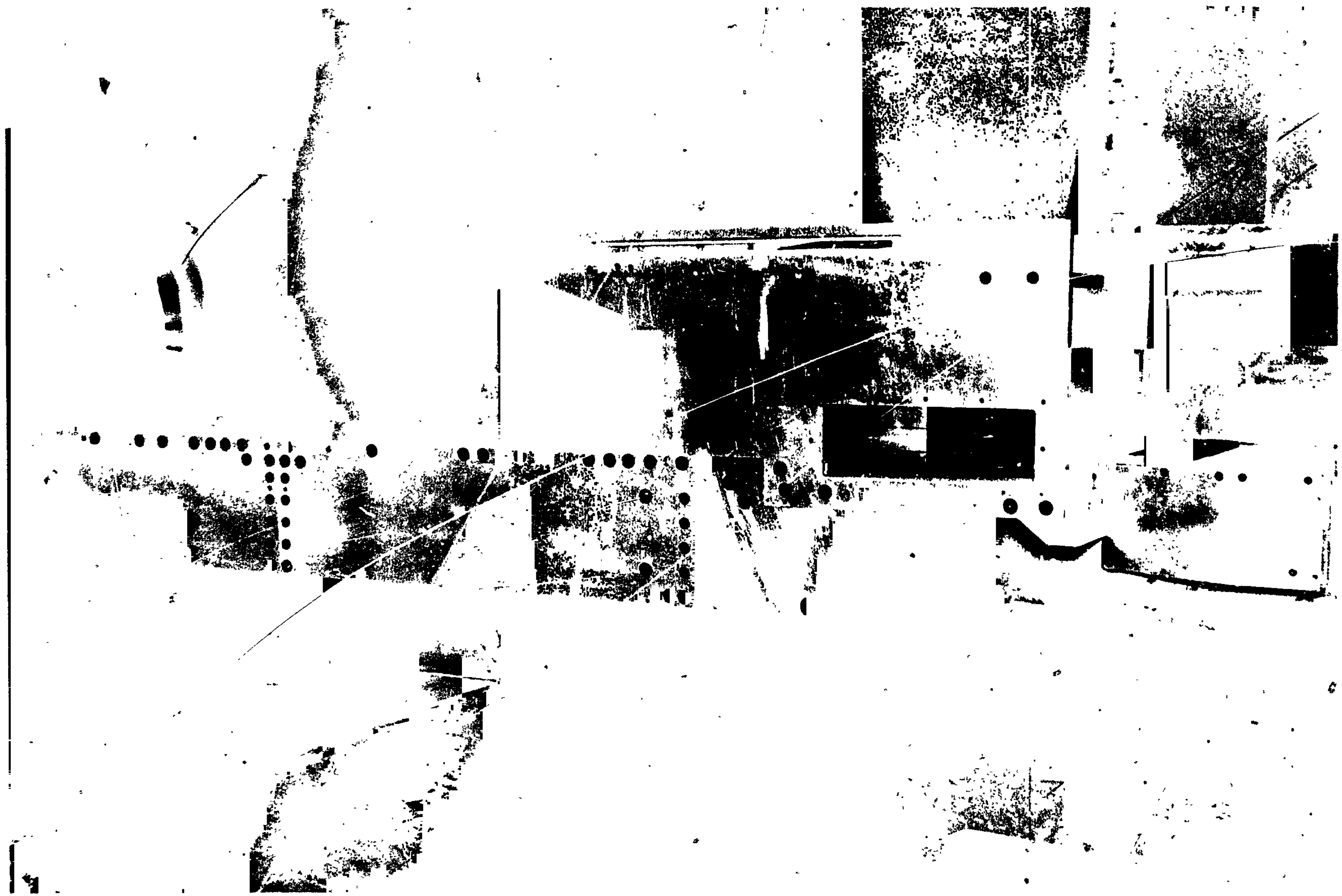

Figure 4.- Flat plate with Mach 3.0 sideplate and shock generator. L-65-9010

Figure 5.- Flat plate with Mach 4.5 sideplate and shock generator. L-65-9011

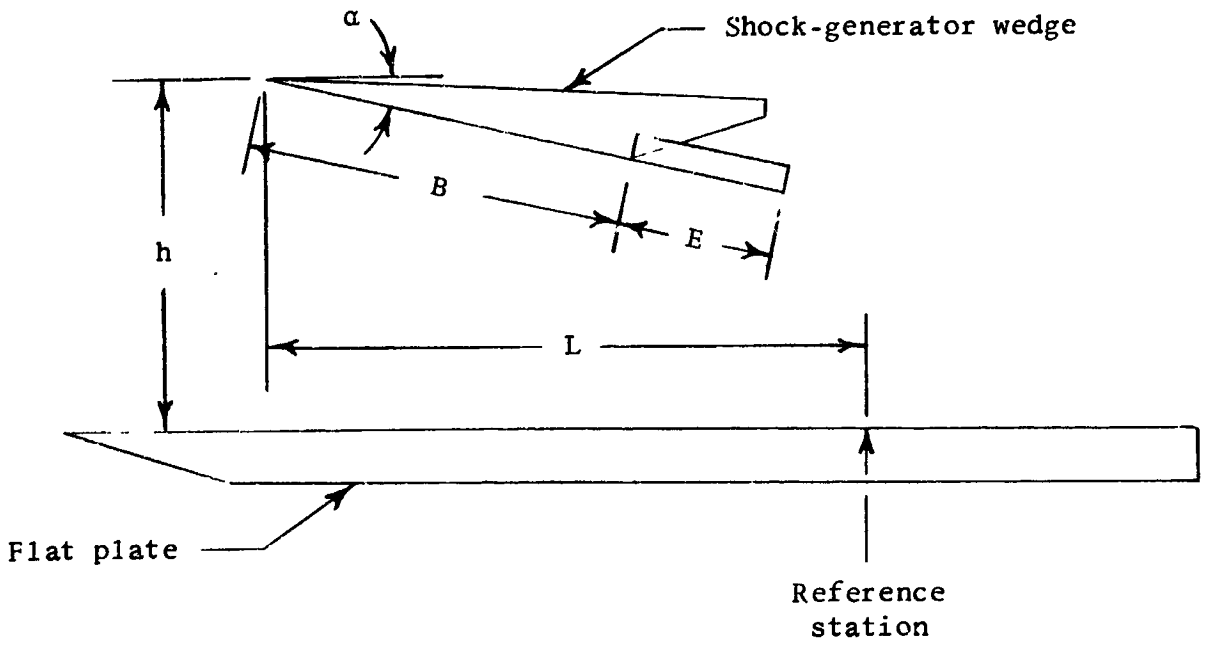

M_{test}	α, deg.	h, in.	Length of flat plate, in.	L, in.	B, in.	E, in.	(B + E), in.
2.0	6 8 10	8.0 8.075 8.0	24	7.77 6.97 6.17	5.926 5.926 5.926	3.0 3.0 1.0	8.926 8.926 6.926
2.4	6 8 10	8.0 8.075 8.0	48	9.87 8.50 8.20	5.926 5.926 5.926	0 0 0	5.926 5.926 5.926
2.99 and 3.2	6 8 10	8.0 8.0 8.0	48	16.97 15.62 14.37	9.744 9.744 9.744	0 0 0	9.744 9.744 9.744
4.2	6 8 10	8.0 8.0 8.0	24	21.09 18.88 16.70	11.855 11.855 11.855	3.5 3.5 2.5	15.355 15.355 14.355
4.36	6 8 10	8.0 8.0 8.0	48	21.09 18.88 16.70	11.855 11.855 11.855	0 0 0	11.855 11.855 11.855

Figure 6.- Shock-generator wedge geometry and position.

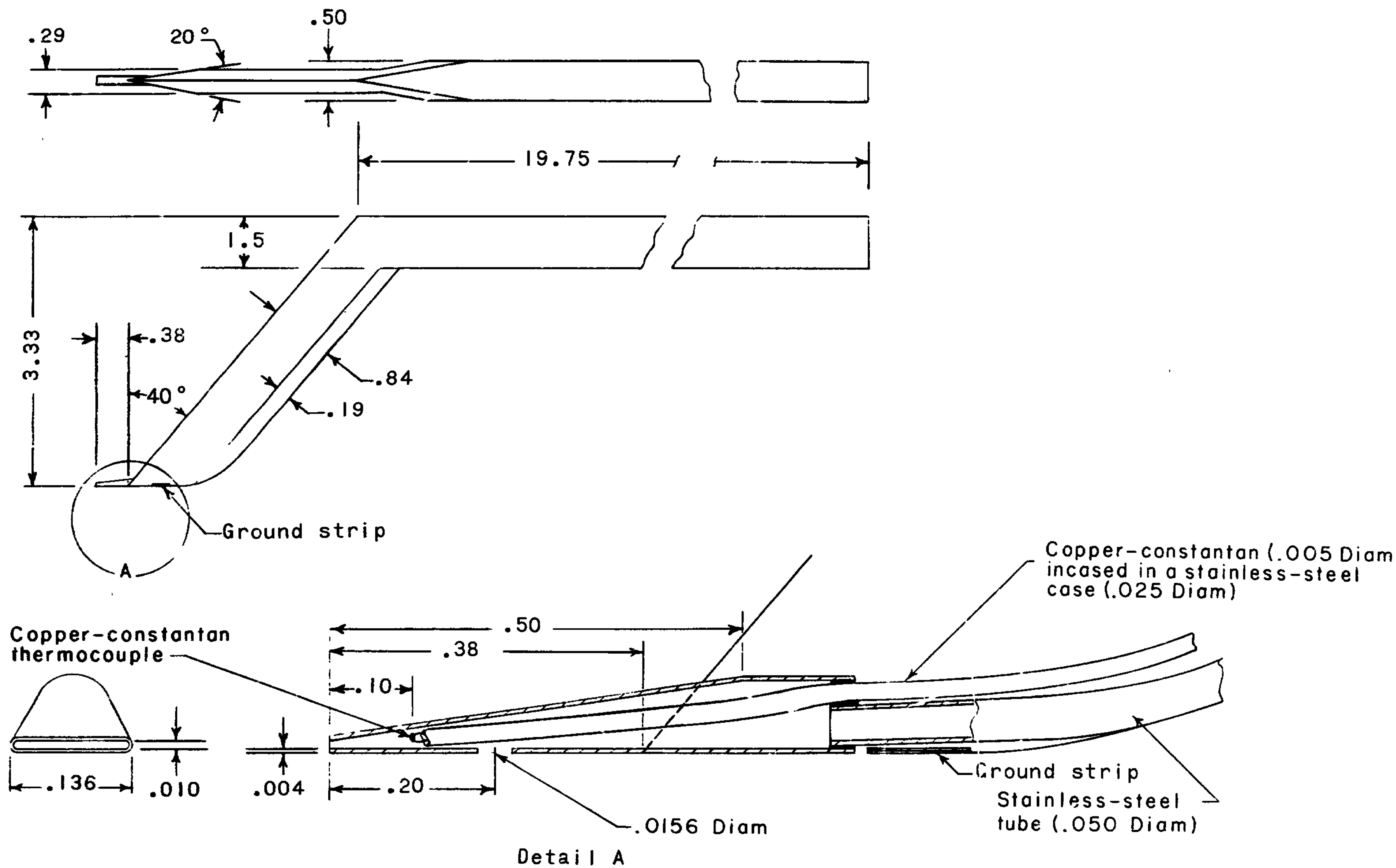

Figure 7.- Combination pitot pressure and total temperature probe. All dimensions are in inches.

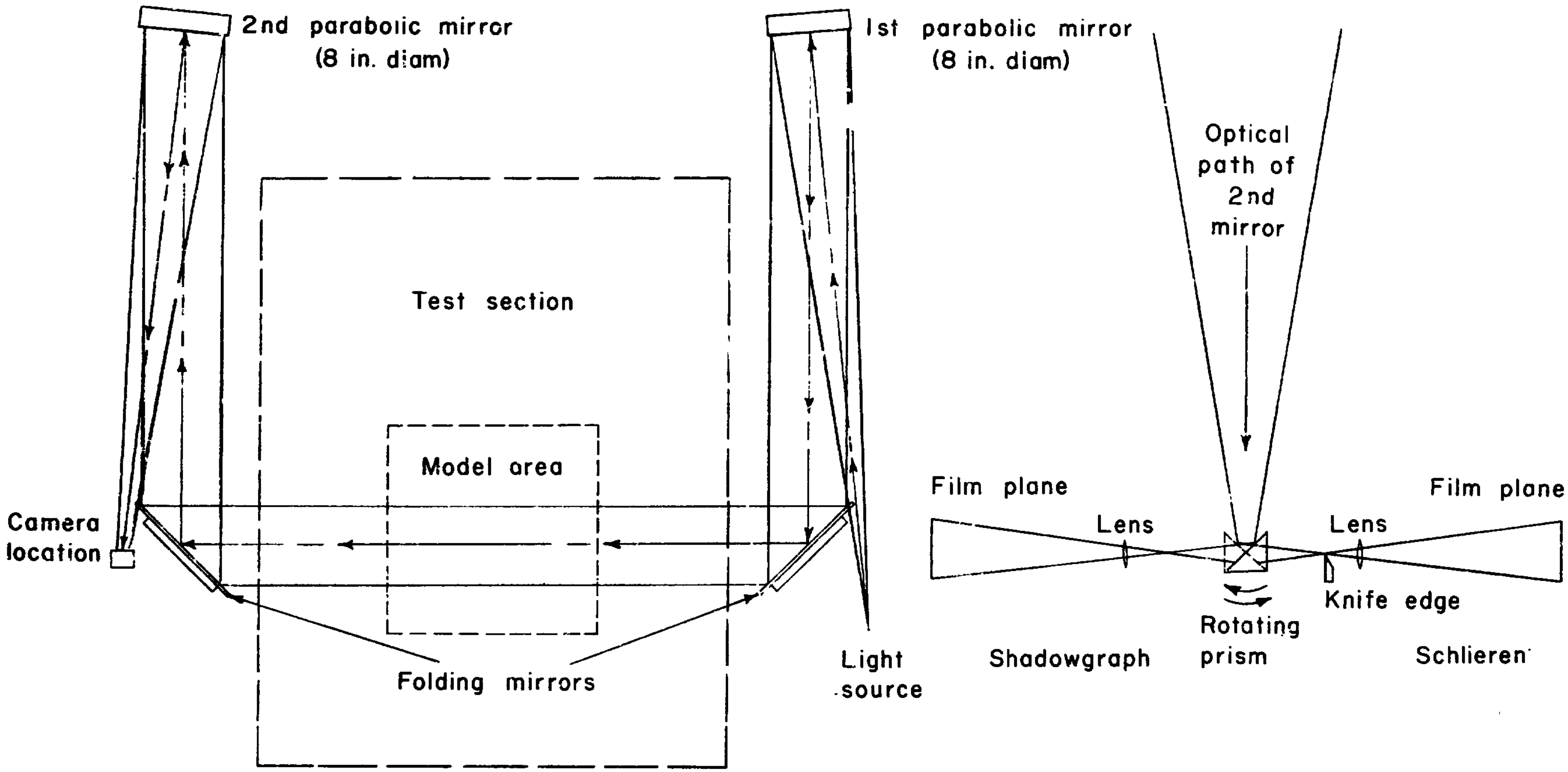

Figure 8.- Combination shadowgraph and schlieren system.

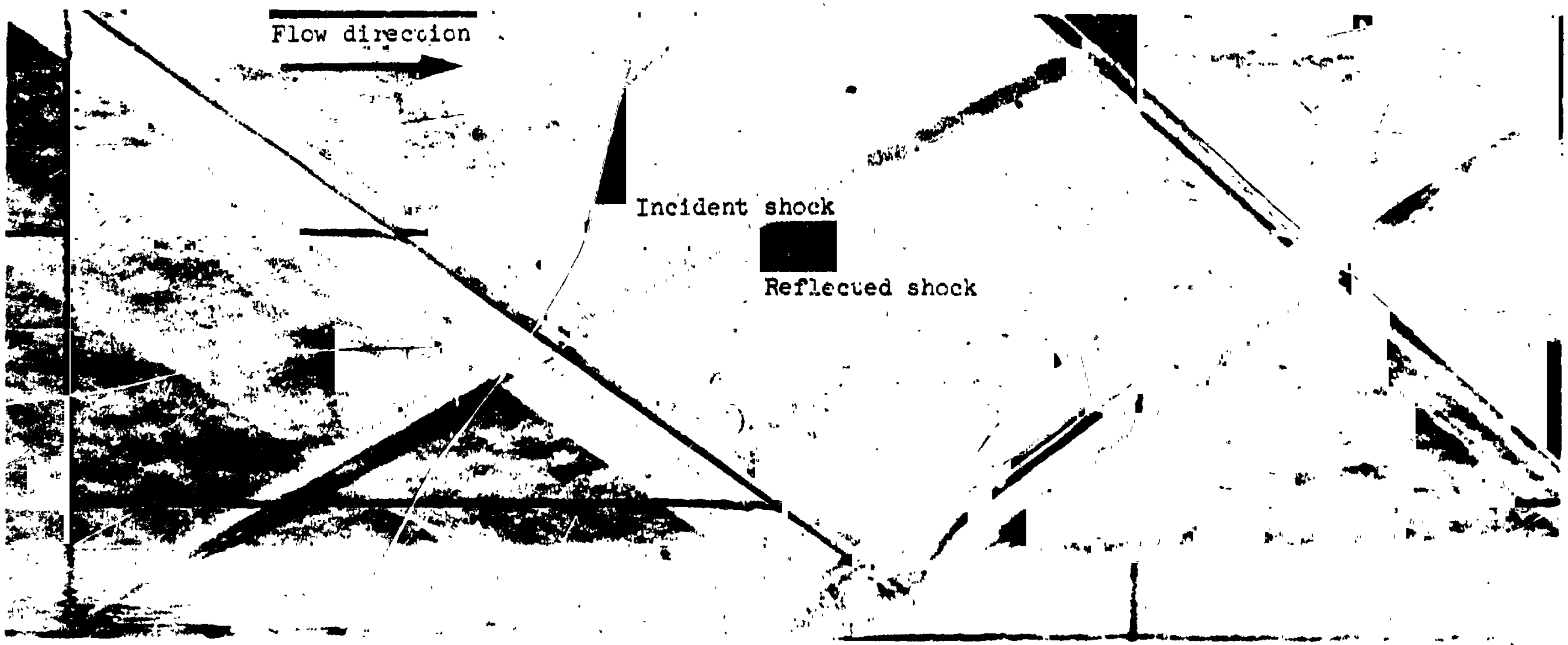

(a) $\alpha = 6^\circ$ (run 63).

L-65-9012

Figure 9.- Shock—boundary-layer intersection for $M_{l,1} = 1.99$.

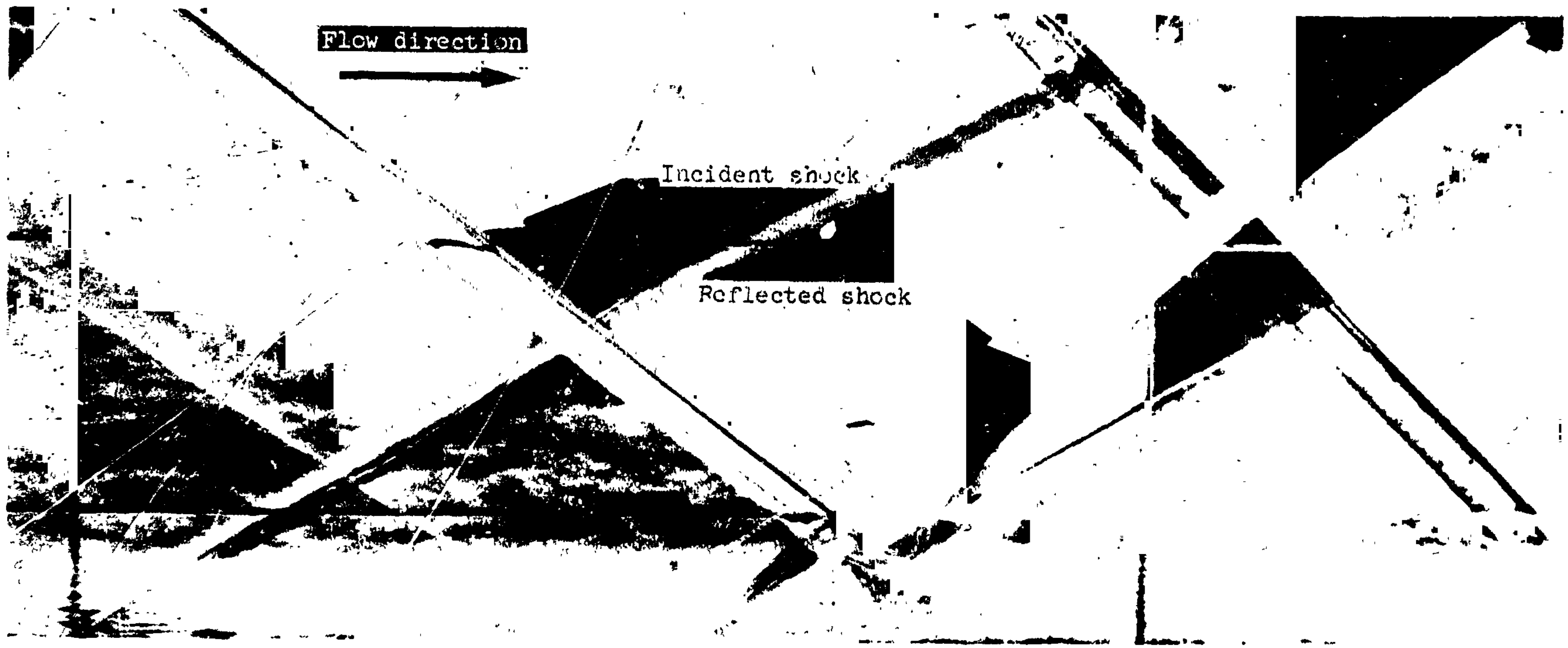

(b) $\alpha = 8^{\circ}$ (run 61).

L-65-9013

Figure 9.- Continued.

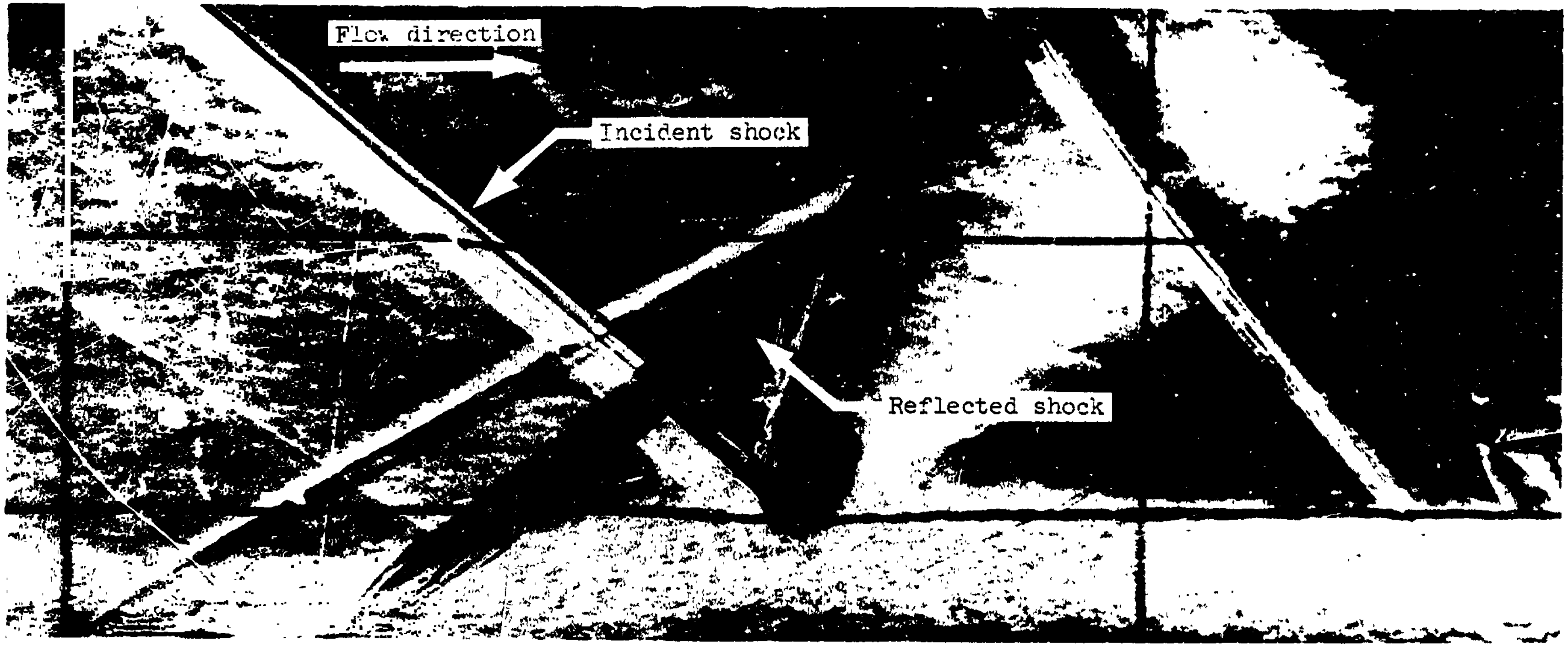

(c) $\alpha = 10^{\circ}$ (run 60).

L-65-9014

Figure 9.- Concluded.

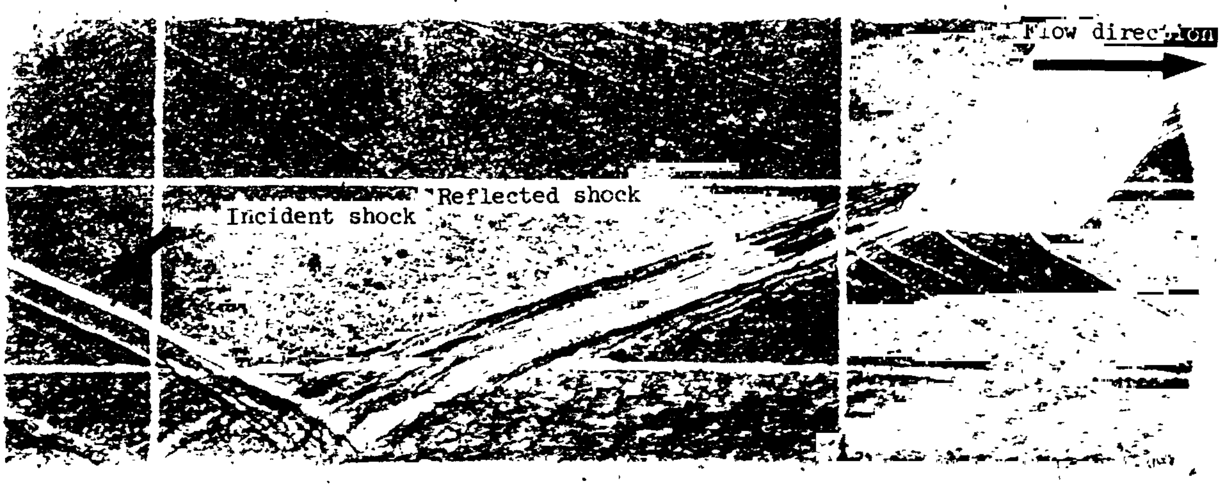

Shadowgraph

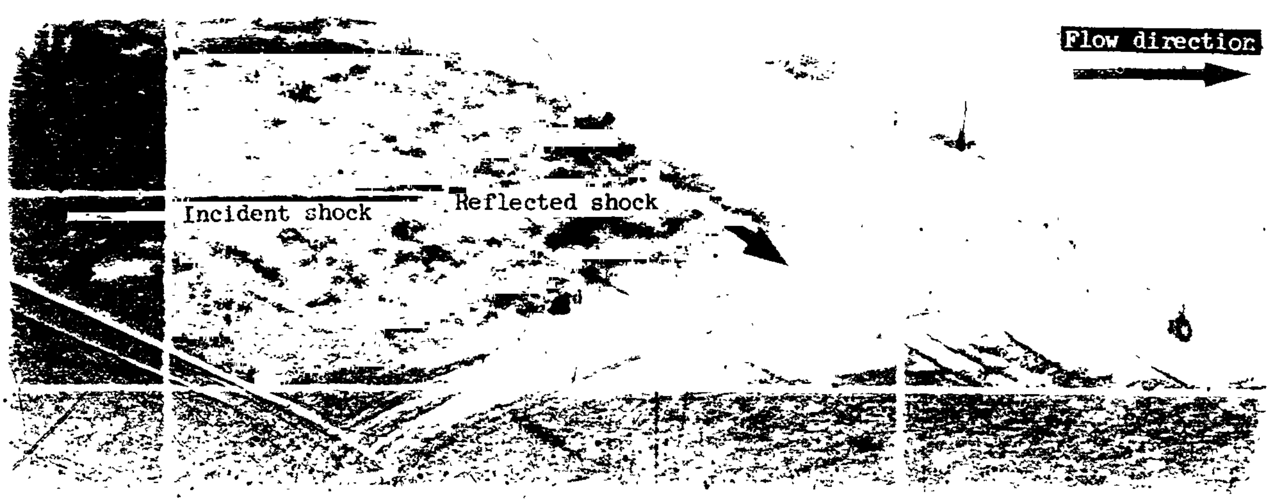

Schlieren photograph

(a) $\alpha = 6^{\circ}$ (run 12).

L-65-9015

Figure 10.- Shock—boundary-layer intersection for $M_{l,1} = 3.03$.

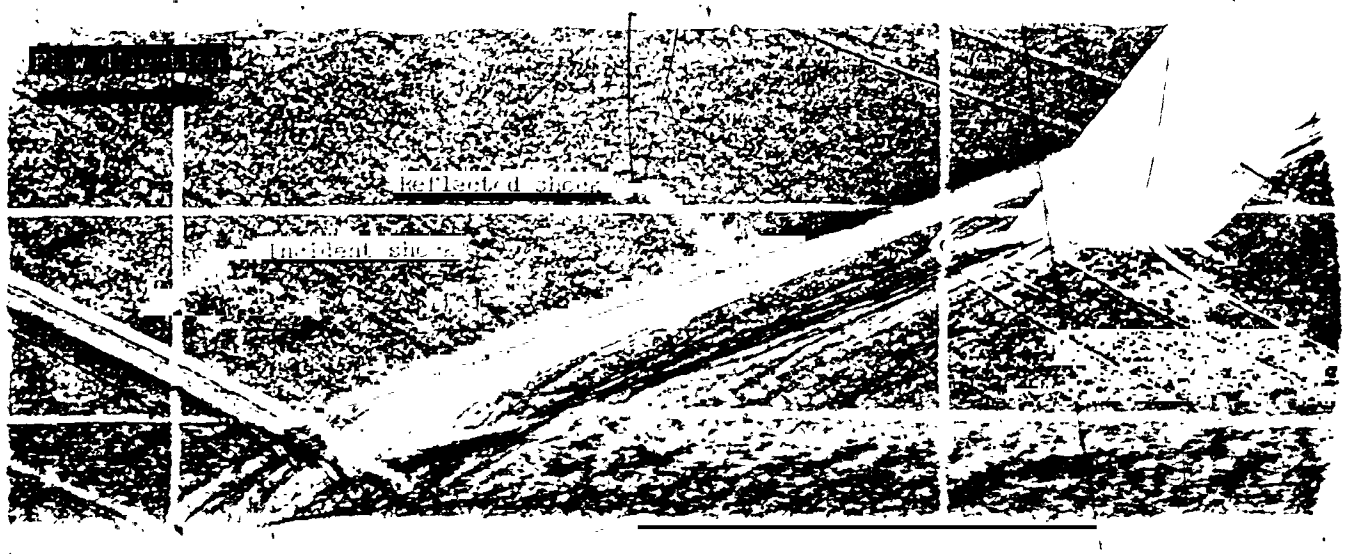

Shadowgraph

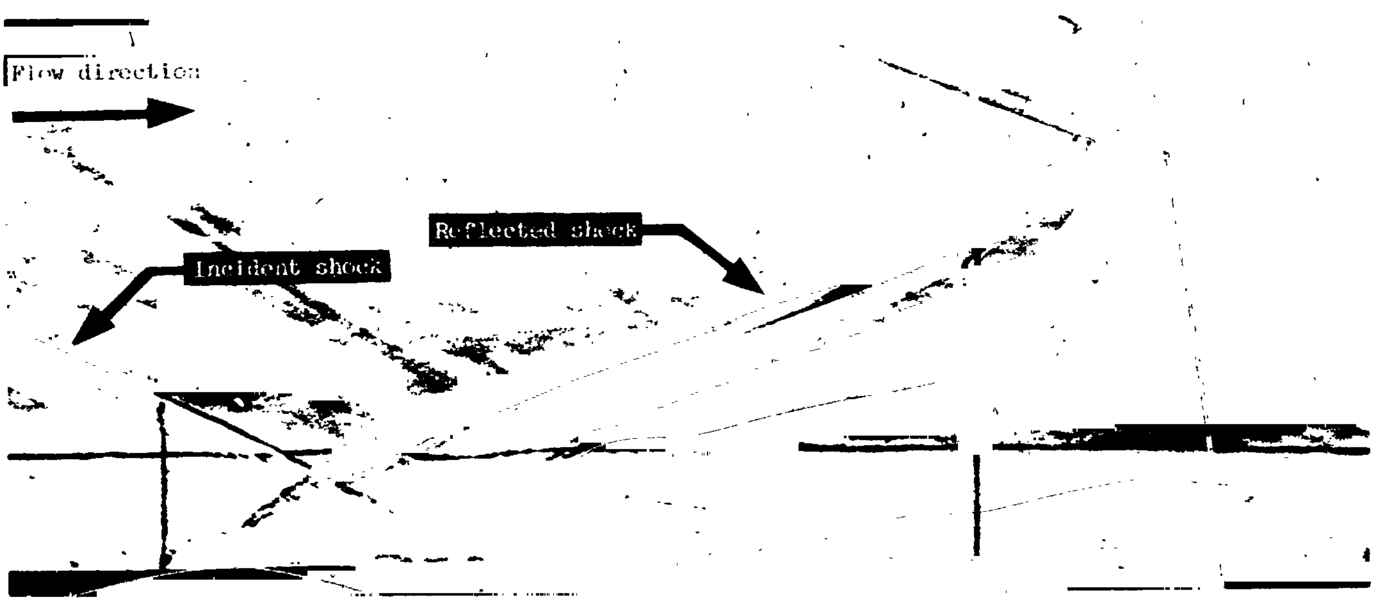

Schlieren photograph

(b) $\alpha = 8^{\circ}$ (run 17). L-65-9016

Figure 10.- Continued.

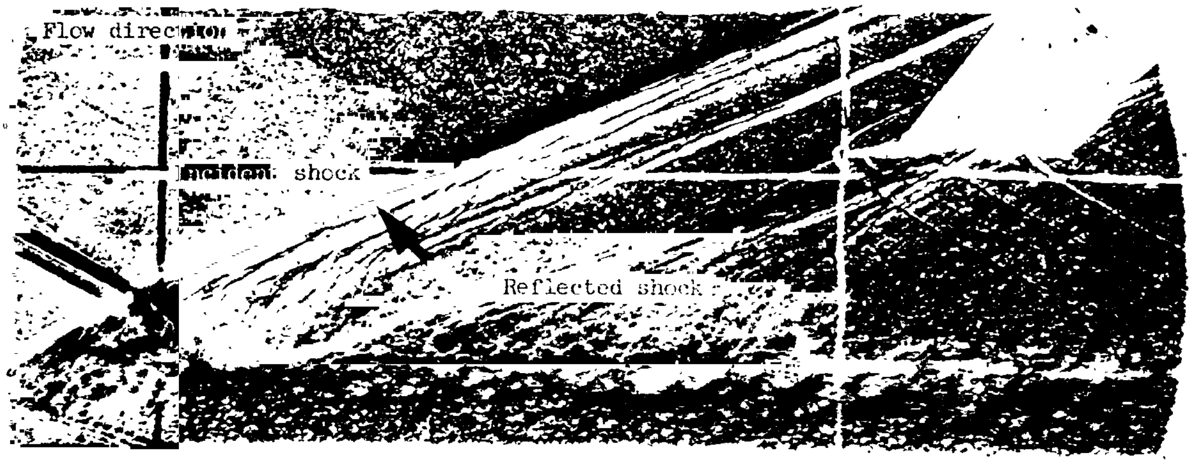

Shadowgraph

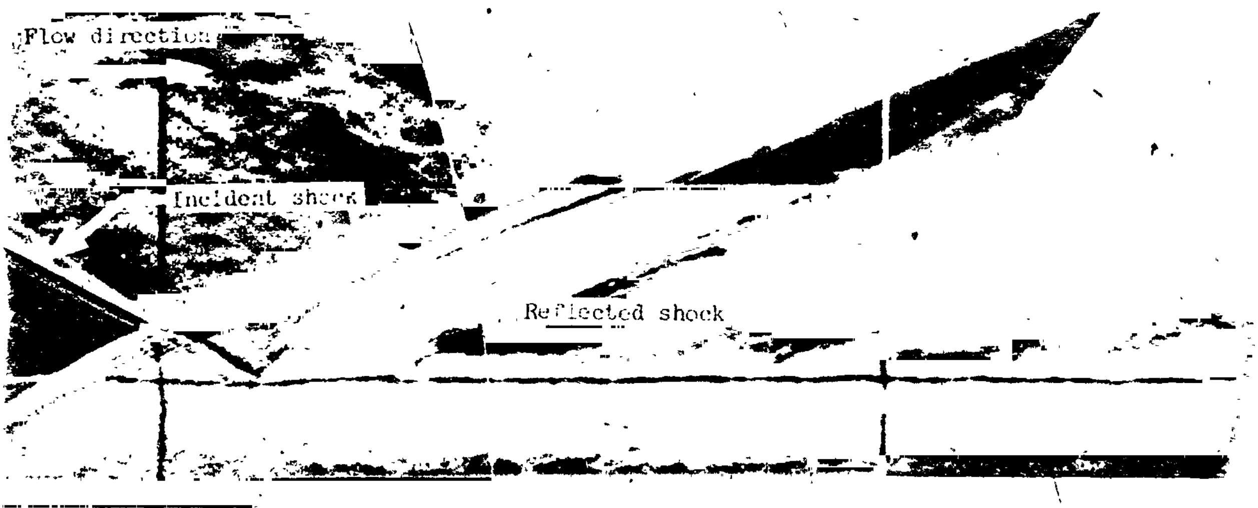

Schlieren photograph

(c) $\alpha = 10^{\circ}$ (run 21). L-65-9017

Figure 10.- Concluded.

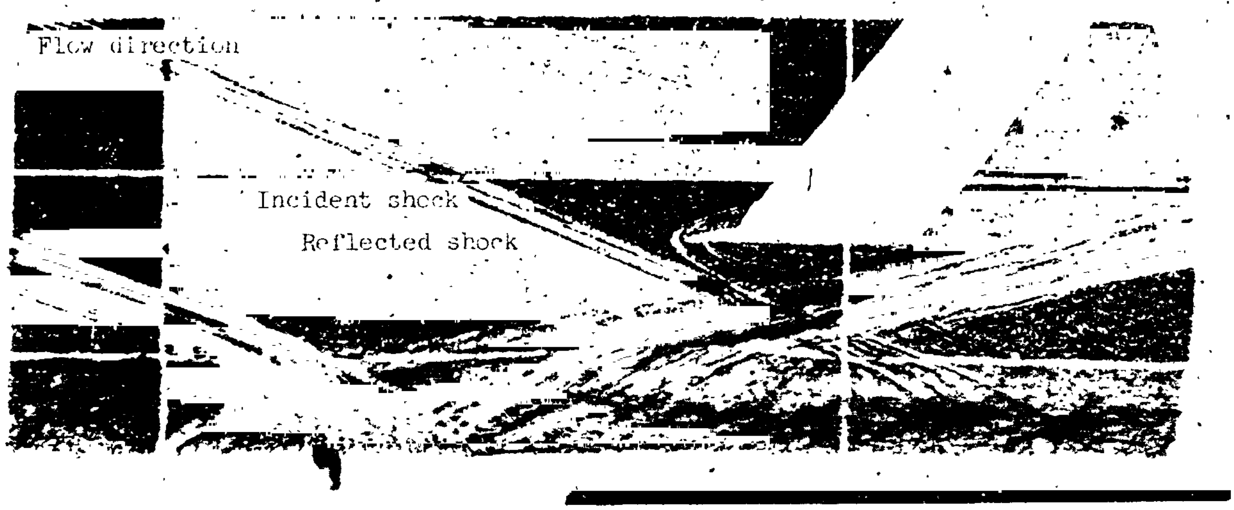

Shadowgraph

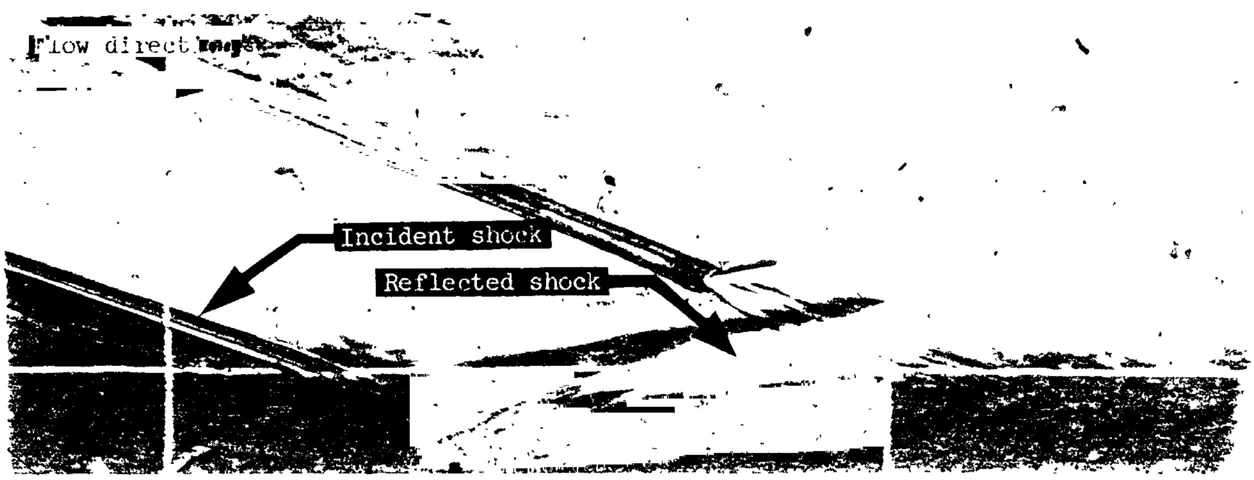

Schlieren photograph

(a) $\alpha = 6^{\circ}$ (run 35).

L-65-9018

Figure 11.- Shock—boundary-layer intersection for $M_{l,1} = 4.27$.

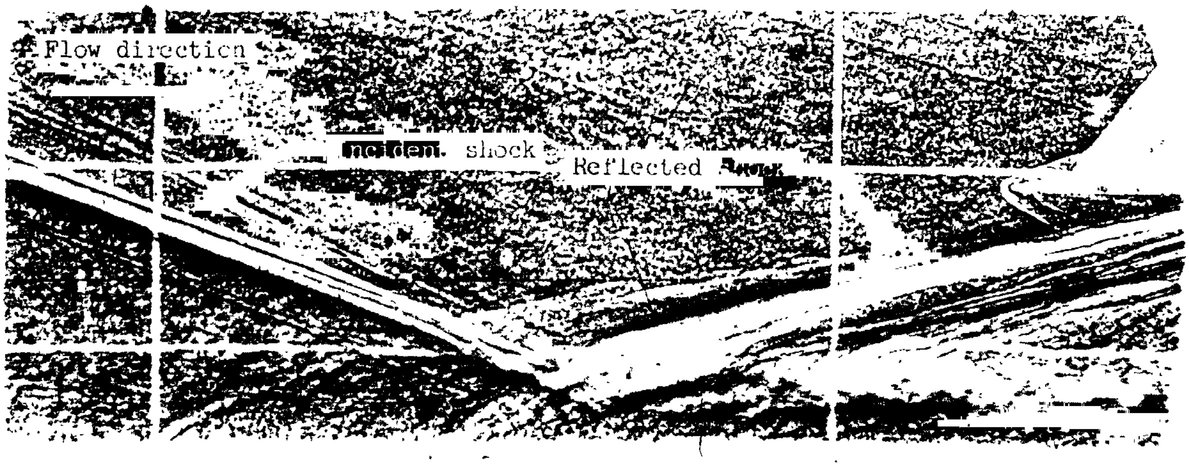

Shadowgraph

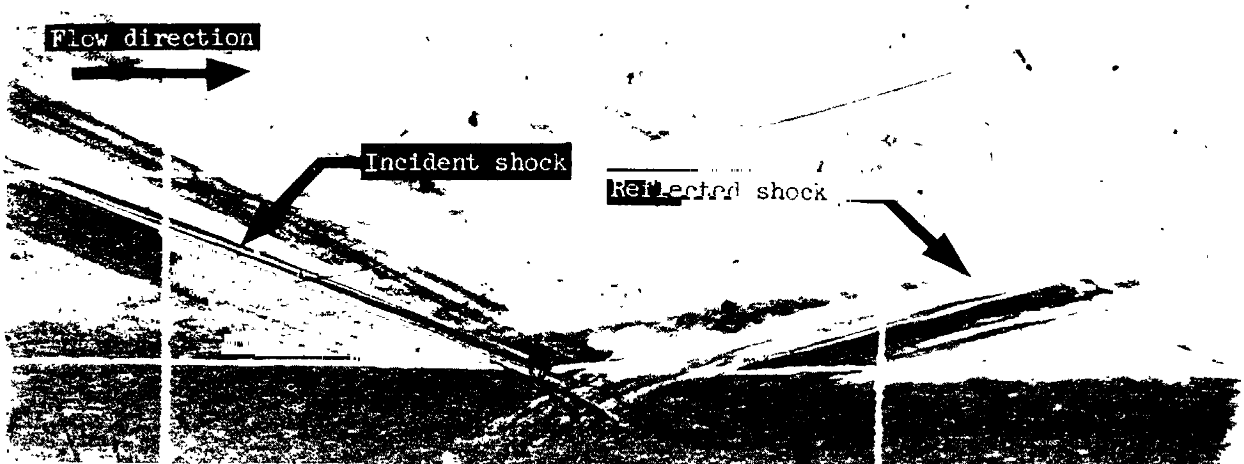

Schlieren photograph

(b) $\alpha = 8^{\circ}$ (run 37). L-65-9019

Figure 11.- Continued.

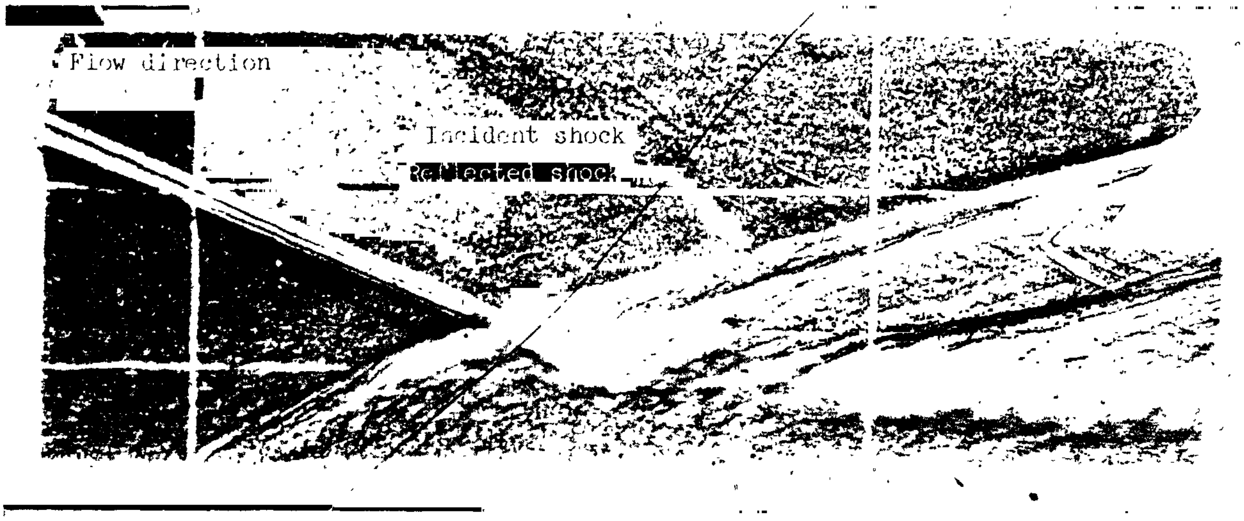

Shadowgraph

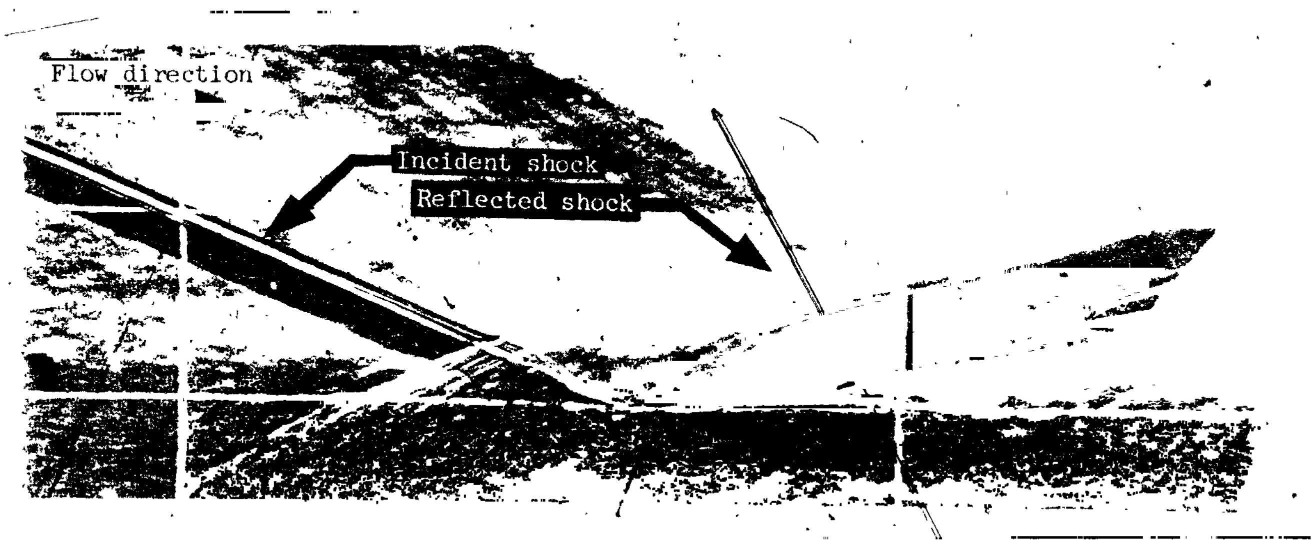

Schlieren photograph

(c) $\alpha = 10^{\circ}$ (run 38).

L-65-9020

Figure 11.- Concluded.

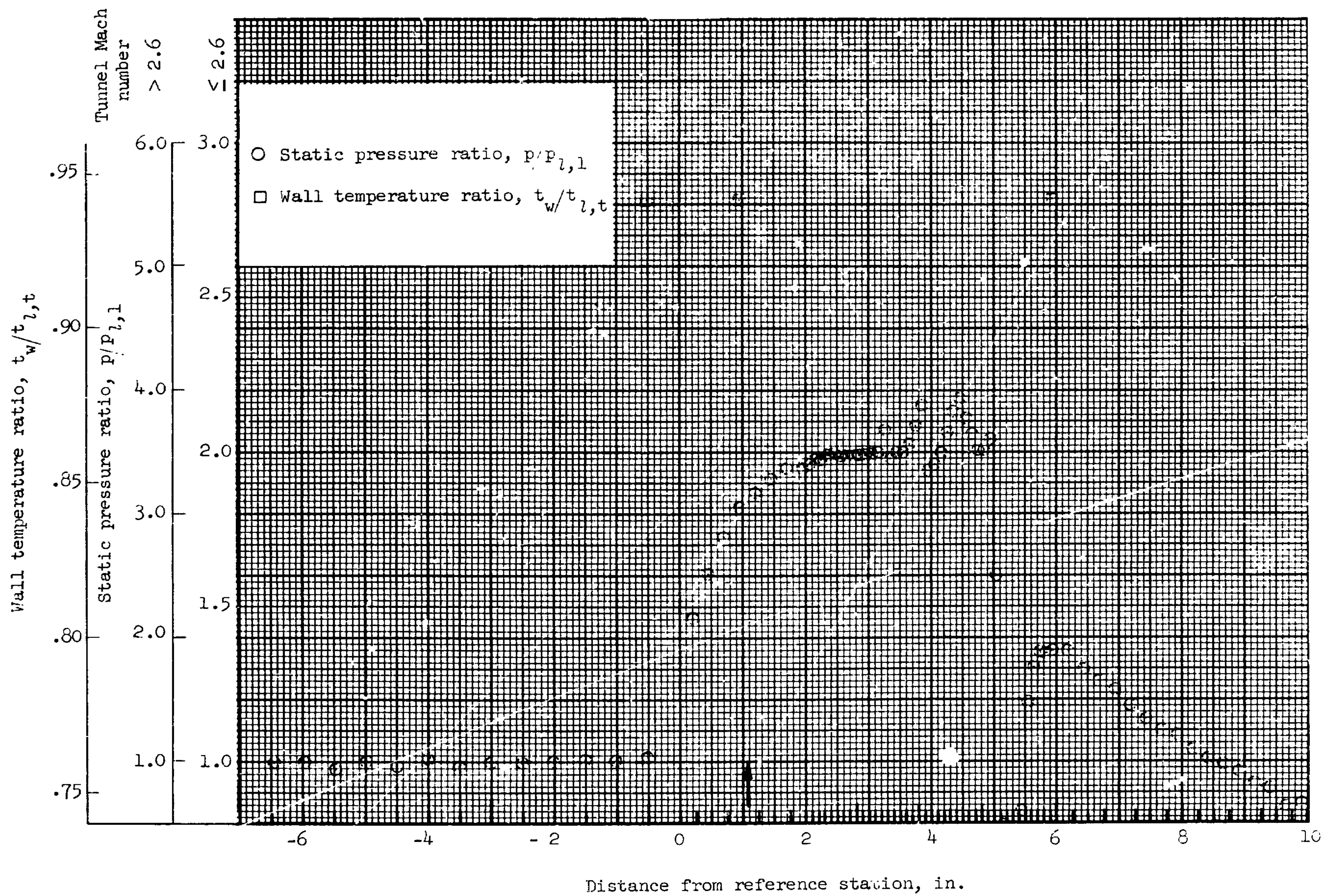

Figure 12.- Flat-plate static-pressure distributions and wall-temperature gradients through the incident-reflecting shock—boundary-layer interaction region for run 1. All identifying conditions are given in table III. The tunnel Mach number is 2.0. Arrow indicates approximate location of intersection of inviscid shock with flat plate.

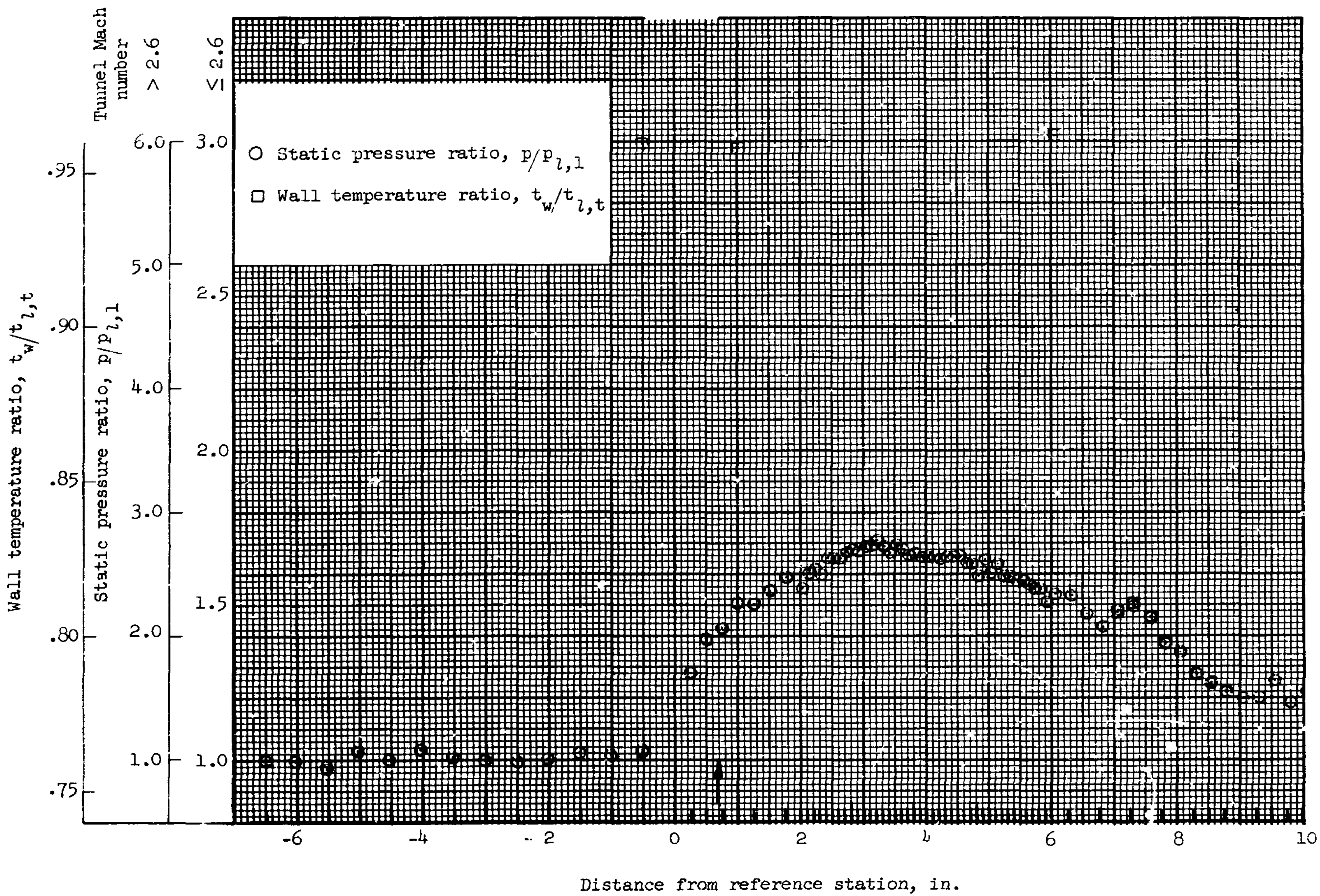

Figure 13.- Flat-plate static-pressure distributions and wall-temperature gradients through the incident-reflecting shock—boundary-layer interaction region for run 11. All identifying conditions are given in table III. The tunnel Mach number is 2.99. Arrow indicates approximate location of intersection of inviscid shock with flat plate.

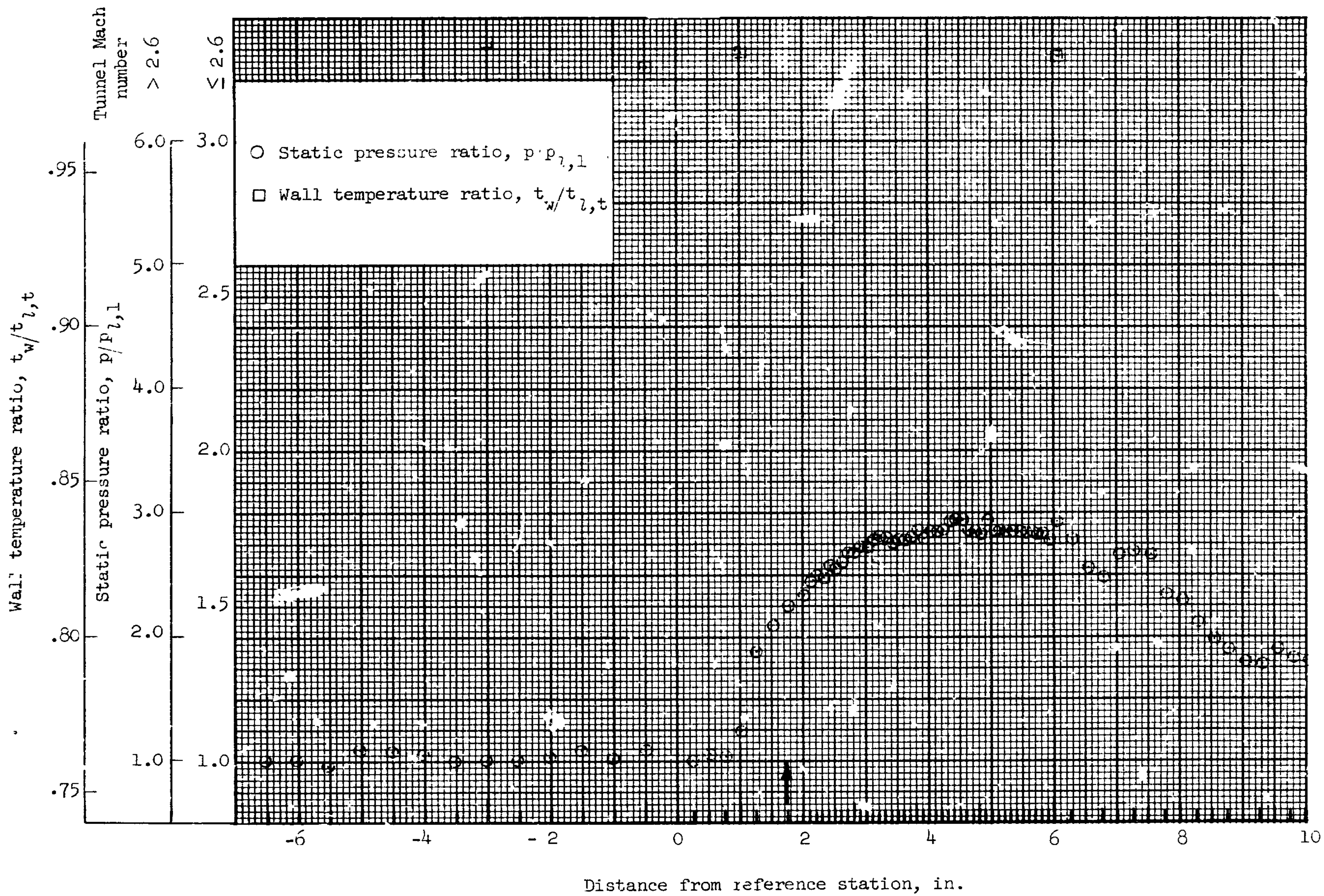

Figure 14.- Flat-plate static-pressure distributions and wall-temperature gradients through the incident-reflecting shock—boundary-layer interaction region for run 12. All identifying conditions are given in table III. The tunnel Mach number is 3.2. Arrow indicates approximate location of intersection of inviscid shock with flat plate.

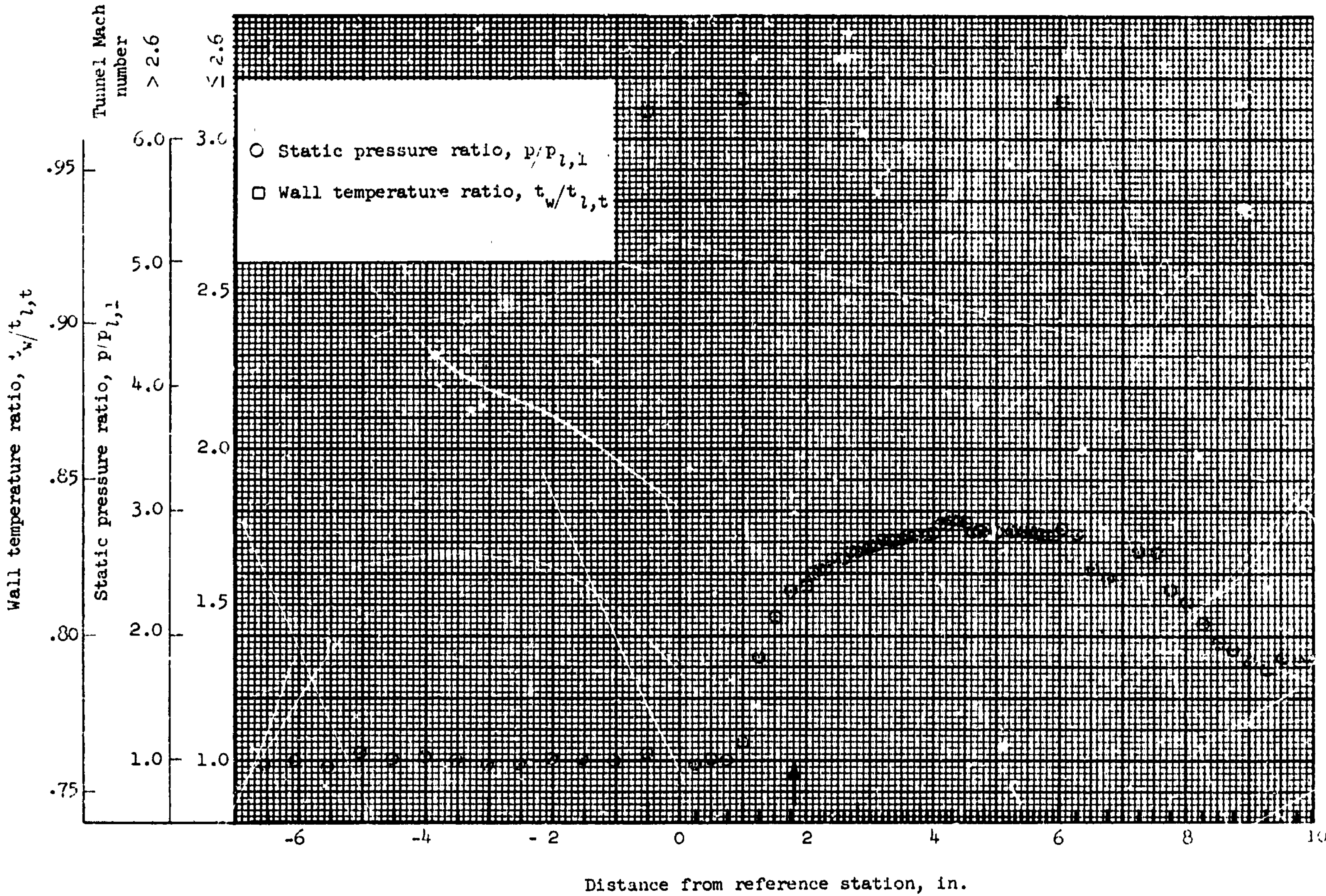

Figure 15.- Flat-plate static-pressure distributions and wall-temperature gradients through the incident-reflecting shock—boundary-layer interaction region for run 13. All identifying conditions are given in table III. The tunnel Mach number is 3.2. Arrow indicates approximate location of intersection of inviscid shock with flat plate.

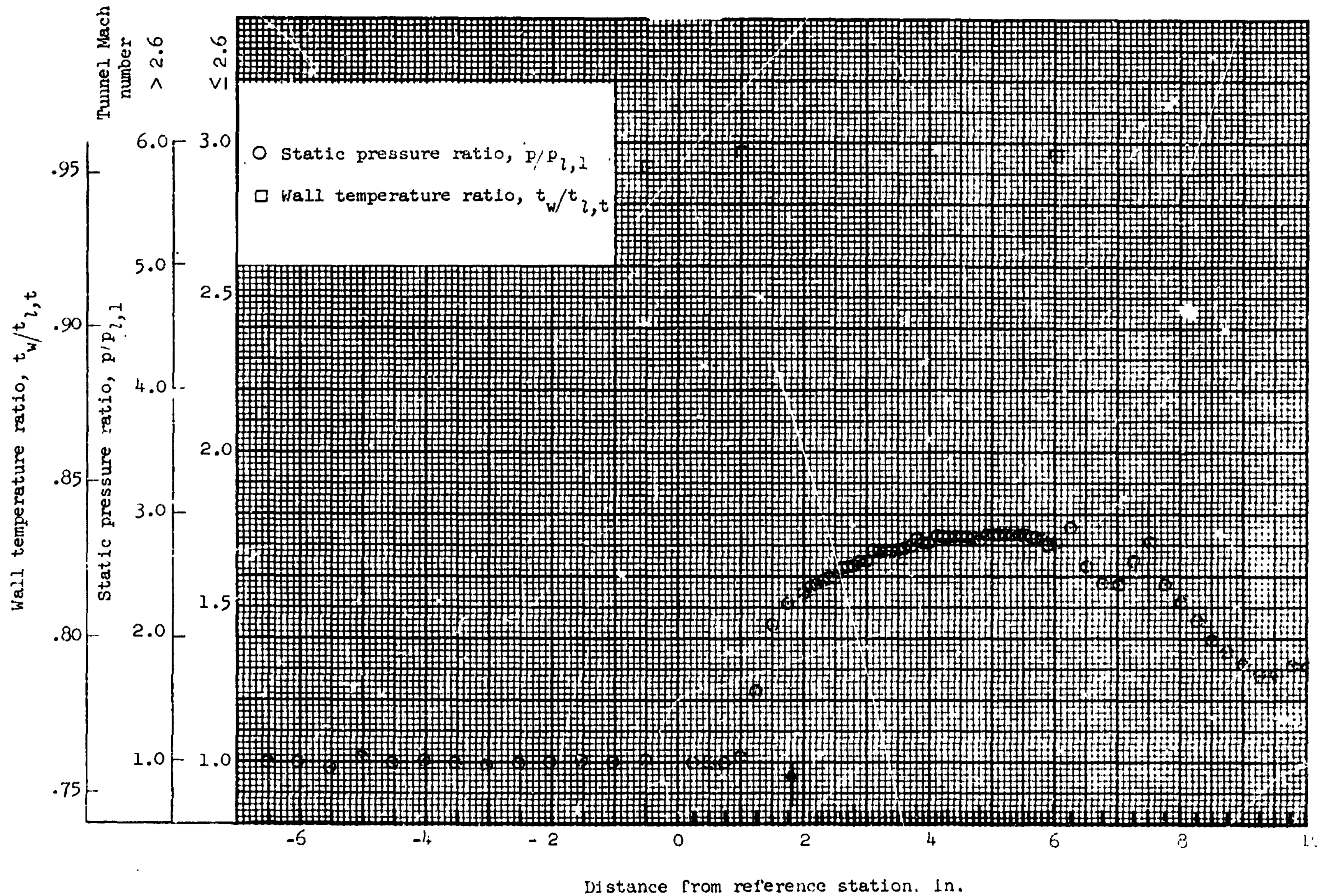

Figure 16.- Flat-plate static-pressure distributions and wall-temperature gradients through the incident-reflecting shock—boundary-layer interaction region for run 14. All identifying conditions are given in table III. The tunnel Mach number is 3.2. Arrow indicates approximate location of intersection of inviscid shock with flat plate.

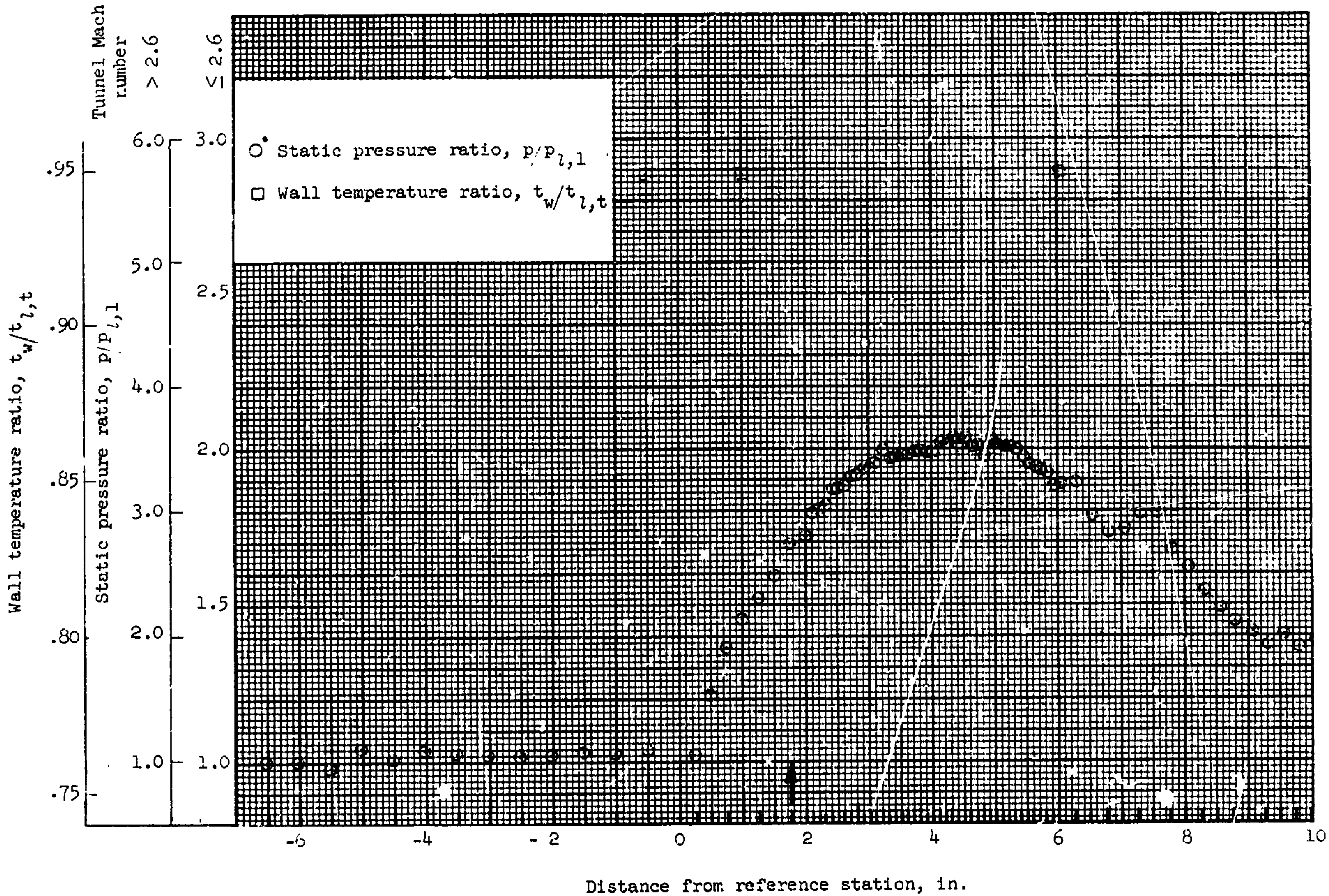

Figure 17.- Flat-plate static-pressure distributions and wall-temperature gradients through the incident-reflecting shock—boundary-layer interaction region for run 17. All identifying conditions are given in table III. The tunnel Mach number is 3.2. Arrow indicates approximate location of intersection of inviscid shock with flat plate.

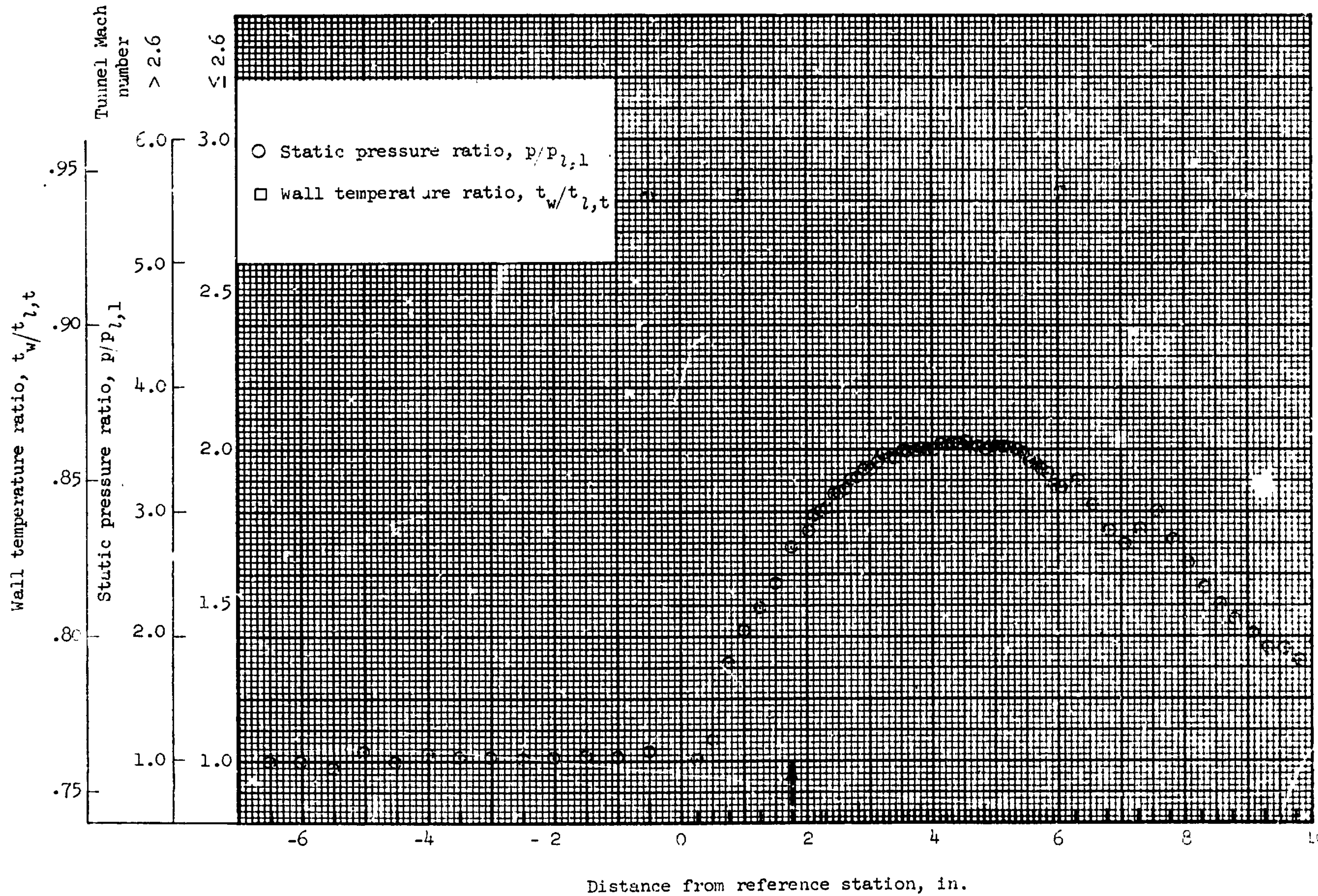

Figure 18.- Flat-plate static-pressure distributions and wall-temperature gradients through the incident-reflecting shock—boundary-layer interaction region for run 18. All identifying conditions are given in table III. The tunnel Mach number is 3.2. Arrow indicates approximate location of intersection of inviscid shock with flat plate.

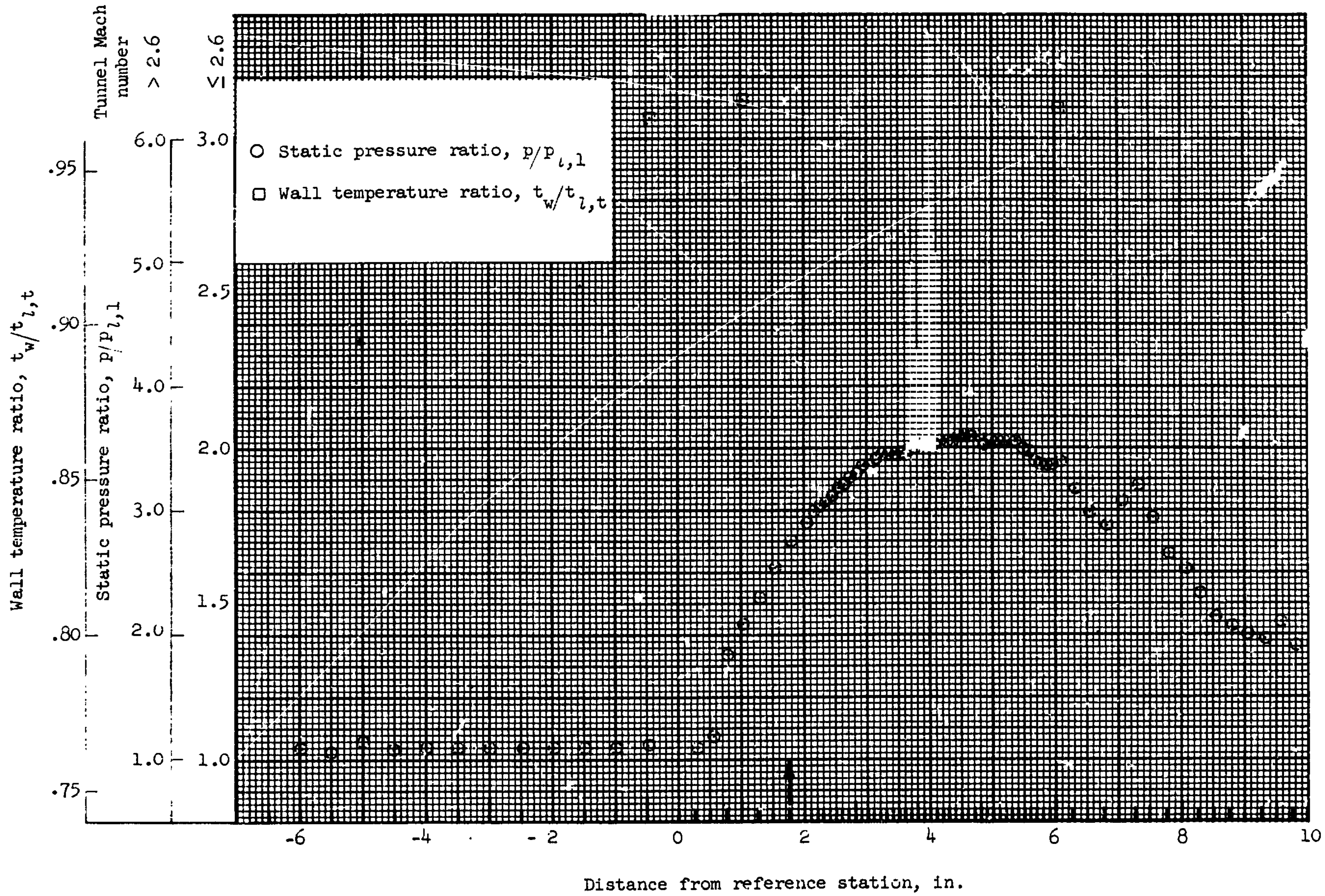

Figure 19.- Flat-plate static-pressure distributions and wall-temperature gradients through the incident-reflecting shock—boundary-layer interaction region for run 19. All identifying conditions are given in table III. The tunnel Mach number is 3.2. Arrow indicates approximate location of intersection of inviscid shock with flat plate.

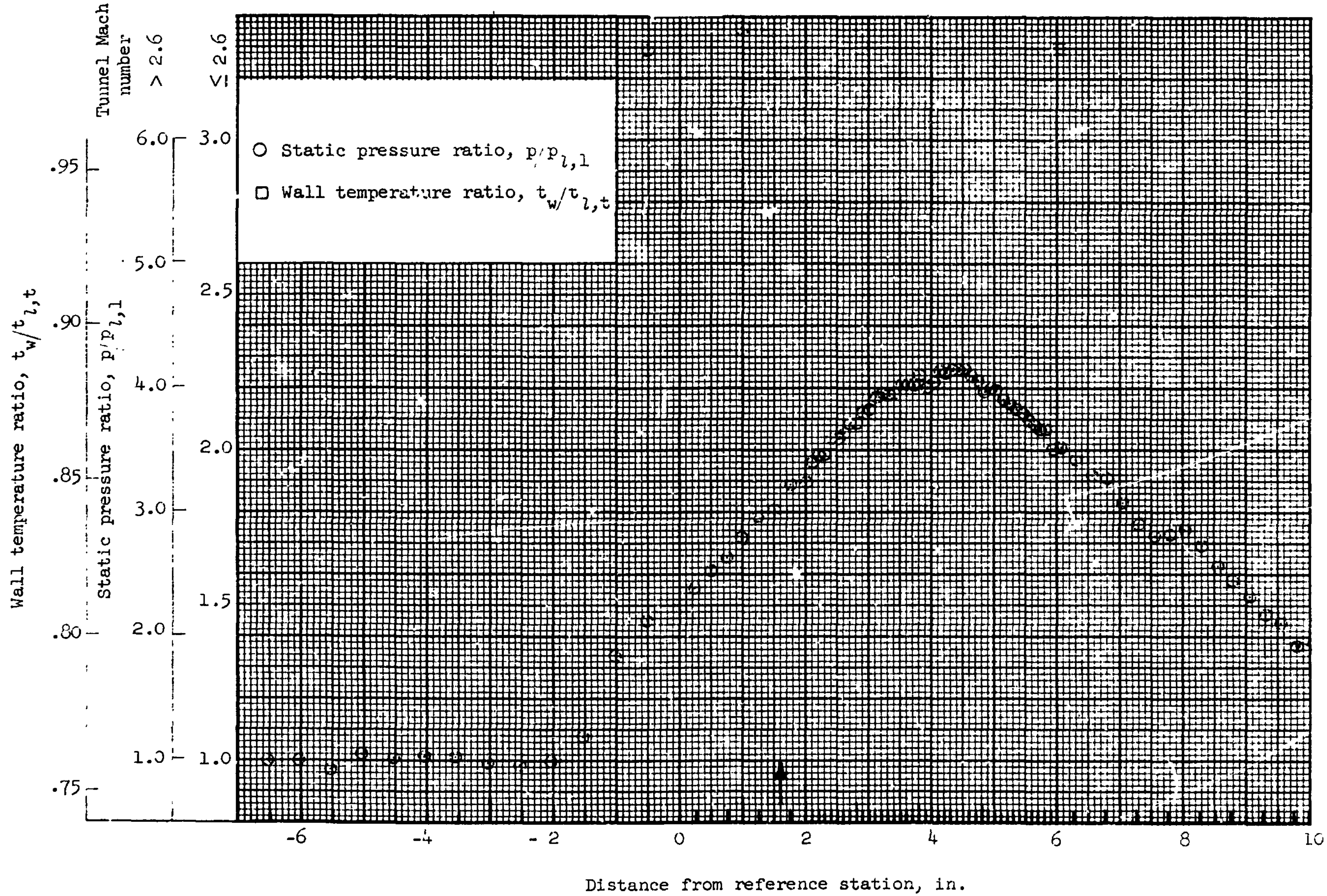

Figure 20.- Flat-plate static-pressure distributions and wall-temperature gradients through the incident-reflecting shock—boundary-layer interaction region for run 21. All identifying conditions are given in table III. The tunnel Mach number is 3.2. Arrow indicates approximate location of intersection of inviscid shock with flat plate.

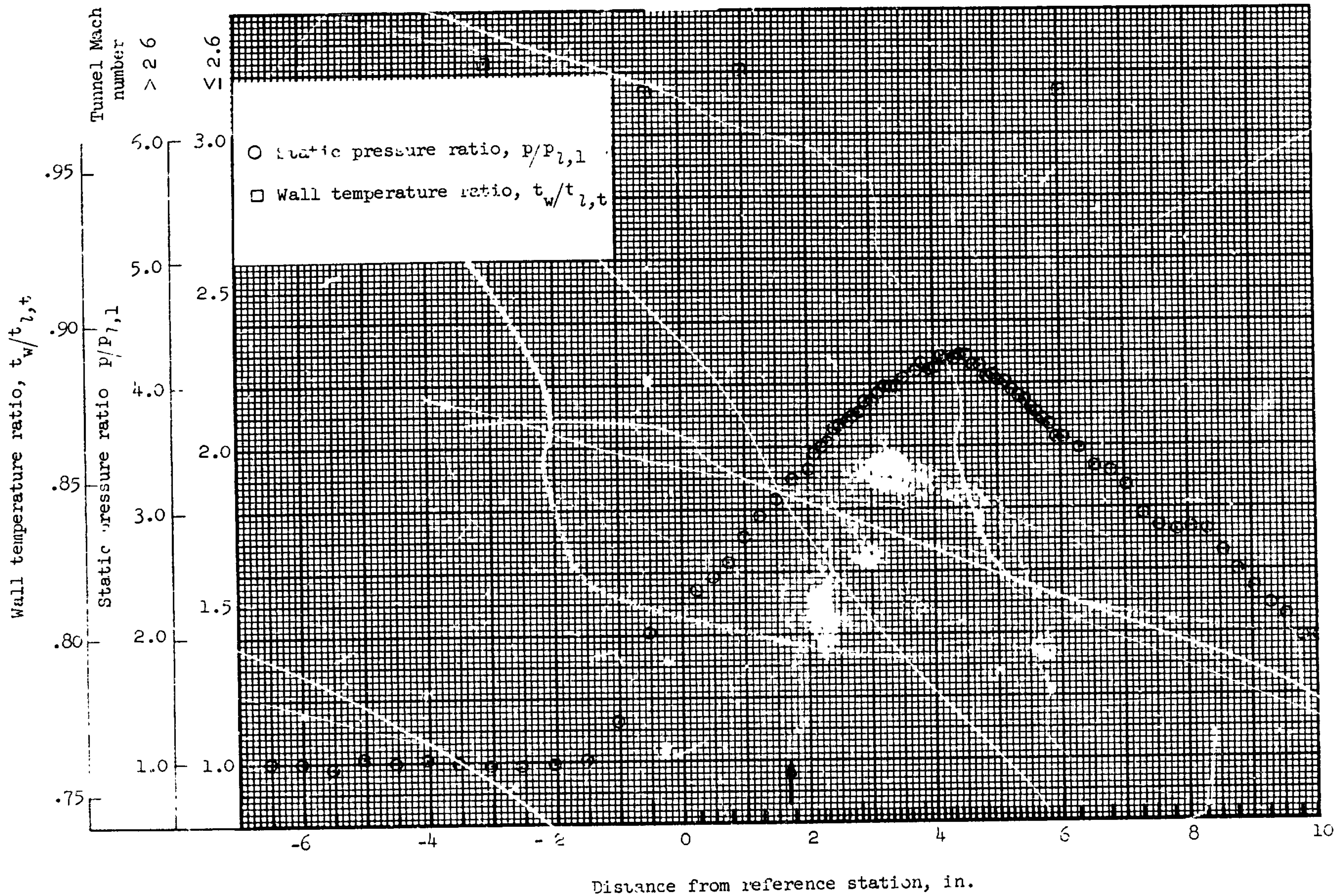

Figure 21.- Flat-plate static-pressure distributions and wall-temperature gradients through the incident-reflecting shock—boundary-layer interaction region for run 22. All identifying conditions are given in table III. The tunnel Mach number is 3.2. Arrow indicates approximate location of intersection of inviscid shock with flat plate.

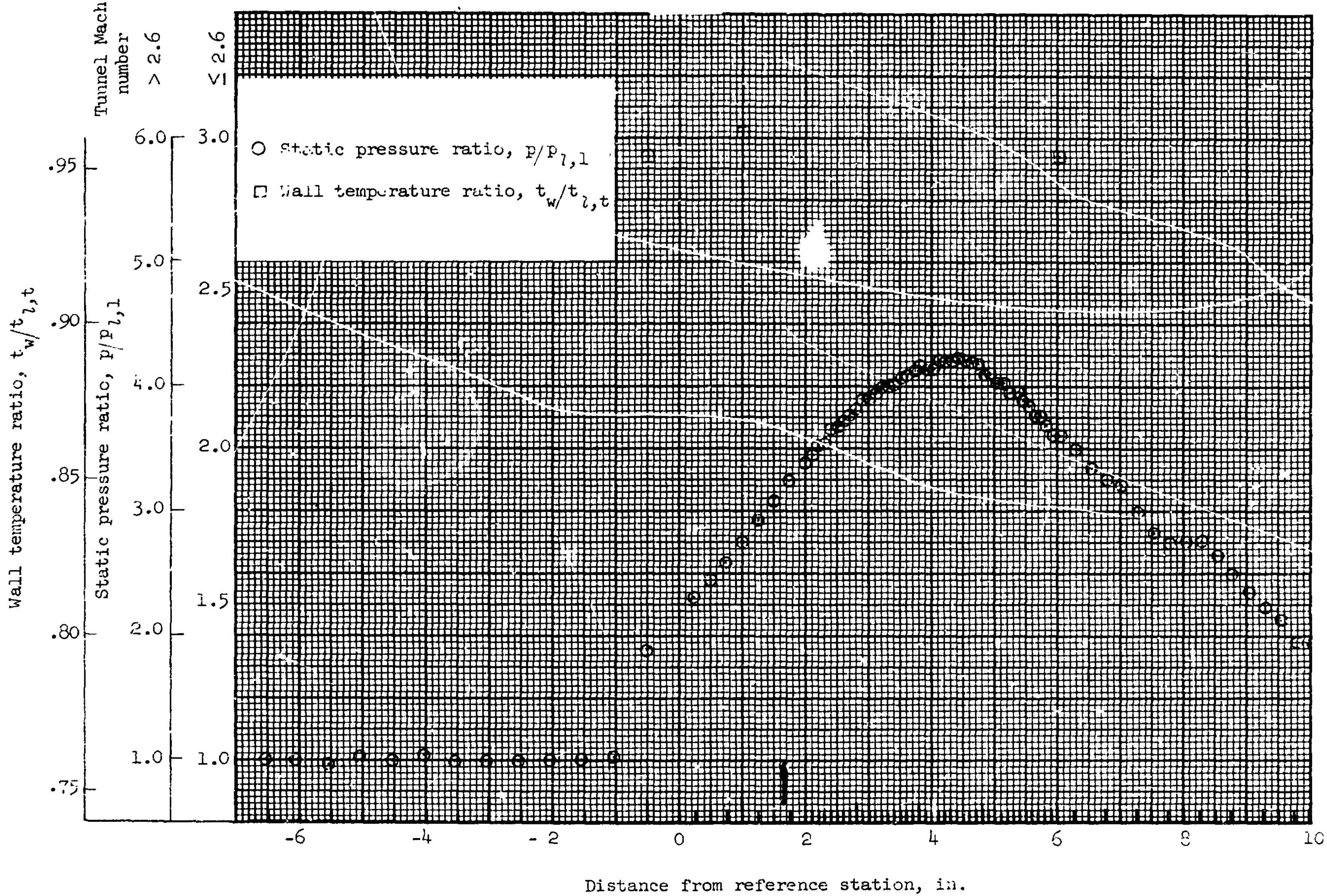

Figure 22.- Flat-plate static-pressure distributions and wall-temperature gradients through the incident-reflecting shock—boundary-layer interaction region for run 23. All identifying conditions are given in table III. The tunnel Mach number is 3.2. Arrow indicates approximate location of intersection of inviscid shock with flat plate.

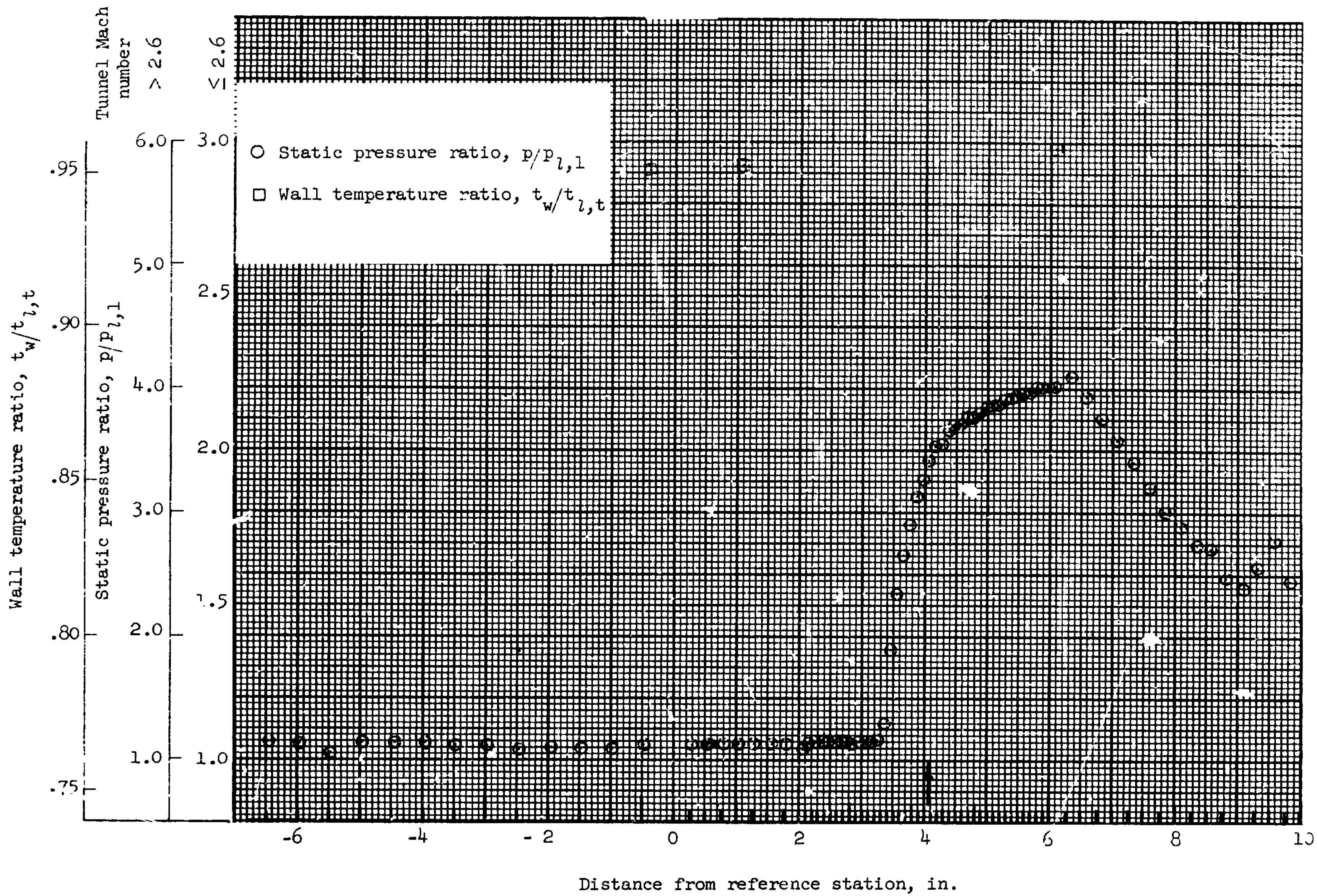

Figure 23.- Flat-plate static-pressure distributions and wall-temperature gradients through the incident-reflecting shock—boundary-layer interaction region for run 28. All identifying conditions are given in table III. The tunnel Mach number is 2.4. Arrow indicates approximate location of intersection of inviscid shock with flat plate.

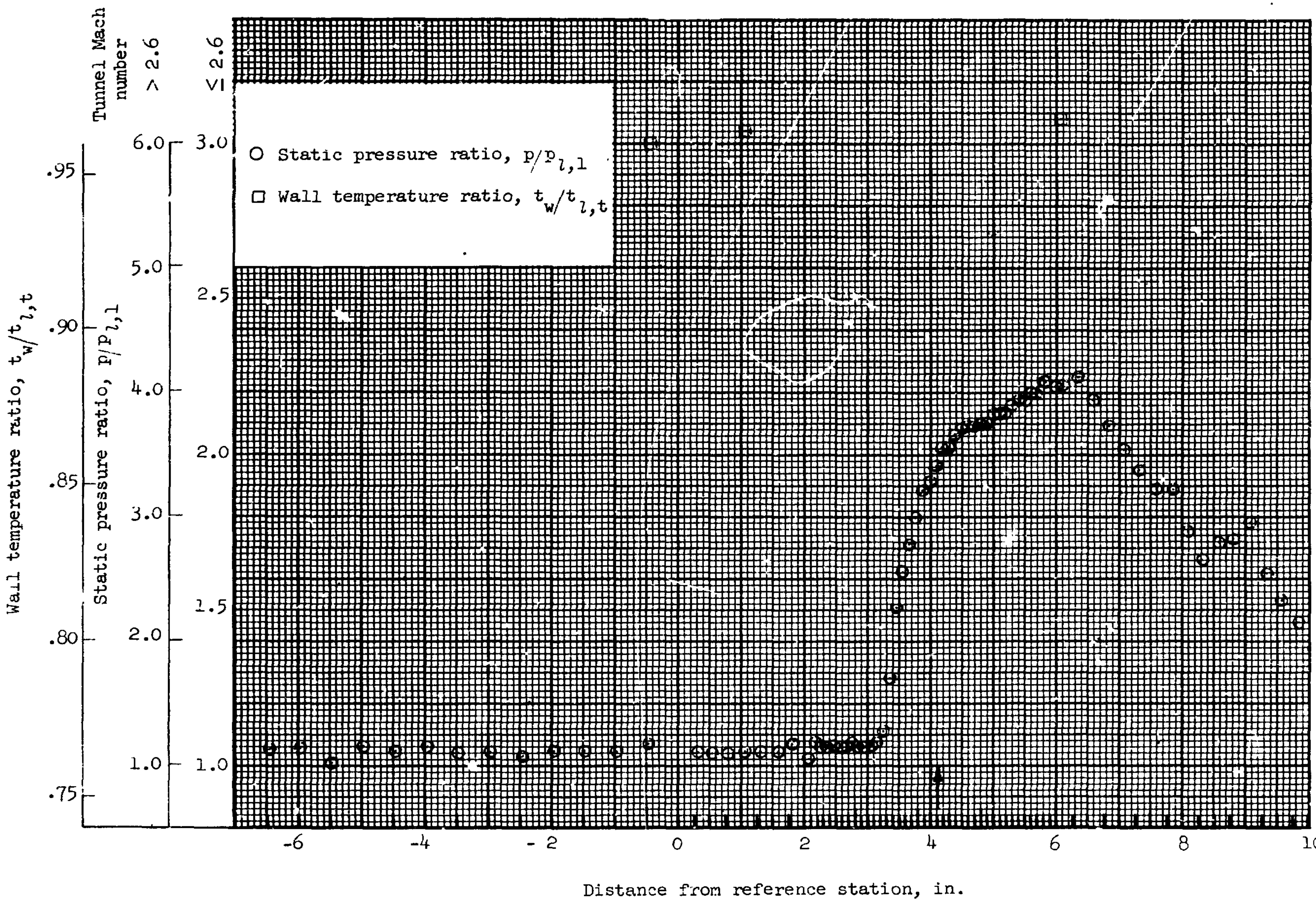

Figure 24.- Flat-plate static-pressure distributions and wall-temperature gradients through the incident-reflecting shock—boundary-layer interaction region for run 29. All identifying conditions are given in table III. The tunnel Mach number is 2.4. Arrow indicates approximate location of intersection of inviscid shock with flat plate.

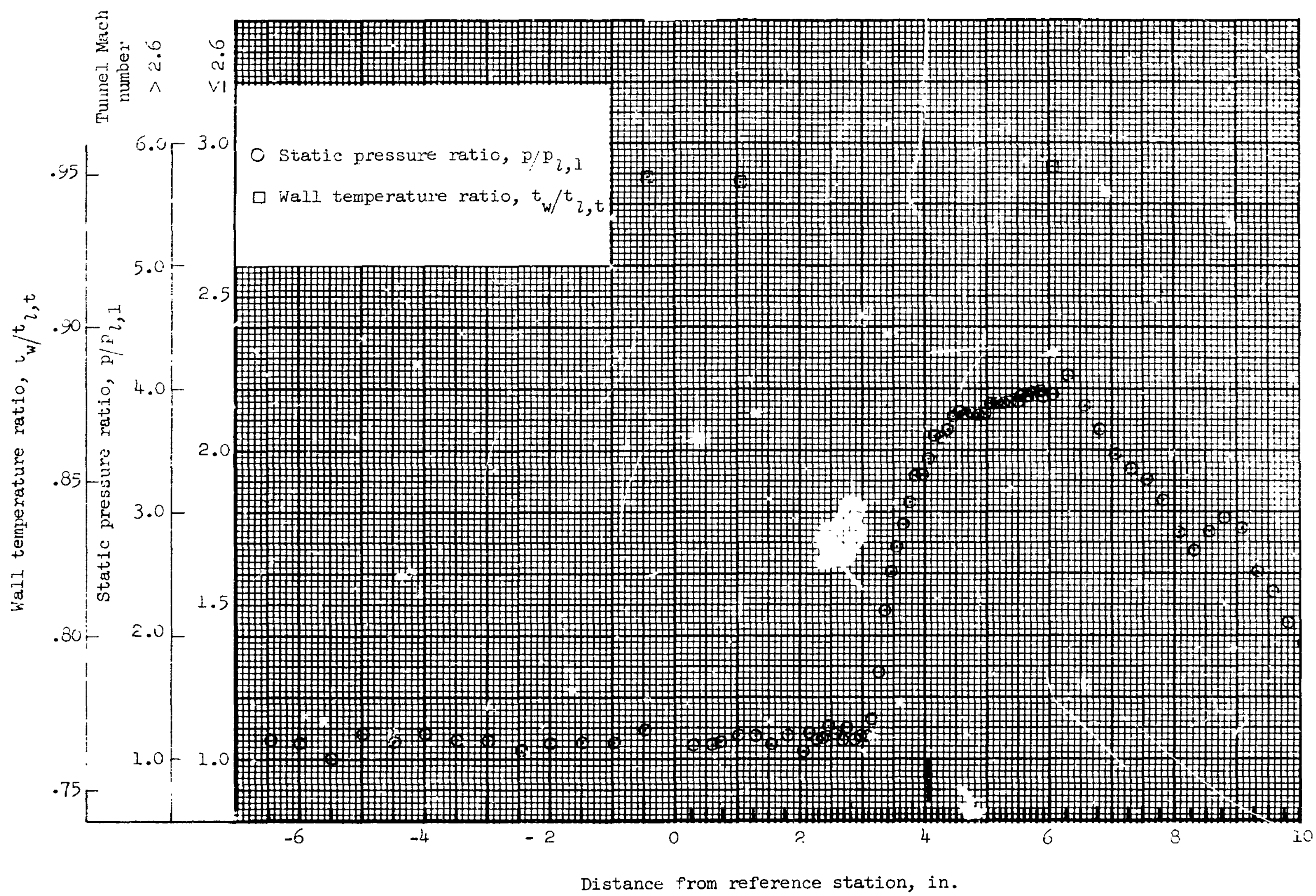

Figure 25.- Flat-plate static-pressure distributions and wall-temperature gradients through the incident-reflecting shock—boundary-layer interaction region for run 30. All identifying conditions are given in table III. The tunnel Mach number is 2.4. Arrow indicates approximate location of intersection of inviscid shock with flat plate.

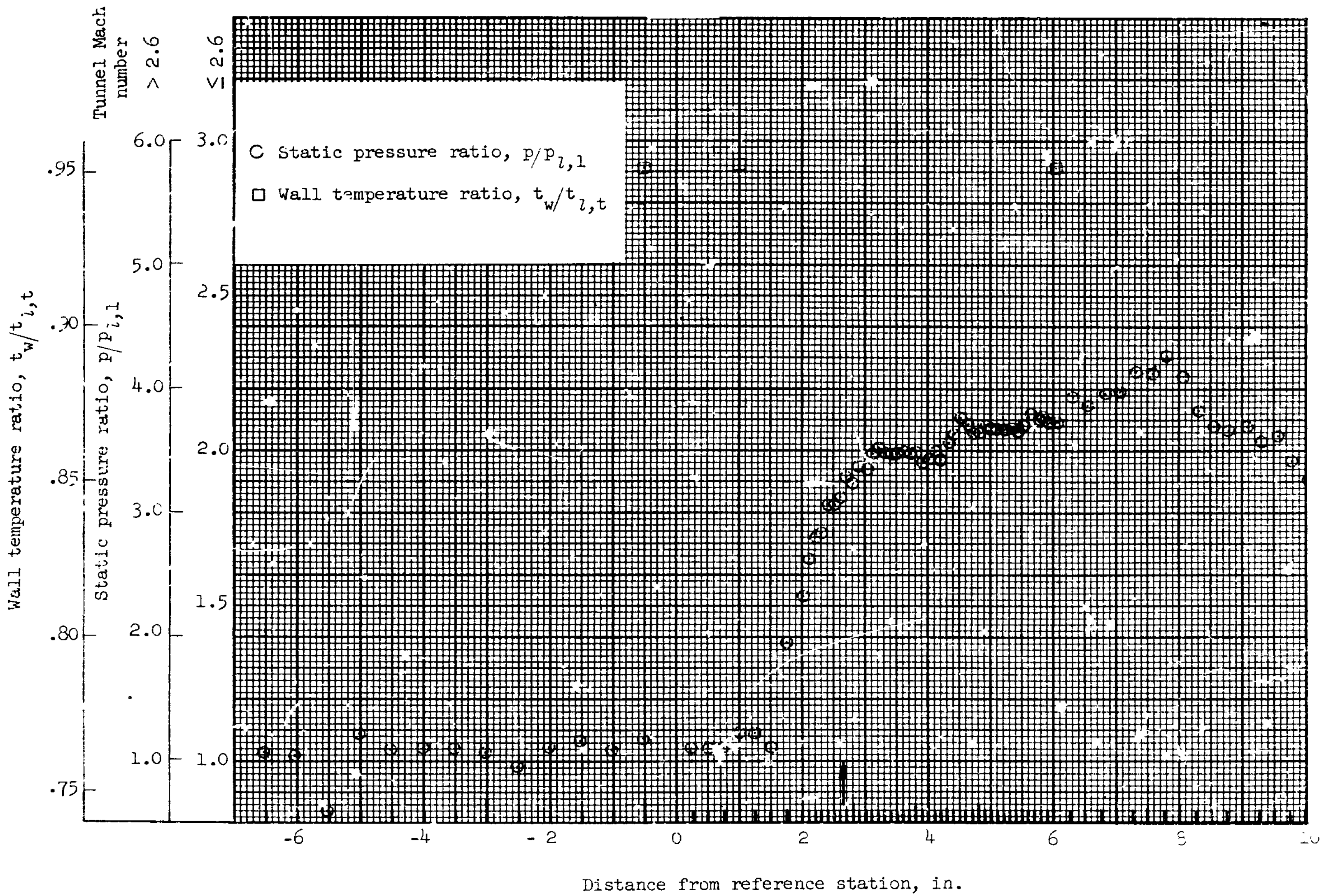

Figure 26.- Flat-plate static-pressure distributions and wall-temperature gradients through the incident-reflecting shock—boundary-layer interaction region for run 32. All identifying conditions are given in table III. The tunnel Mach number is 4.36. Arrow indicates approximate location of intersection of inviscid shock with flat plate.

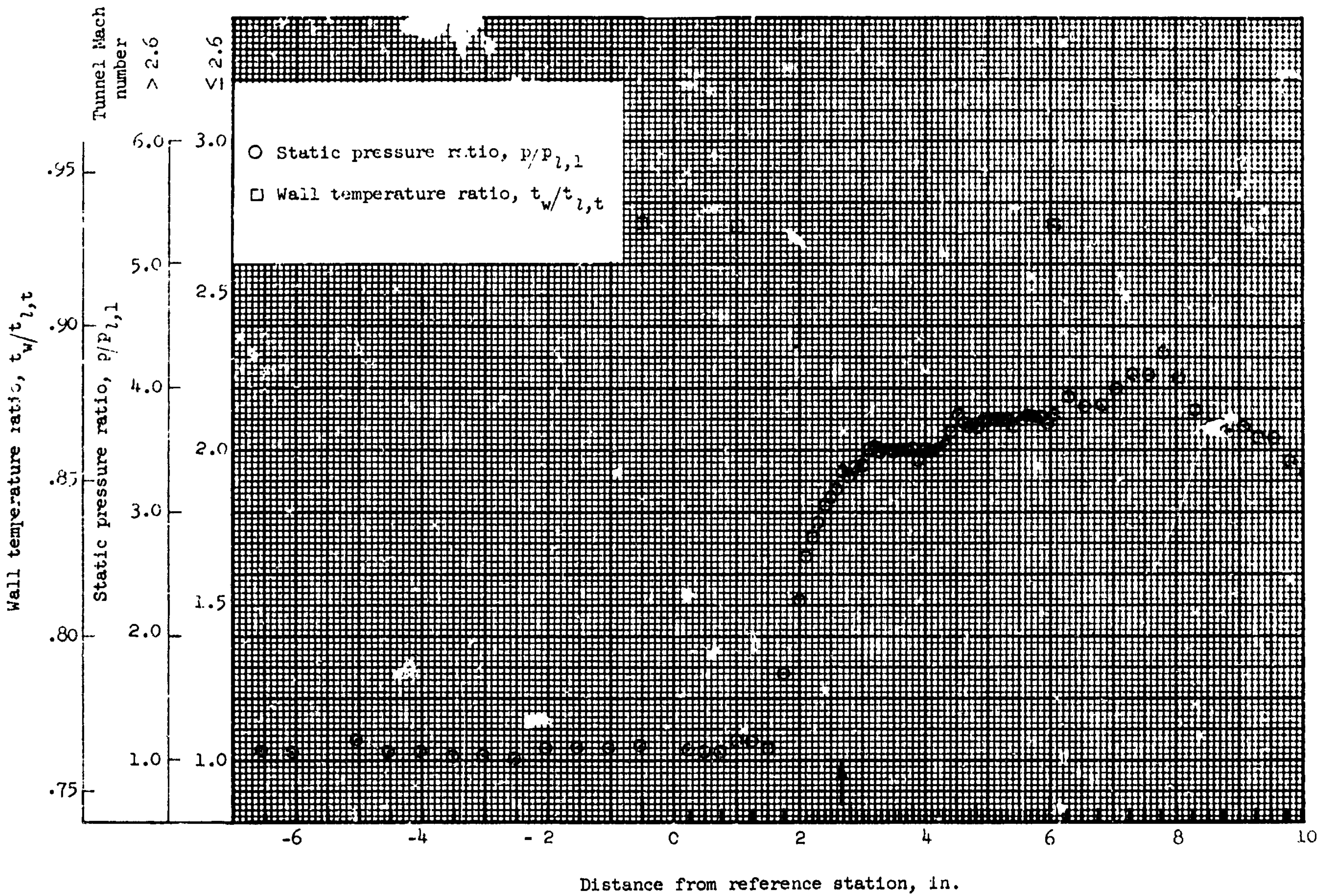

Figure 27.- Flat-plate static-pressure distributions and wall-temperature gradients through the incident-reflecting shock—boundary-layer interaction region for run 33. All identifying conditions are given in table III. The tunnel Mach number is 4.36. Arrow indicates approximate location of intersection of inviscid shock with flat plate.

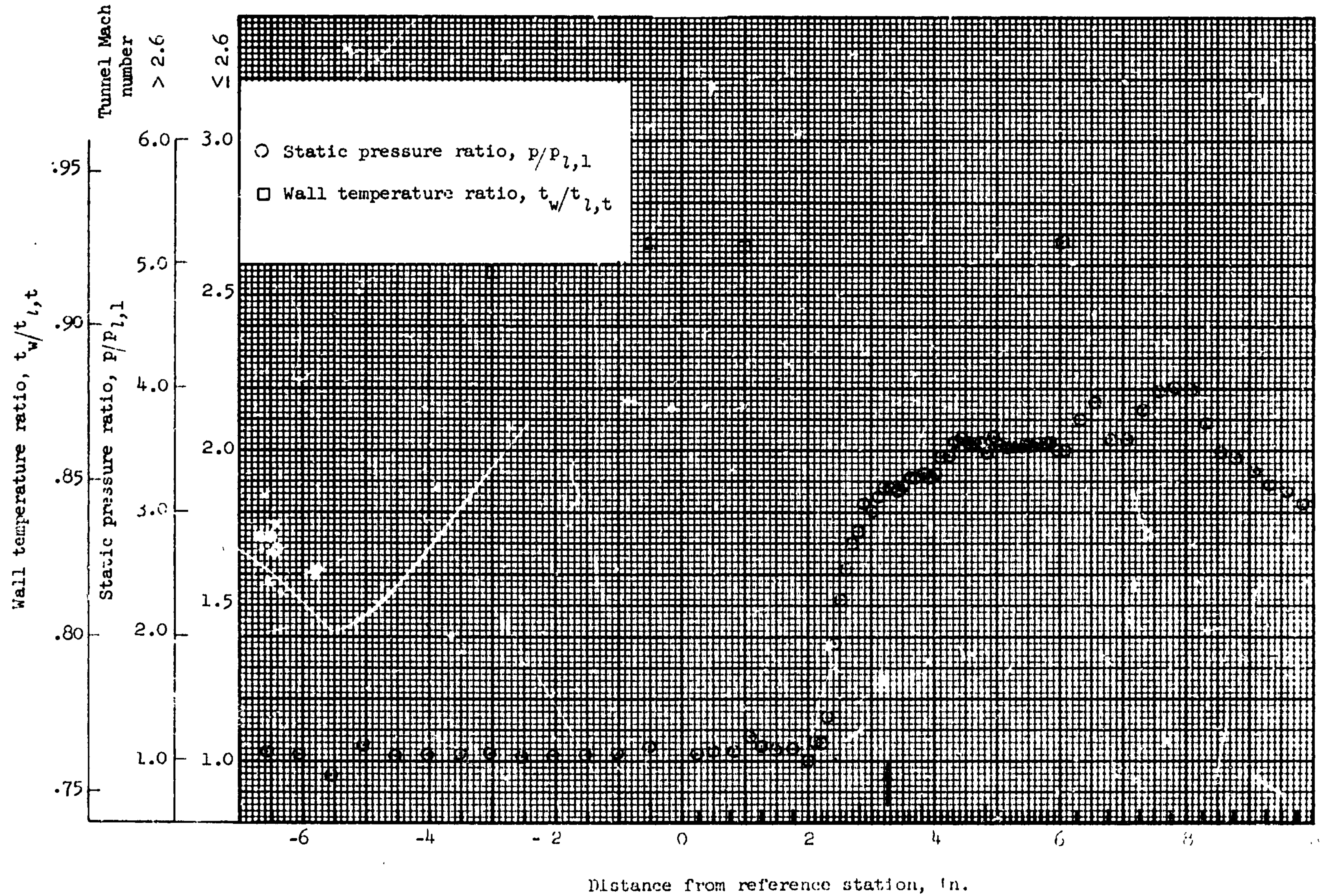

Figure 28.- Flat-plate static-pressure distributions and wall-temperature gradients through the incident-reflecting shock—boundary-layer interaction region for run 34. All identifying conditions are given in table III. The tunnel Mach number is 4.36. Arrow indicates approximate location of intersection of inviscid shock with flat plate.

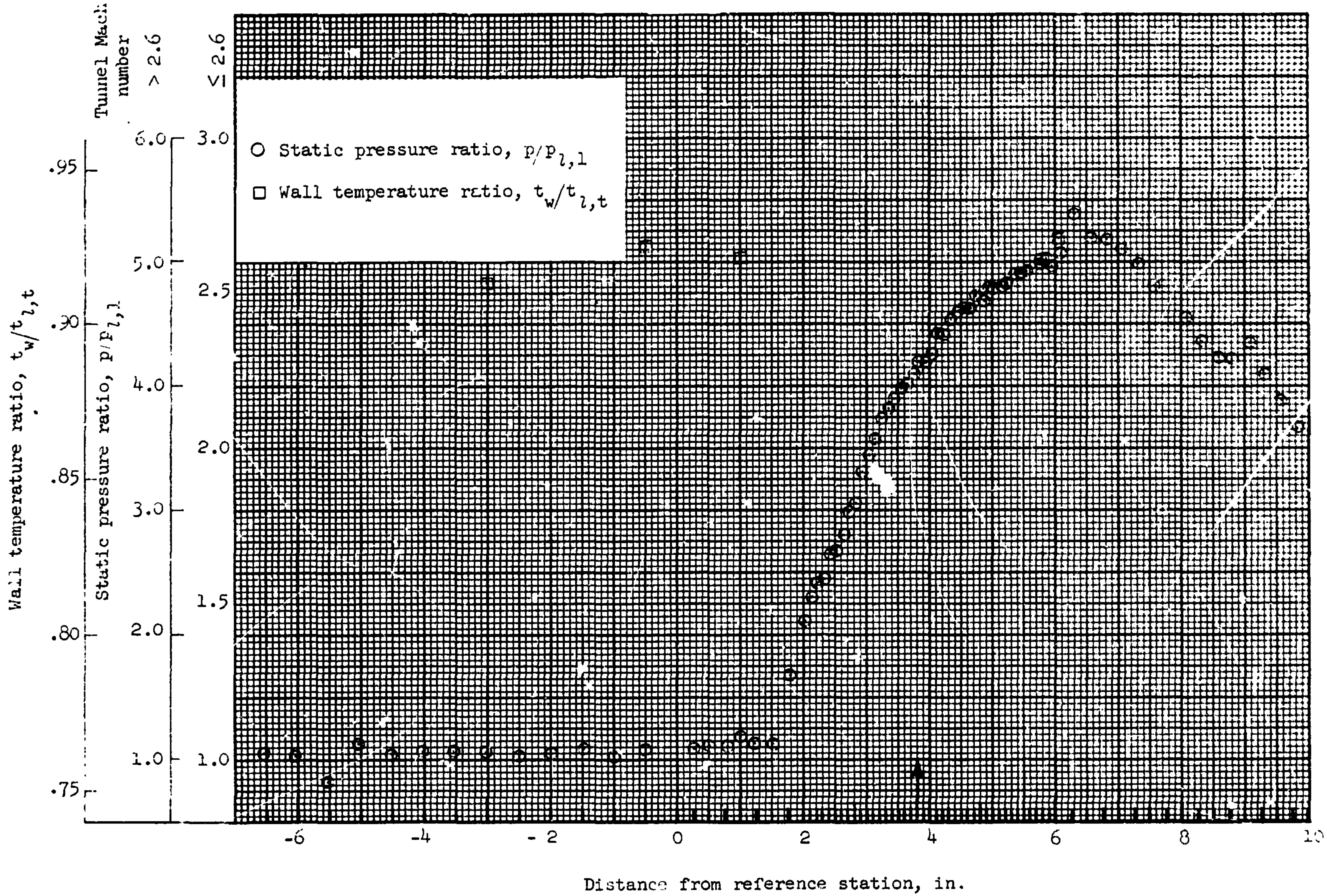

Figure 29.- Flat-plate static-pressure distributions and wall-temperature gradients through the incident-reflecting shock—boundary-layer interaction region for run 36. All identifying conditions are given in table III. The tunnel Mach number is 4.36. Arrow indicates approximate location of intersection of inviscid shock with flat plate.

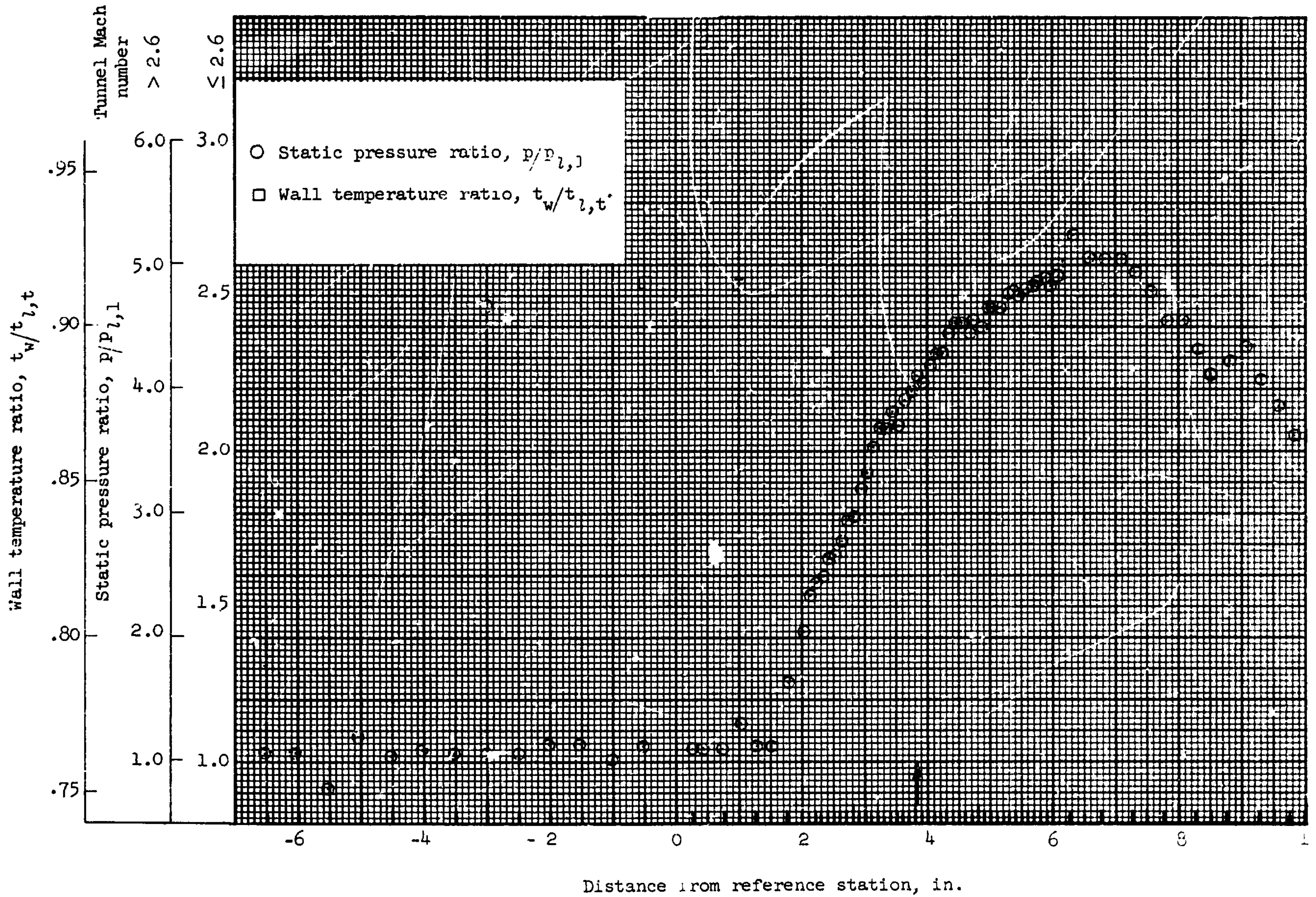

Figure 30.- Flat-plate static-pressure distributions and wall-temperature gradients through the incident-reflecting shock—boundary-layer interaction region for run 37. All identifying conditions are given in table III. The tunnel Mach number is 4.36. Arrow indicates approximate location of intersection of inviscid shock with flat plate.

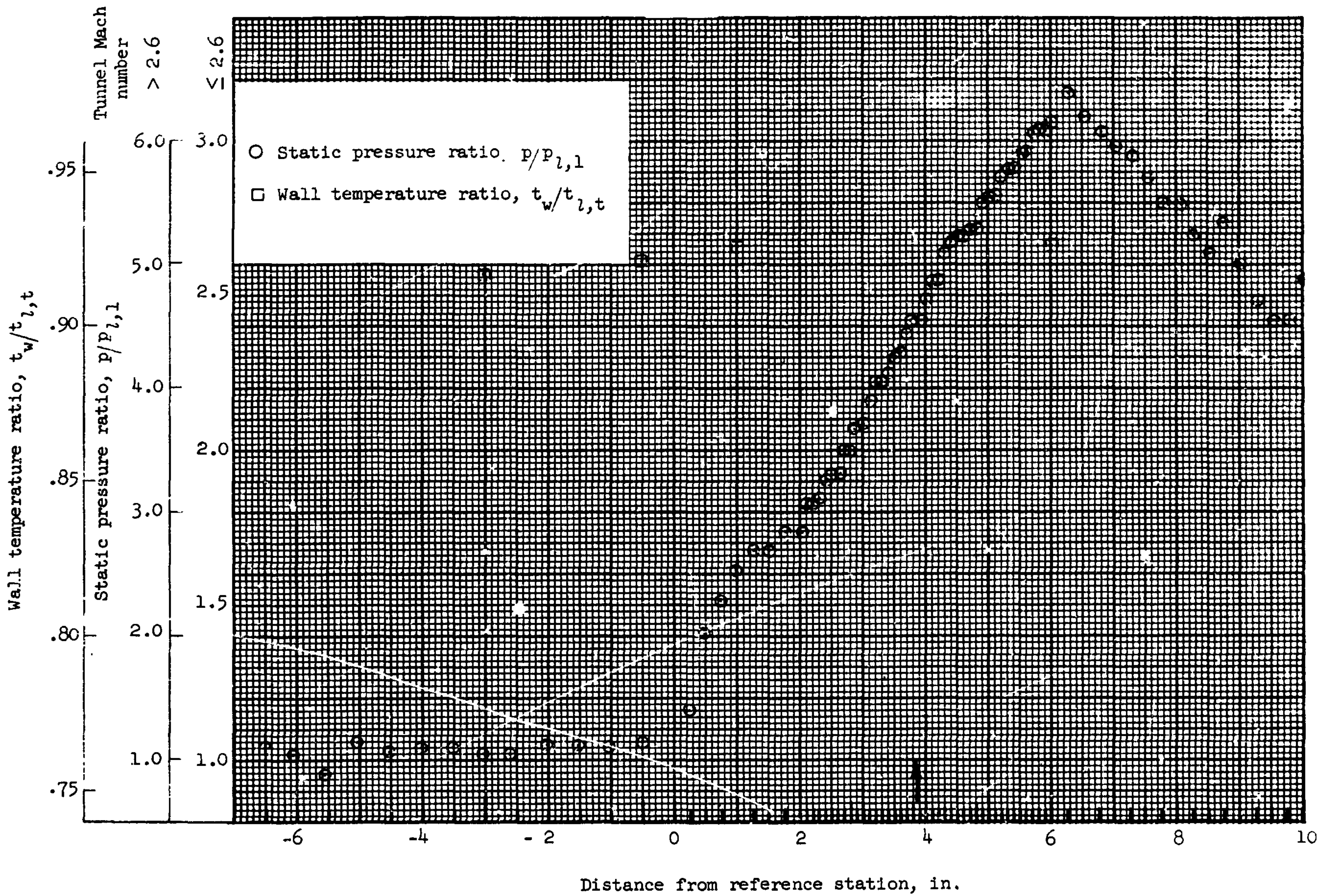

Figure 31.- Flat-plate static-pressure distributions and wall-temperature gradients through the incident-reflecting shock—boundary-layer interaction region for run 38. All identifying conditions are given in table III. The tunnel Mach number is 4.36. Arrow indicates approximate location of intersection of inviscid shock with flat plate.

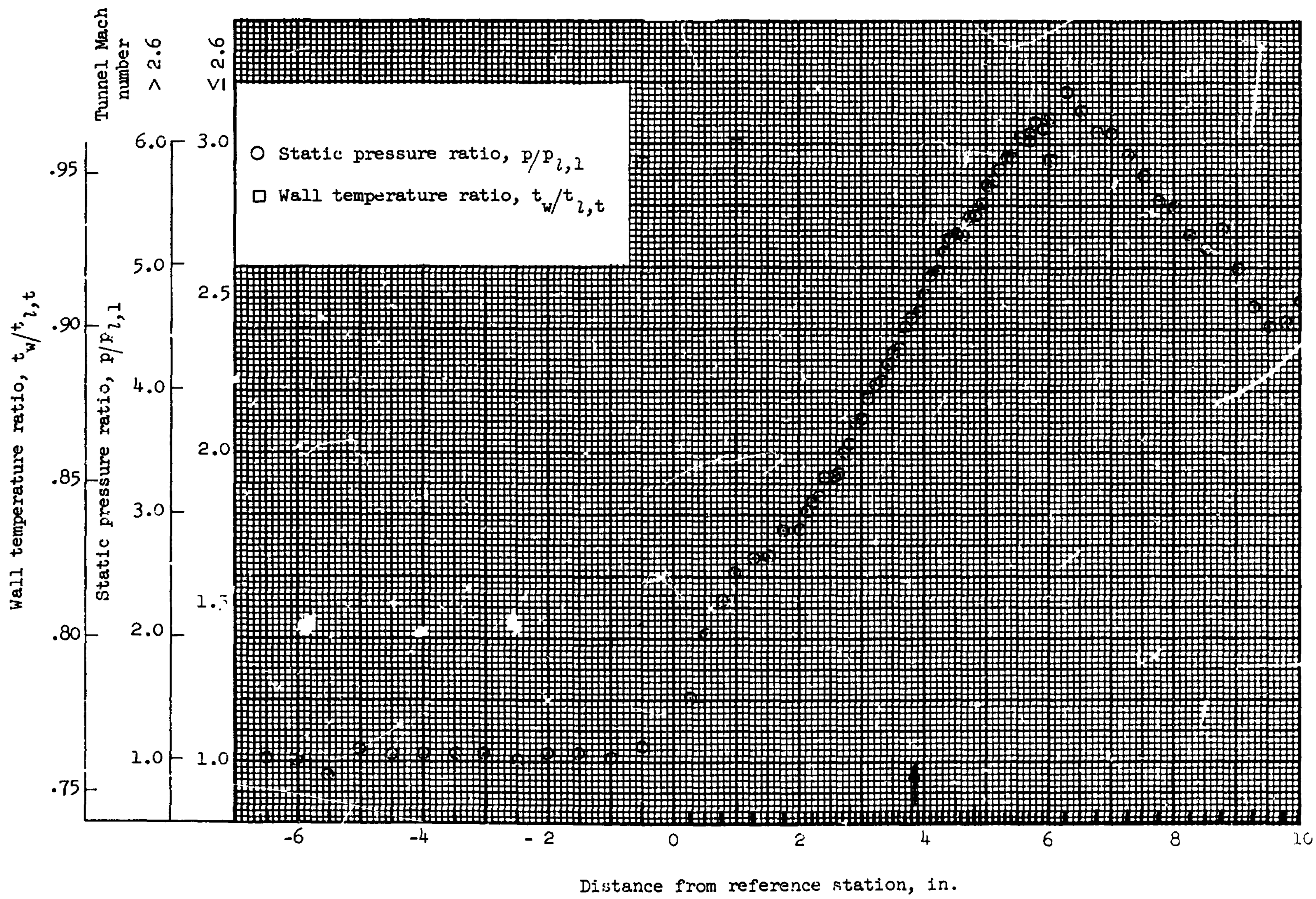

Figure 32.- Flat-plate static-pressure distributions and wall-temperature gradients through the incident-reflecting shock—boundary-layer interaction region for run 39. All identifying conditions are given in table III. The tunnel Mach number is 4.36. Arrow indicates approximate location of intersection of inviscid shock with flat plate.

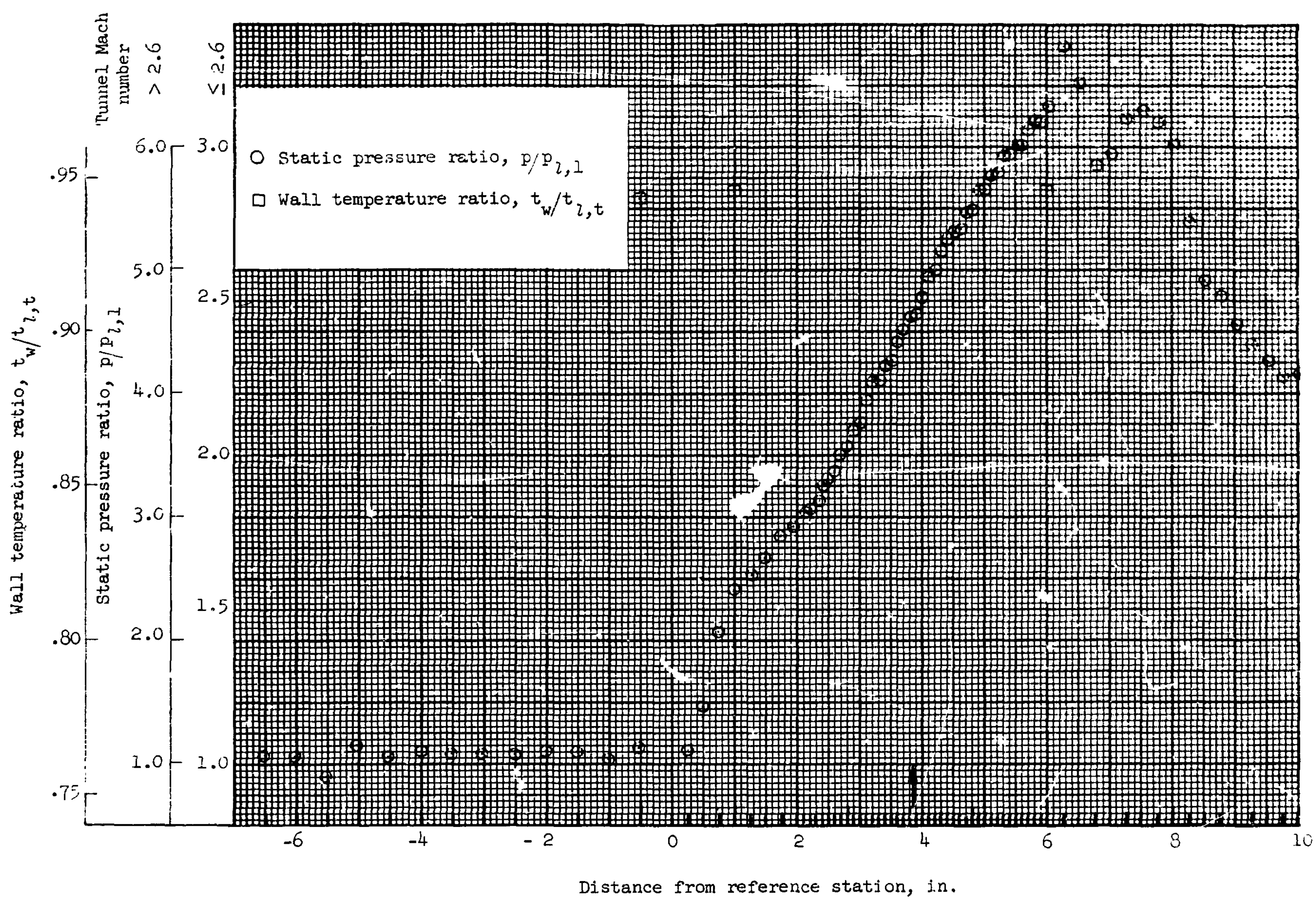

Figure 33.- Flat-plate static-pressure distributions and wall-temperature gradients through the incident-reflecting shock—boundary-layer interaction region for run 40. All identifying conditions are given in table III. The tunnel Mach number is 4.36. Arrow indicates approximate location of intersection of inviscid shock with flat plate.

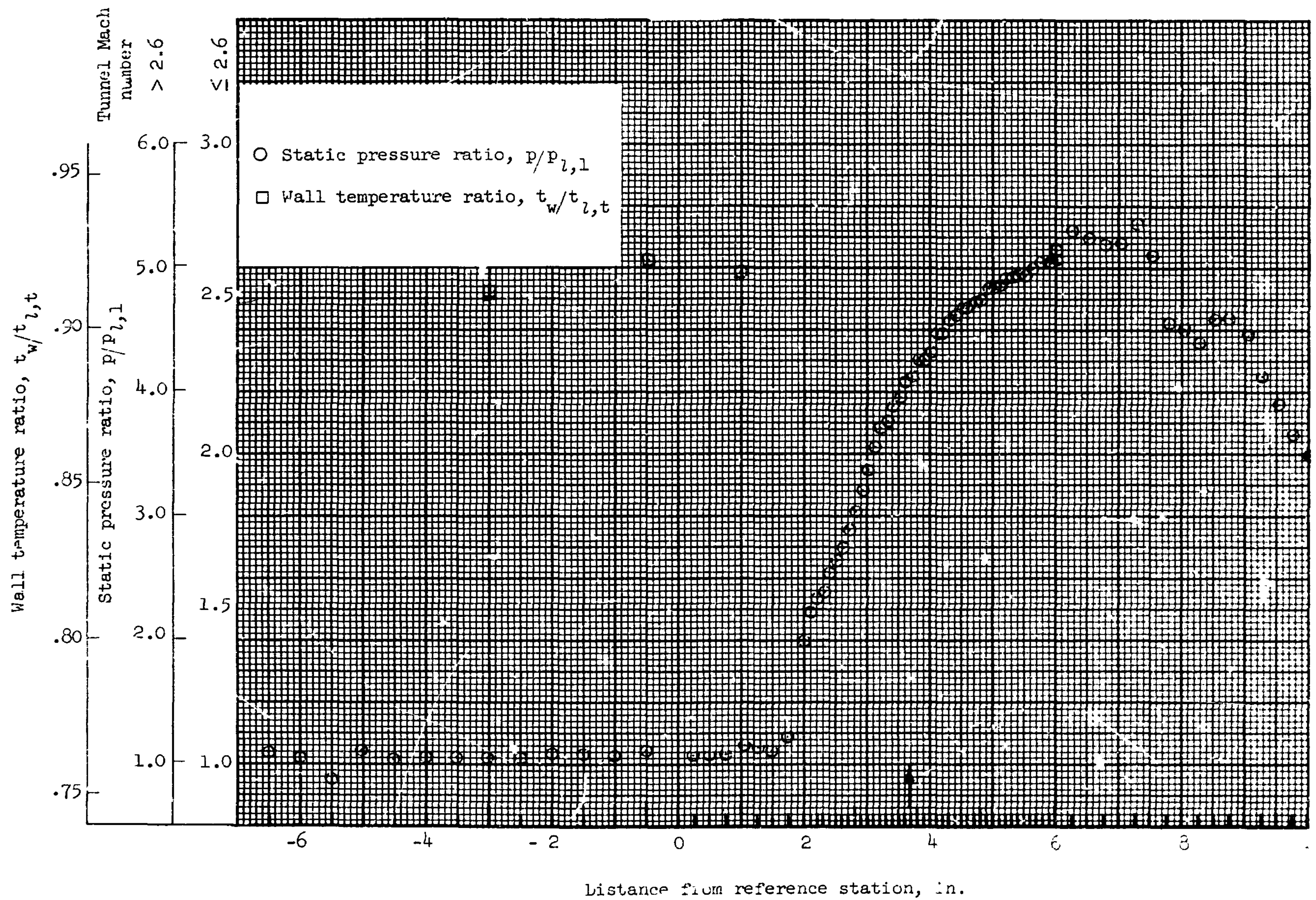

Figure 34.- Flat-plate static-pressure distributions and wall-temperature gradients through the incident-reflecting shock—boundary-layer interaction region for run 41. All identifying conditions are given in table III. The tunnel Mach number is 4.36. Arrow indicates approximate location of intersection of inviscid shock with flat plate.

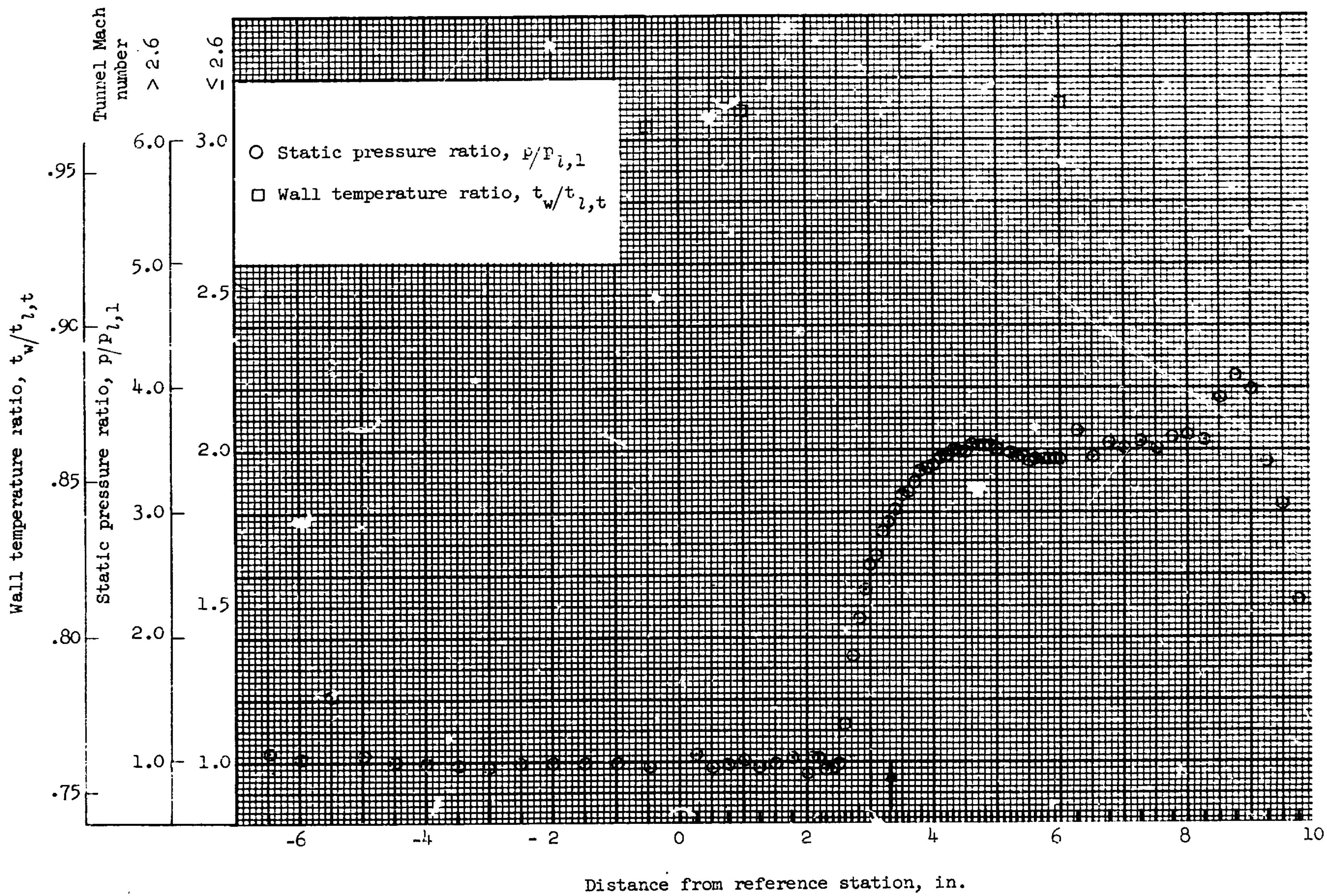

Figure 35.- Flat-plate static-pressure distributions and wall-temperature gradients through the incident-reflecting shock—boundary-layer interaction region for run 48. All identifying conditions are given in table III. The tunnel Mach number is 2.0. Arrow indicates approximate location of intersection of inviscid shock with flat plate.

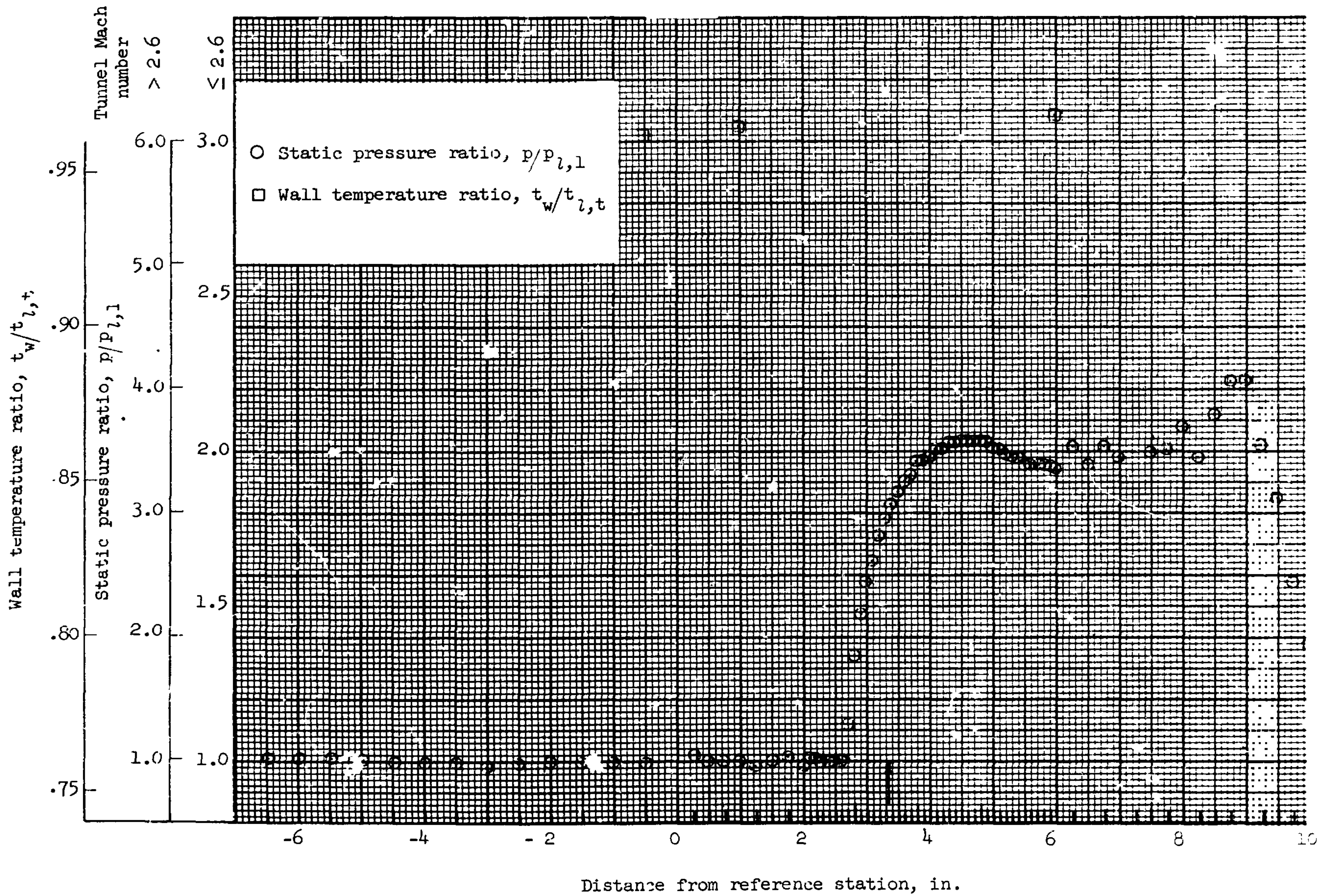

Figure 36.- Flat-plate static-pressure distributions and wall-temperature gradients through the incident-reflecting shock—boundary-layer interaction region for run 49. All identifying conditions are given in table III. The tunnel Mach number is 2.0. Arrow indicates approximate location of intersection of invis id shock with flat plate.

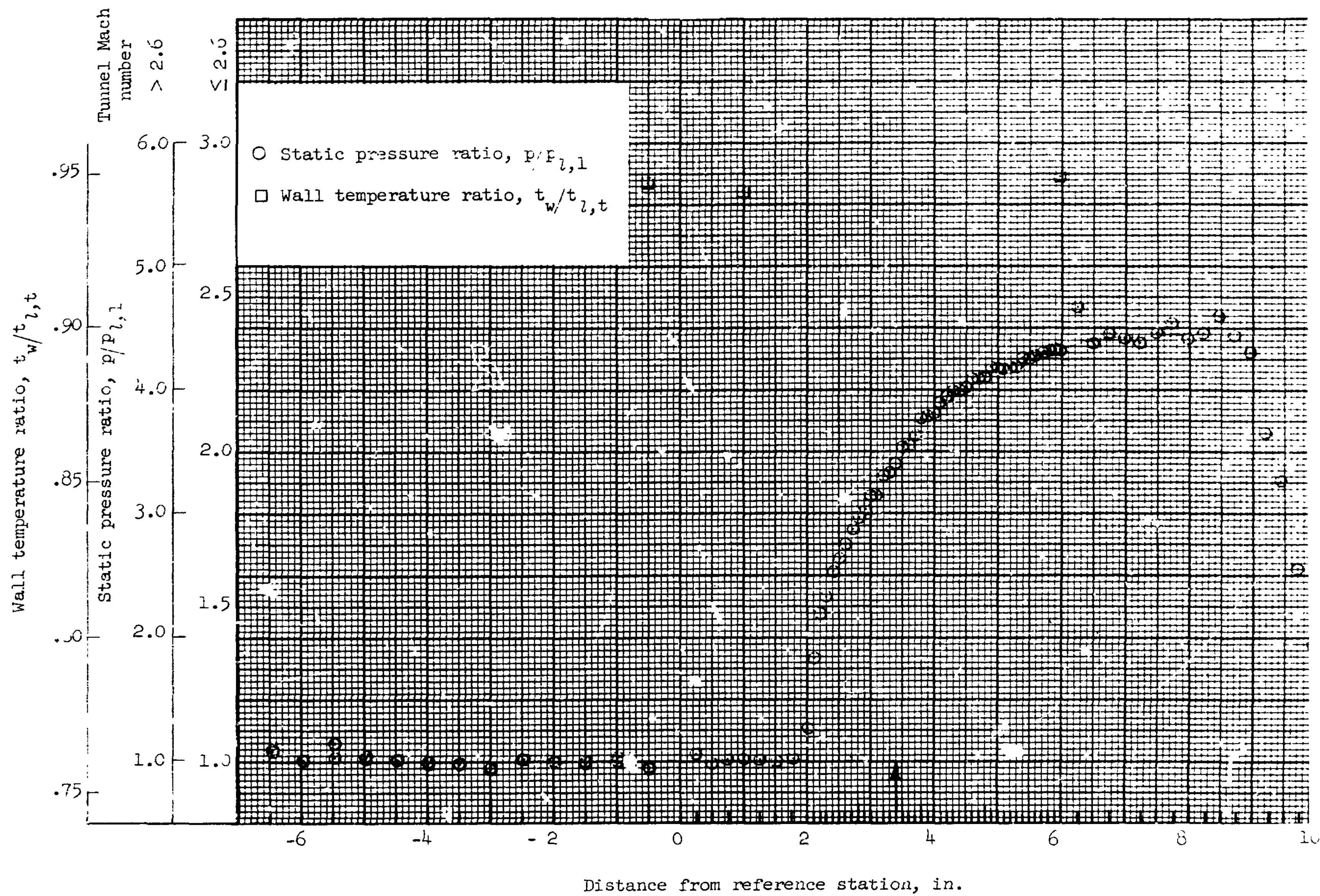

Figure 37.- Flat-plate static-pressure distributions and wall-temperature gradients through the incident-reflecting shock—boundary-layer interaction region for run 53. All identifying conditions are given in table III. The tunnel Mach number is 2.0. Arrow indicates approximate location of intersection of inviscid shock with flat plate.

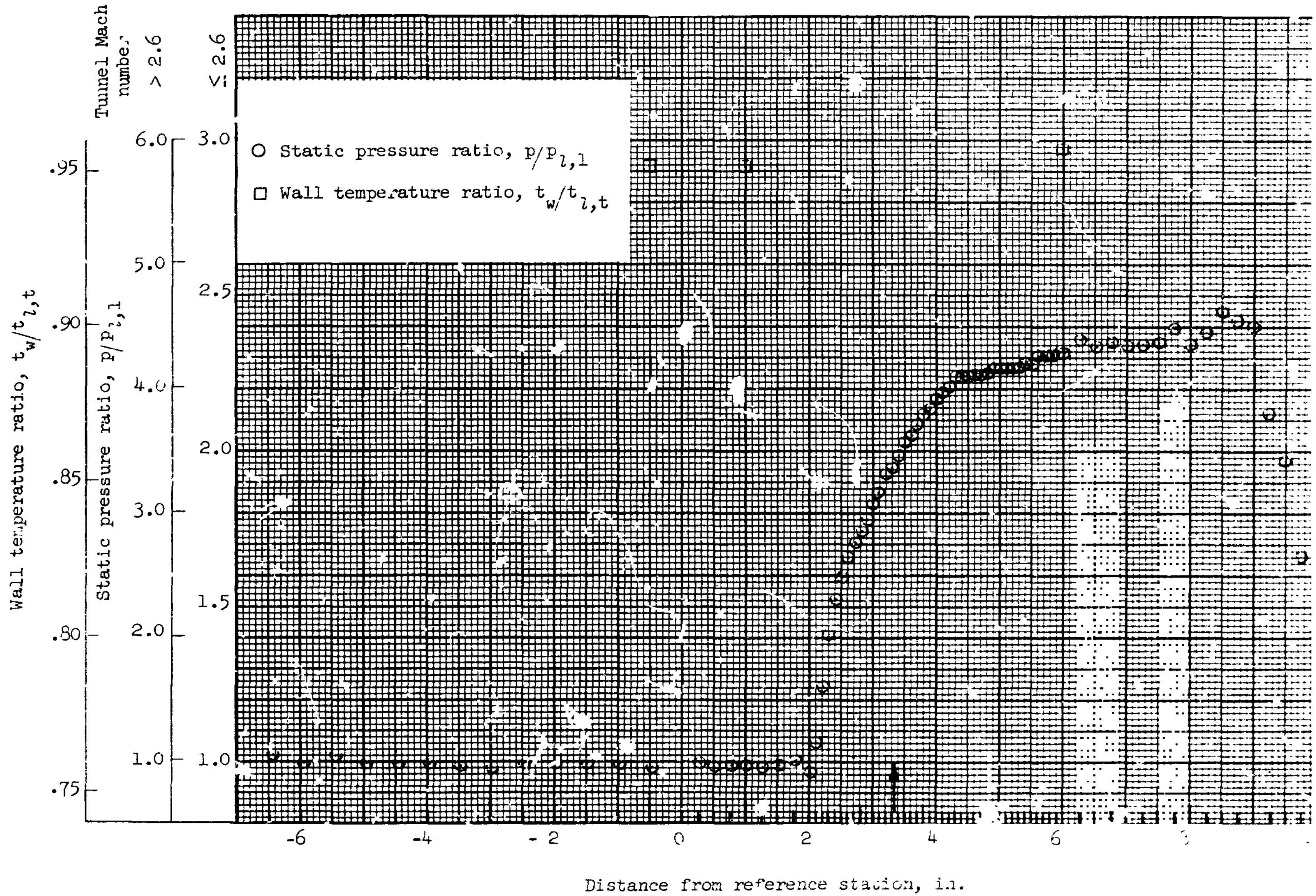

Figure 38.- Flat-plate static-pressure distributions and wall-temperature gradients through the incident-reflecting shock—boundary-layer interaction region for run 54. All identifying conditions are given in table III. The tunnel Mach number is 2.0. Arrow indicates approximate location of intersection of inviscid shock with flat plate.

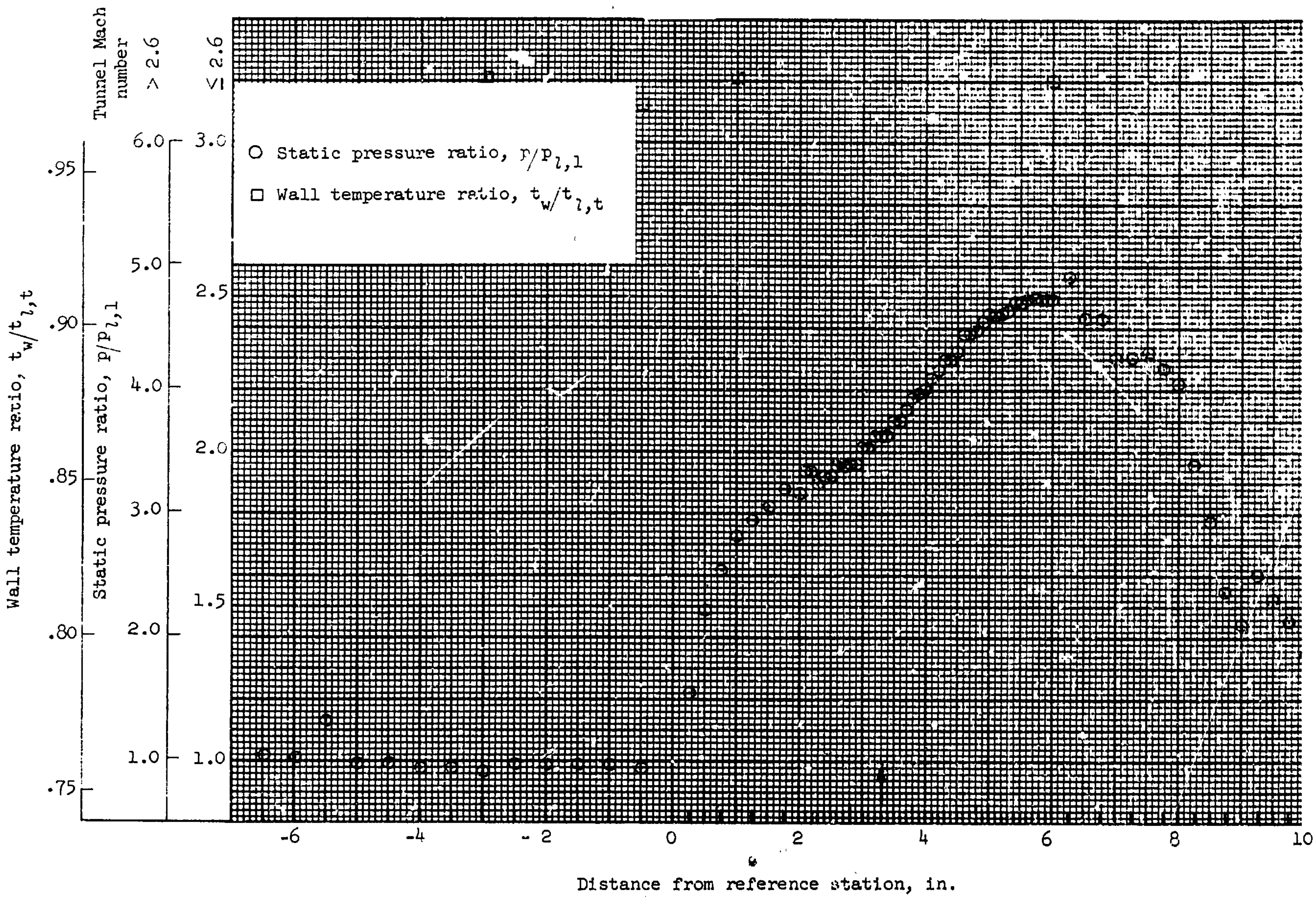

Figure 39.- Flat-plate static-pressure distributions and wall-temperature gradients through the incident-reflecting shock—boundary-layer interaction region for run 57. All identifying conditions are given in table III. The tunnel Mach number is 2.0. Arrow indicates approximate location of intersection of inviscid shock with flat plate.

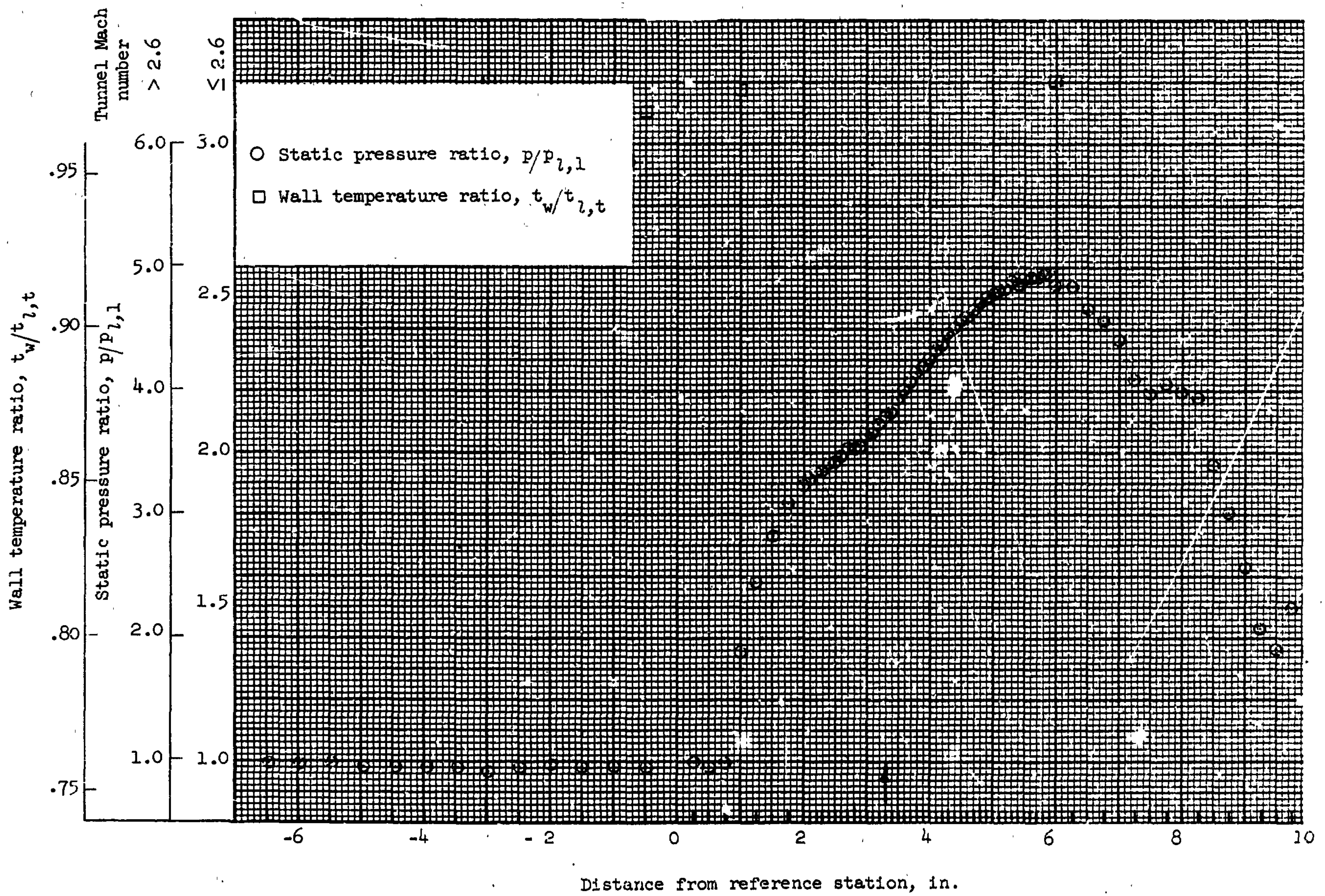

Figure 40.- Flat-plate static-pressure distributions and wall-temperature gradients through the incident-reflecting shock—boundary-layer interaction region for run 58. All identifying conditions are given in table III. The tunnel Mach number is 2.0. Arrow indicates approximate location of intersection of inviscid shock with flat plate.

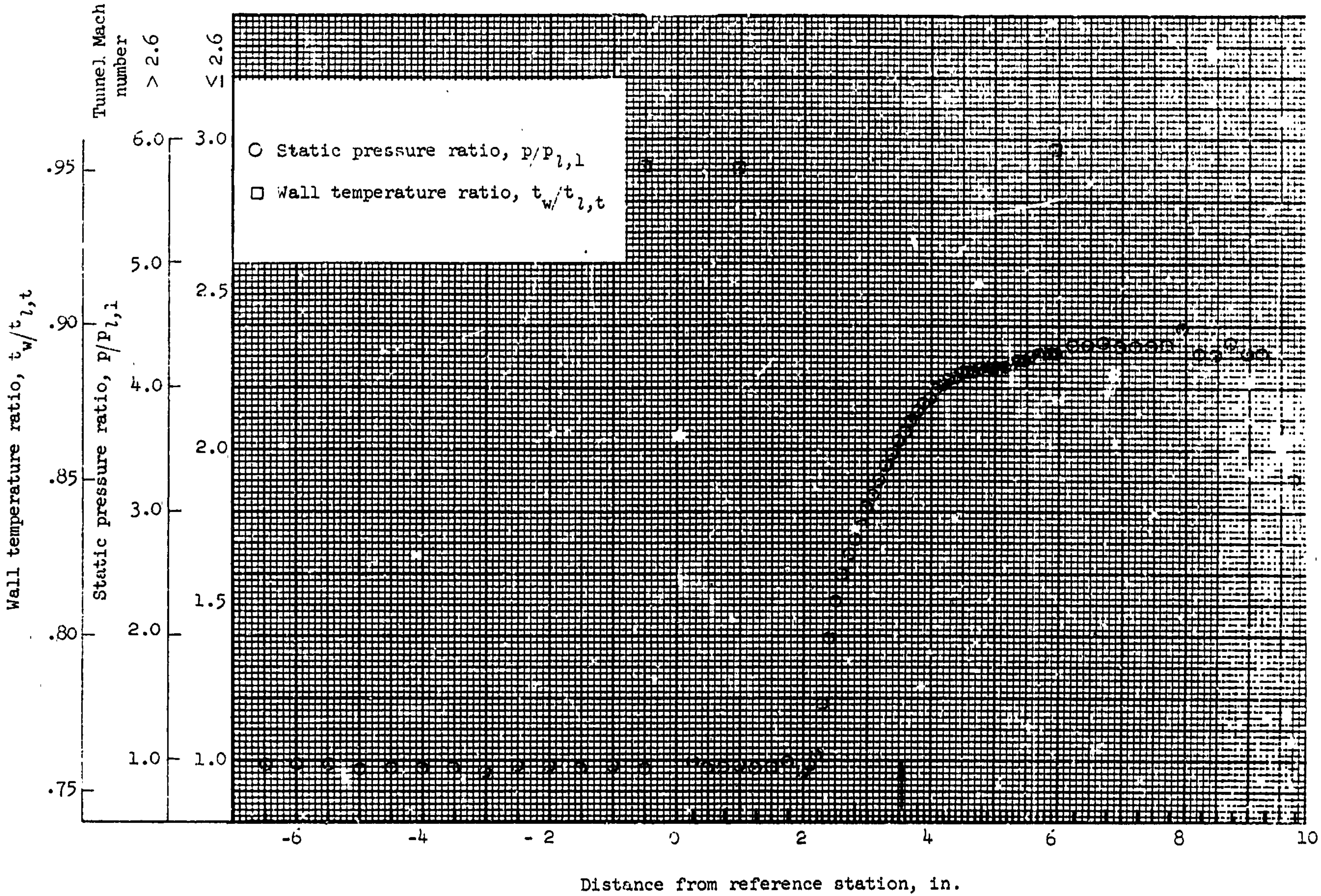

Figure 41.- Flat-plate static-pressure distributions and wall-temperature gradients through the incident-reflecting shock—boundary-layer interaction region for run 61. All identifying conditions are given in table III. The tunnel Mach number is 2.0. Arrow indicates approximate location of intersection of inviscid shock with flat plate.

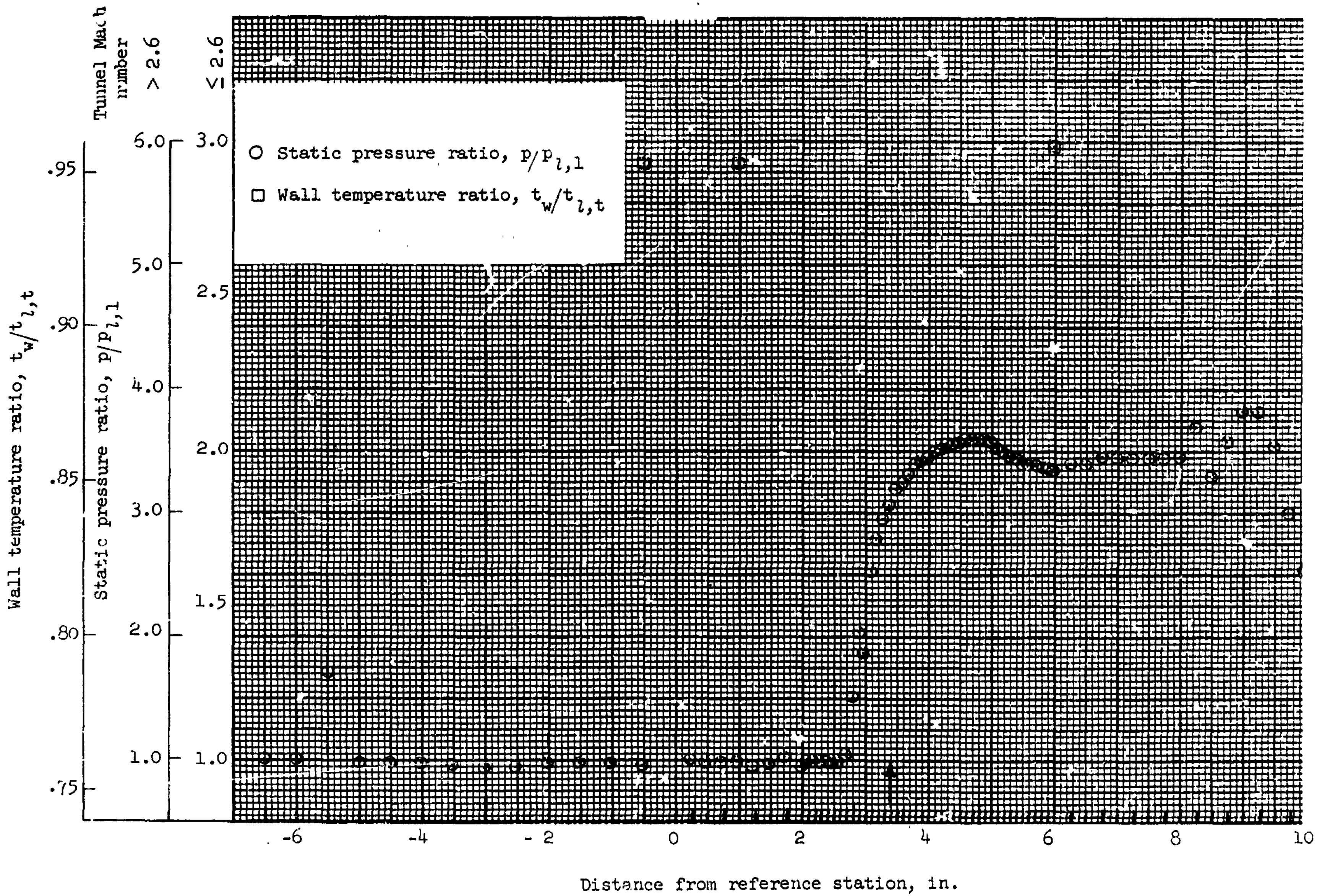

Figure 42.- Flat-plate static-pressure distributions and wall-temperature gradients through the incident-reflecting shock—boundary-layer interaction region for run 63. All identifying conditions are given in table III. The tunnel Mach number is 2.0. Arrow indicates approximate location of intersection of inviscid shock with flat plate.

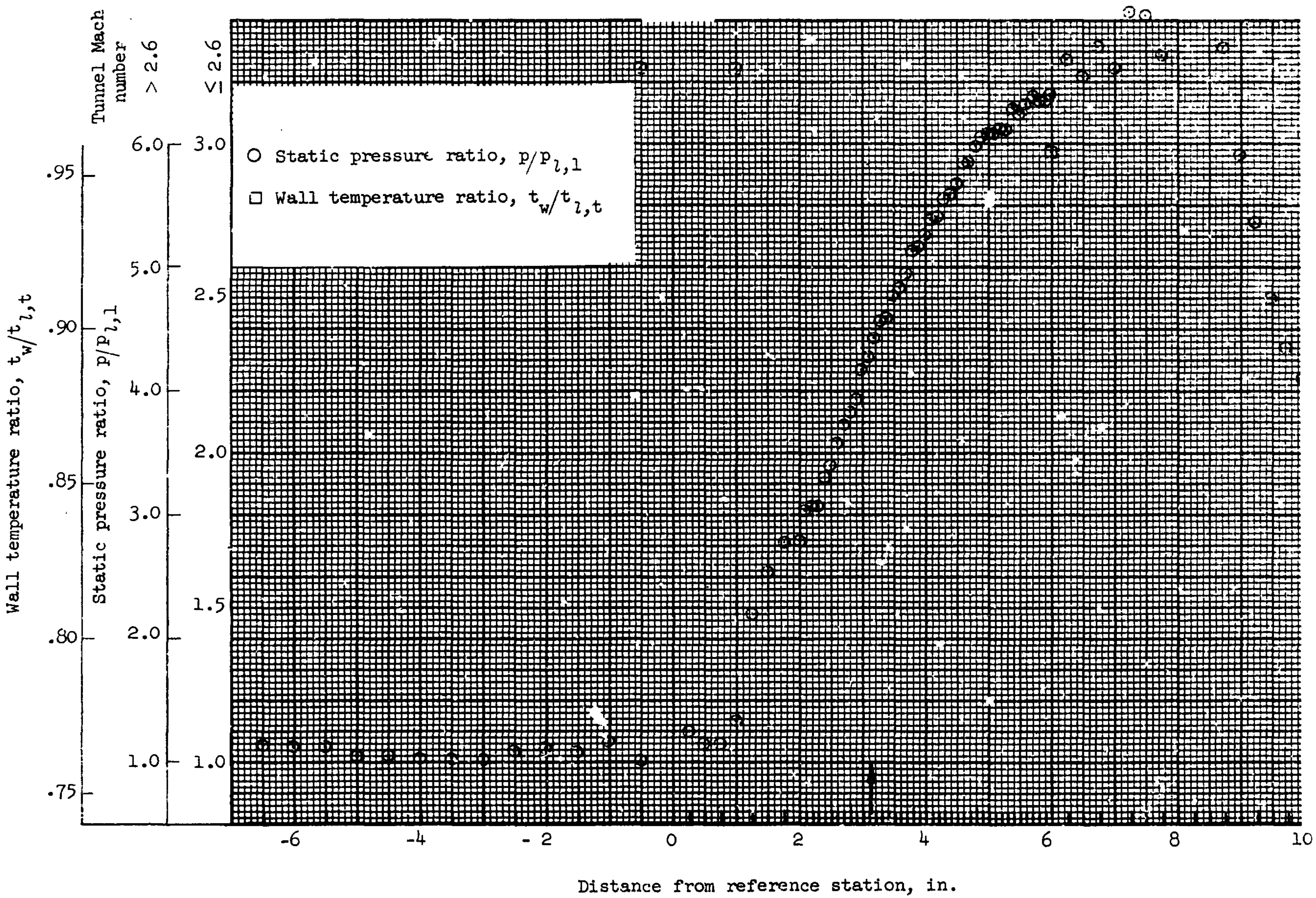

Figure 43.- Flat-plate static-pressure distributions and wall-temperature gradients through the incident-reflecting shock—boundary-layer interaction region for run 68. All identifying conditions are given in table III. The tunnel Mach number is 4.2. Arrow indicates approximate location of intersection of inviscid shock with flat plate.

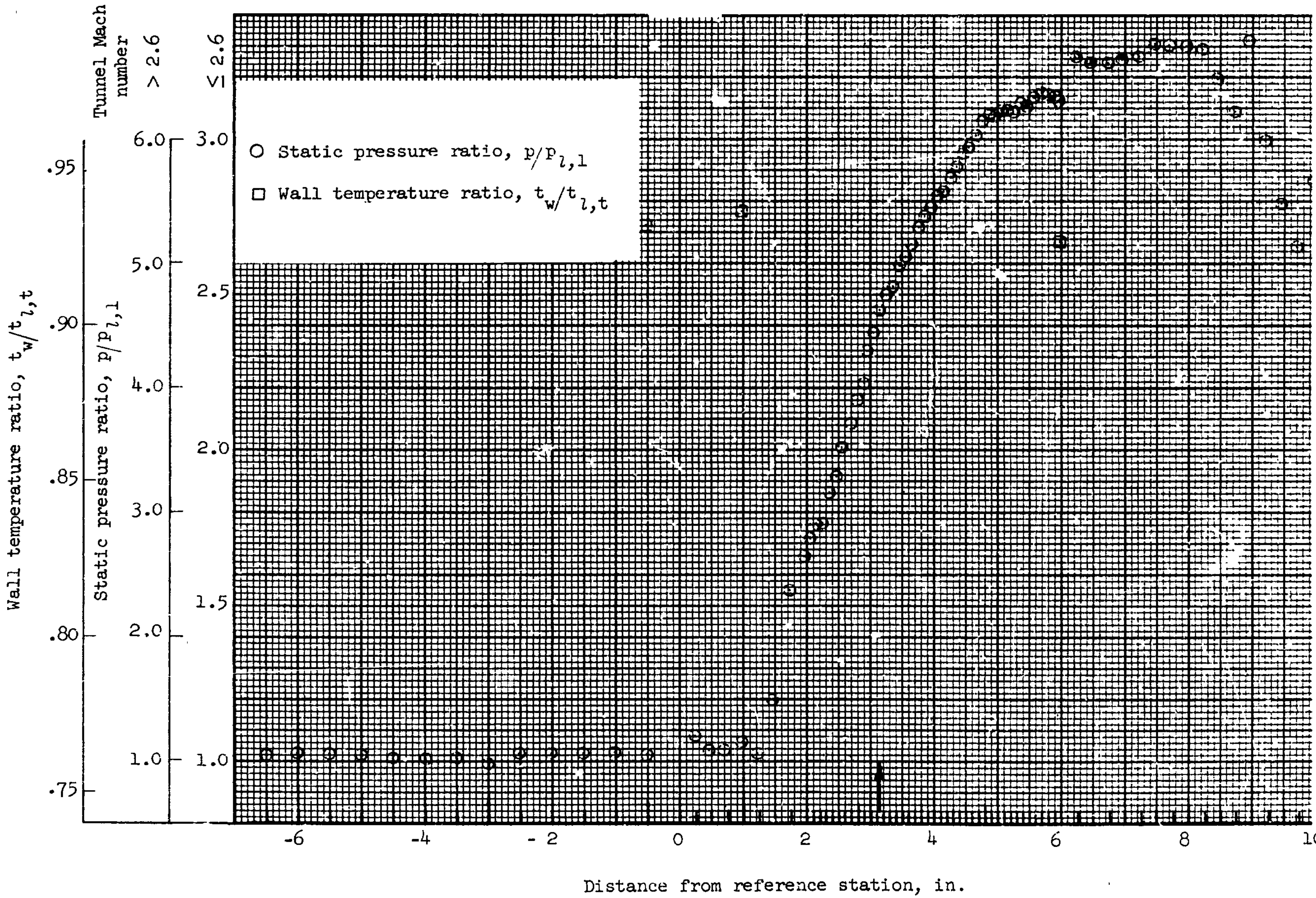

Figure 44.- Flat-plate static-pressure distributions and wall-temperature gradients through the incident-reflecting shock—boundary-layer interaction region for run 70. All identifying conditions are given in table III. The tunnel Mach number is 4.2. Arrow indicates approximate location of intersection of inviscid shock with flat plate.

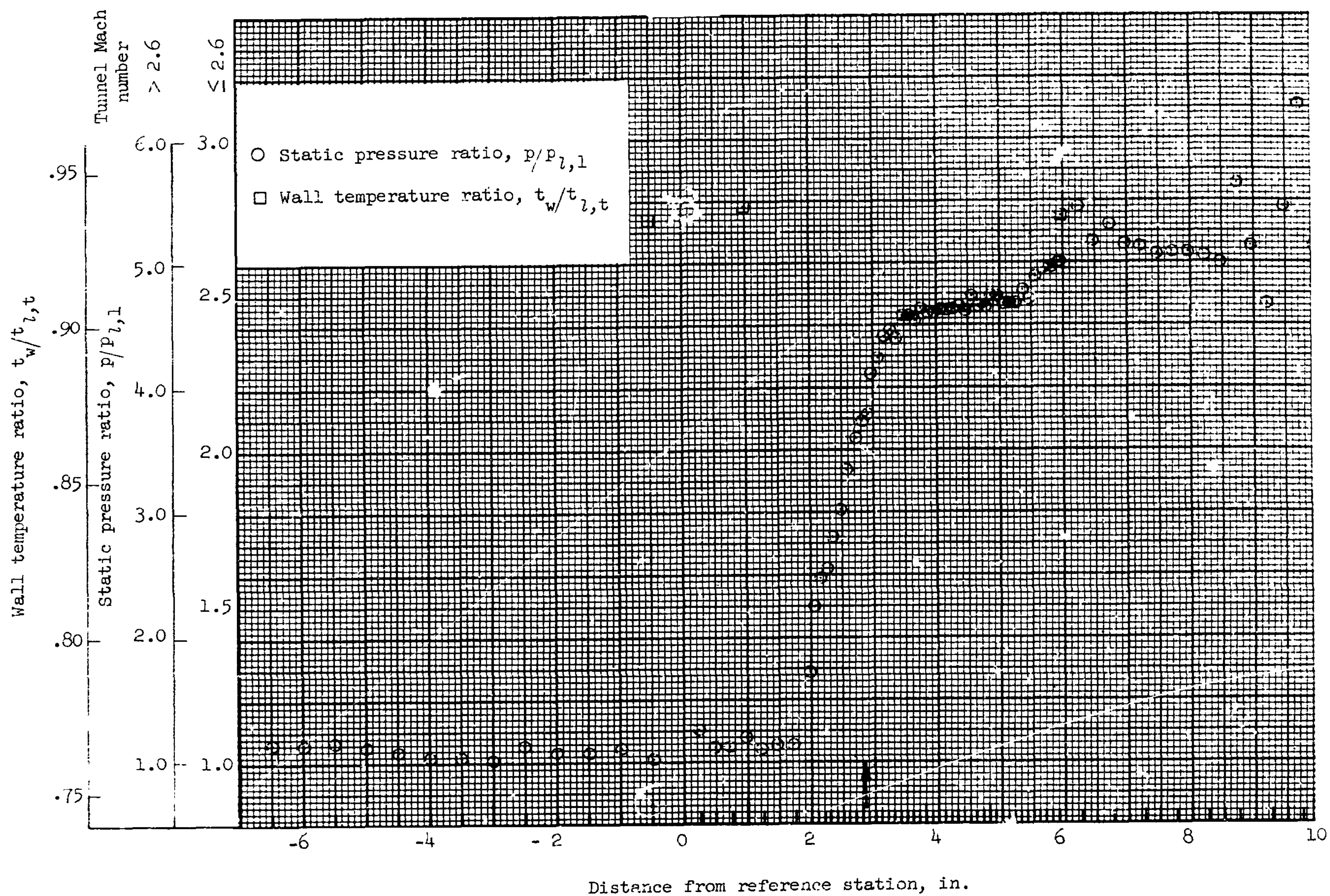

Figure 45.- Flat-plate static-pressure distributions and wall-temperature gradients through the incident-reflecting shock—boundary-layer interaction region for run 72. All identifying conditions are given in table III. The tunnel Mach number is 4.2. Arrow indicates approximate location of intersection of inviscid shock with flat plate.

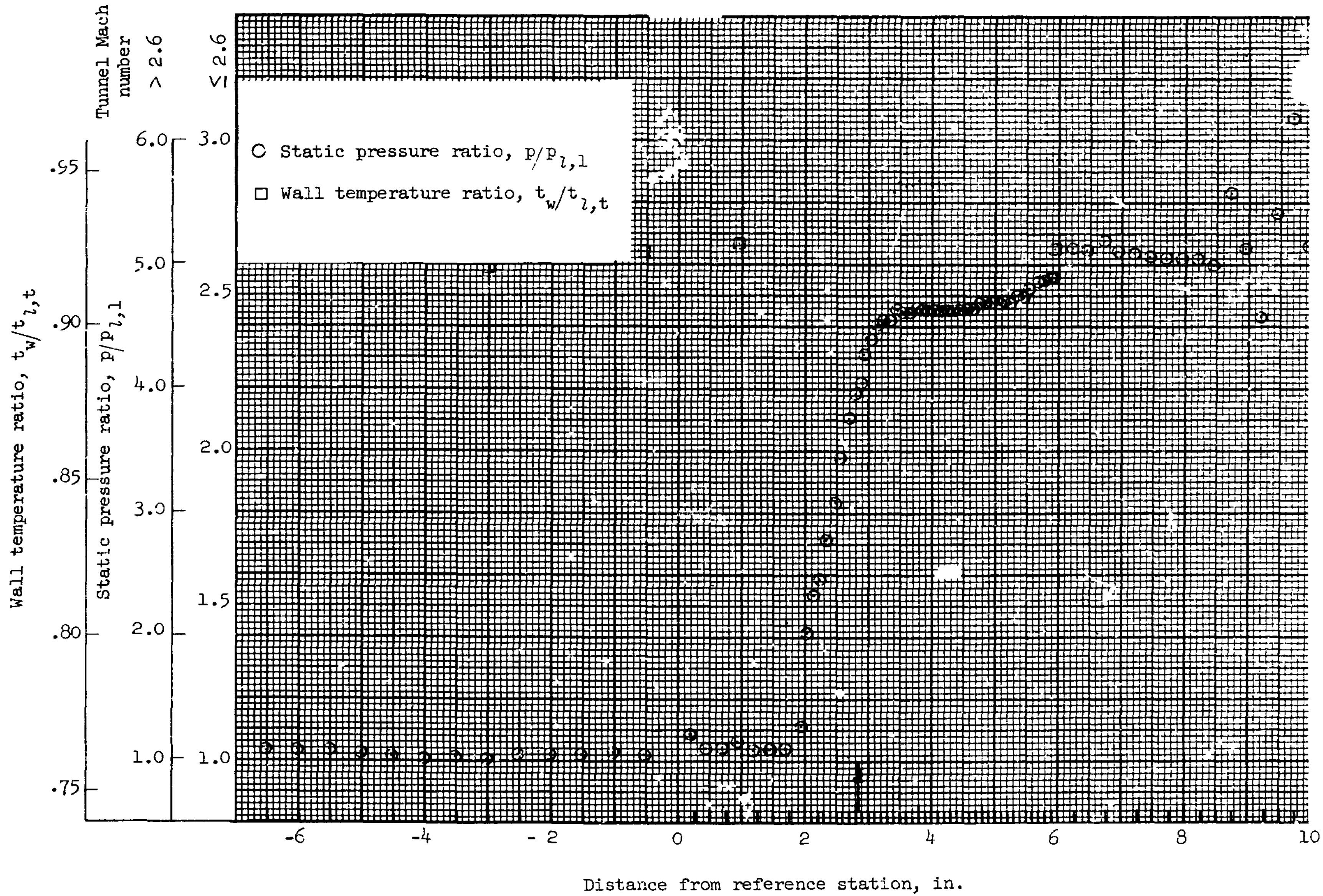

Figure 46.- Flat plate static-pressure distributions and wall-temperature gradients through the incident-reflecting shock—boundary-layer interaction region for run 73. All identifying conditions are given in table III. The tunnel Mach number is 4.2. Arrow indicates approximate location of intersection of inviscid shock with flat plate.

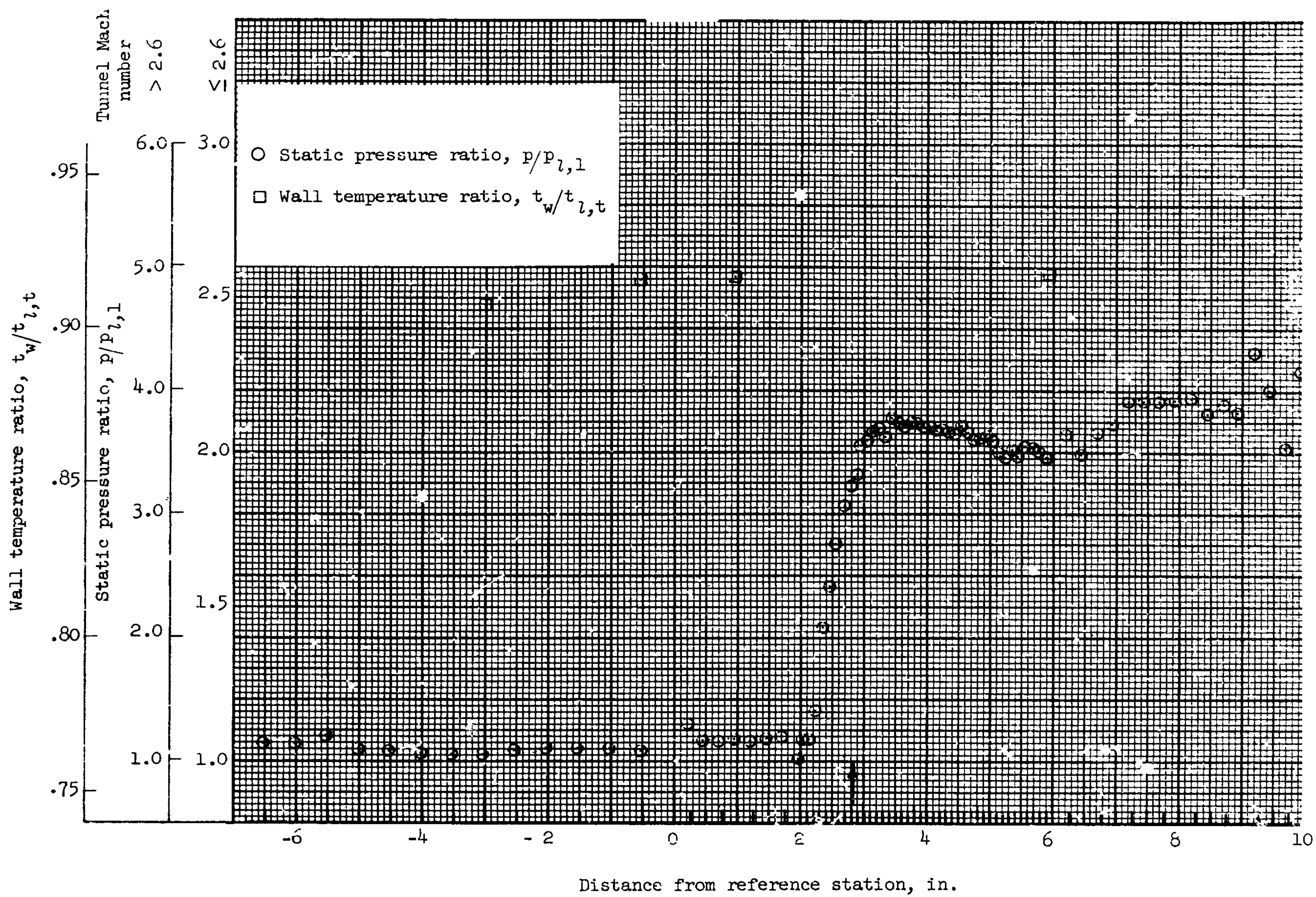

Figure 47.- Flat-plate static-pressure distributions and wall-temperature gradients through the incident-reflecting shock—boundary-layer interaction region for run 76. All identifying conditions are given in table III. The tunnel Mach number is 4.2. Arrow indicates approximate location of intersection of inviscid shock with flat plate.

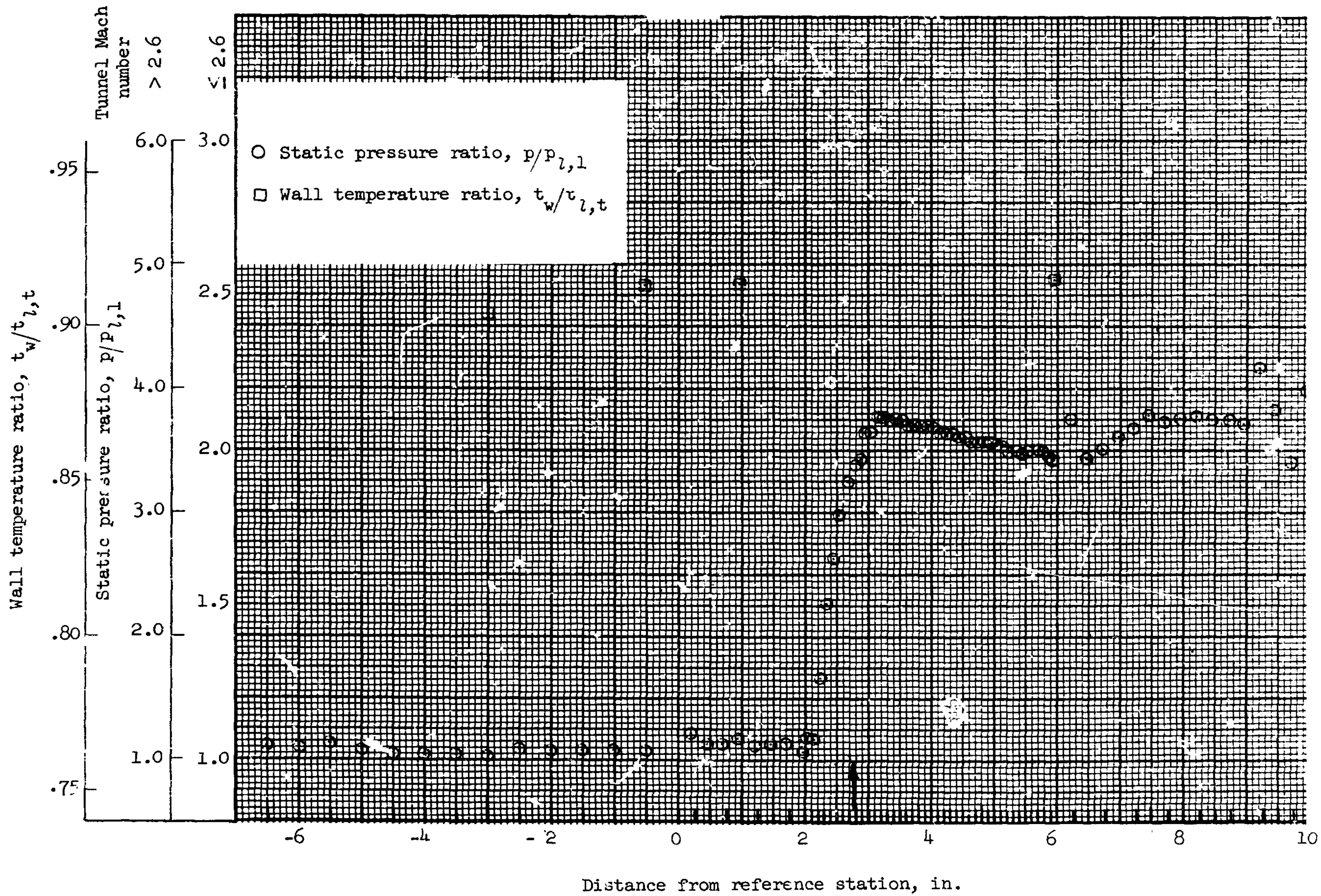

Figure 48.- Flat-plate static-pressure distributions and wall-temperature gradients through the incident-reflecting shock—boundary-layer interaction region for run 77. All identifying conditions are given in table III. The tunnel Mach number is 4.2. Arrow indicates approximate location of intersection of inviscid shock with flat plate.

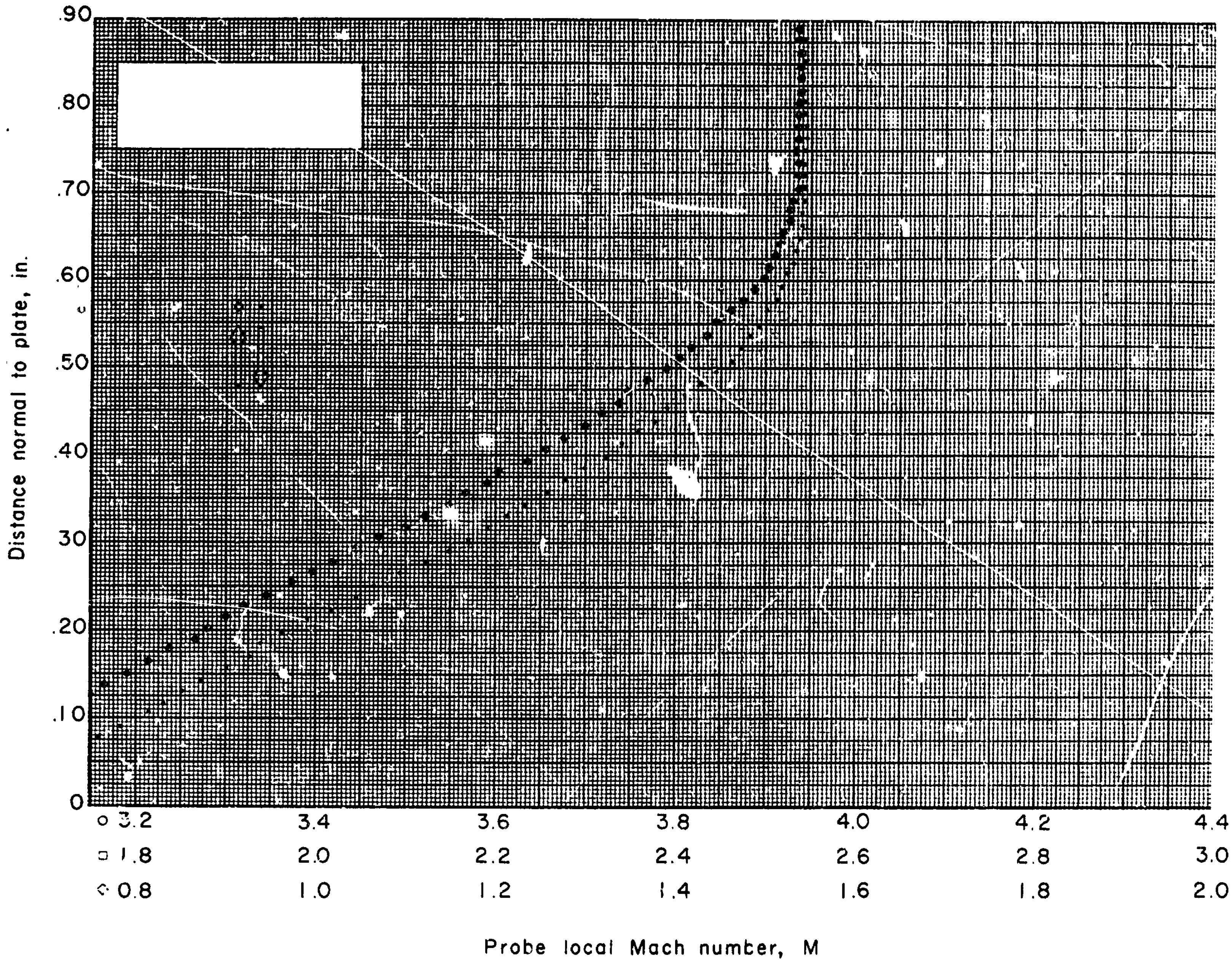

Figure 49.- Boundary-layer Mach number distribution for run 1. All identifying conditions are given in table III. Arrows identify direction of probe travel across the boundary layer.

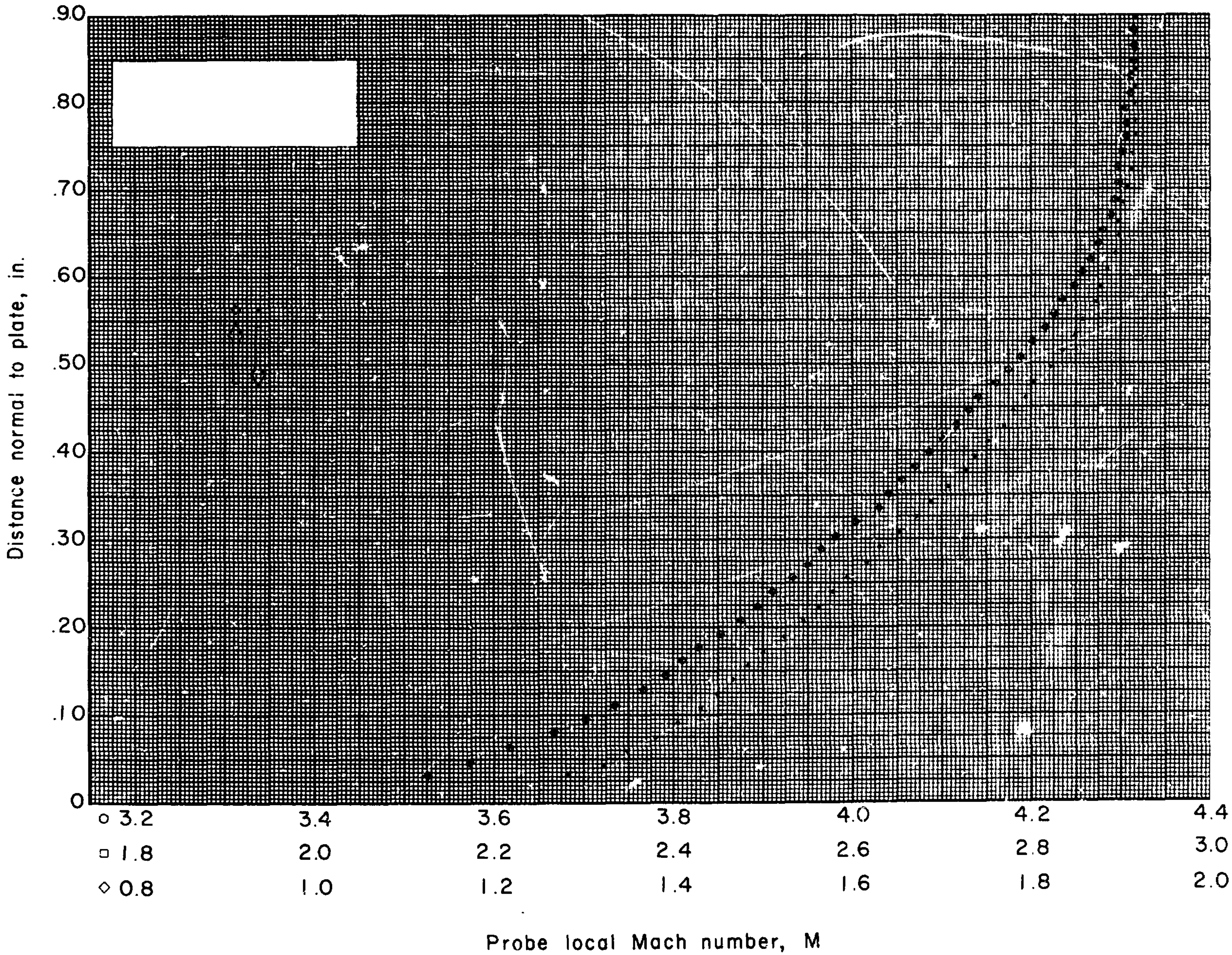

Figure 50.- Boundary-layer Mach number distribution for run 2. All identifying conditions are given in table III. Arrows identify direction of probe travel across the boundary layer.

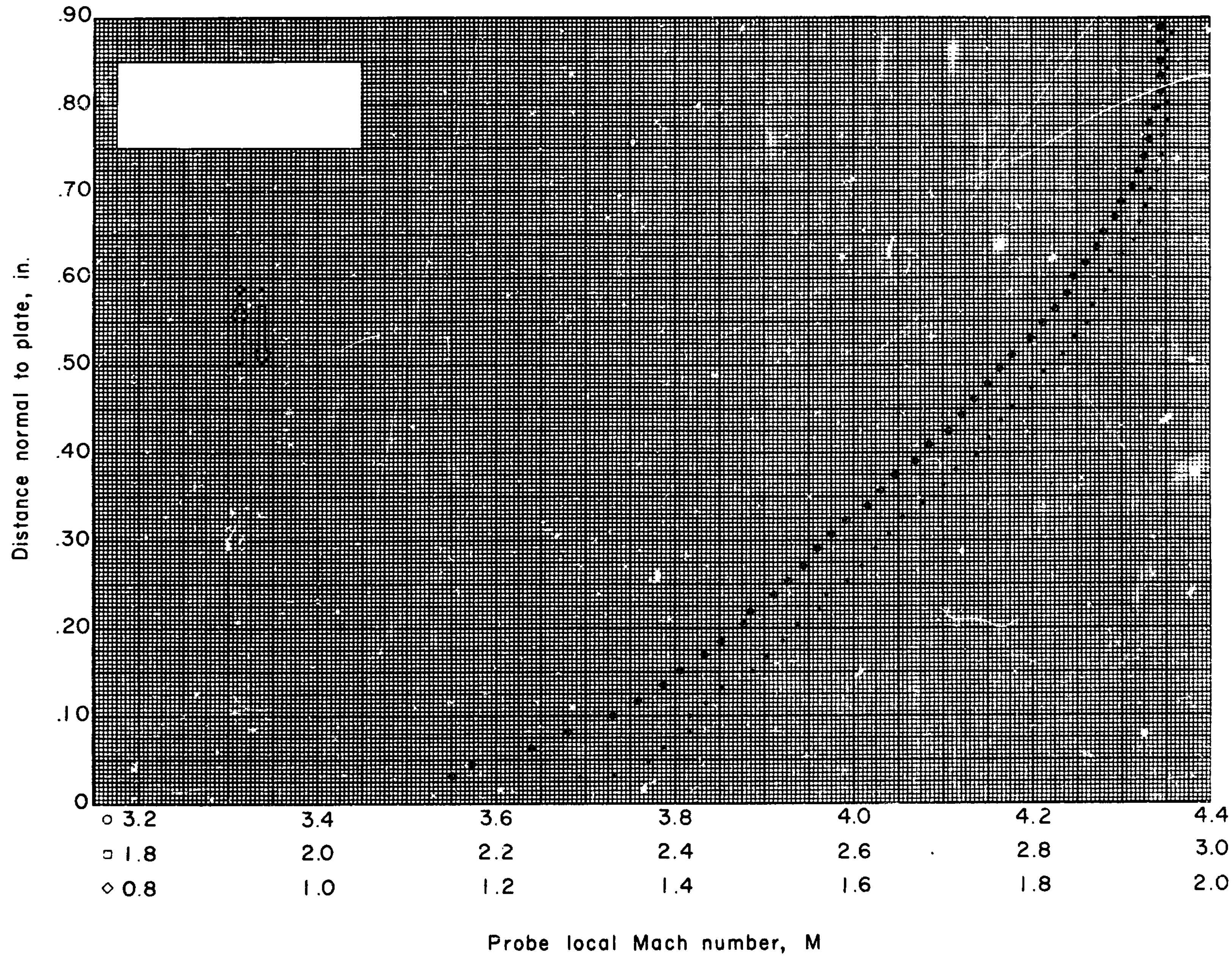

Figure 51.- Boundary-layer Mach number distribution for run 3. All identifying conditions are given in table III. Arrows identify direction of probe travel across the boundary layer.

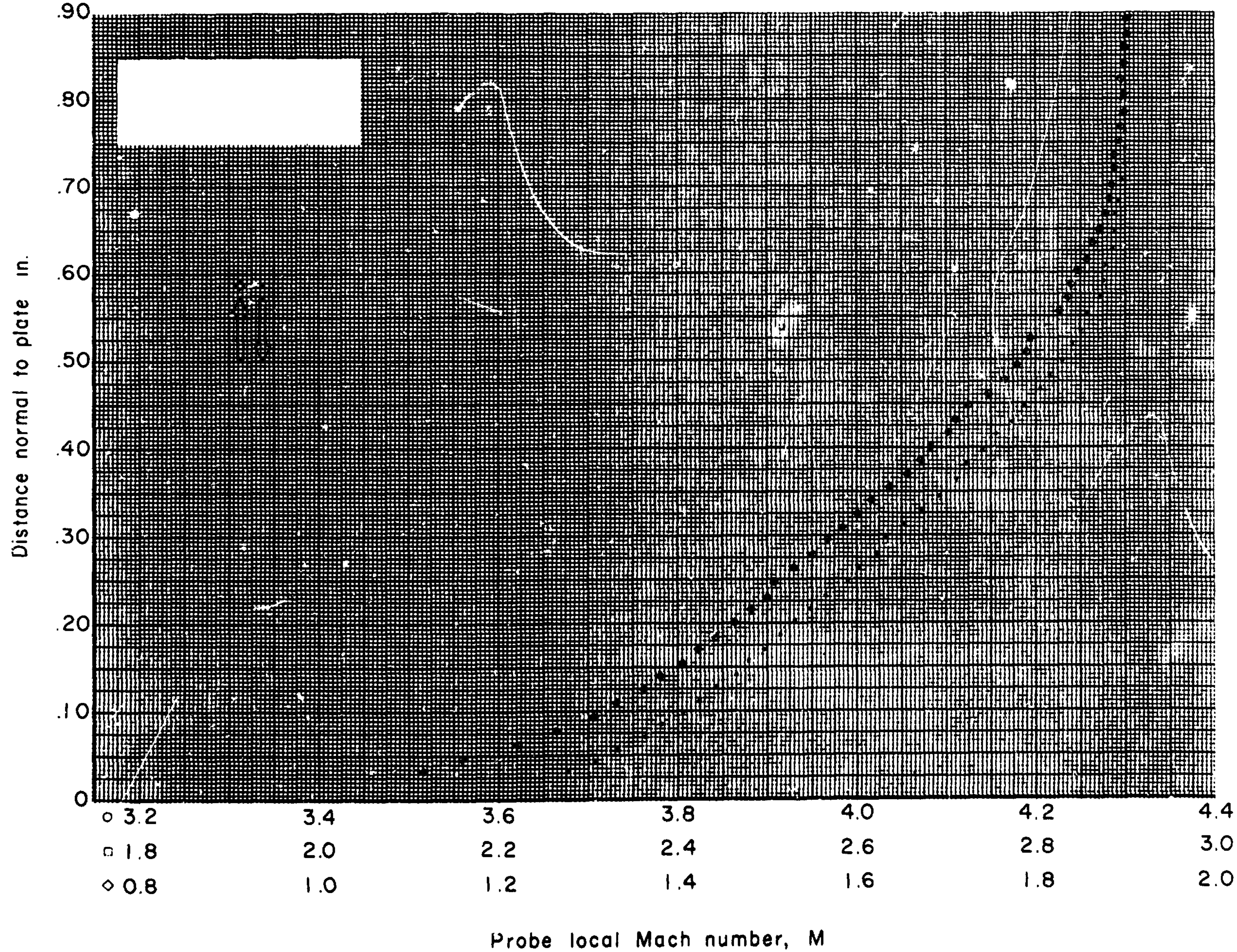

Figure 52.- Boundary-layer Mach number distribution for run 4. All identifying conditions are given in table III. Arrows identify direction of probe travel across the boundary layer.

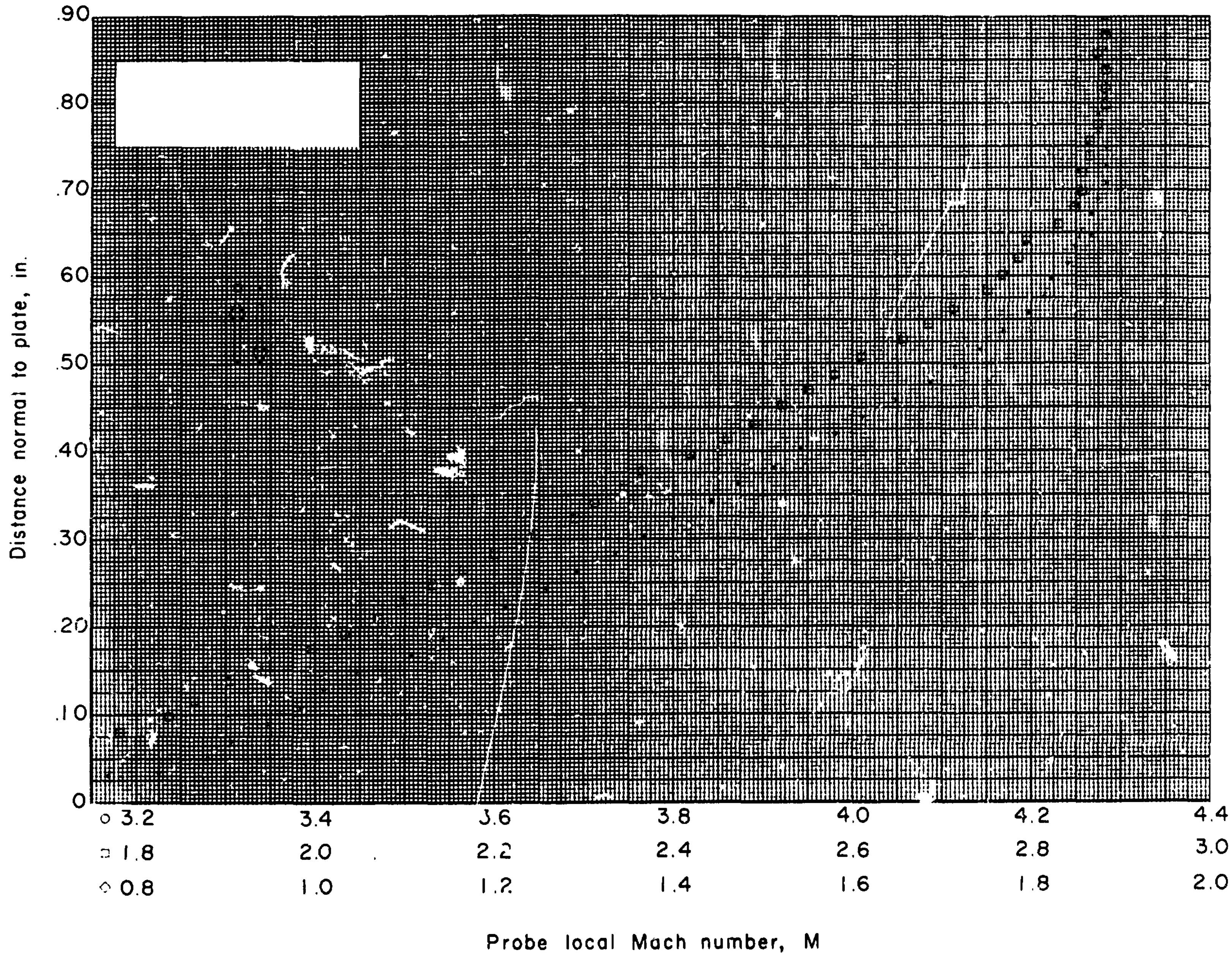

Figure 53.- Boundary-layer Mach number distribution for run 5. All identifying conditions are given in table III. Arrows identify direction of probe travel across the boundary layer.

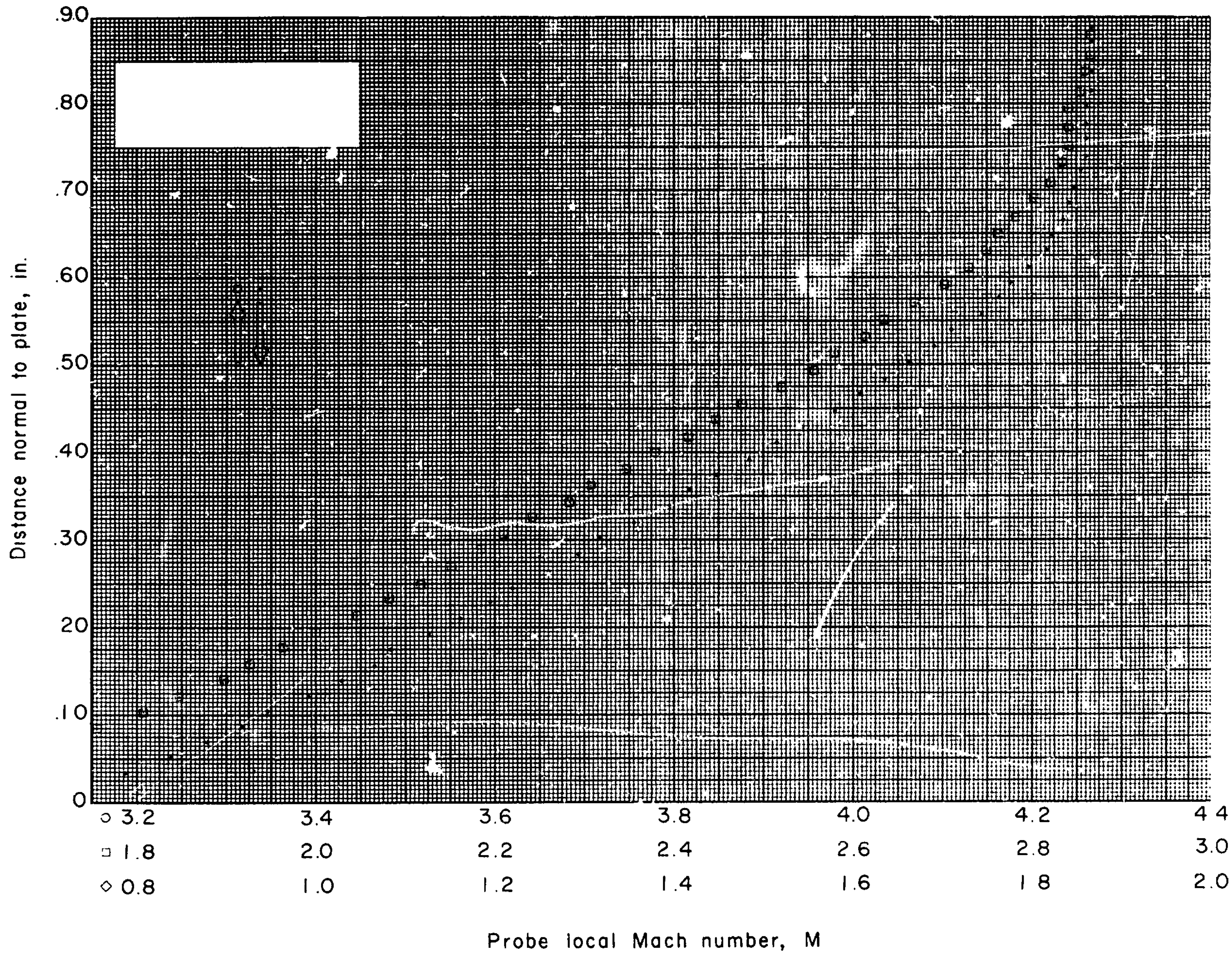

Figure 54.- Boundary-layer Mach number distribution for run 6. All identifying conditions are given in table III. Arrows identify direction of probe travel across the boundary layer.

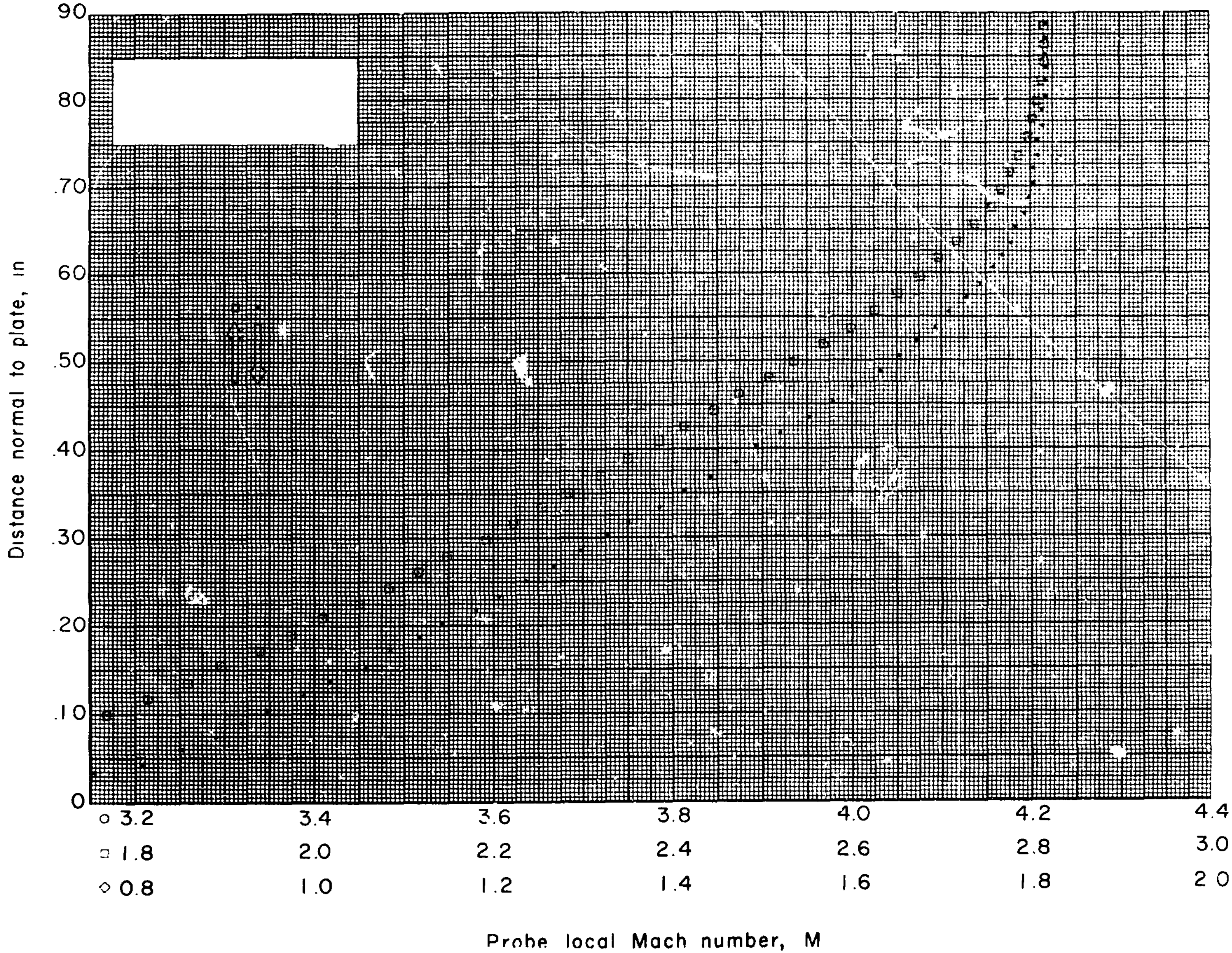

Figure 55.- Boundary-layer Mach number distribution for run 7. All identifying conditions are given in table III. Arrows identify direction of probe travel across the boundary layer.

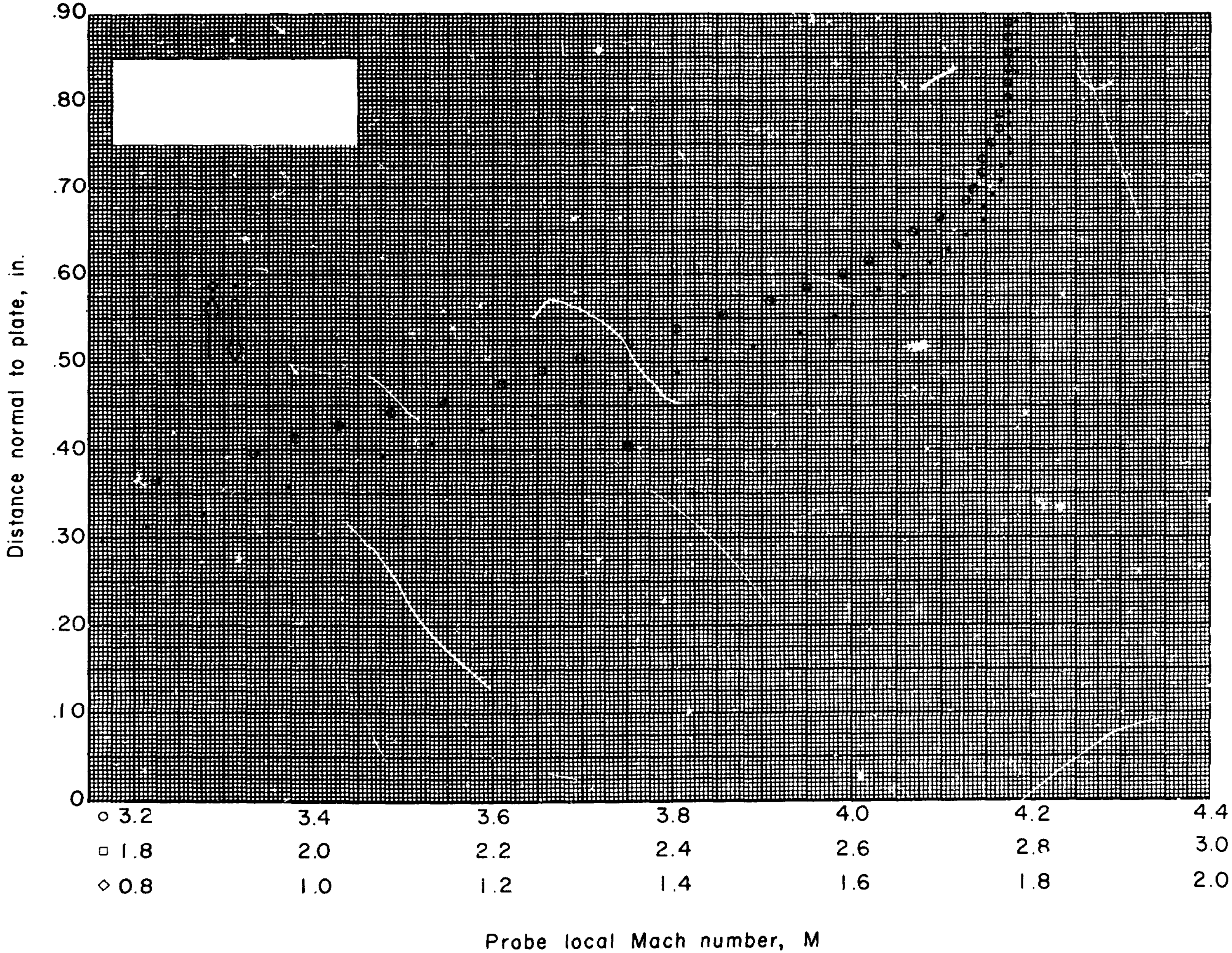

Figure 56.- Boundary-layer Mach number distribution for run 8. All identifying conditions are given in table III. Arrows identify direction of probe travel across the boundary layer.

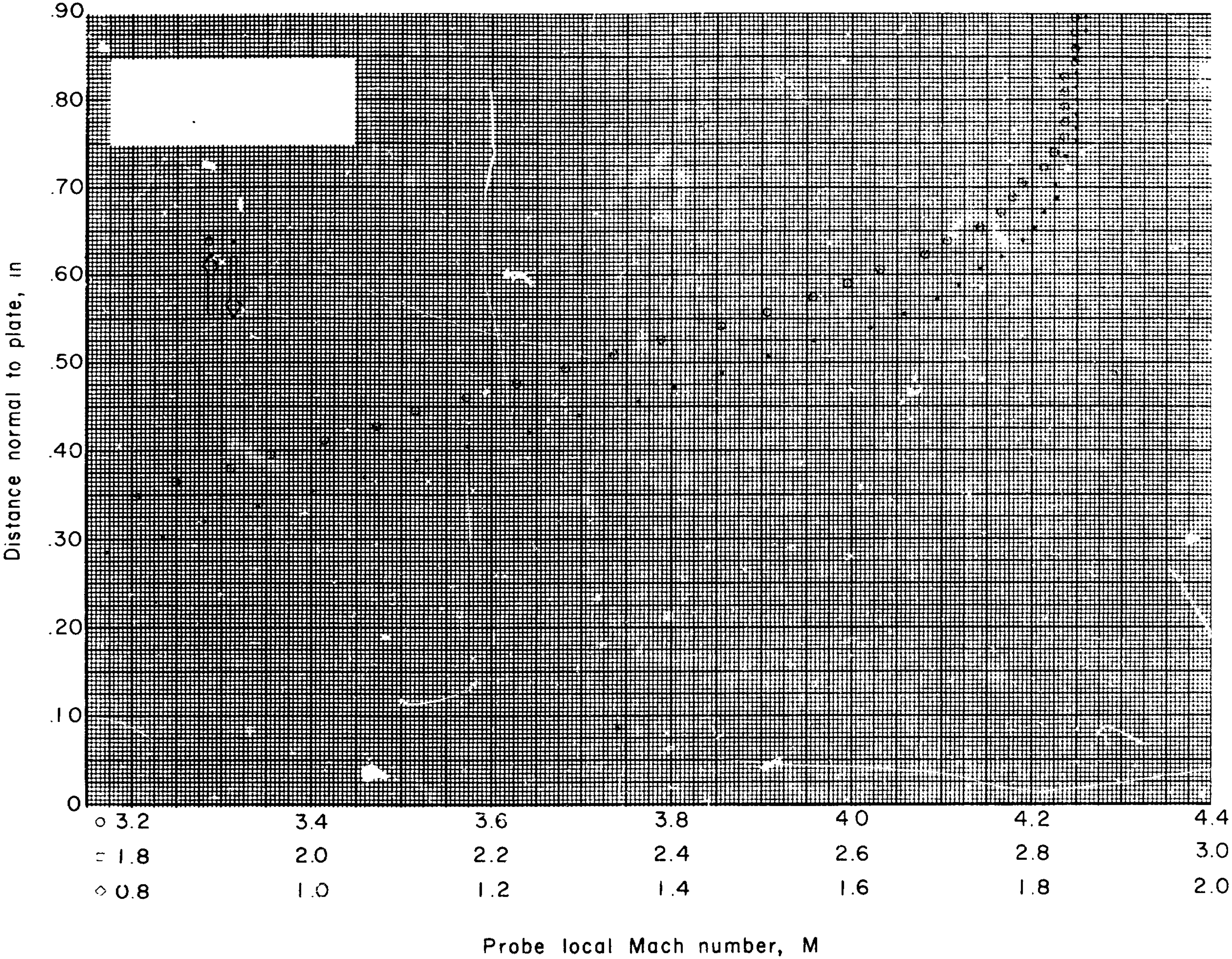

Figure 57.- Boundary-layer Mach number distribution for run 9. All identifying conditions are given in table III. Arrows identify direction of probe travel across the boundary layer.

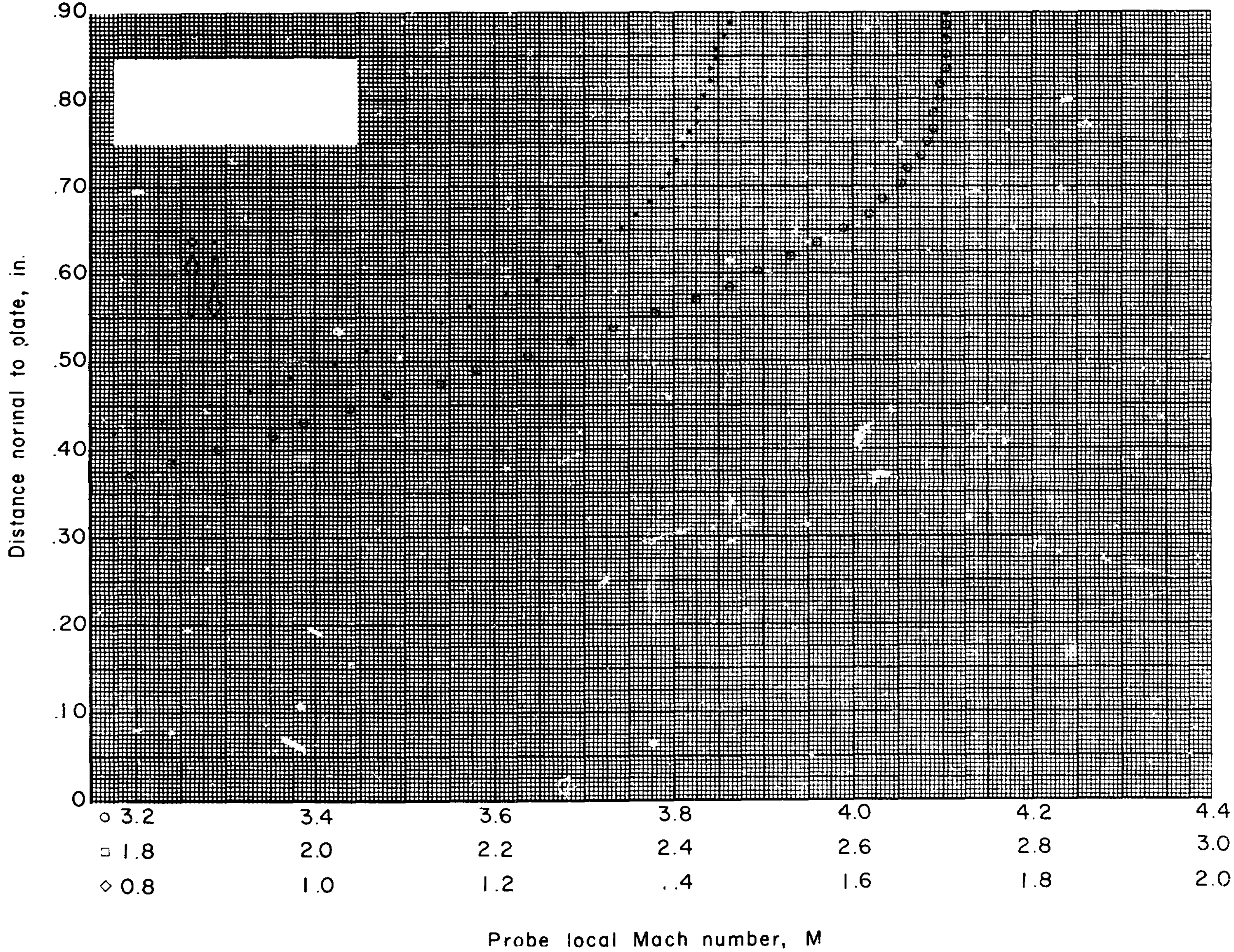

Figure 58.- Boundary-layer Mach number distribution for run 10. All identifying conditions are given in table III. Arrows identify direction of probe travel across the boundary layer.

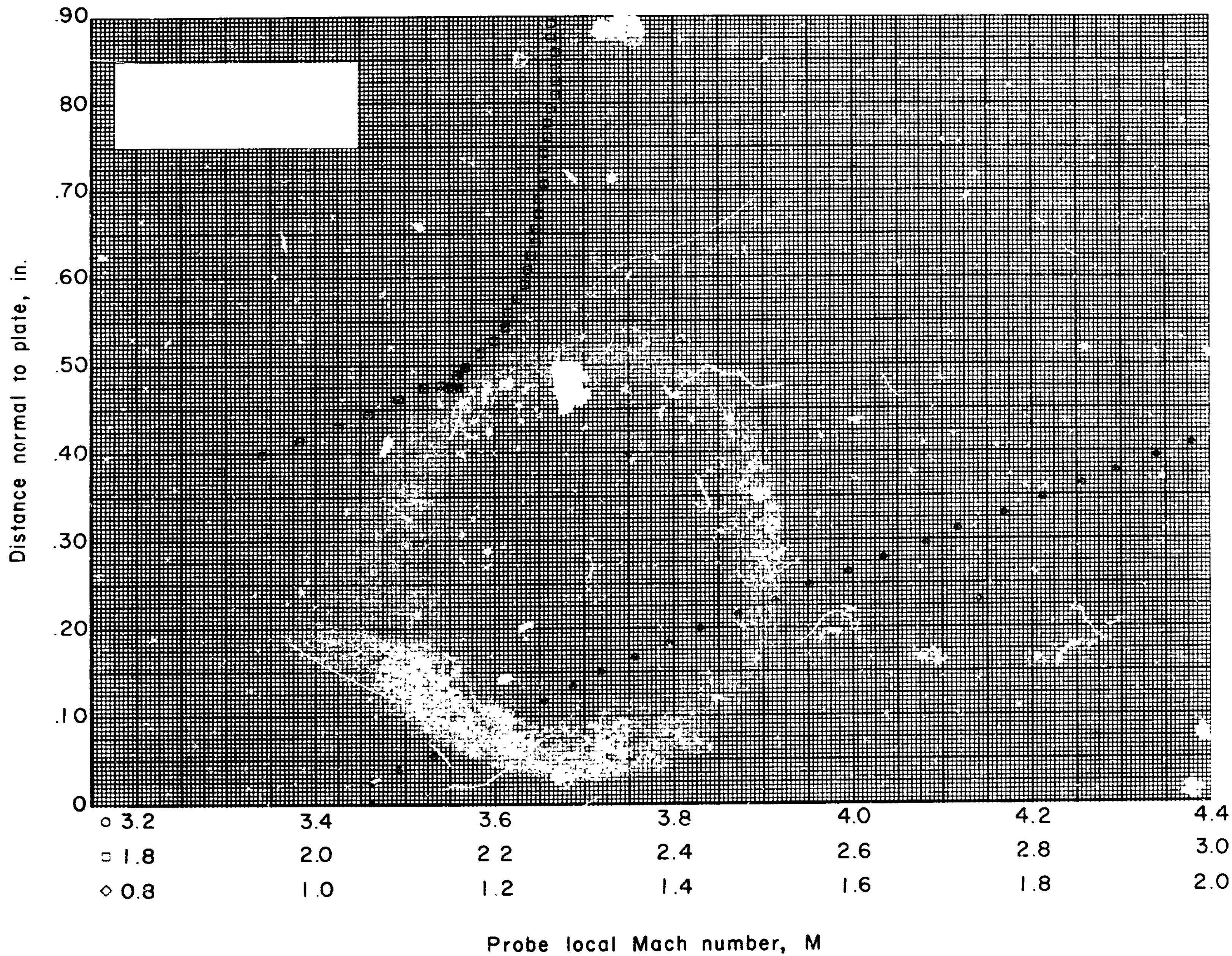

Figure 59.- Boundary-layer Mach number distribution for run 11. All identifying conditions are given in table III. Data points at a distance from the plate of 0.475 inch indicate effect of time lag on Mach number values.

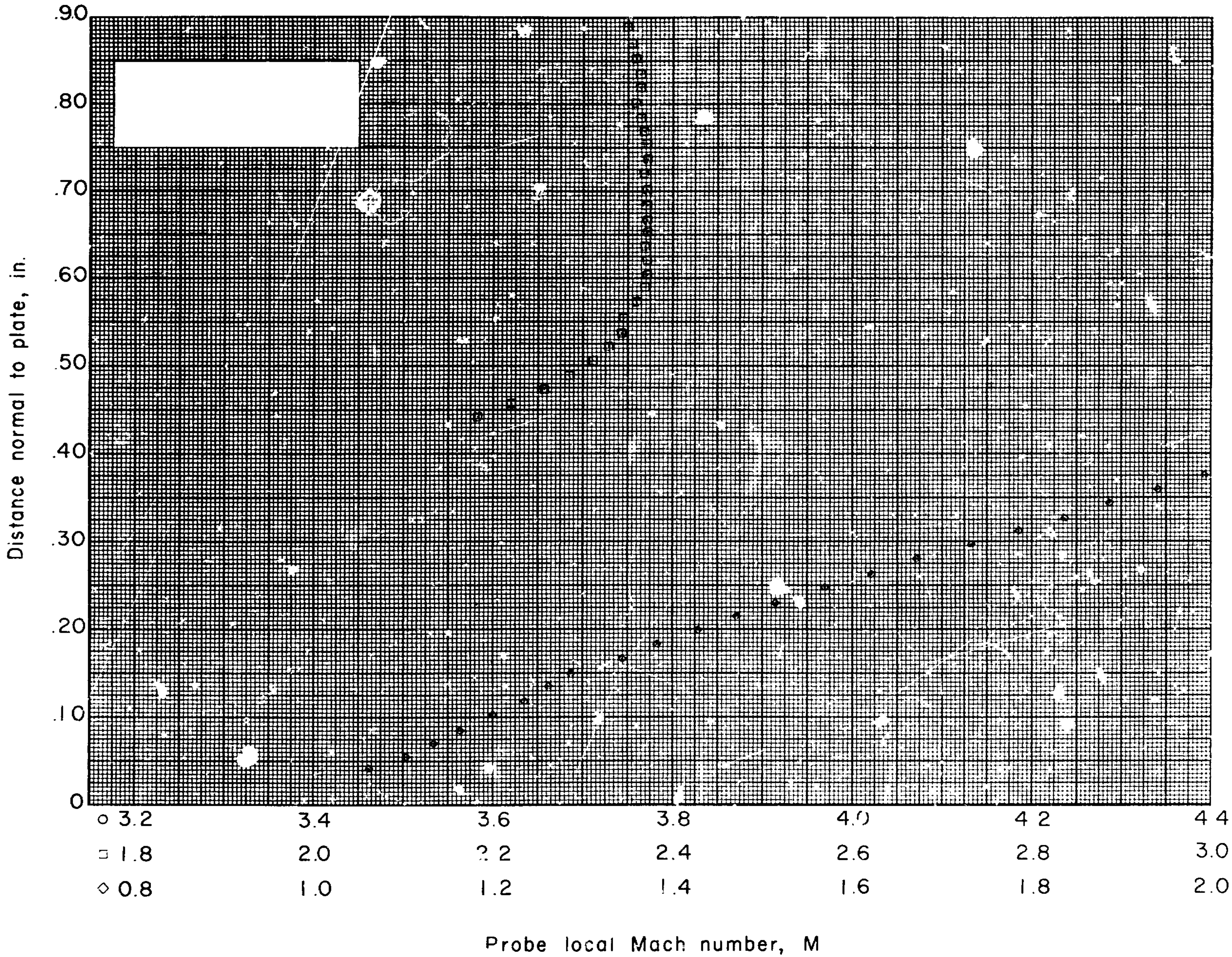

Figure 60.- Boundary-layer Mach number distribution for run 12. All identifying conditions are given in table III

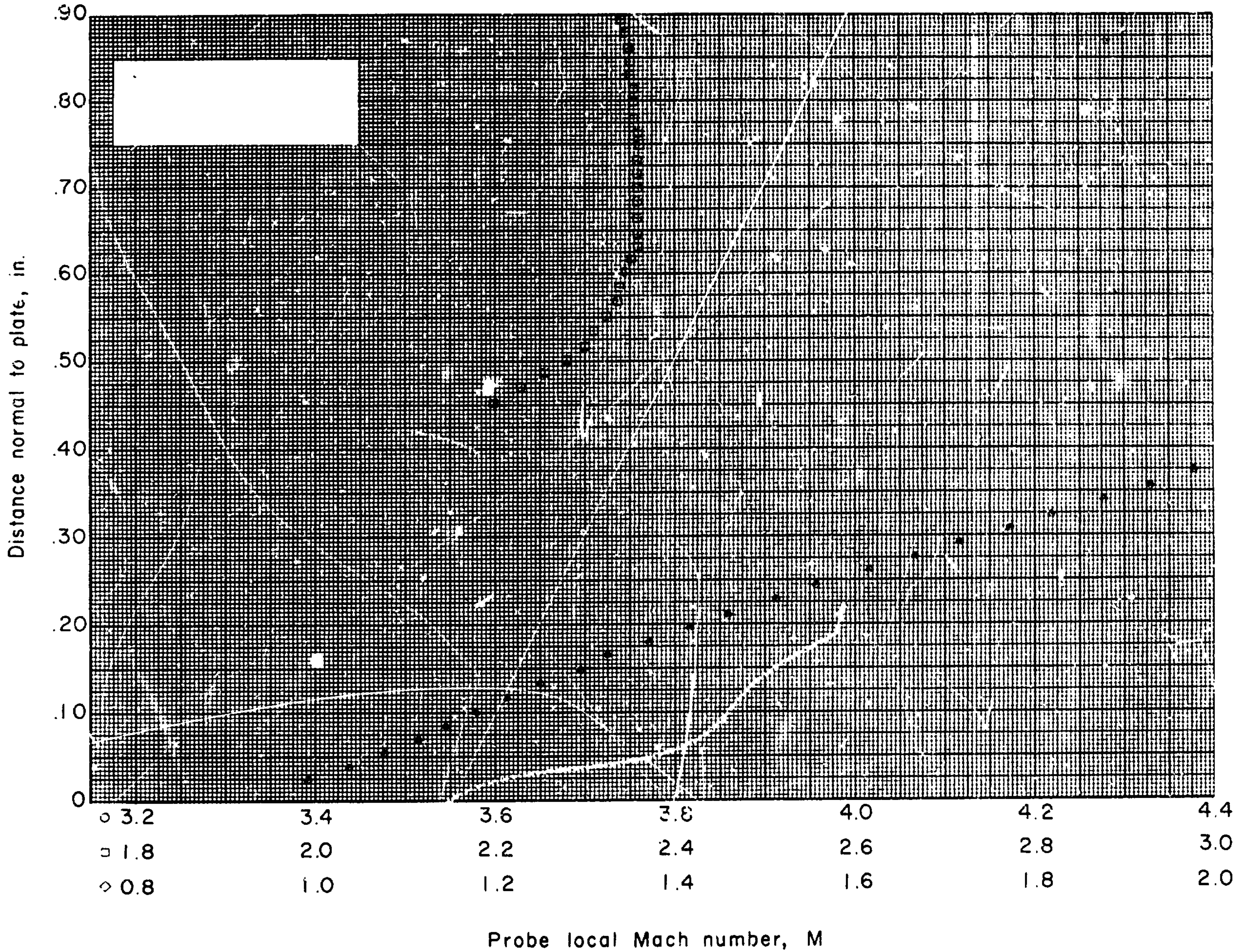

Figure 61.- Boundary-layer Mach number distribution for run 13. All identifying conditions are given in table III.

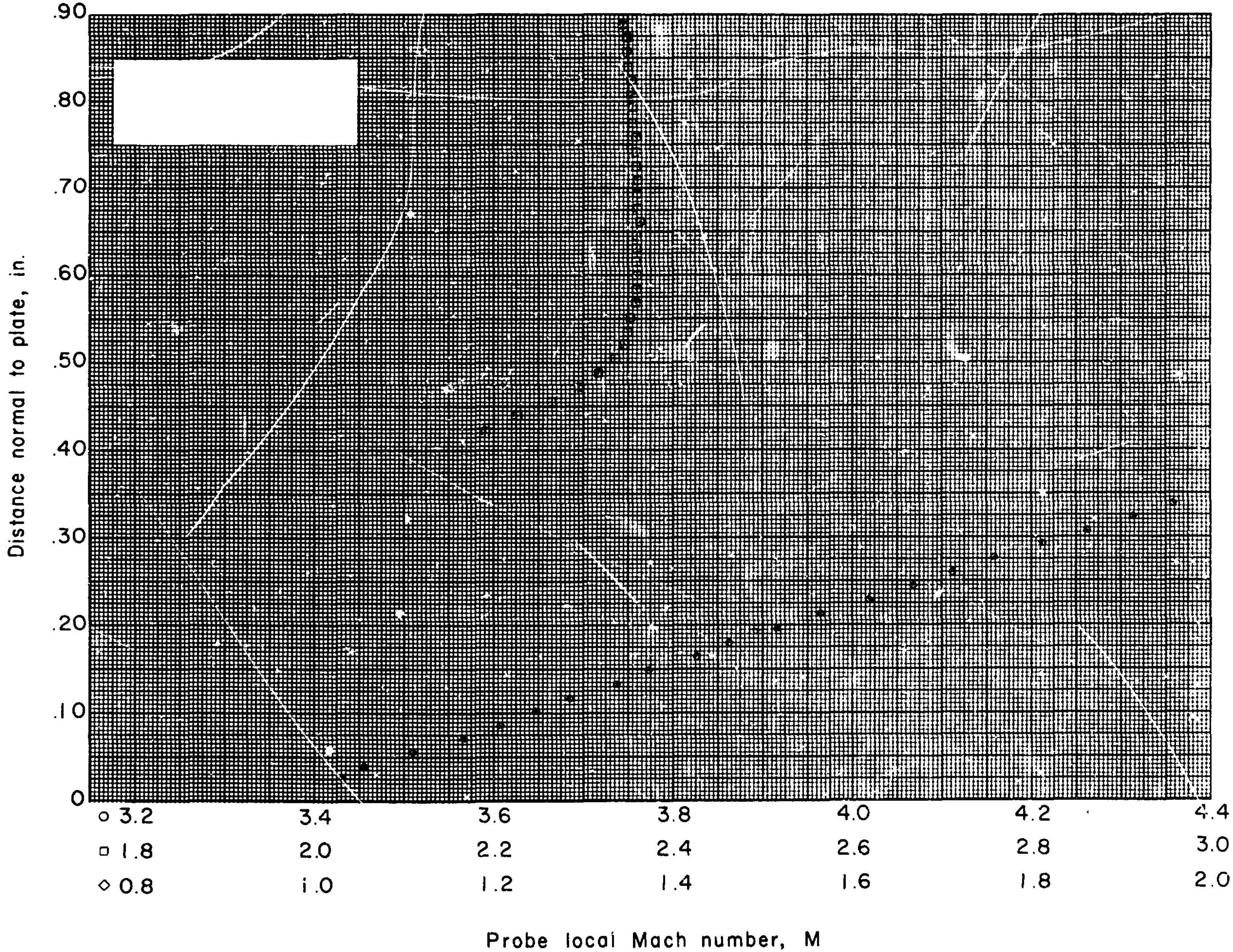

Figure 62.- Boundary-layer Mach number distribution for run 14. All identifying conditions are given in table III.

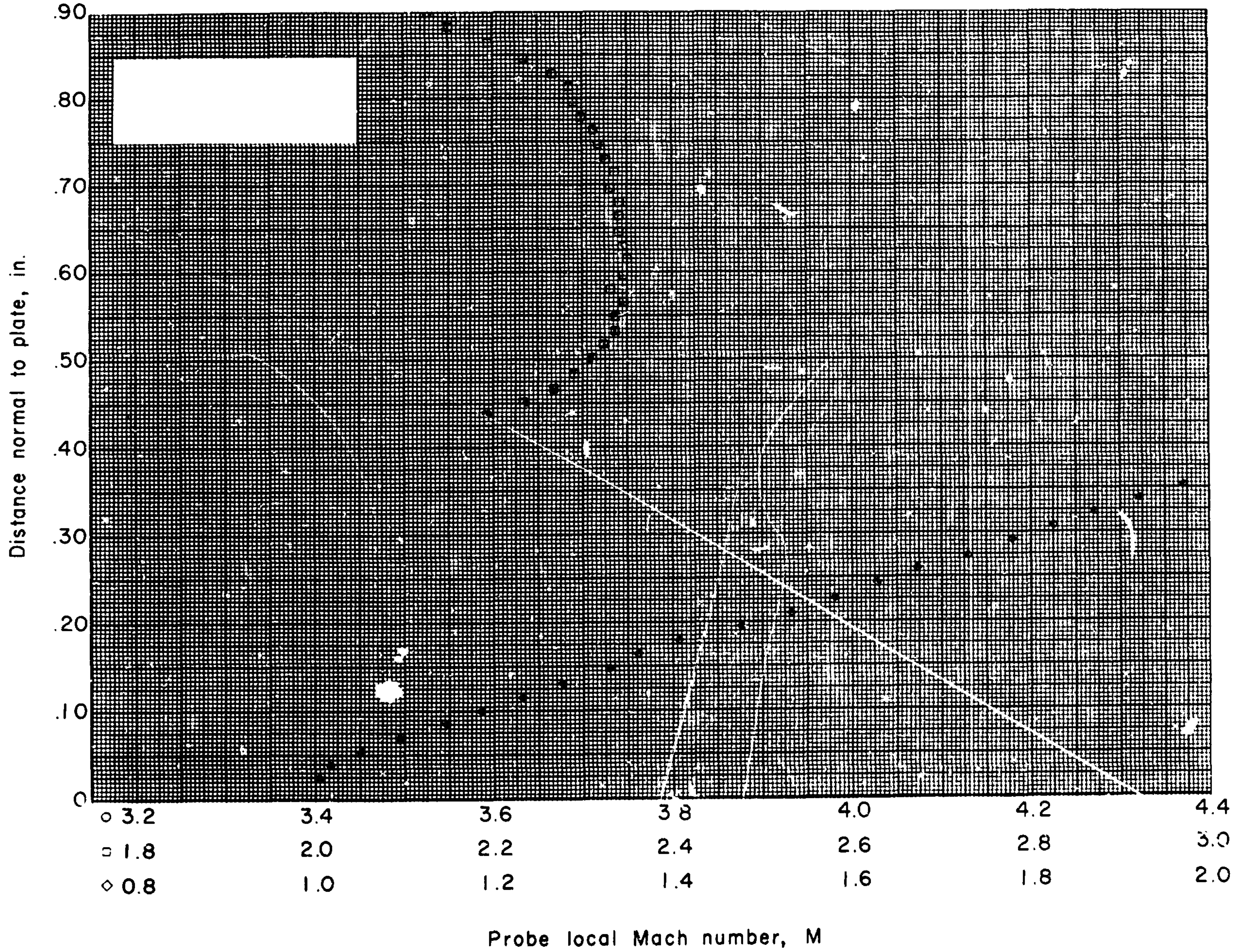

Figure 63.- Boundary-layer Mach number distribution for run 15. All identifying conditions are given in table III.

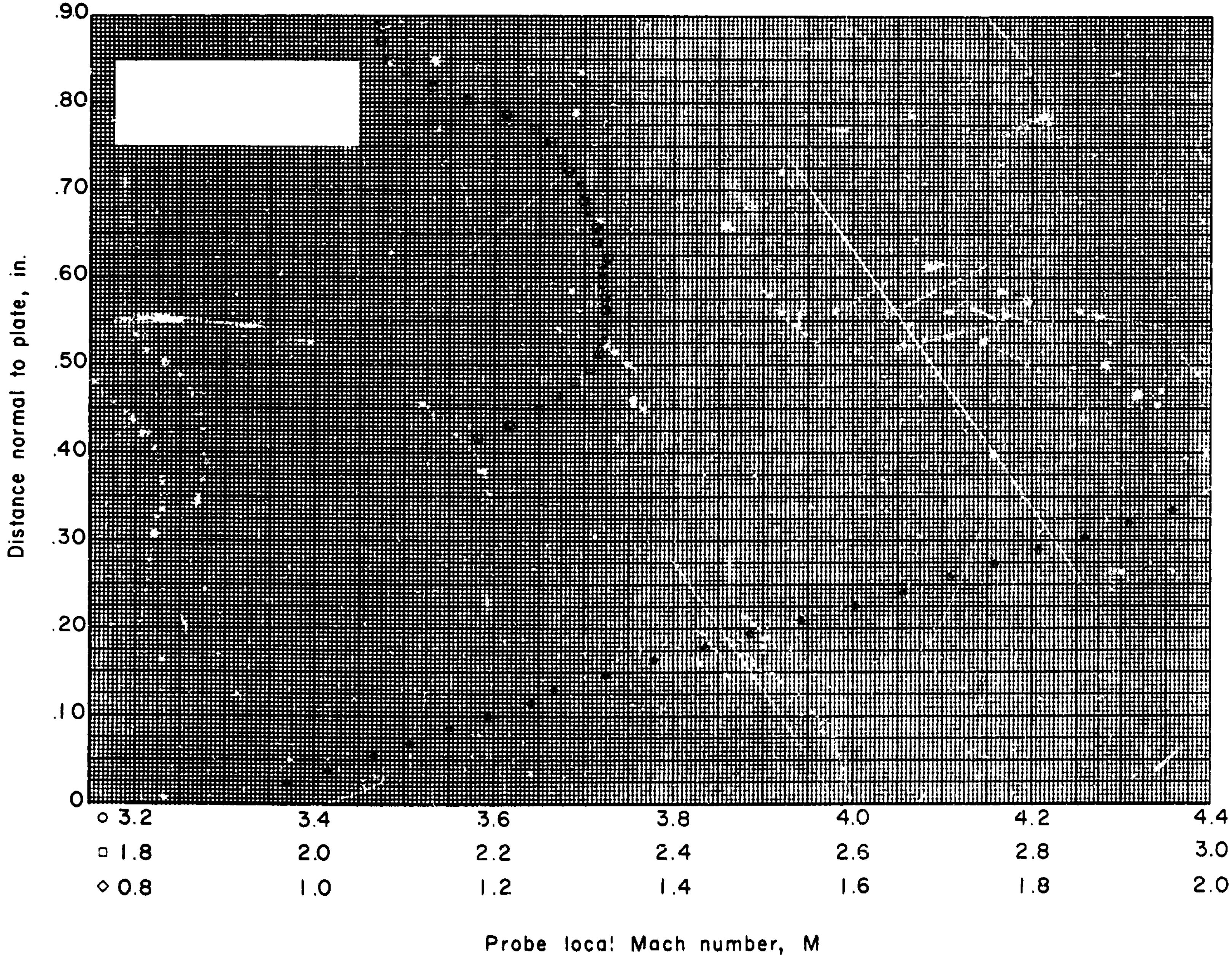

Figure 64.- Boundary-layer Mach number distribution for run 16. All identifying conditions are given in table III.

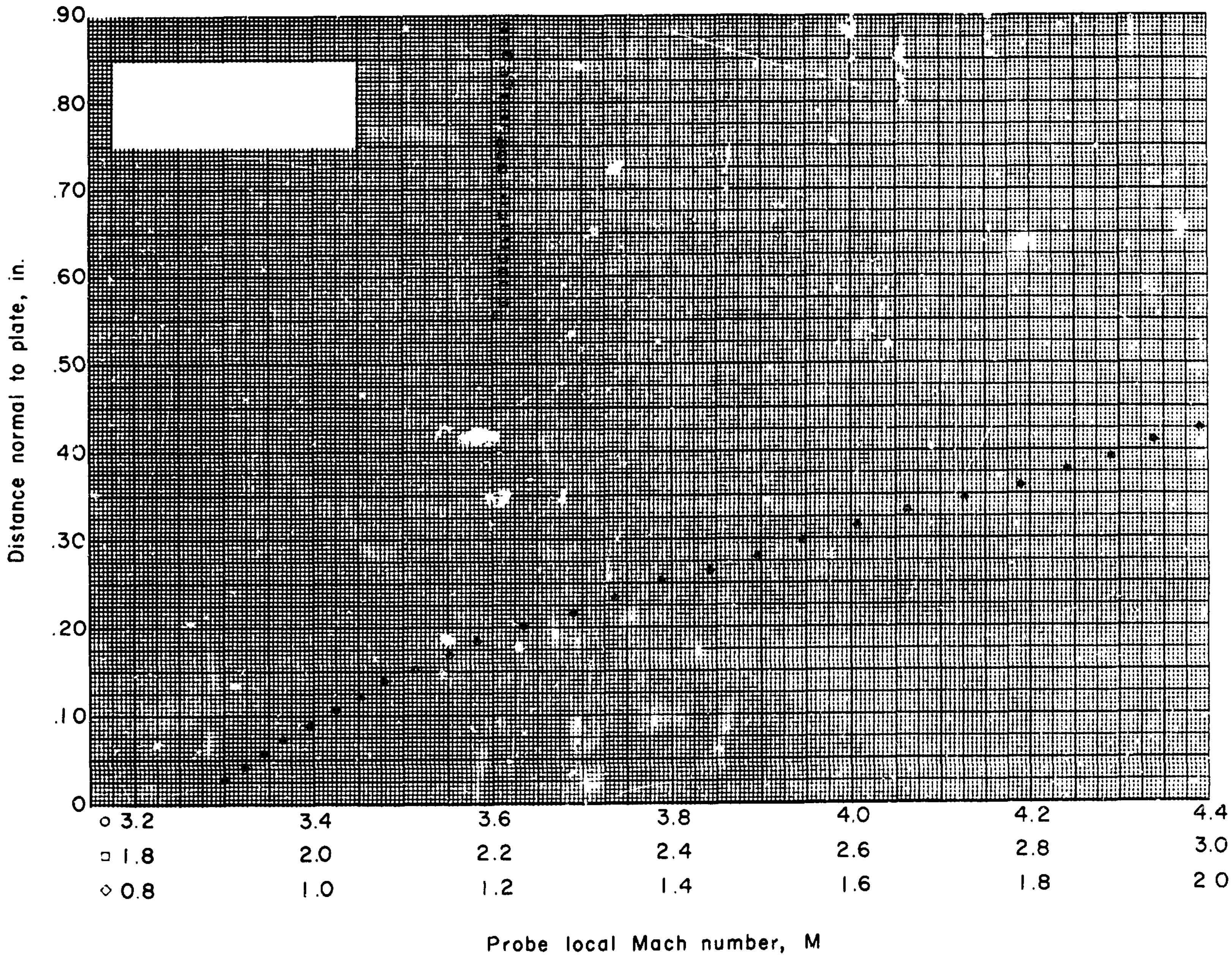

Figure 65.- Boundary-layer Mach number distribution for run 17. All identifying conditions are given in table III.

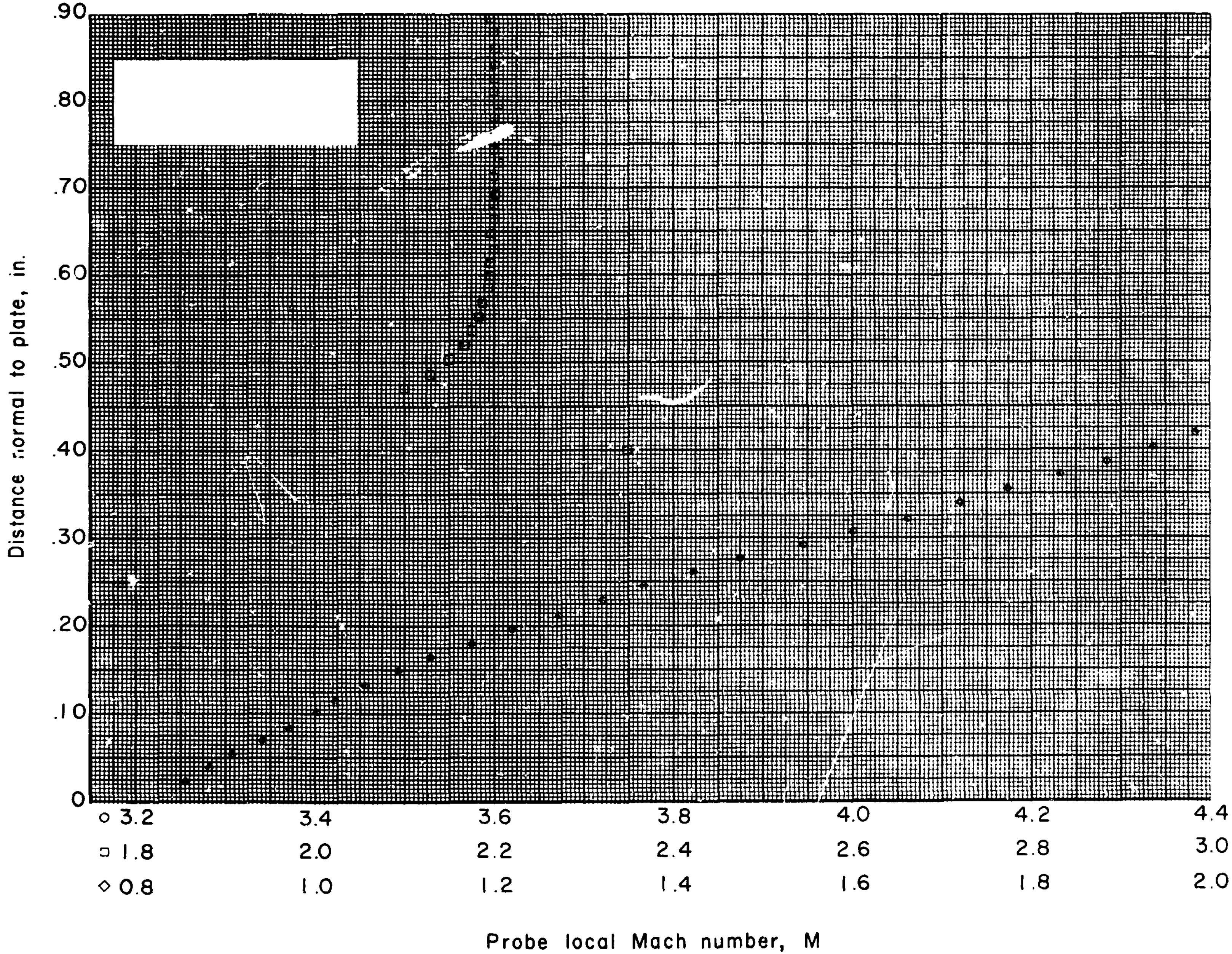

Figure 66.- Boundary-layer Mach number distribution for run 18. All identifying conditions are given in table III.

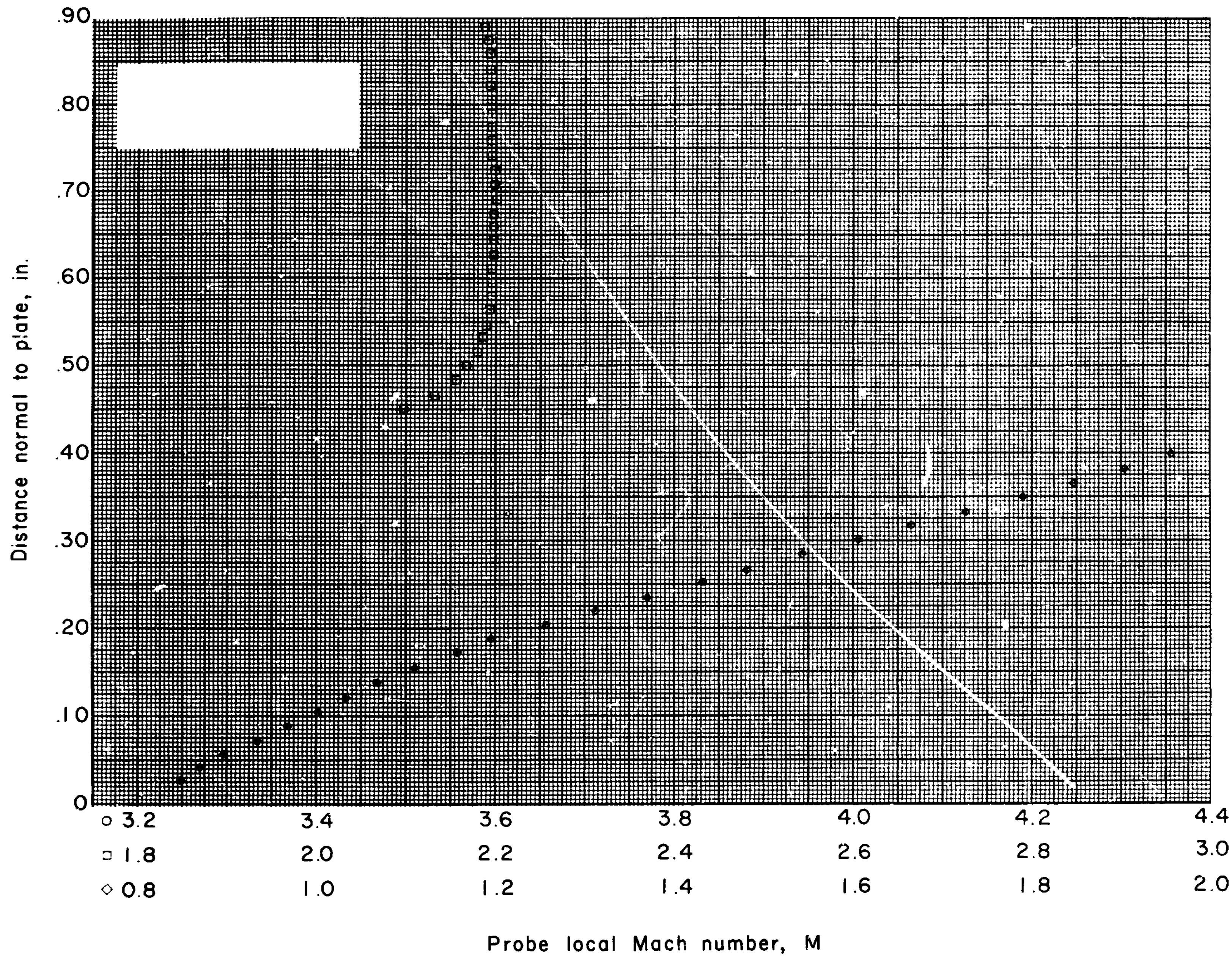

Figure 67.- Boundary-layer Mach number distribution for run 19. All identifying conditions are given in table III.

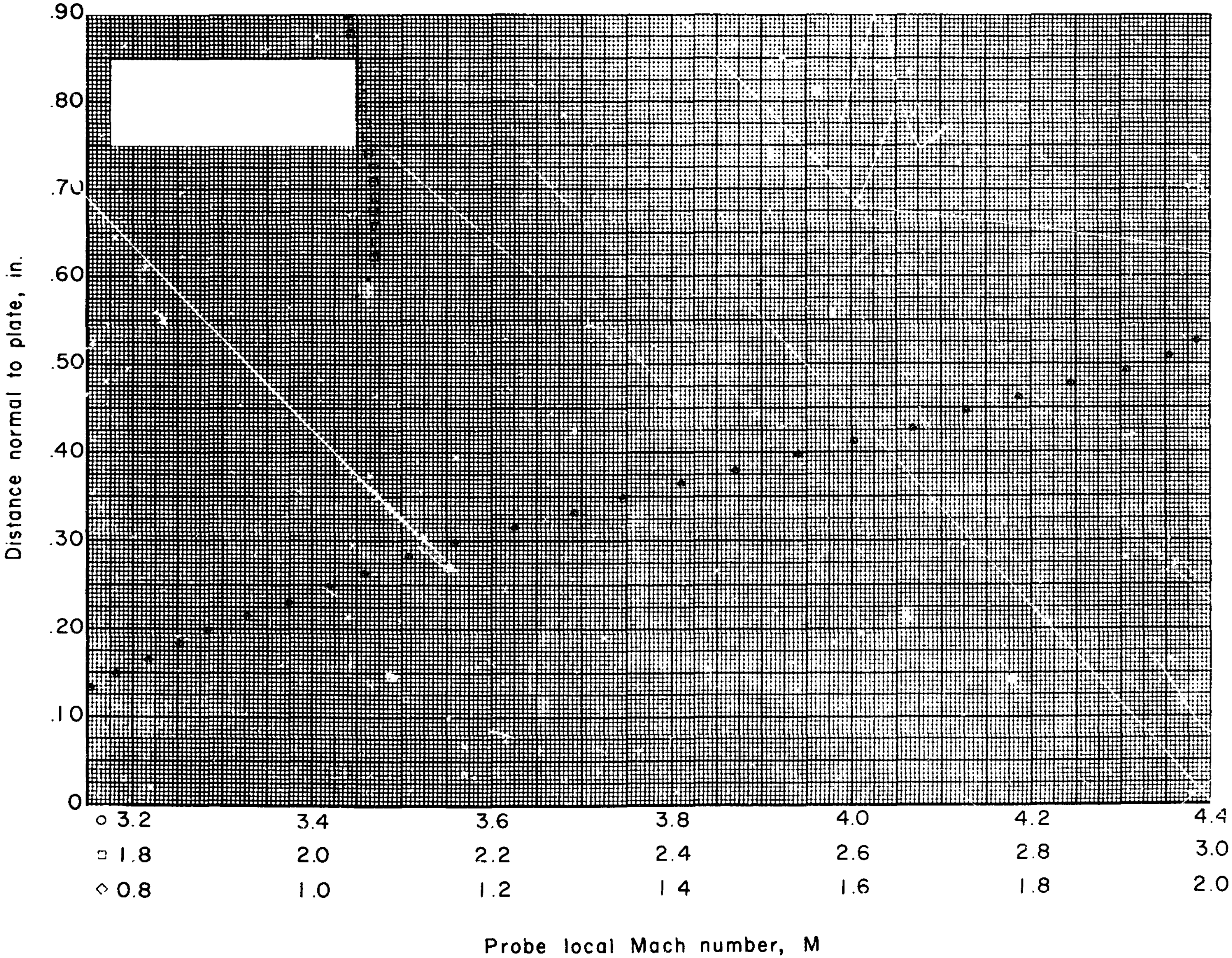

Figure 68.- Boundary-layer Mach number distribution for run 20. All identifying conditions are given in table III.

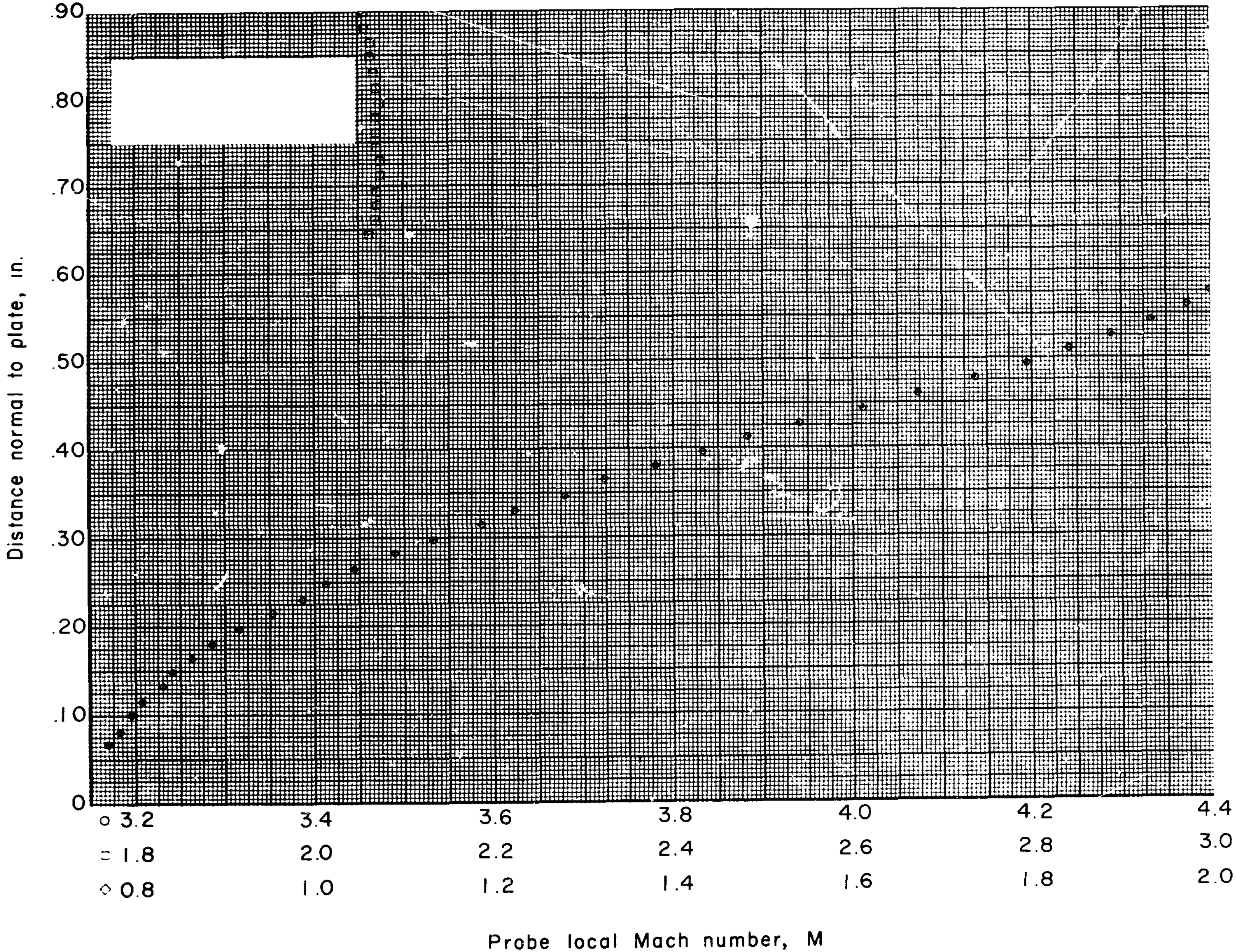

Figure 69 - Boundary-layer Mach number distribution for run 21. All identifying conditions are given in table III.

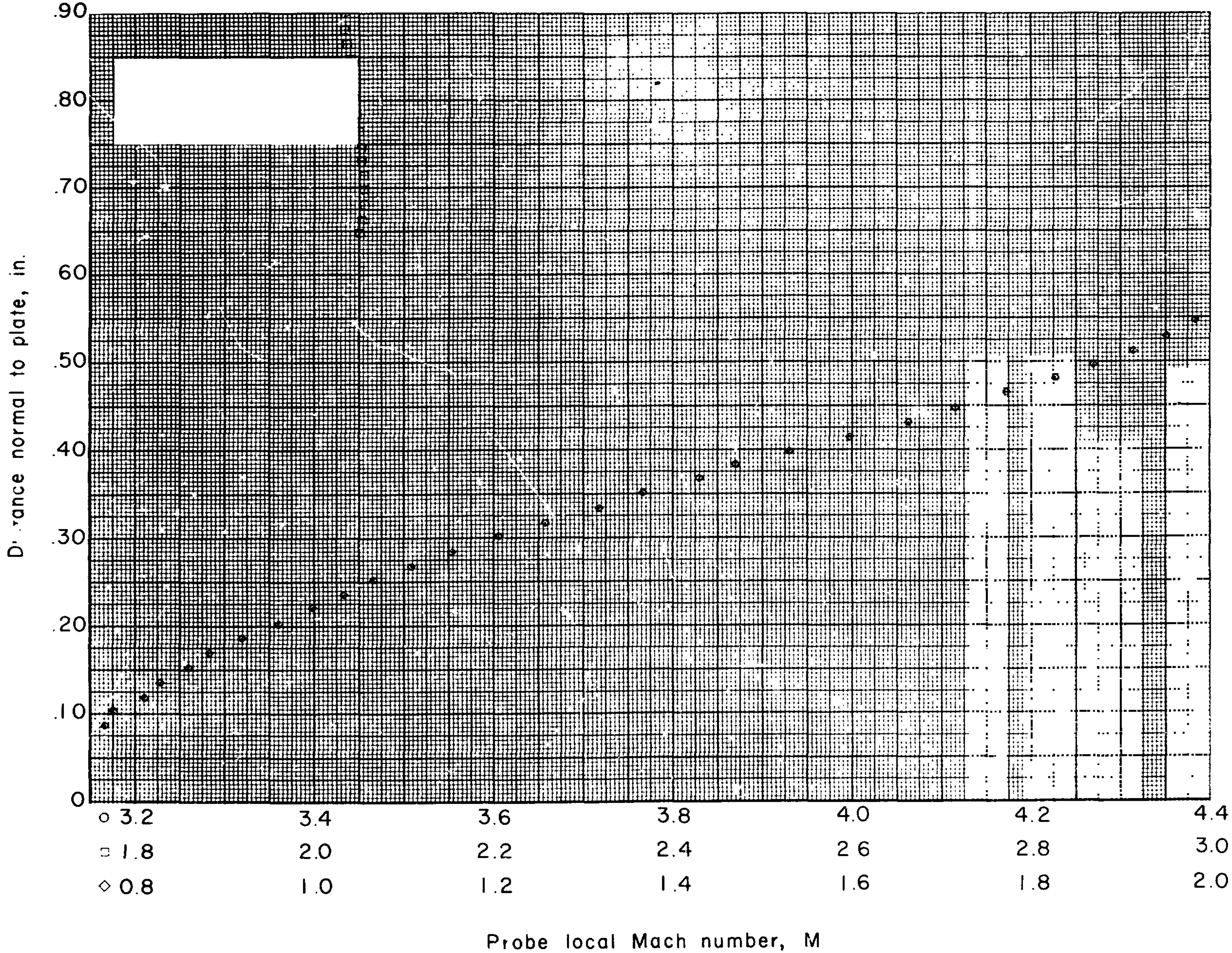

Figure 70.- Boundary-layer Mach number distribution for run 22. All identifying conditions are given in table III.

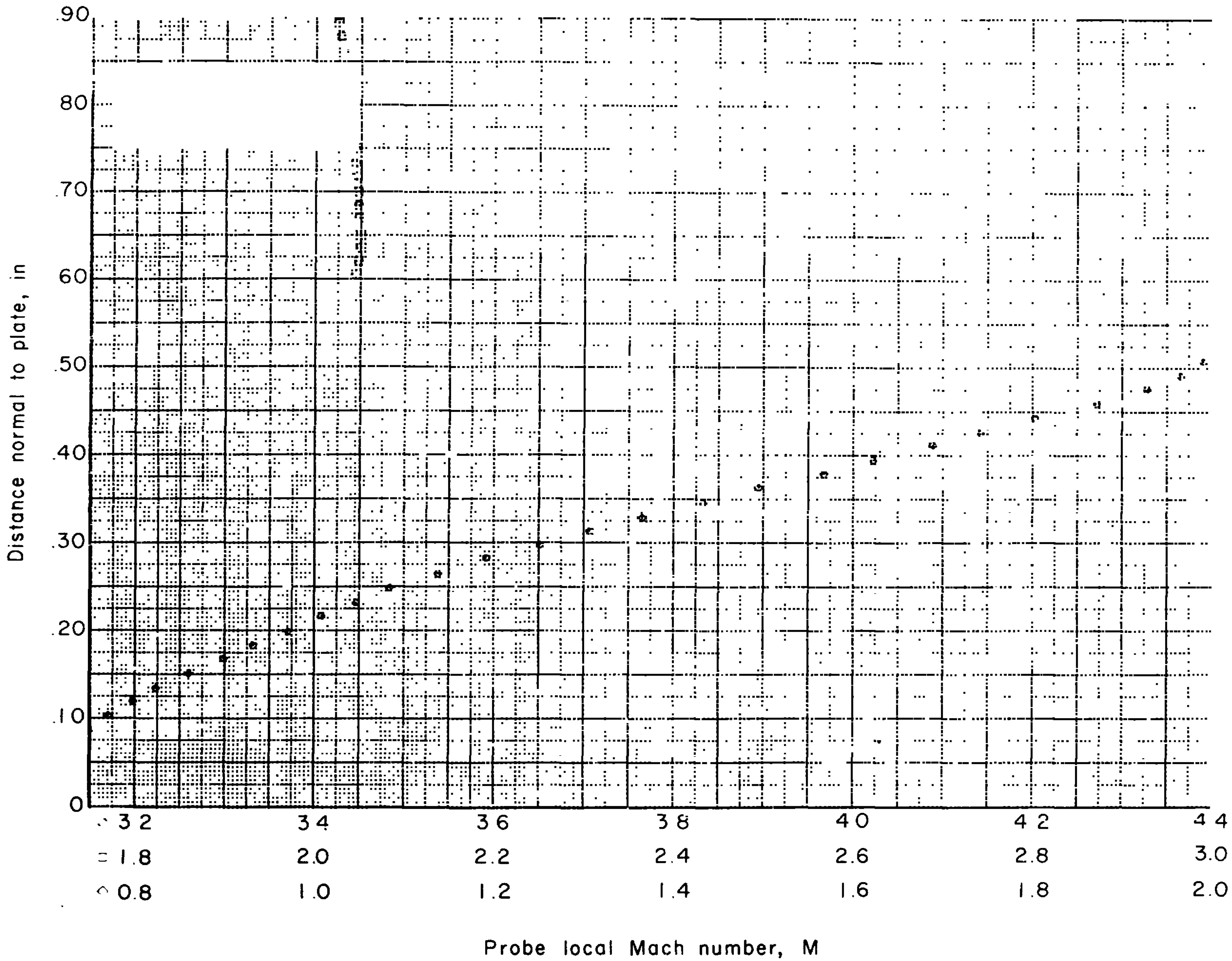

Figure 71.- Boundary-layer Mach number distribution for run 23. All identifying conditions are given in table III.

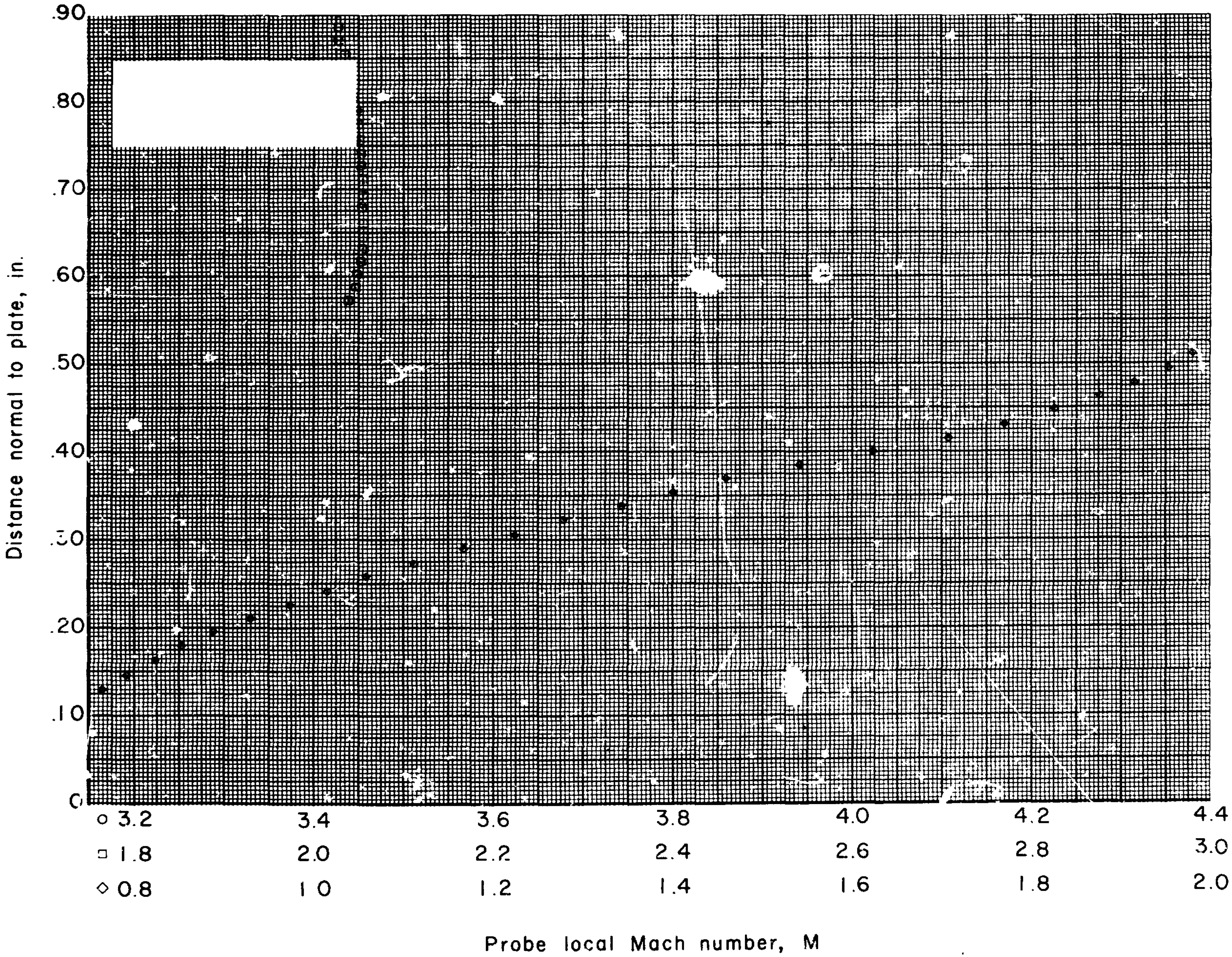

Figure 72.- Boundary-layer Mach number distribution for run 24. All identifying conditions are given in table III.

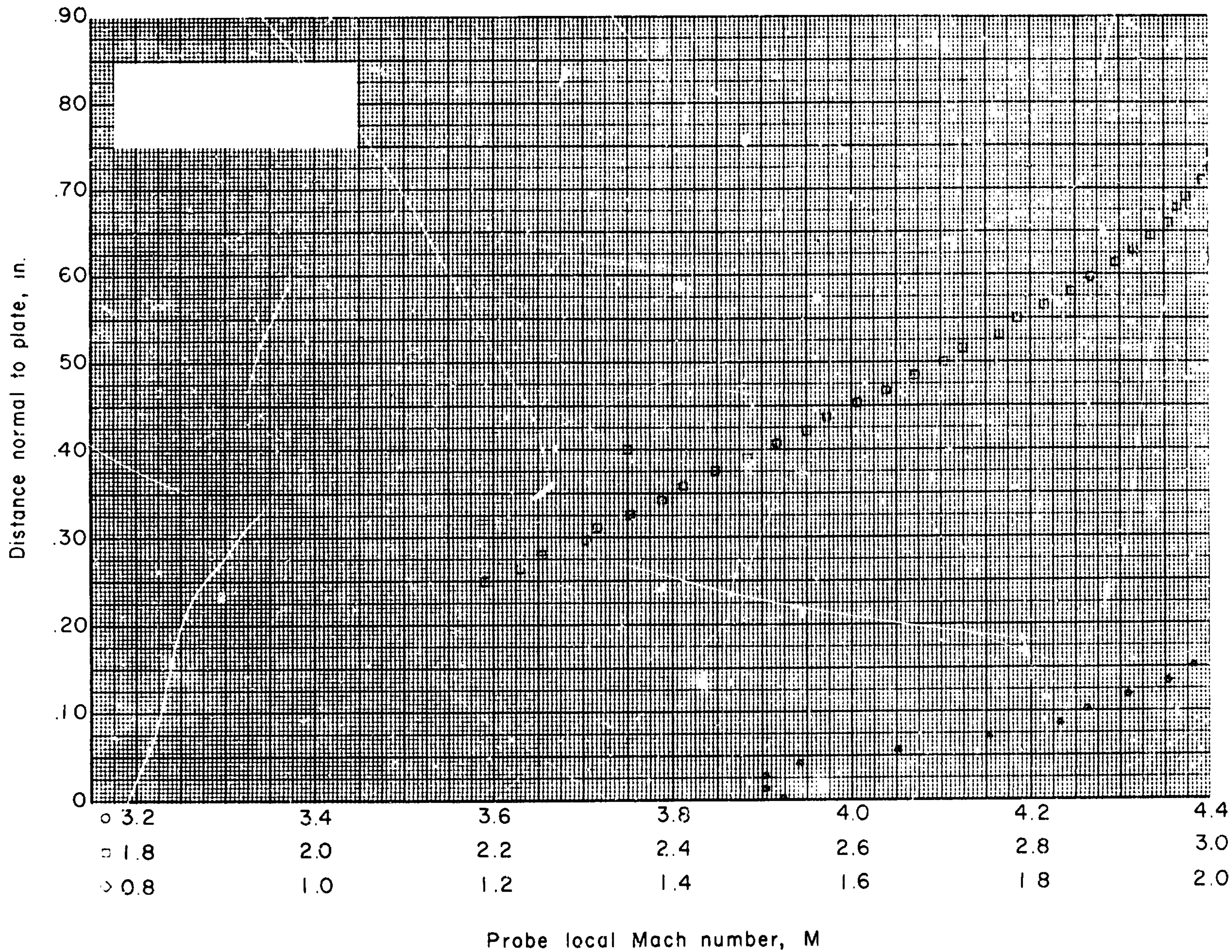

Figure 73.- Boundary-layer Mach number distribution for run 25. All identifying conditions are given in table III.

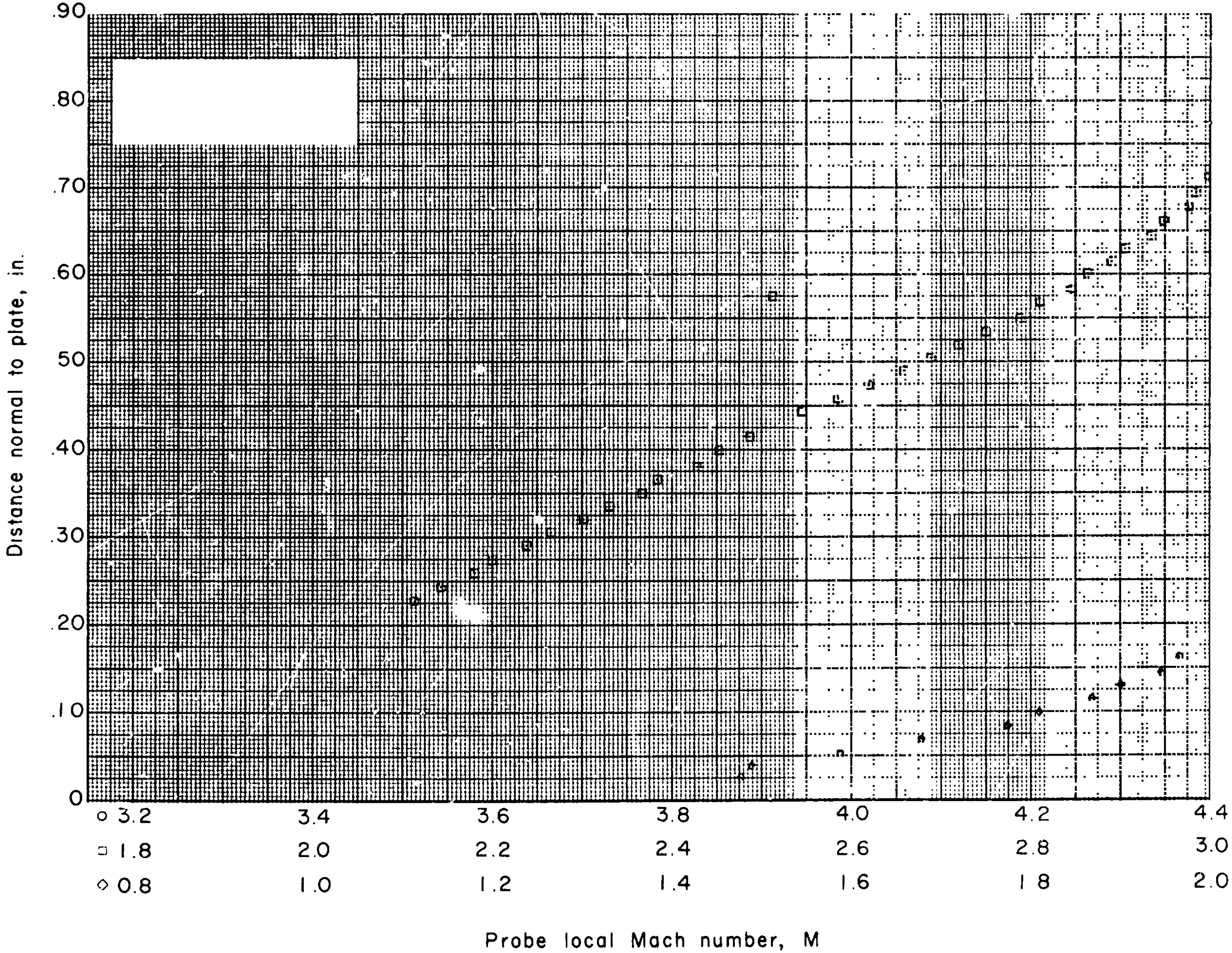

Figure 74.- Boundary-layer Mach number distribution for run 26. All identifying conditions are given in table III.

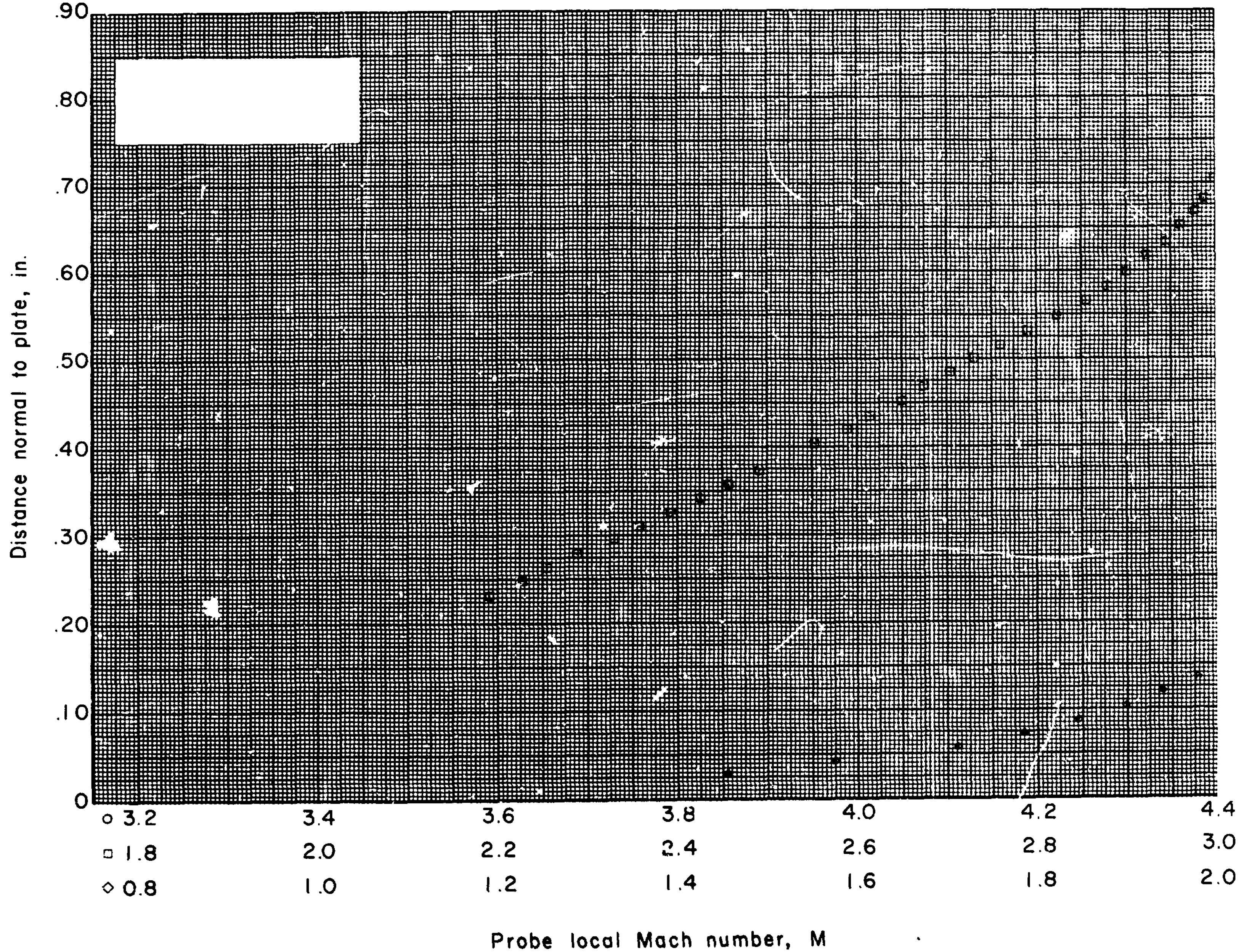

Figure 75.- Boundary-layer Mach number distribution for run 27. All identifying conditions are given in table III.

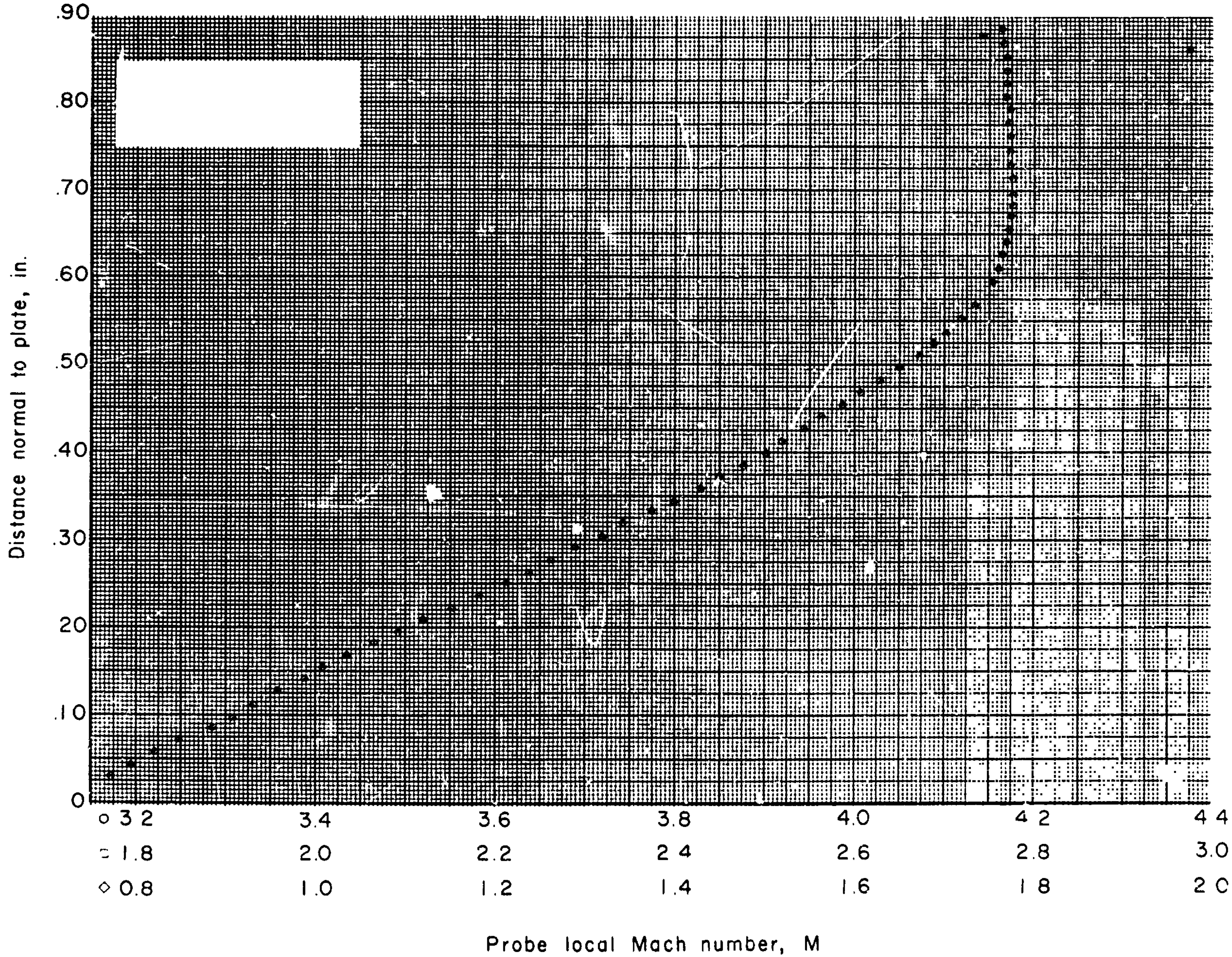

Figure 76.- Boundary-layer Mach number distribution for run 28. All identifying conditions are given in table III.

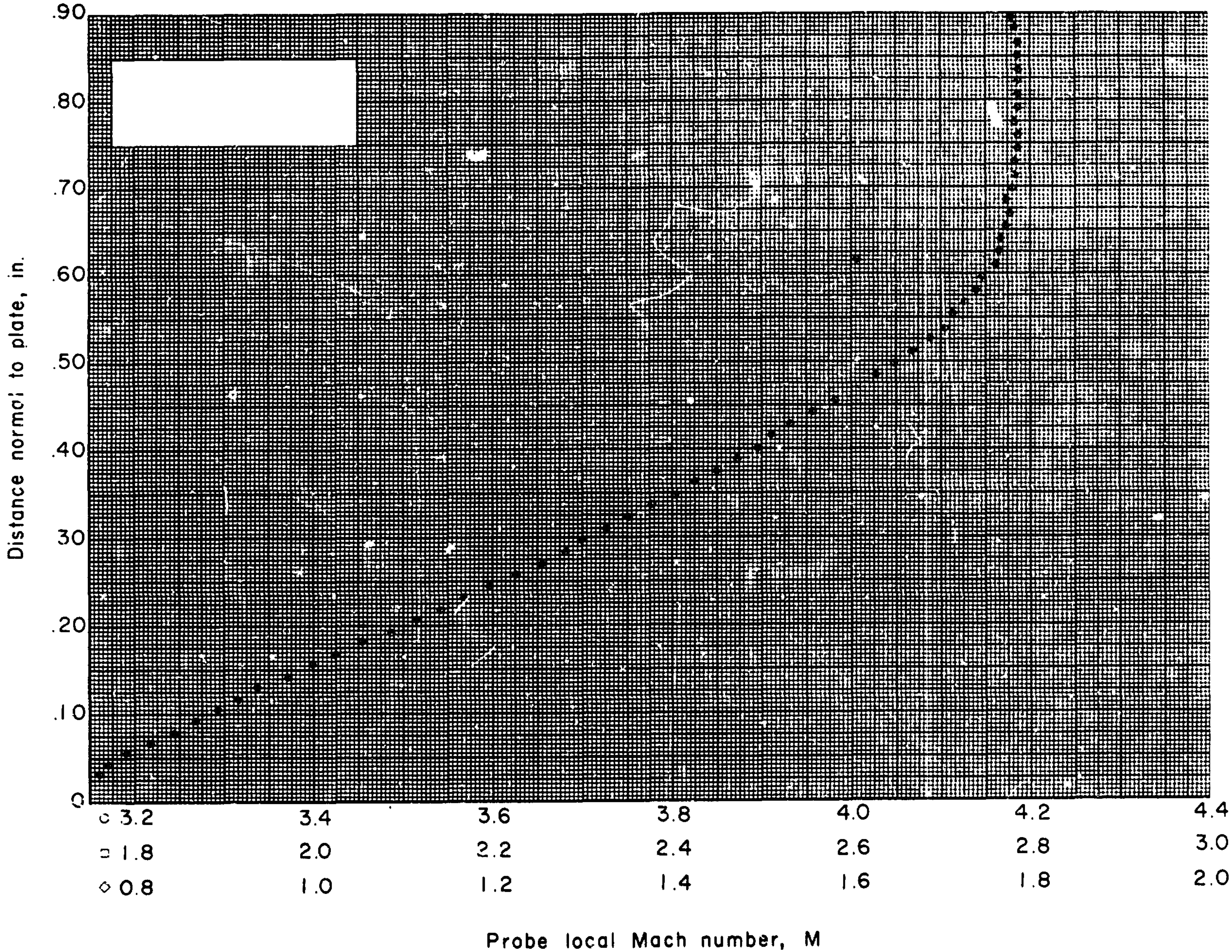

Figure 77.- Boundary-layer Mach number distribution for run 29. All identifying conditions are given in table III.

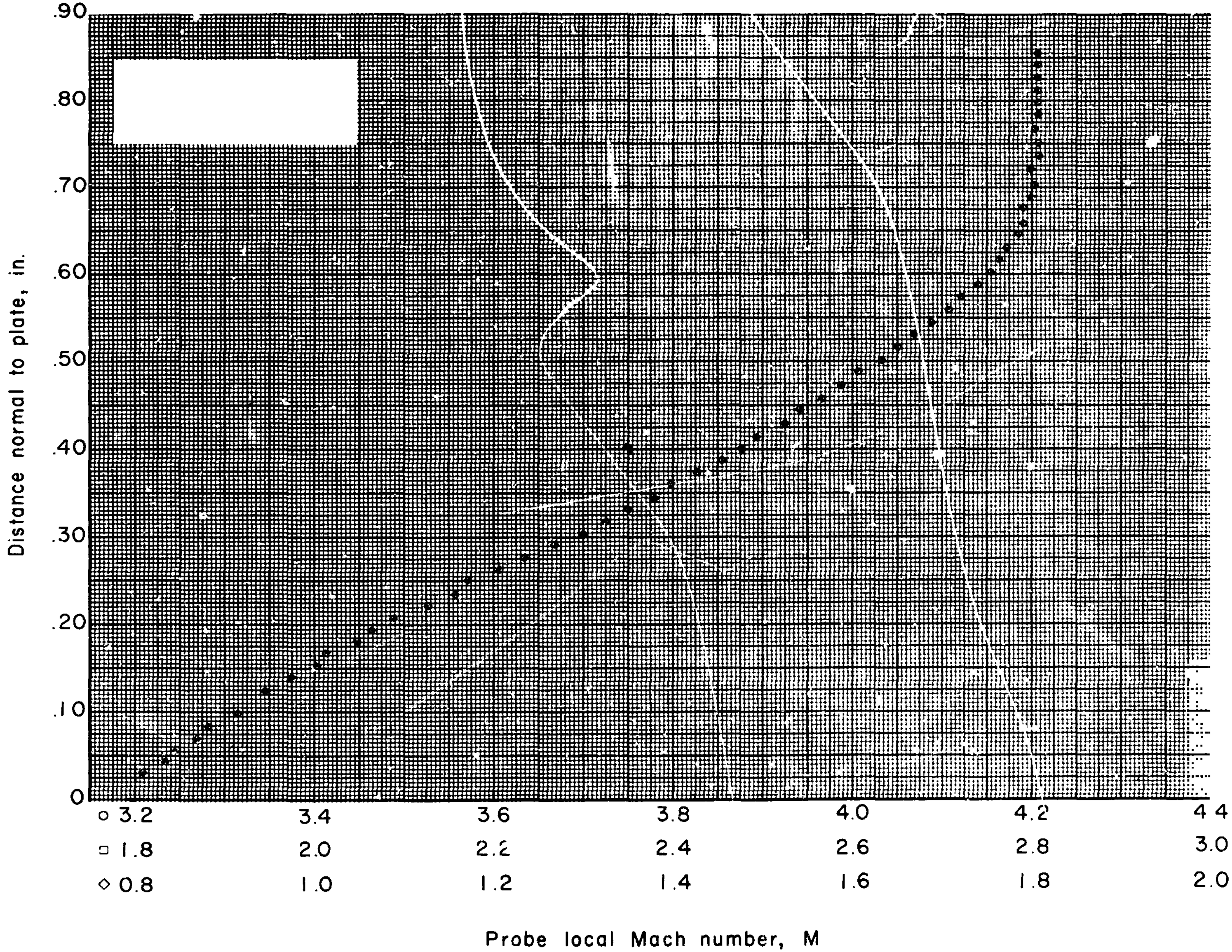

Figure 78.- Boundary-layer Mach number distribution for run 30. All identifying conditions are given in table III.

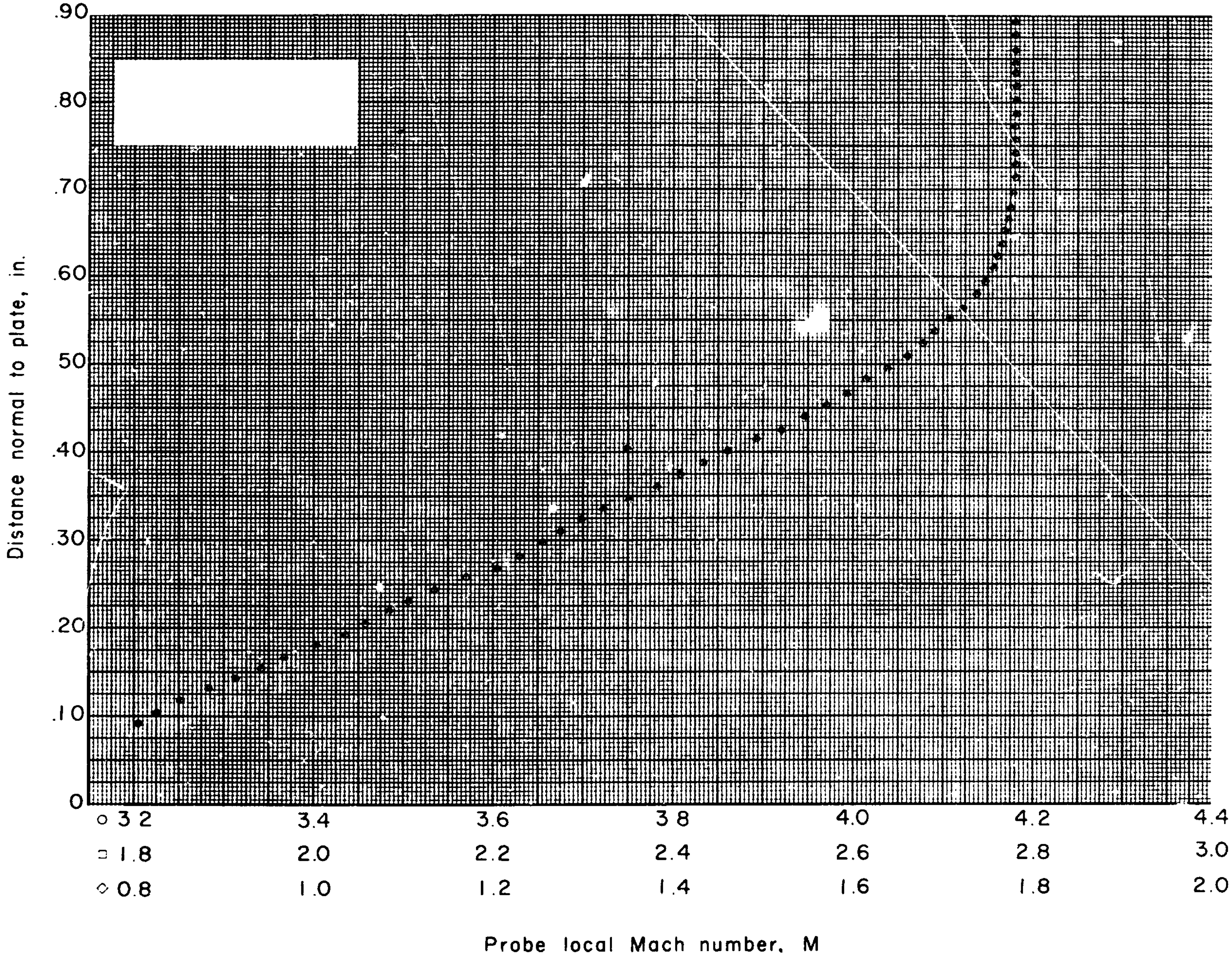

Figure 79.- Boundary-layer Mach number distribution for run 31. All identifying conditions are given in table III.

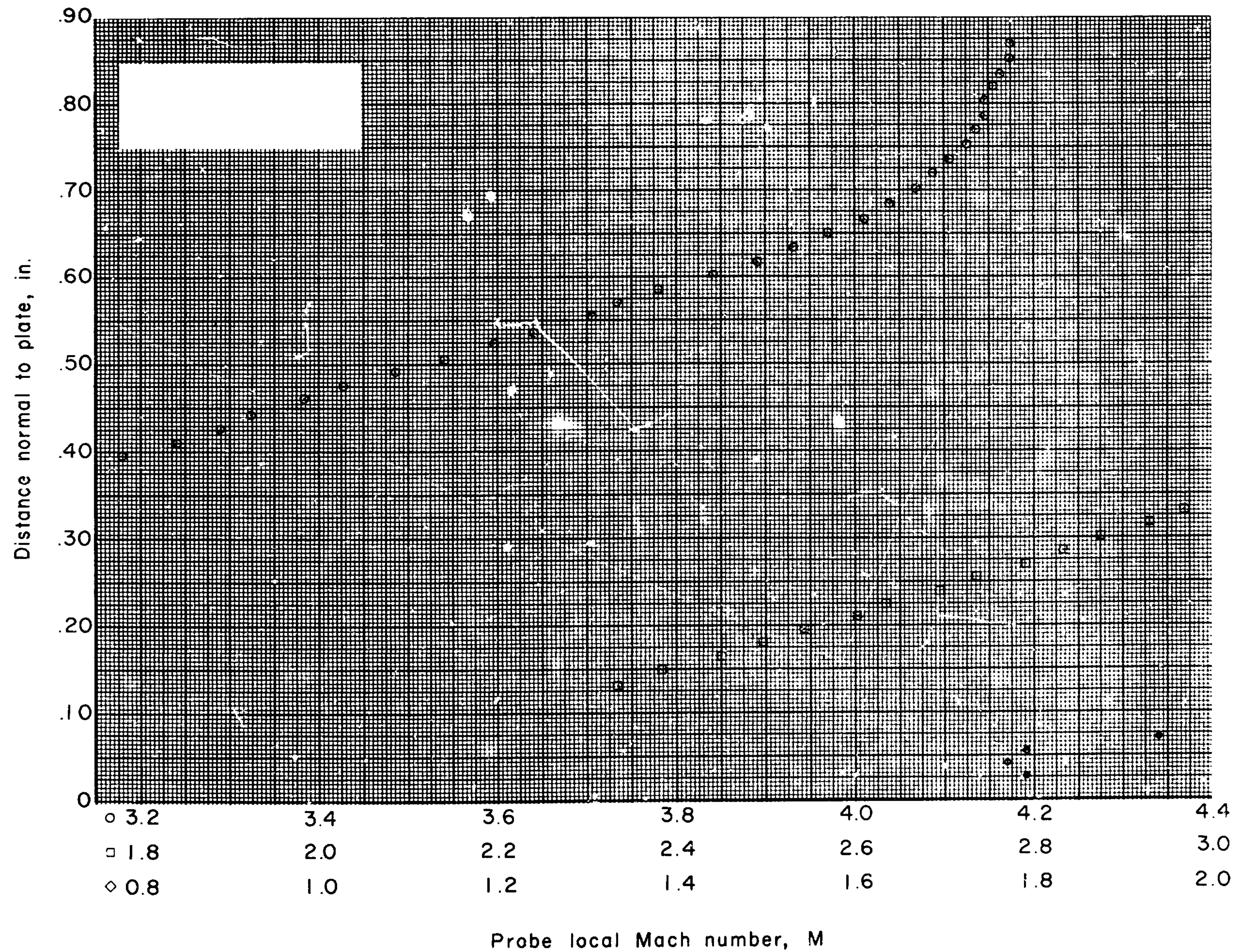

Figure 80.- Boundary-layer Mach number distribution for run 42. All identifying conditions are given in table III.

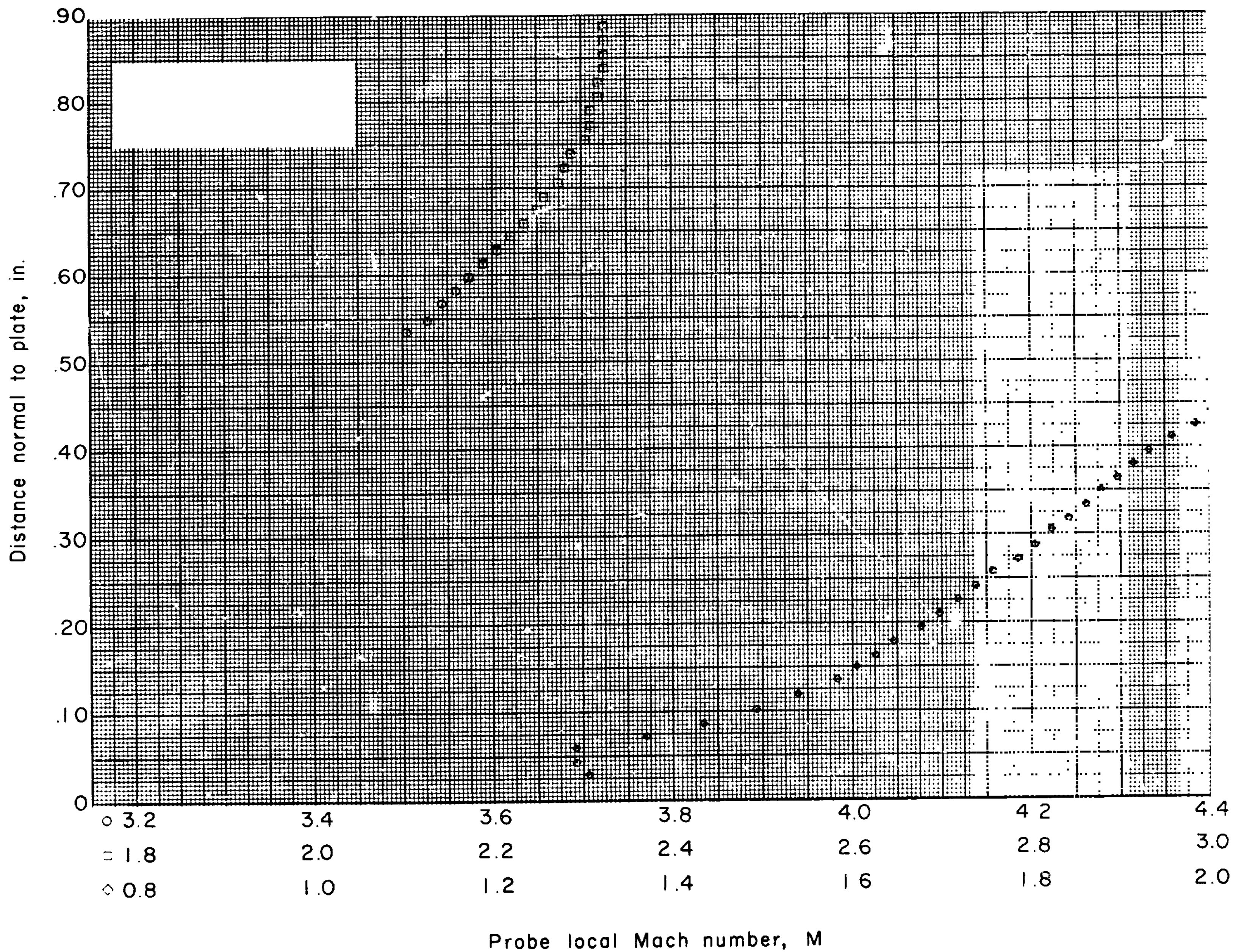

Figure 81.- Boundary-layer Mach number distribution for run 43. All identifying conditions are given in table III.

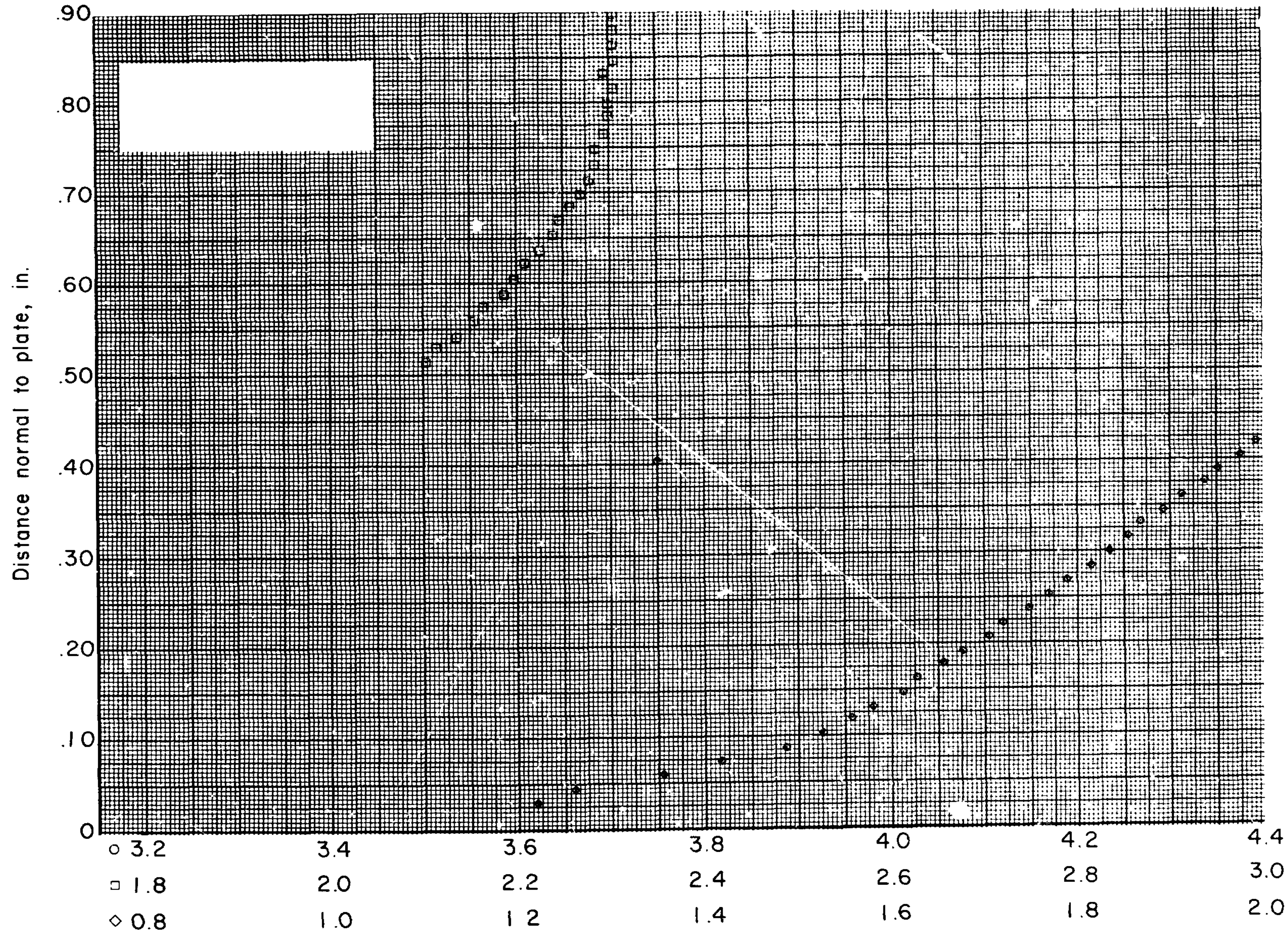

Figure 82.- Boundary-layer Mach number distribution for run 44. All identifying conditions are given in table III.

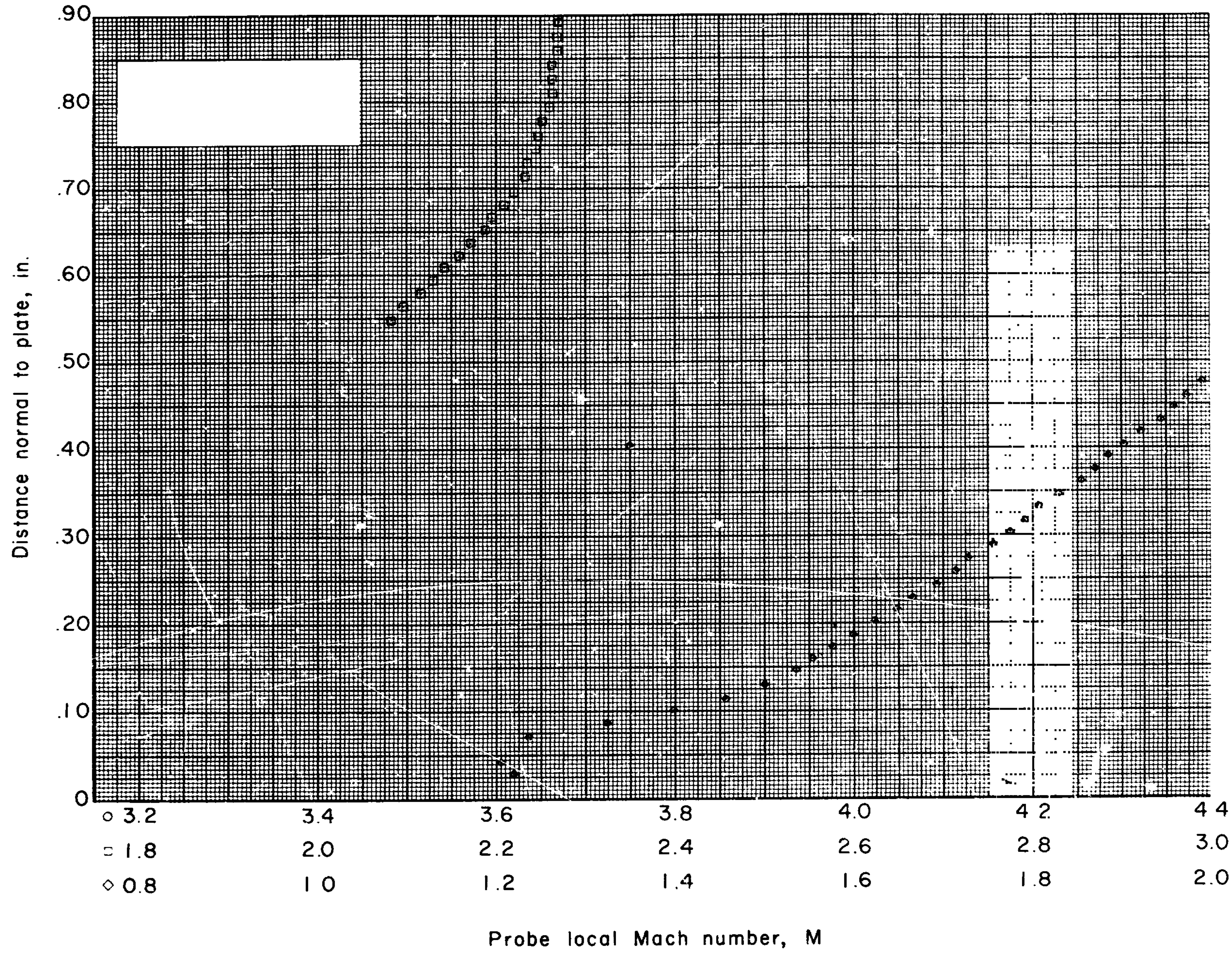

Figure 83.- Boundary-layer Mach number distribution for run 45. All identifying conditions are given in table III.

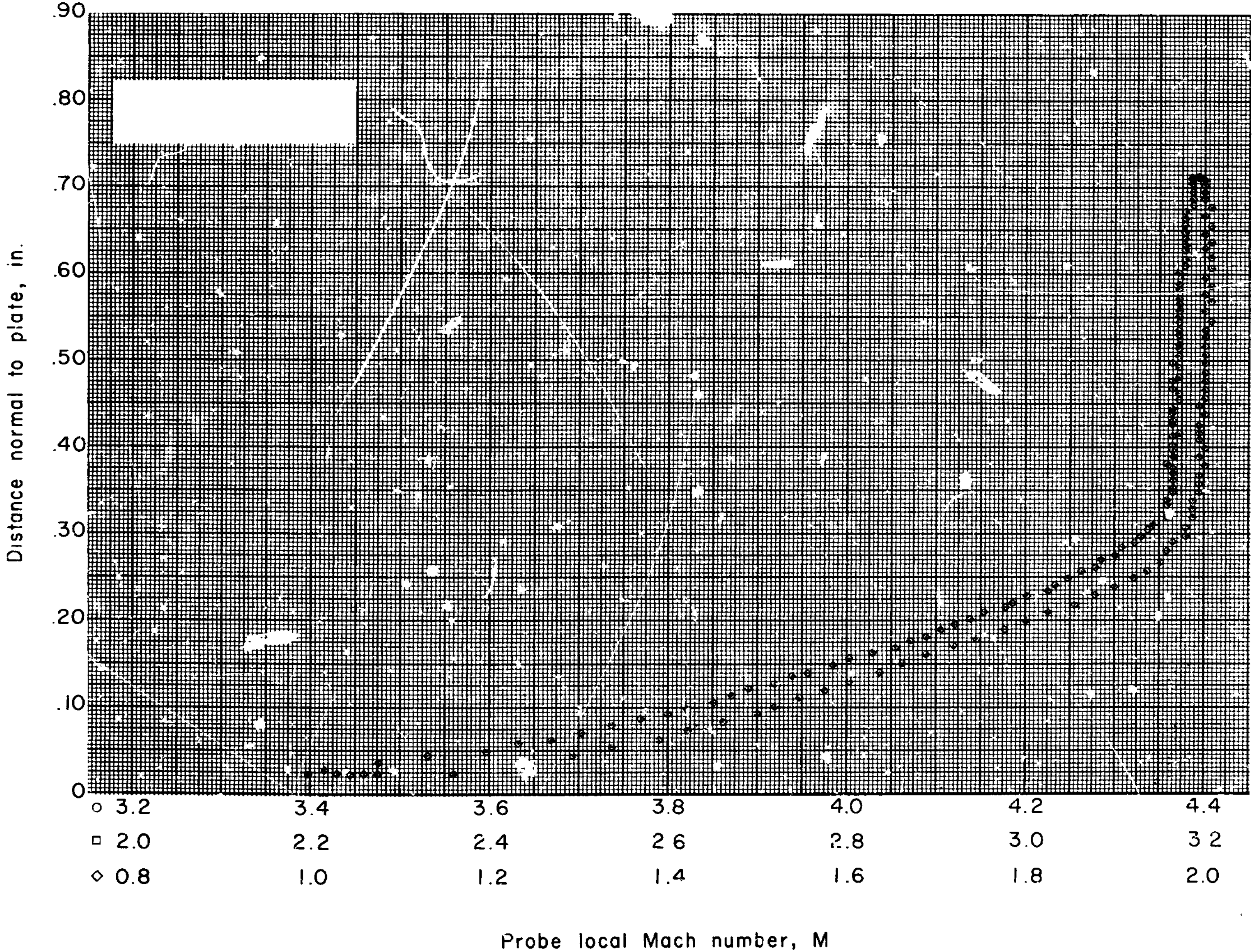

Figure 84.- Boundary-layer Mach number distribution for run 46. All identifying conditions are given in table III.

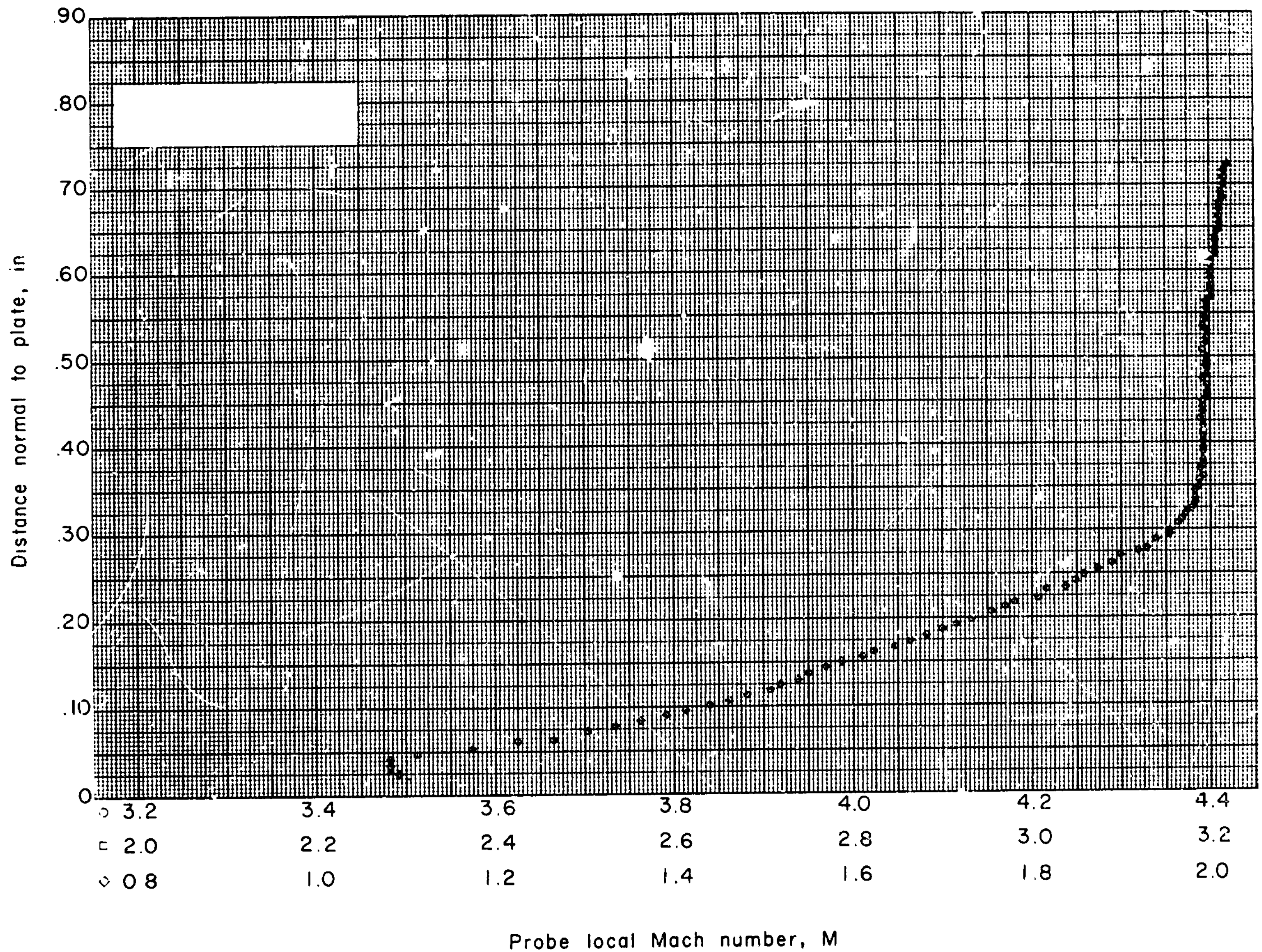

Figure 85.- Boundary-layer Mach number distribution for run 47. All identifying conditions are given in table III.

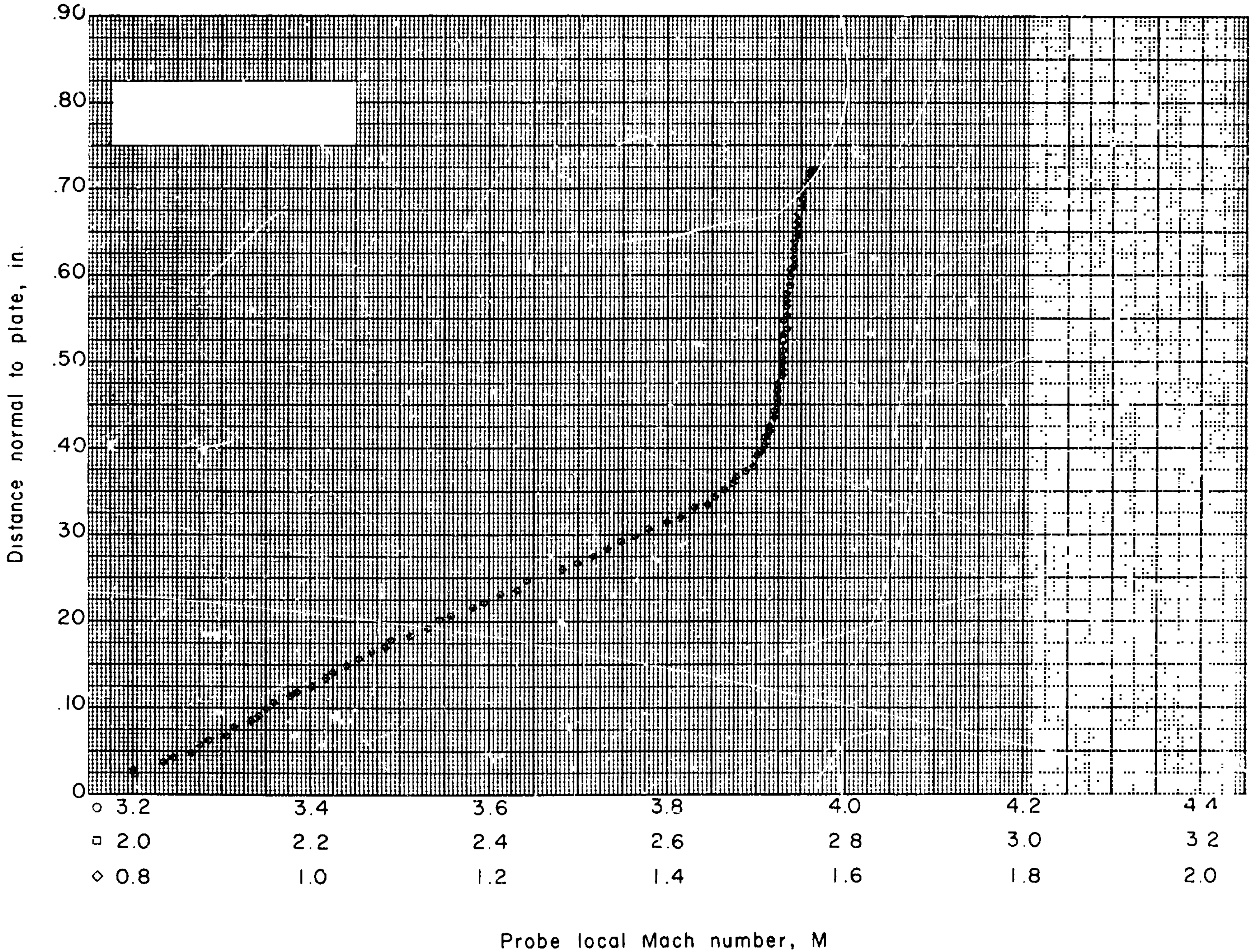

Figure 86.- Boundary-layer Mach number distribution for run 48. All identifying conditions are given in table III.

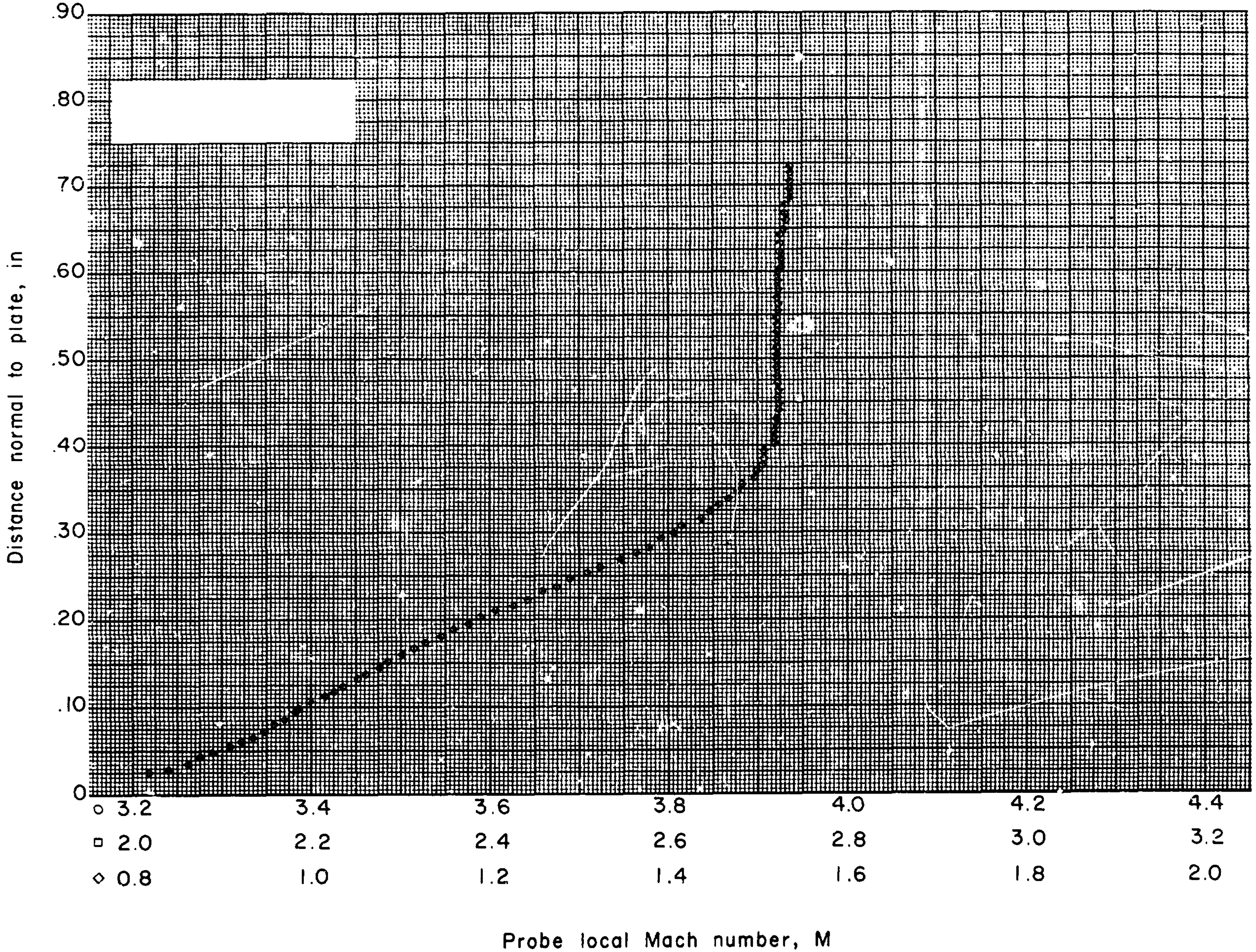

Figure 87.- Boundary-layer Mach number distribution for run 49. All identifying conditions are given in table III.

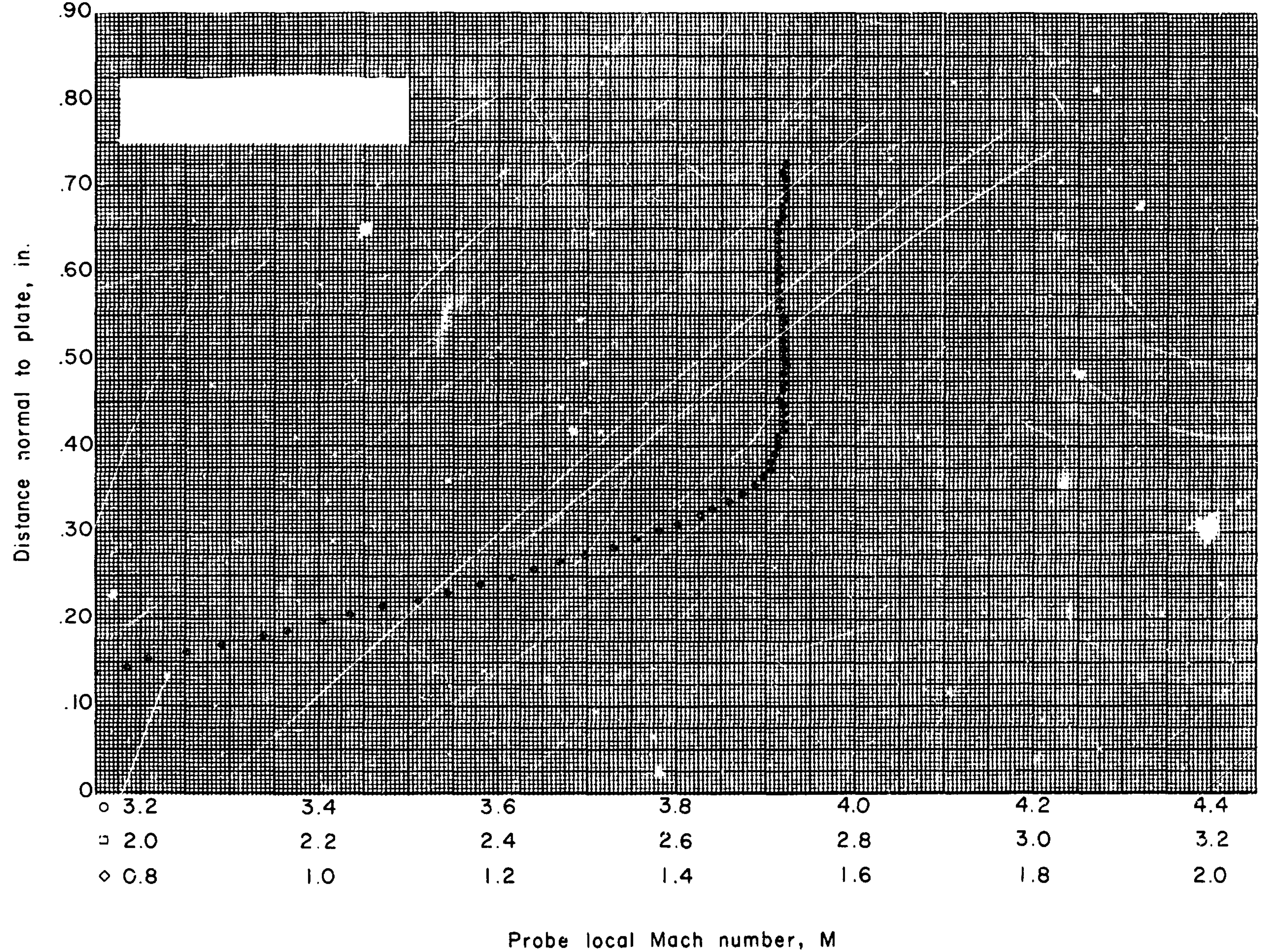

Figure 88.- Boundary-layer Mach number distribution for run 50. All identifying conditions are given in table III.

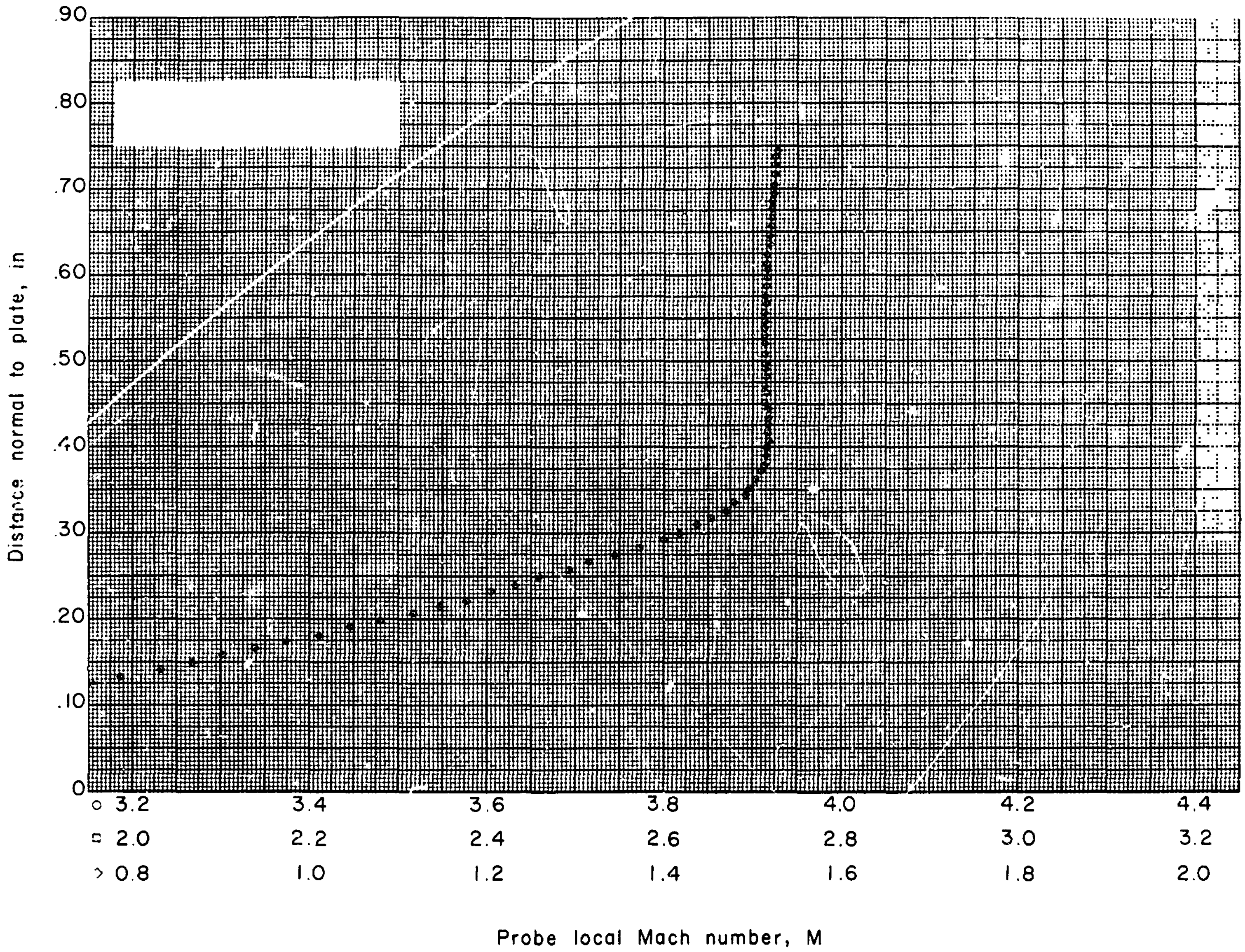

Figure 89.- Boundary-layer Mach number distribution for run 51. All identifying conditions are given in table III.

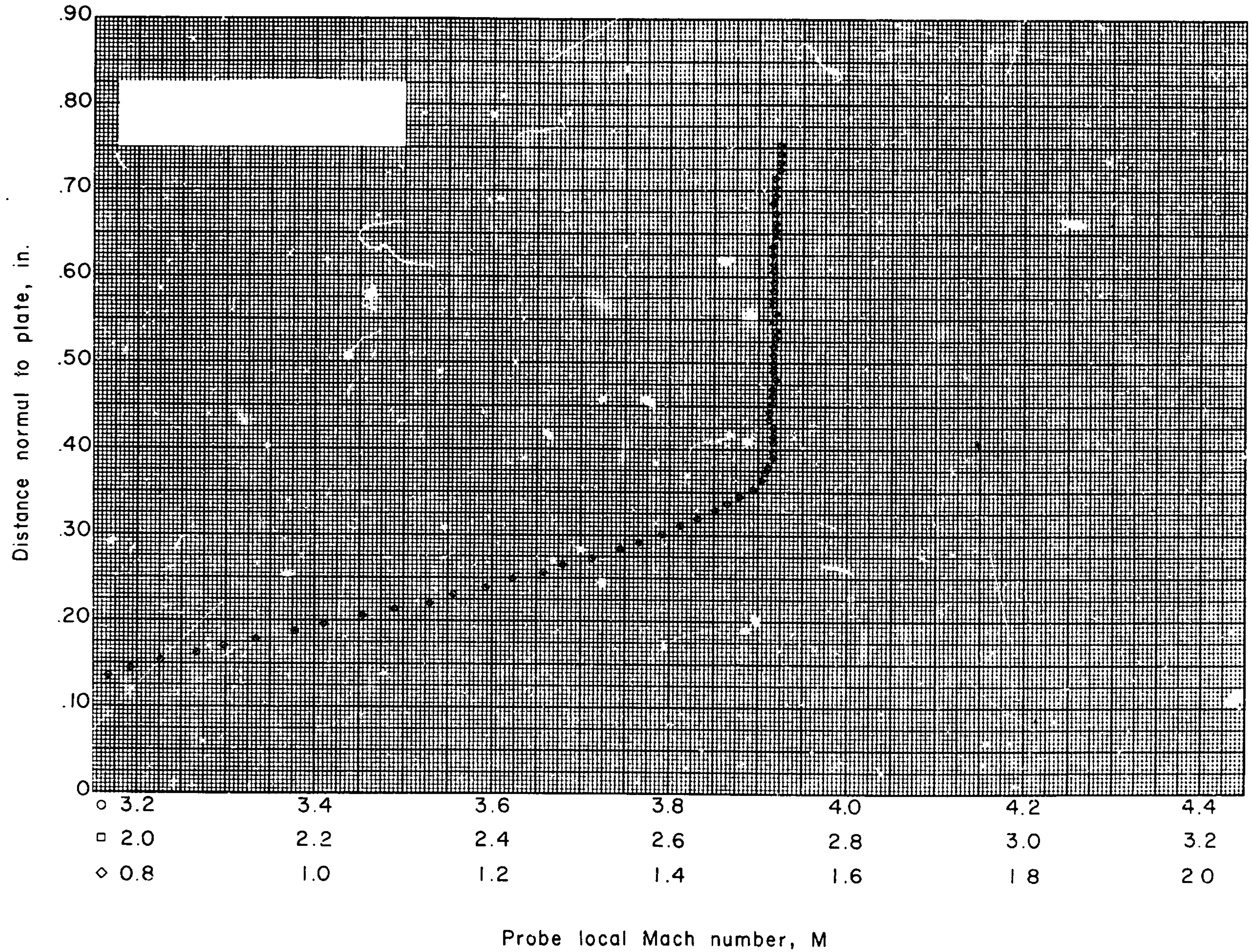

Figure 90.- Boundary-layer Mach number distribution for run 52. All identifying conditions are given in table III.

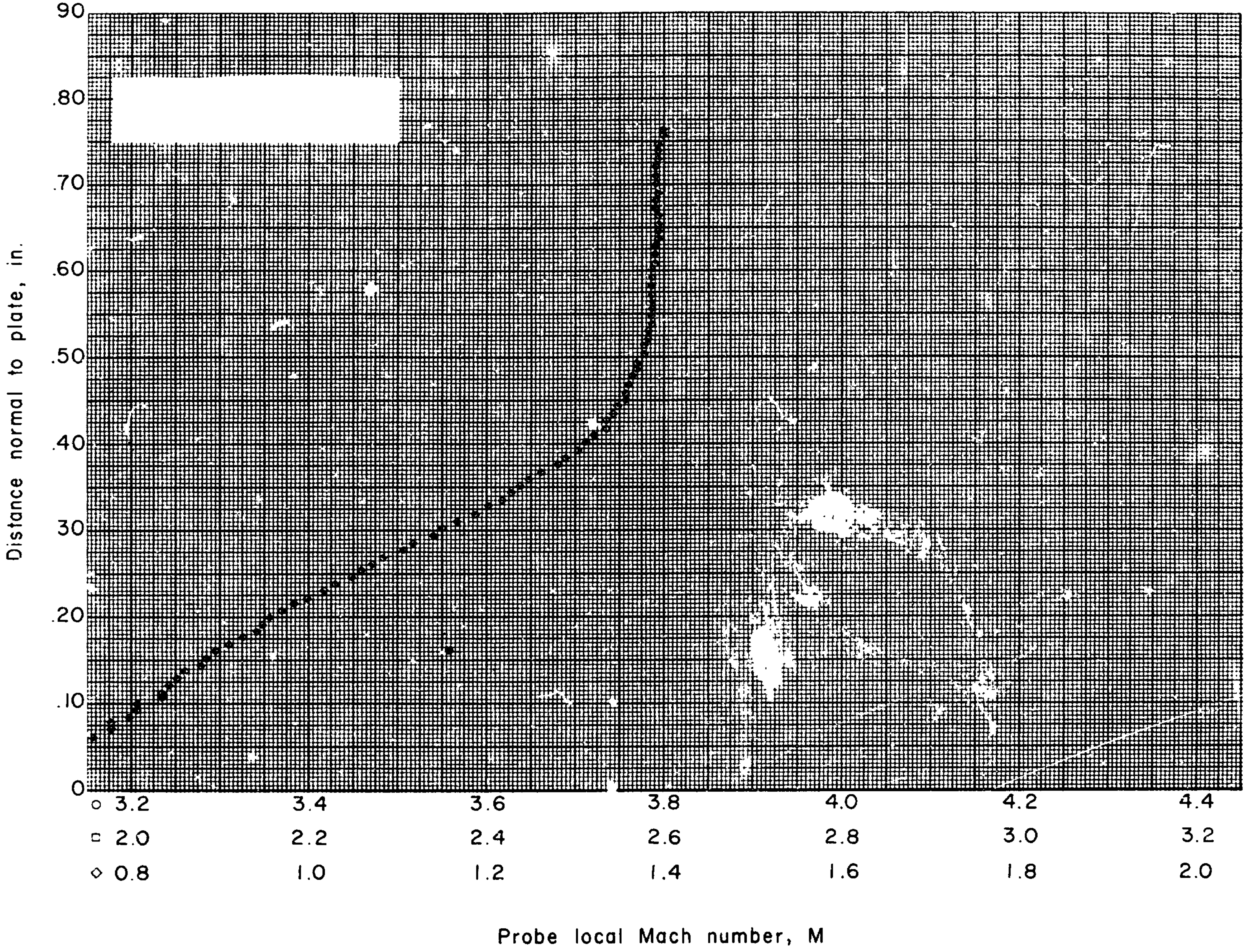

Figure 91.- Boundary-layer Mach number distribution for run 53. All identifying conditions are given in table III.

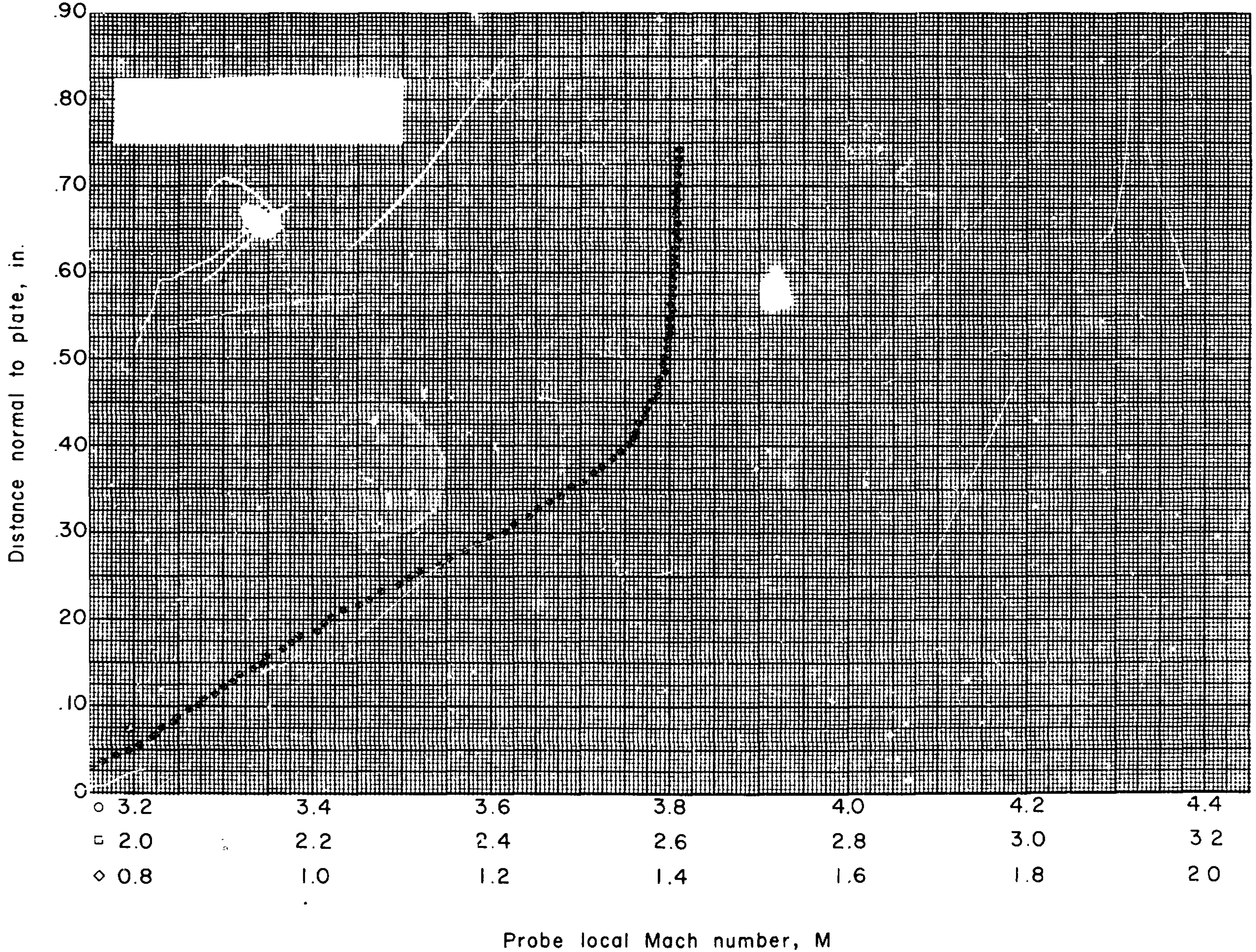

Figure 92.- Boundary-layer Mach number distribution for run 54. All identifying conditions are given in table III.

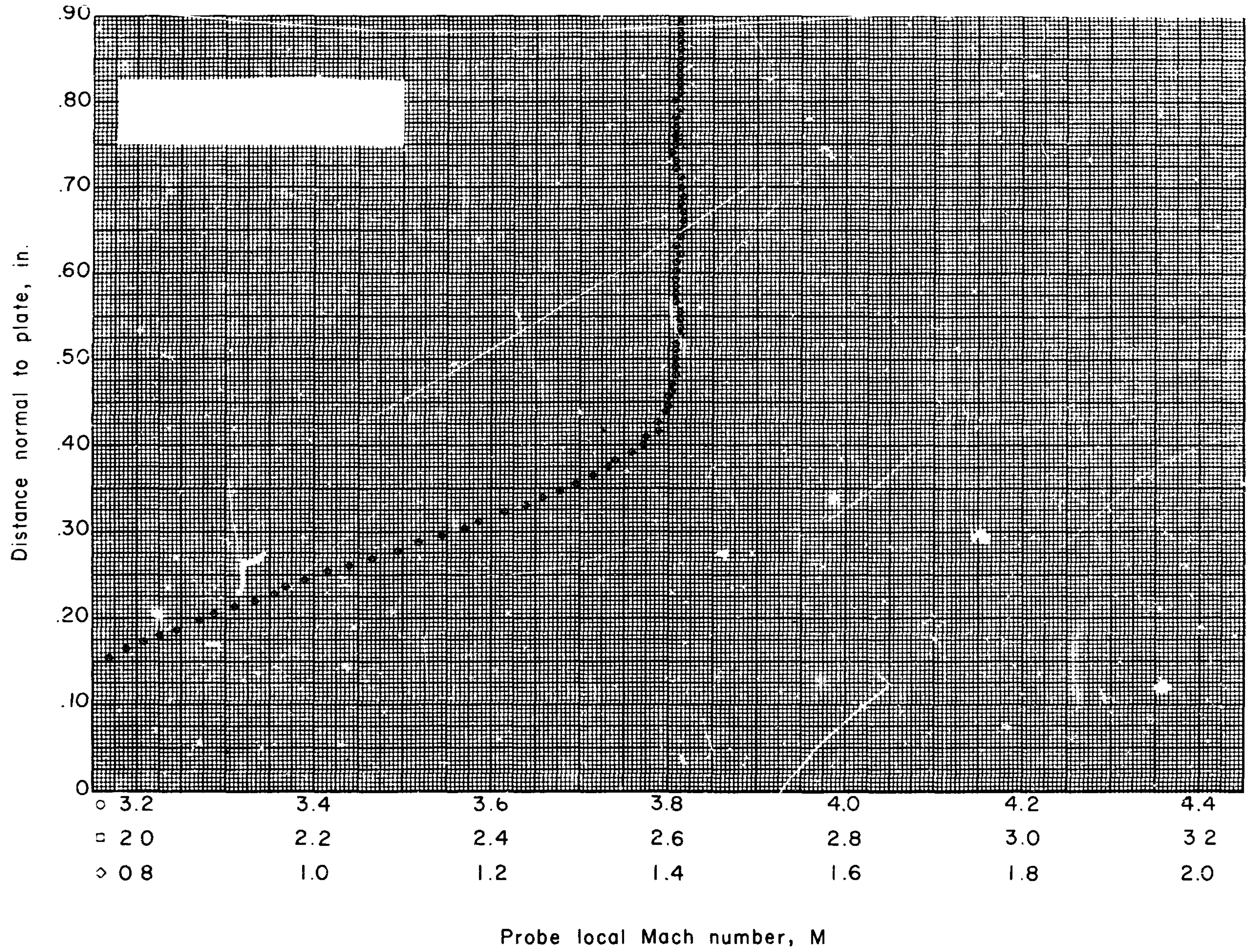

Figure 93.- Boundary-layer Mach number distribution for run 55. All identifying conditions are given in table III.

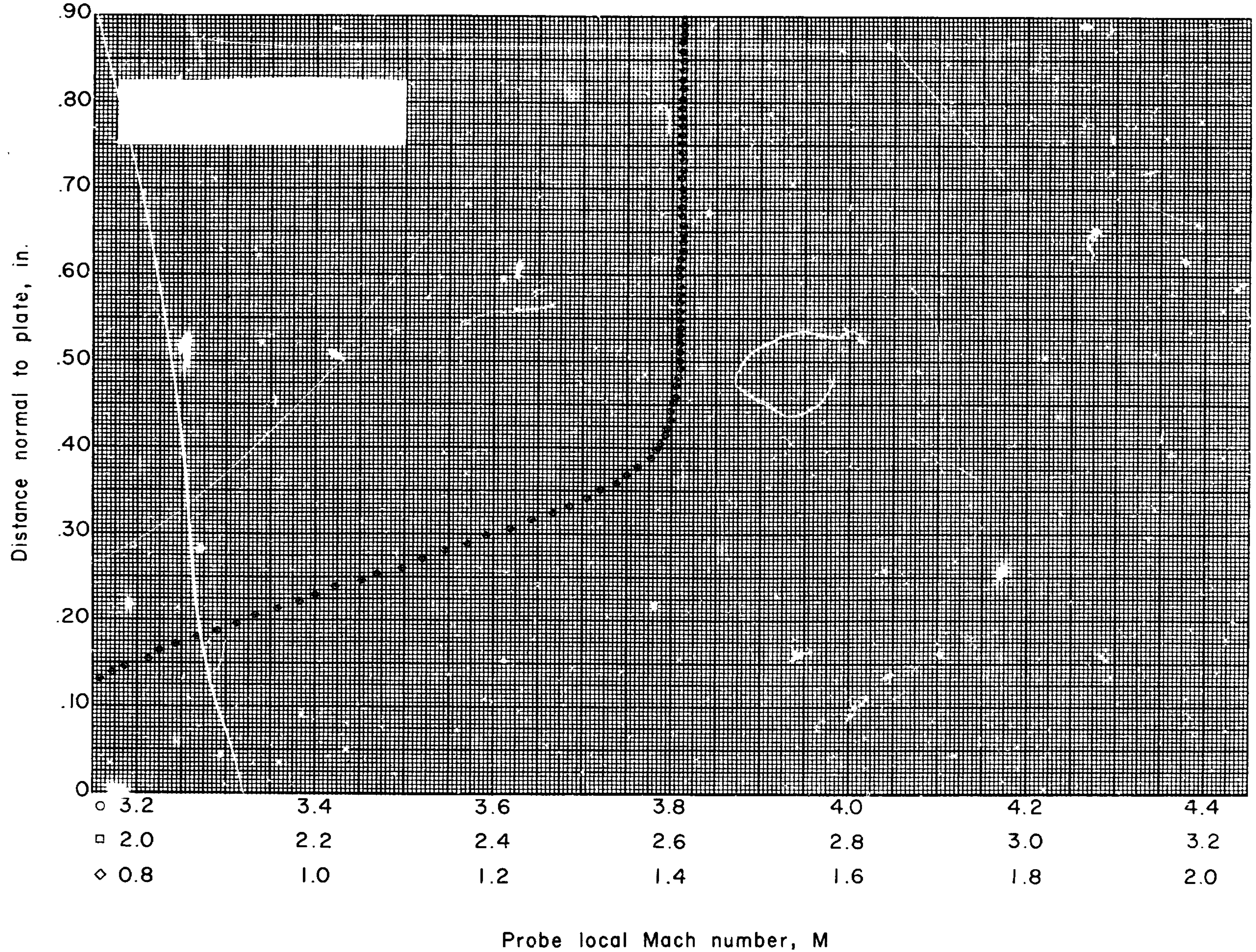

Figure 94.- Boundary-layer Mach number distribution for run 56. All identifying conditions are given in table III.

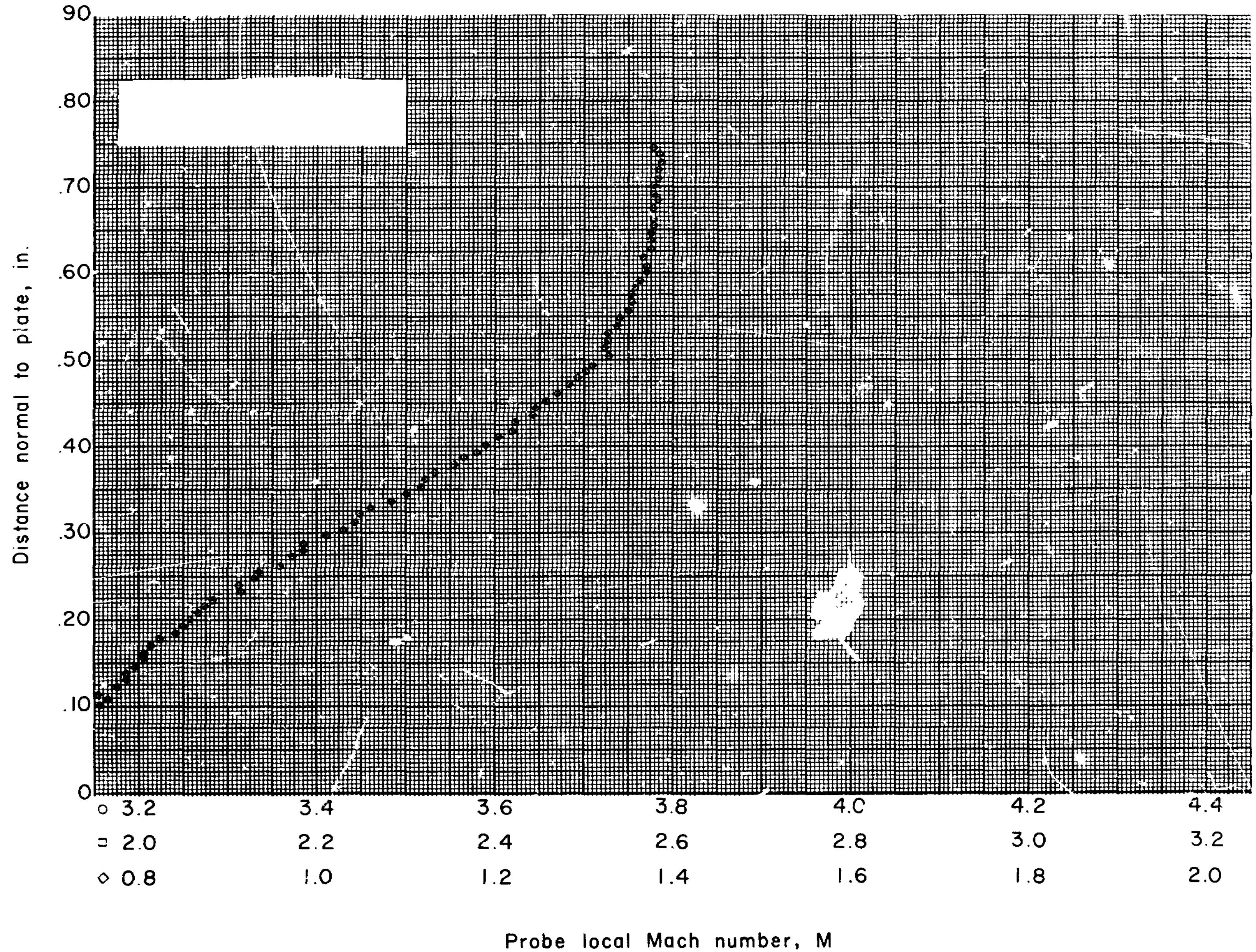

Figure 95.- Boundary-layer Mach number distribution for run 57. All identifying conditions are given in table III.

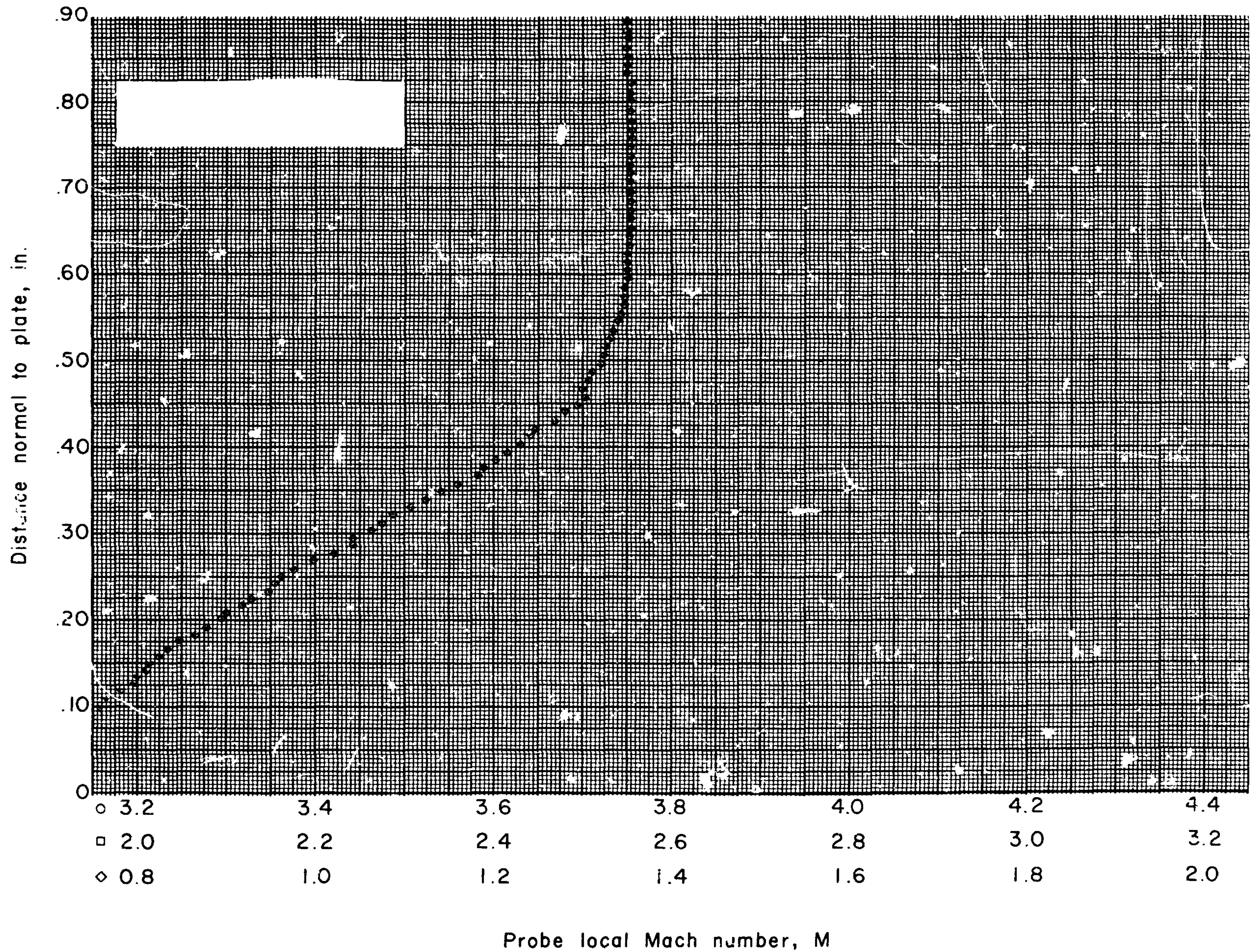

Figure 96.- Boundary-layer Mach number distribution for run 58. All identifying conditions are given in table III.

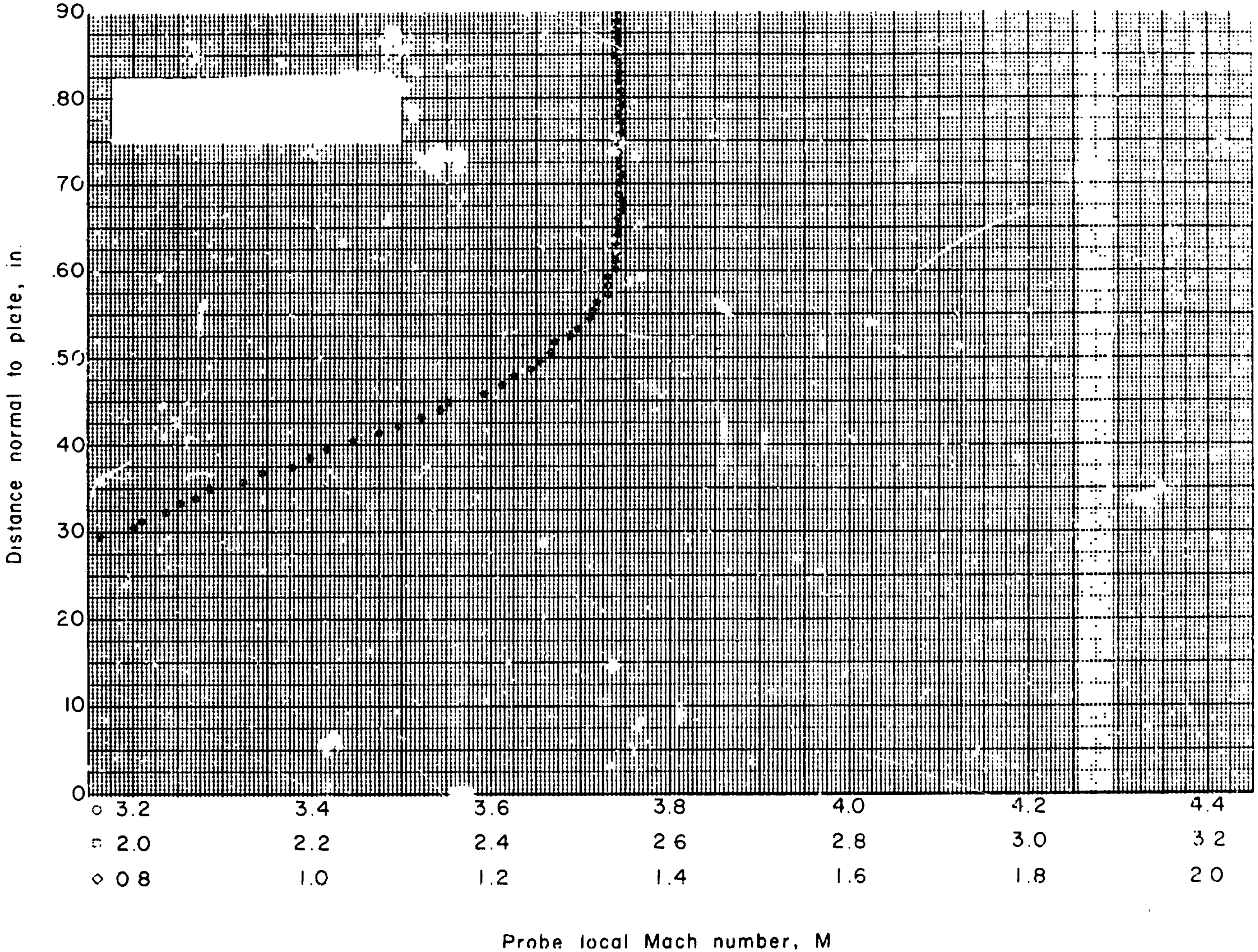

Figure 97.- Boundary-layer Mach number distribution for run 59. All identifying conditions are given in table II.

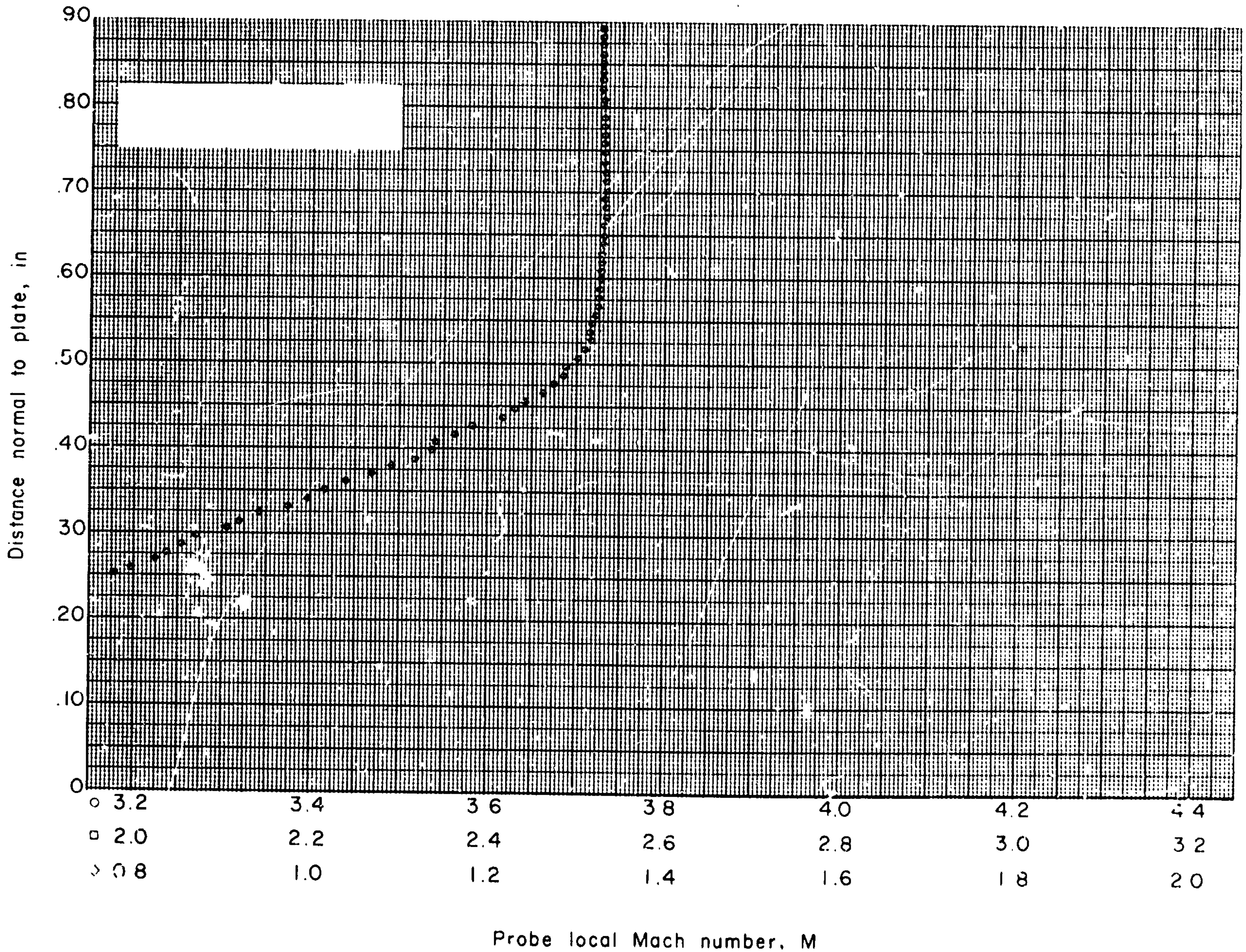

Figure 98.- Boundary-layer Mach number distribution for run 60. All identifying conditions are given in table III.

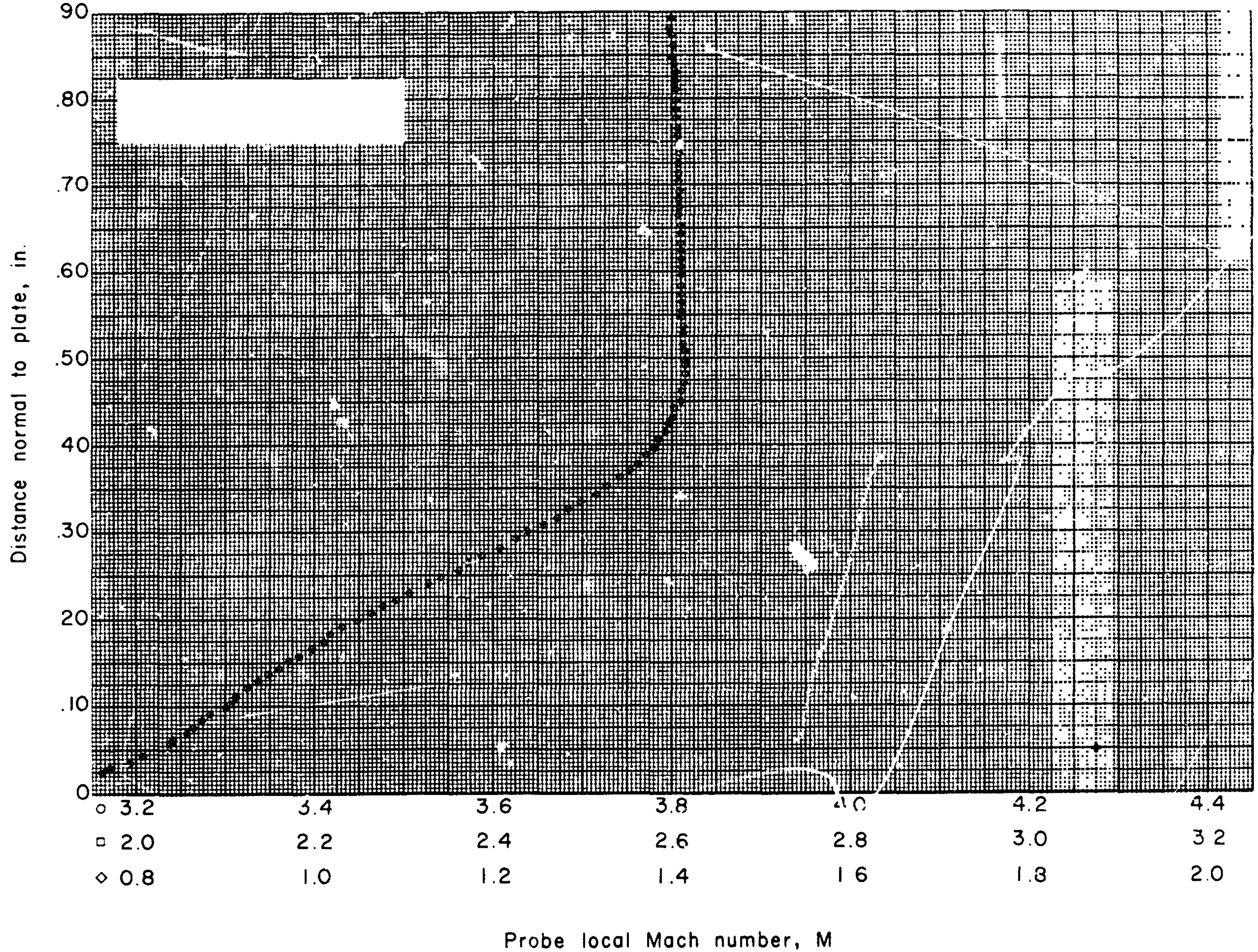

Figure 99.- Boundary-layer Mach number distribution for run 61. All identifying conditions are given in table III.

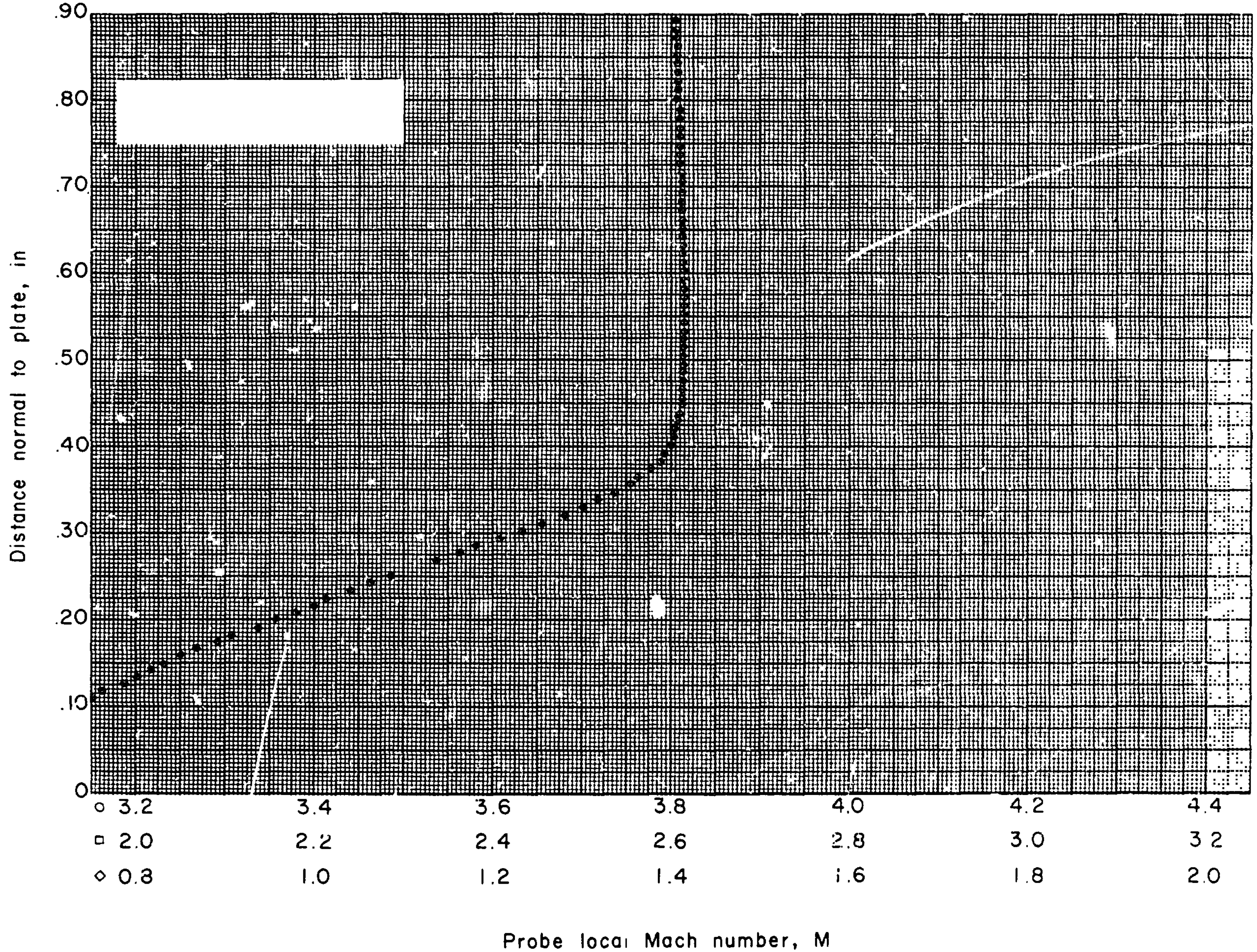

Figure 100.- Boundary-layer Mach number distribution for run 62. All identifying conditions are given in table III.

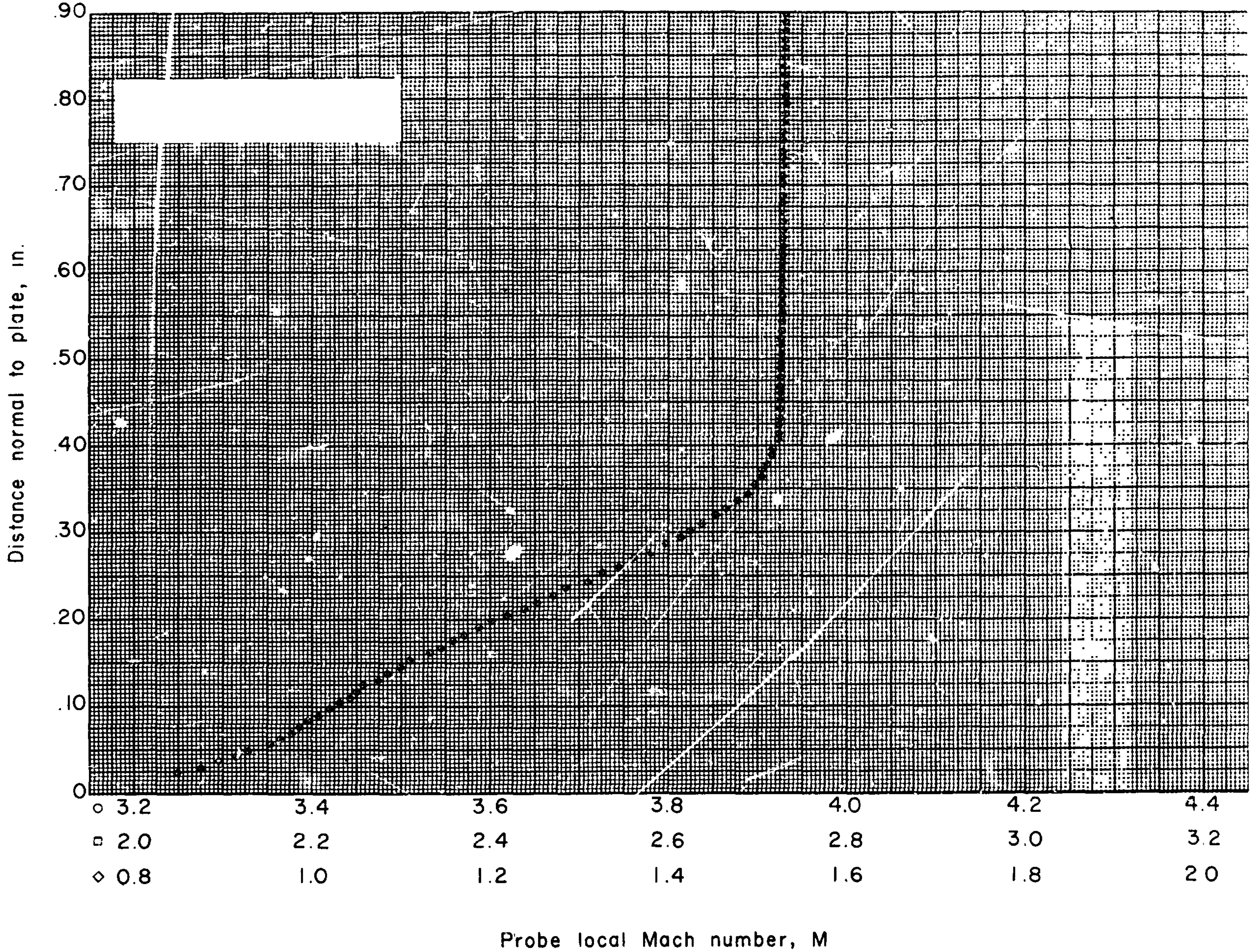

Figure 101.- Boundary-layer Mach number distribution for run 65. All identifying conditions are given in table III.

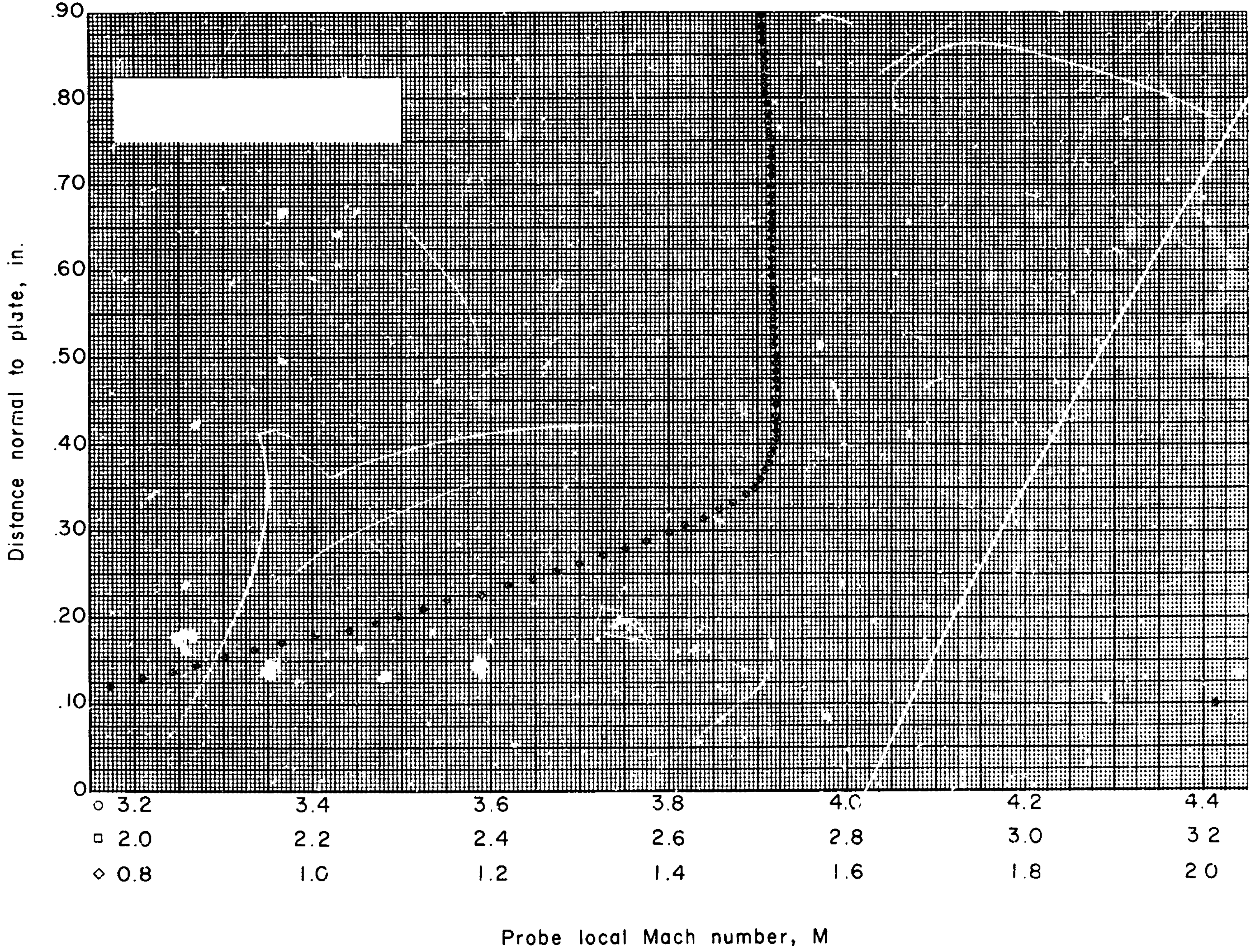

Figure 102.- Boundary-layer Mach number distribution for run 64. All identifying conditions are given in table III.

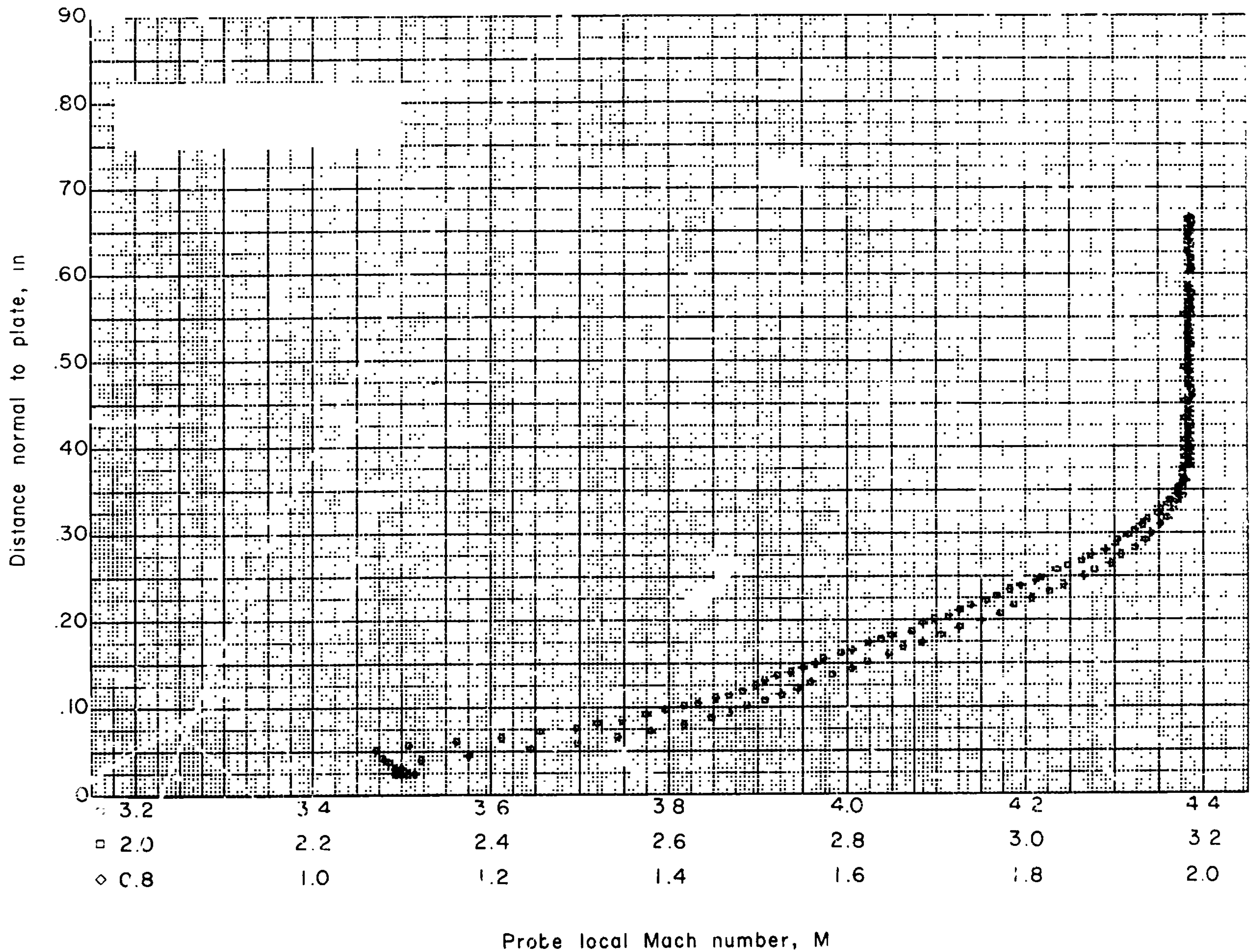

Figure 103.- Boundary-layer Mach number distribution for run 65. All identifying conditions are given in table III.

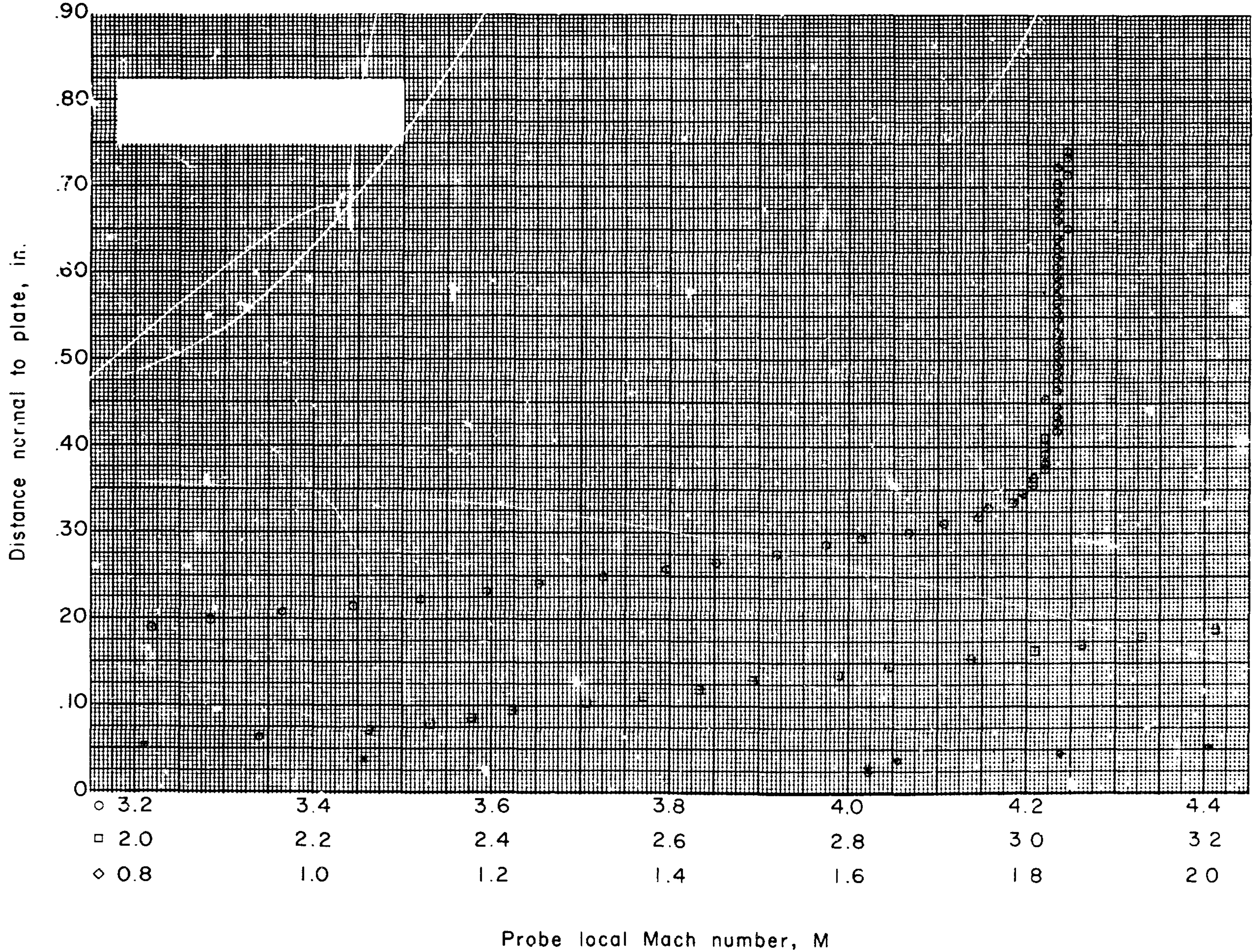

Figure 104.- Boundary-layer Mach number distribution for run 66. All identifying conditions are given in table III.

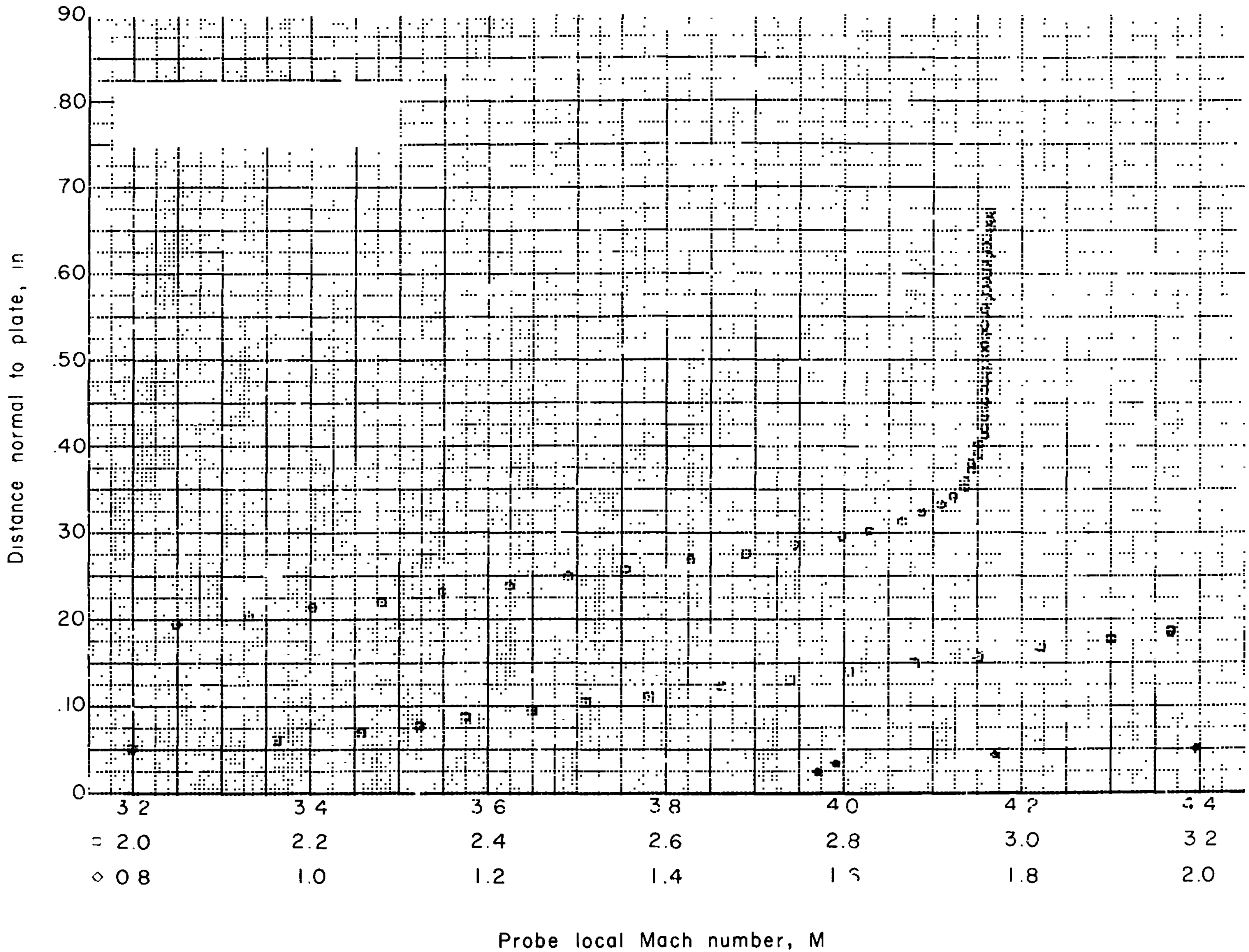

Figure 105.- Boundary-layer Mach number distribution for run 67. All identifying conditions are given in table III.

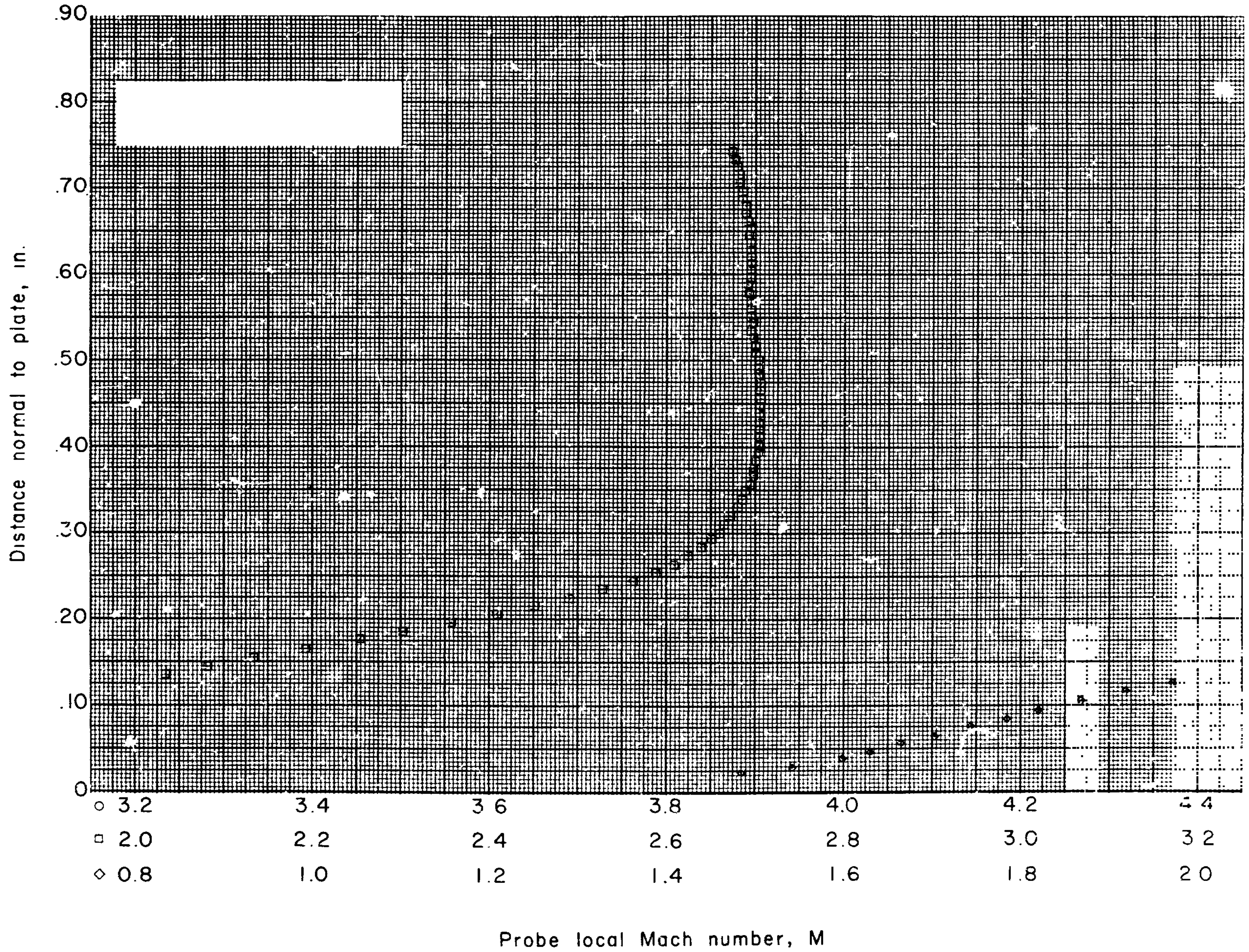

Figure 106.- Boundary-layer Mach number distribution for run 69. All identifying conditions are given in table III.

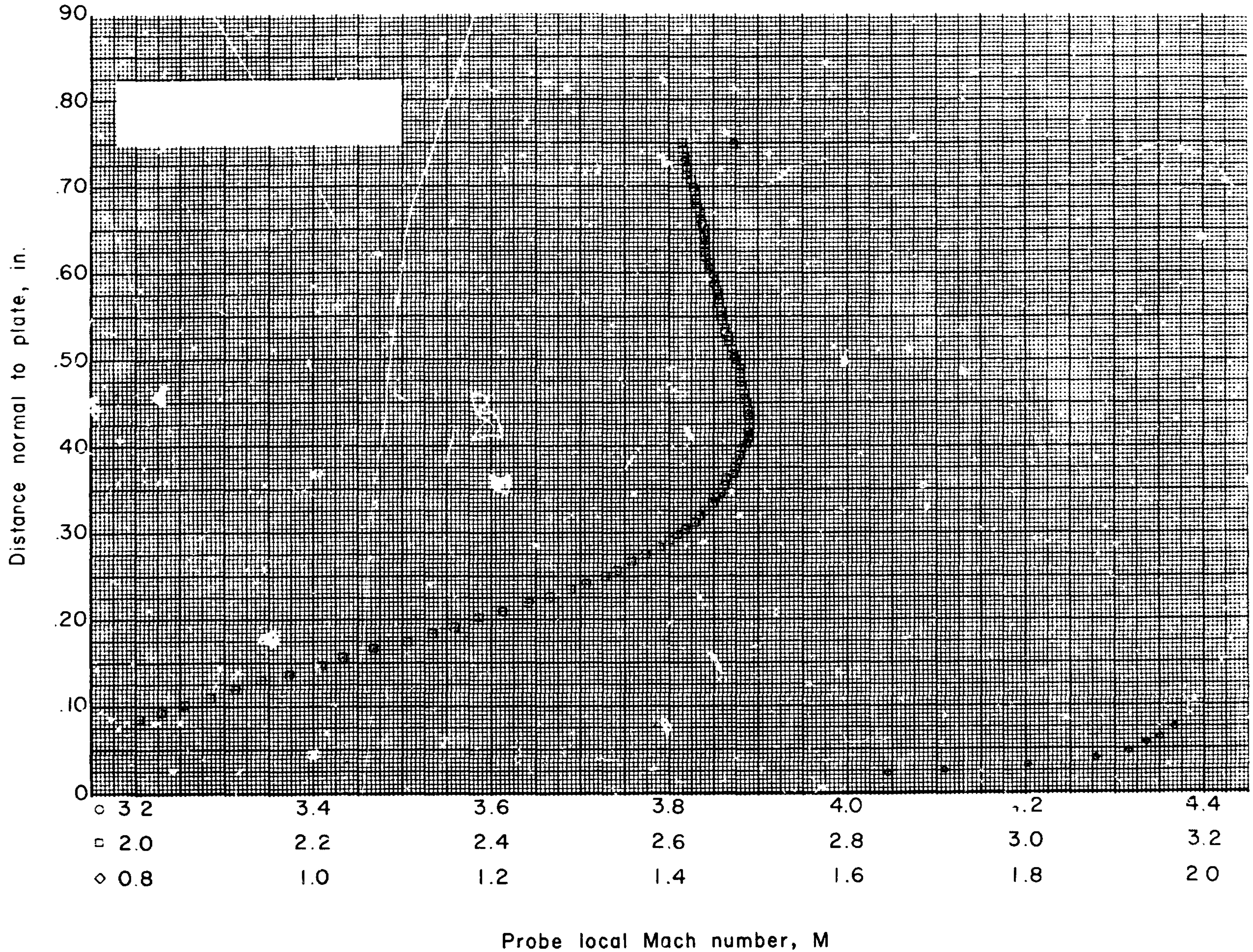

Figure 107.- Boundary-layer Mach number distribution for run 70. All identifying conditions are given in table III.

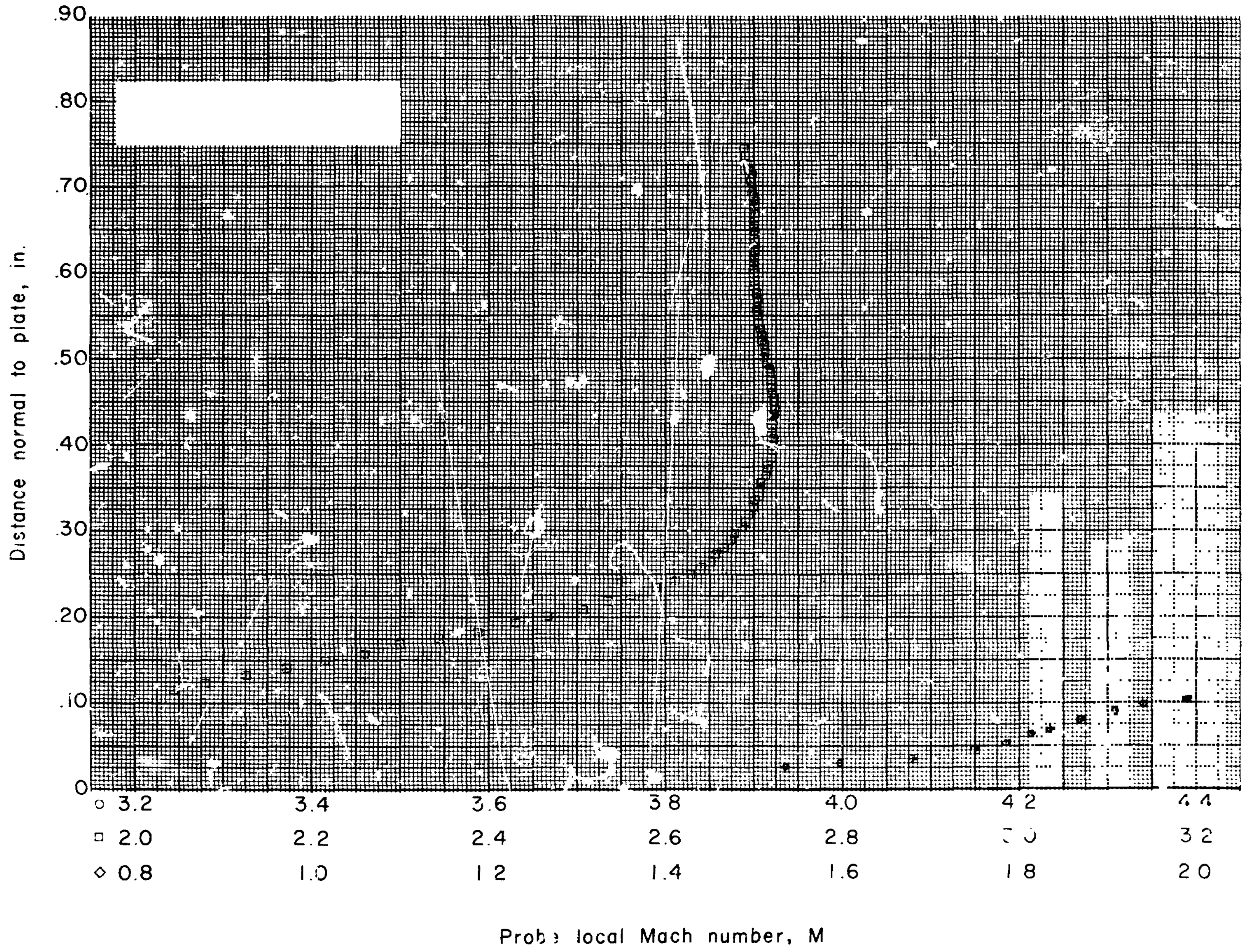

Figure 108.- Boundary-layer Mach number distribution for run 71. All identifying conditions are given in table III.

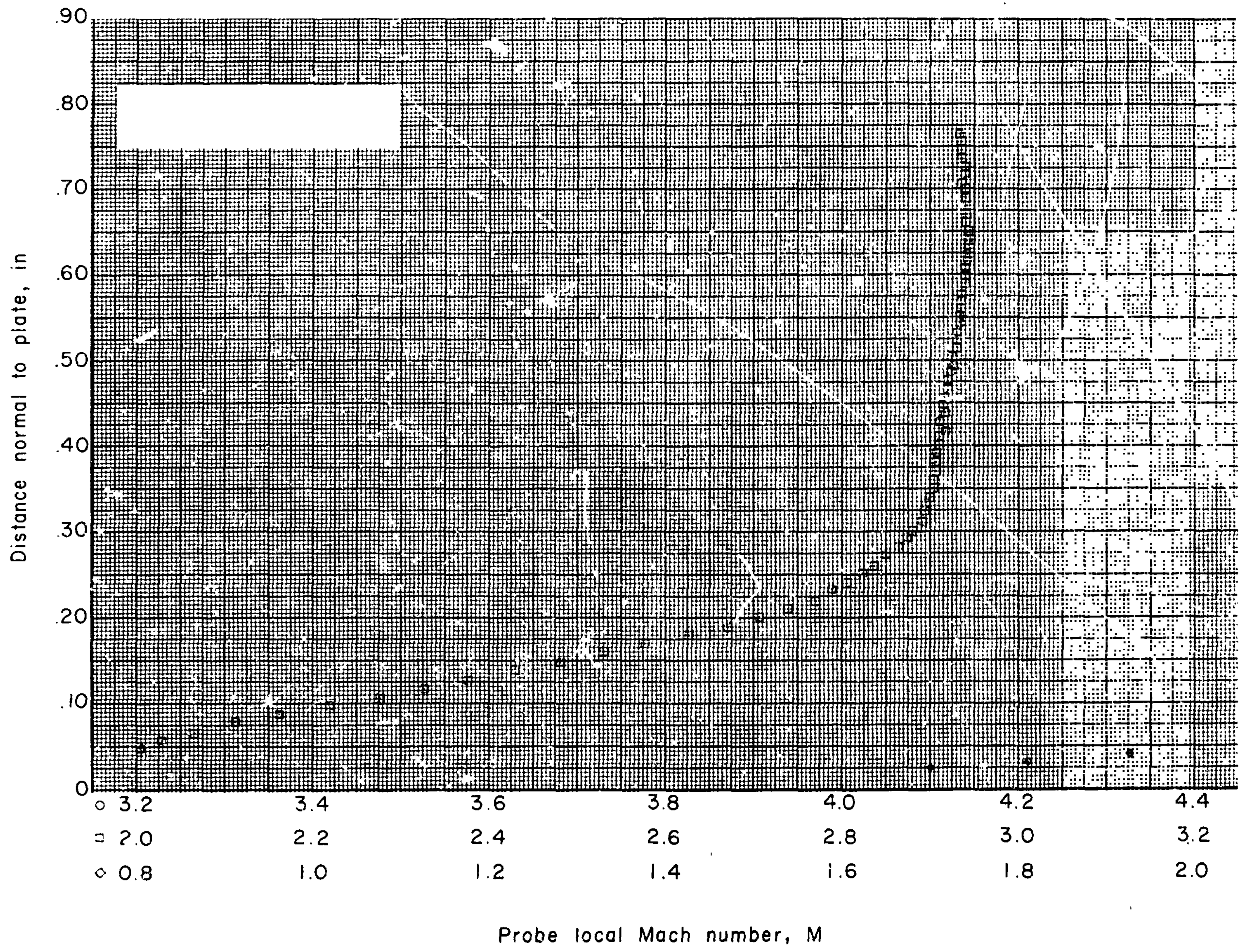

Figure 109.- Boundary-layer Mach number distribution for run 72. All identifying conditions are given in table III.

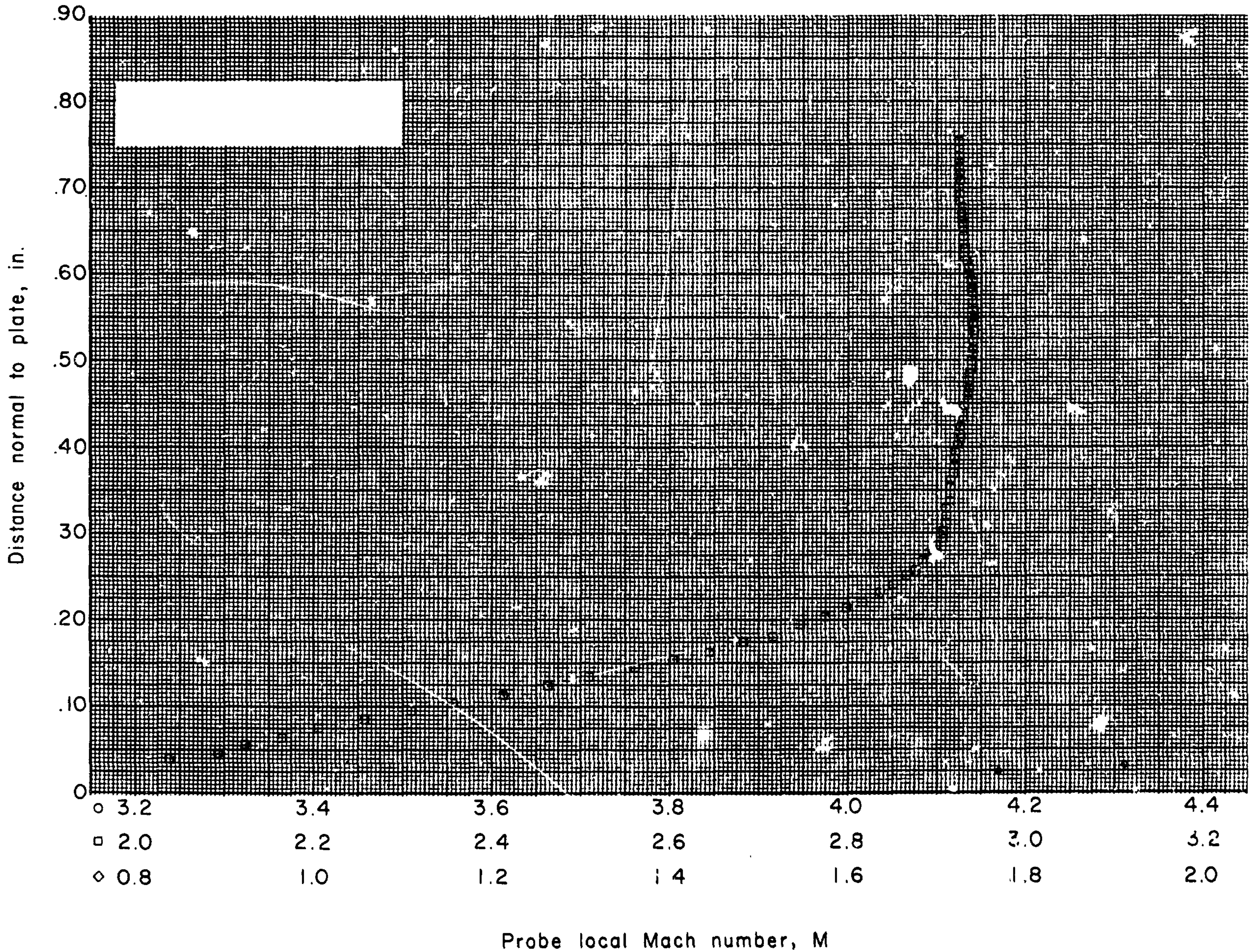

Figure 110.- Boundary-layer Mach number distribution for run 73. All identifying conditions are given in table III.

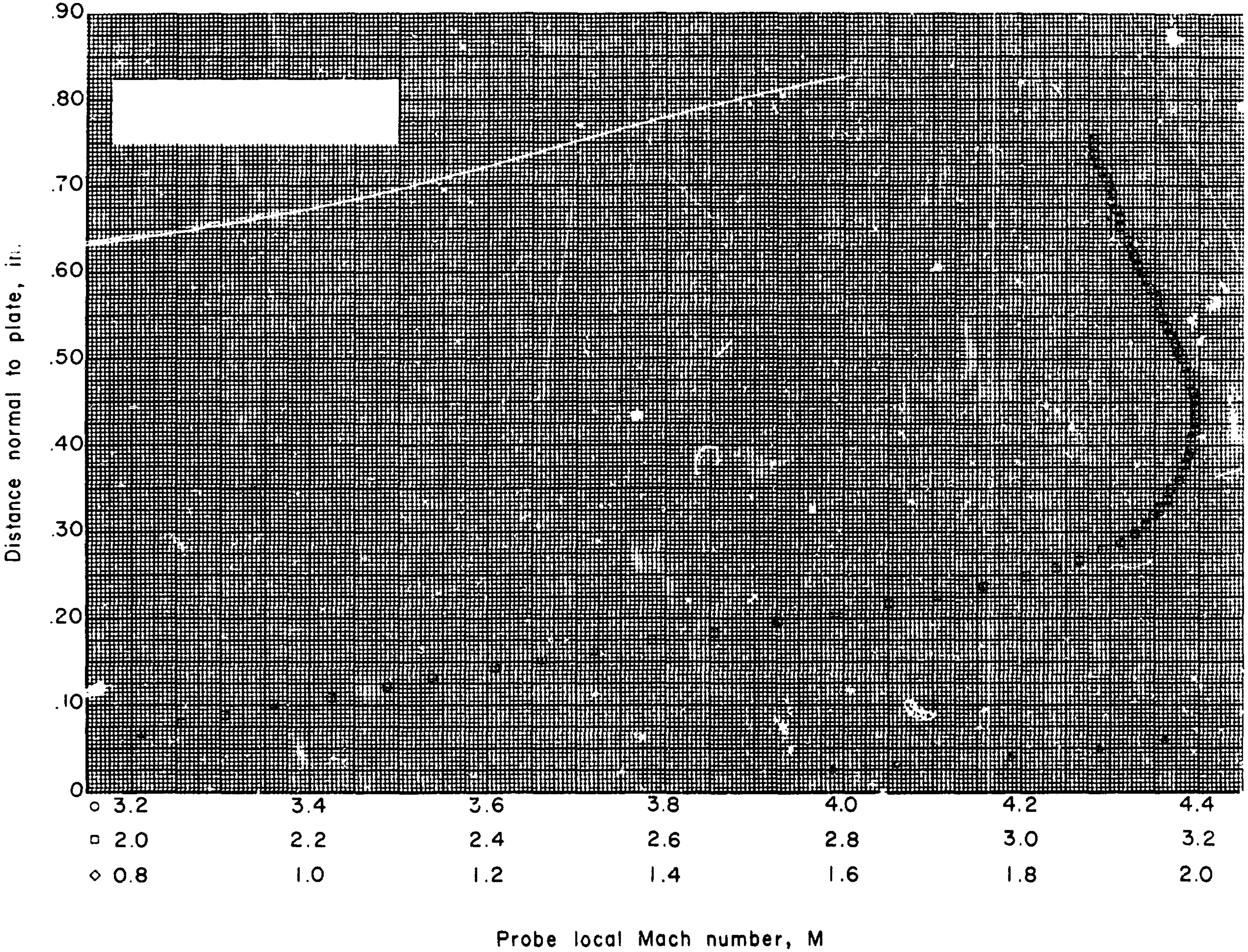

Figure 111.- Boundary-layer Mach number distribution for run 76. All identifying conditions are given in table III.

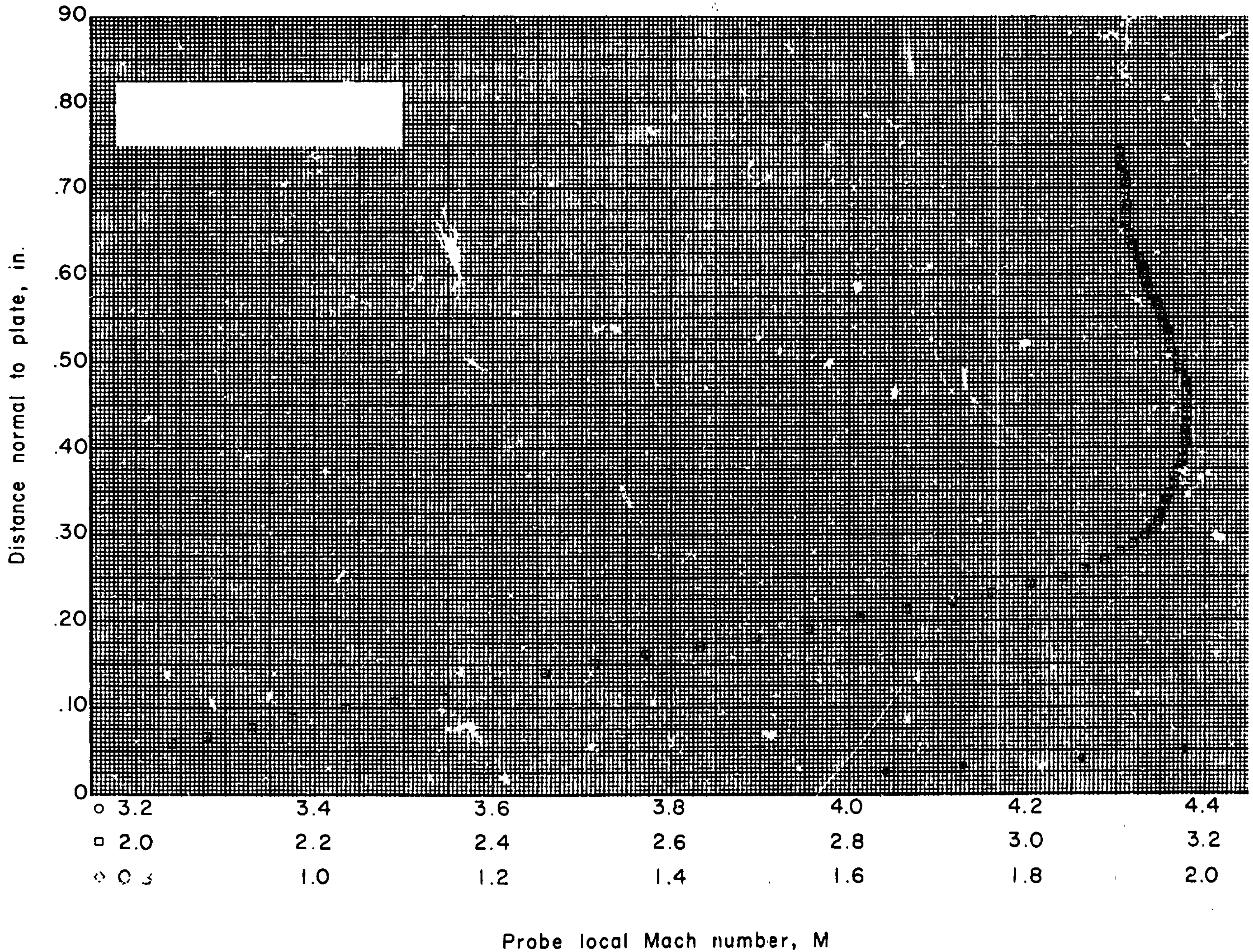

Figure 112.- Boundary-layer Mach number distribution for run 77. All identifying conditions are given in table III.

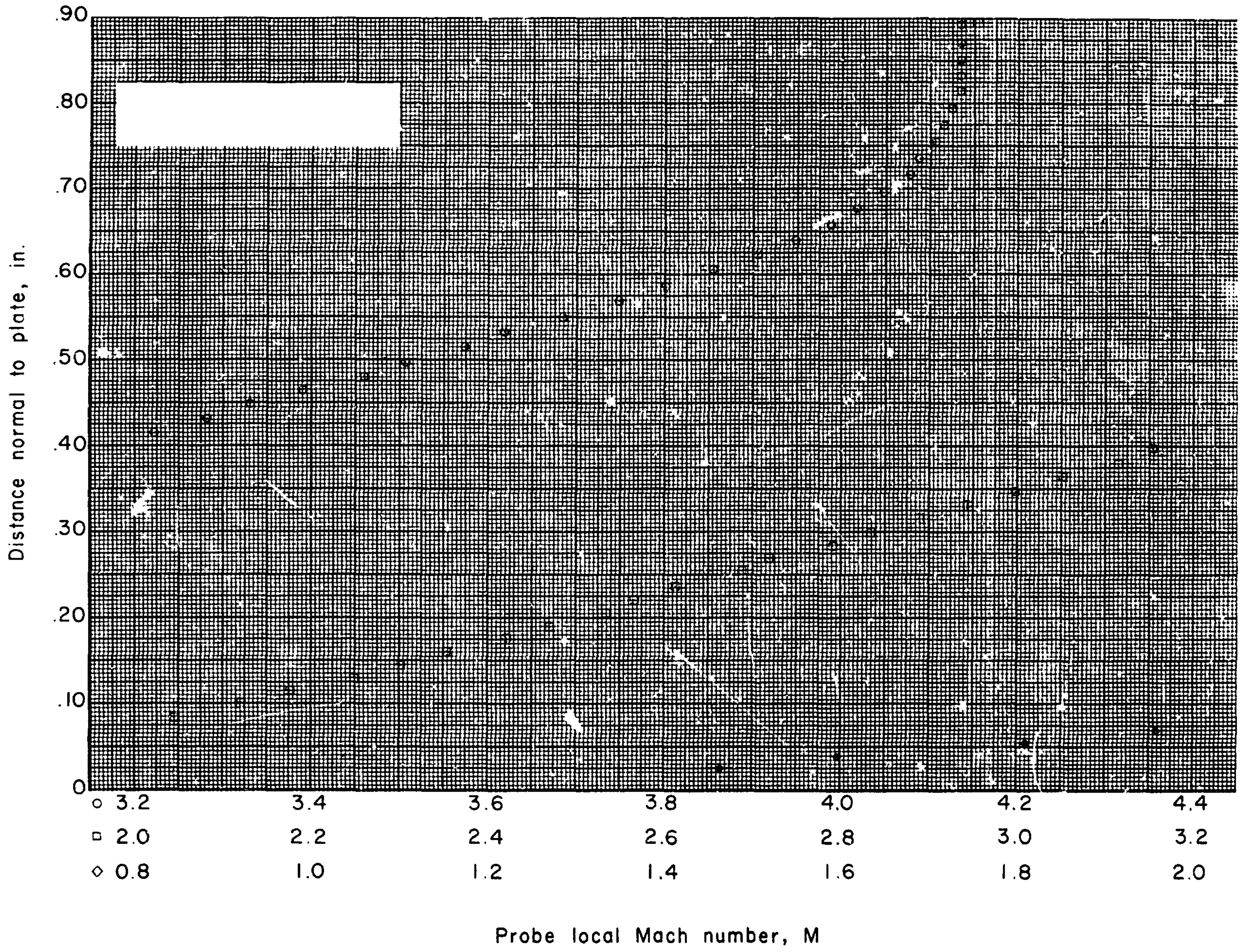

Figure 113.- Boundary-layer Mach number distribution for run 80. All identifying conditions are given in table III.

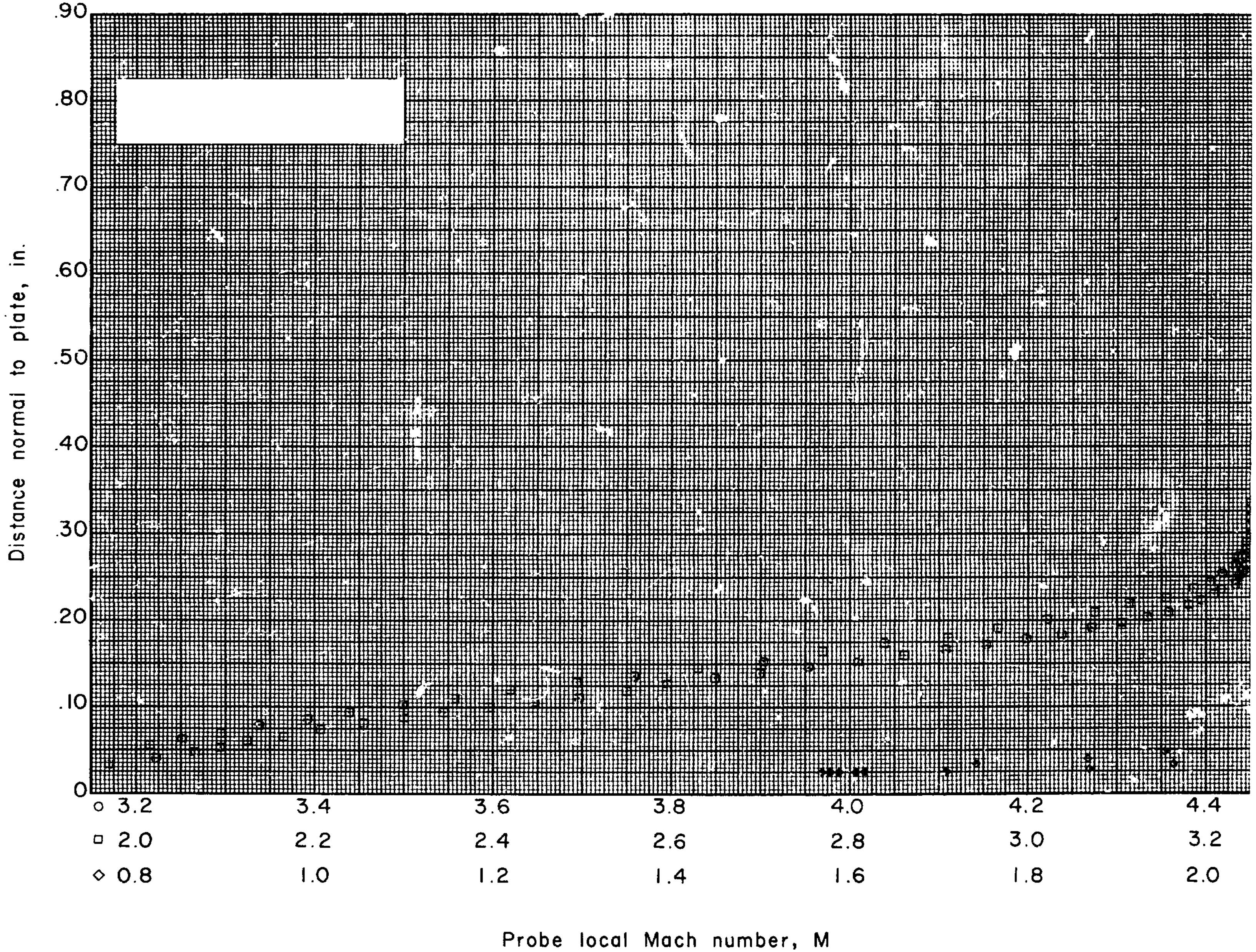

Figure 114.- Boundary-layer Mach number distribution for run 81. All identifying conditions are given in table III.

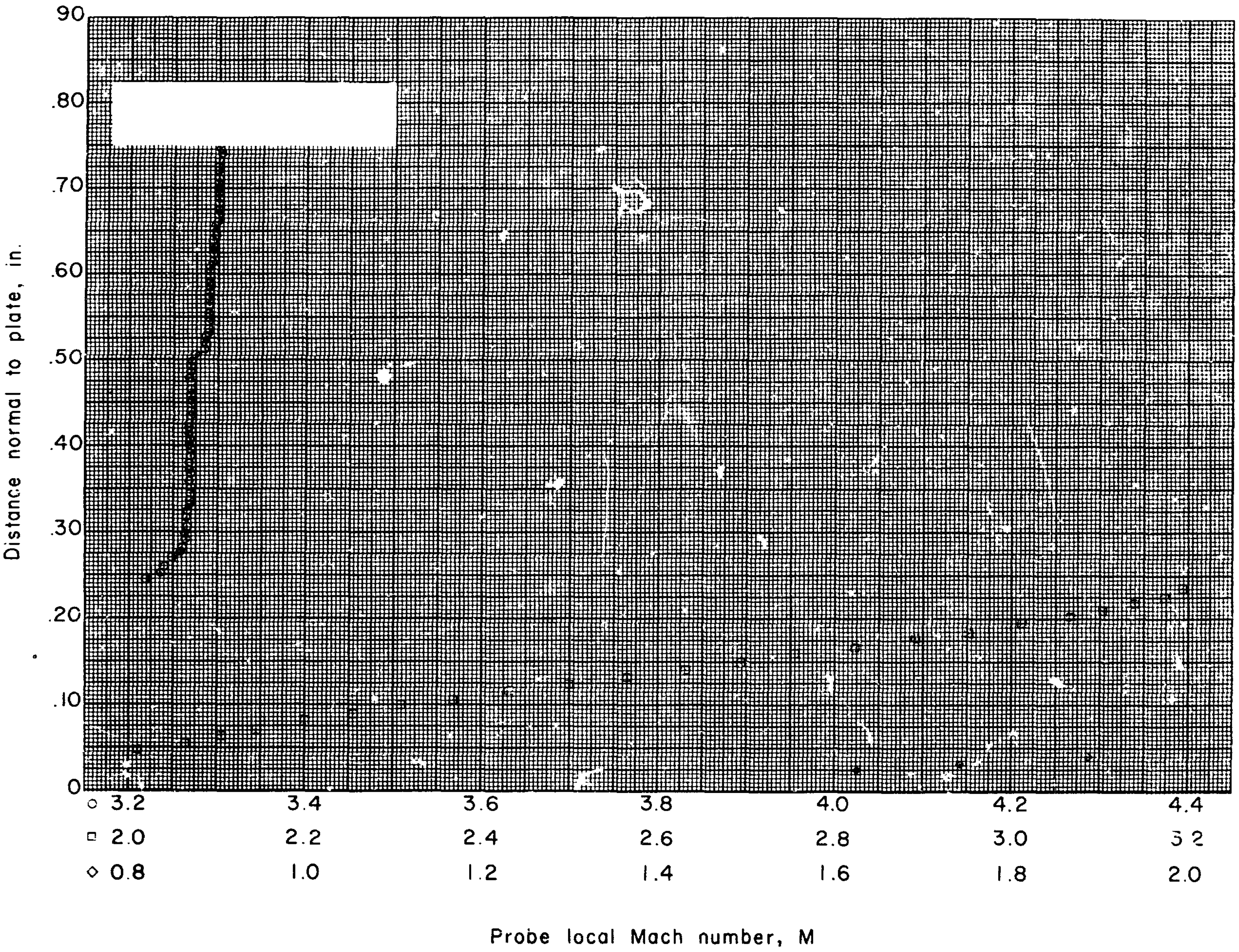

Figure 115.- Boundary-layer Mach number distribution for run 82. All identifying conditions are given in table III.

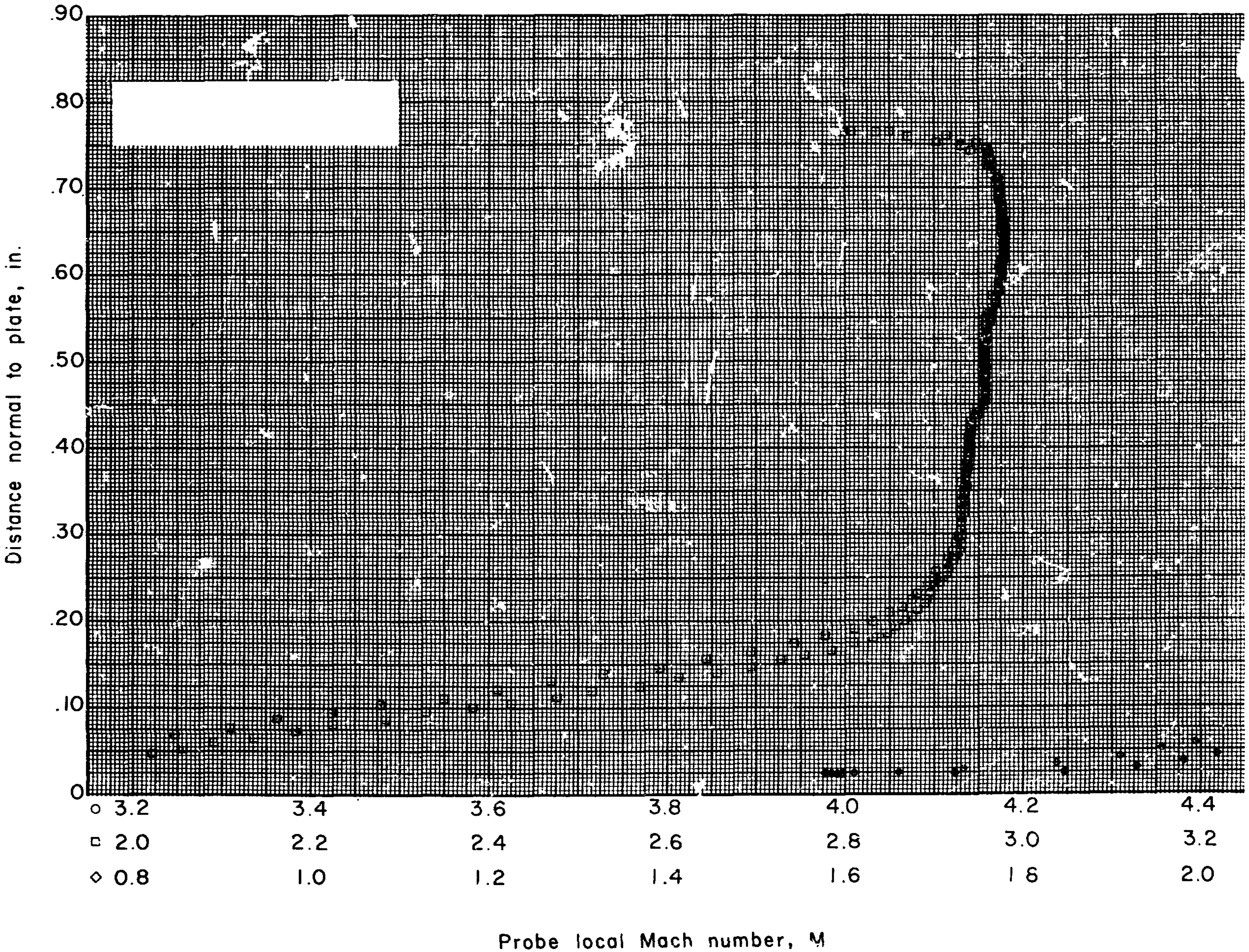

Figure 116.- Boundary-layer Mach number distribution for run 83. All identifying conditions are given in table III.

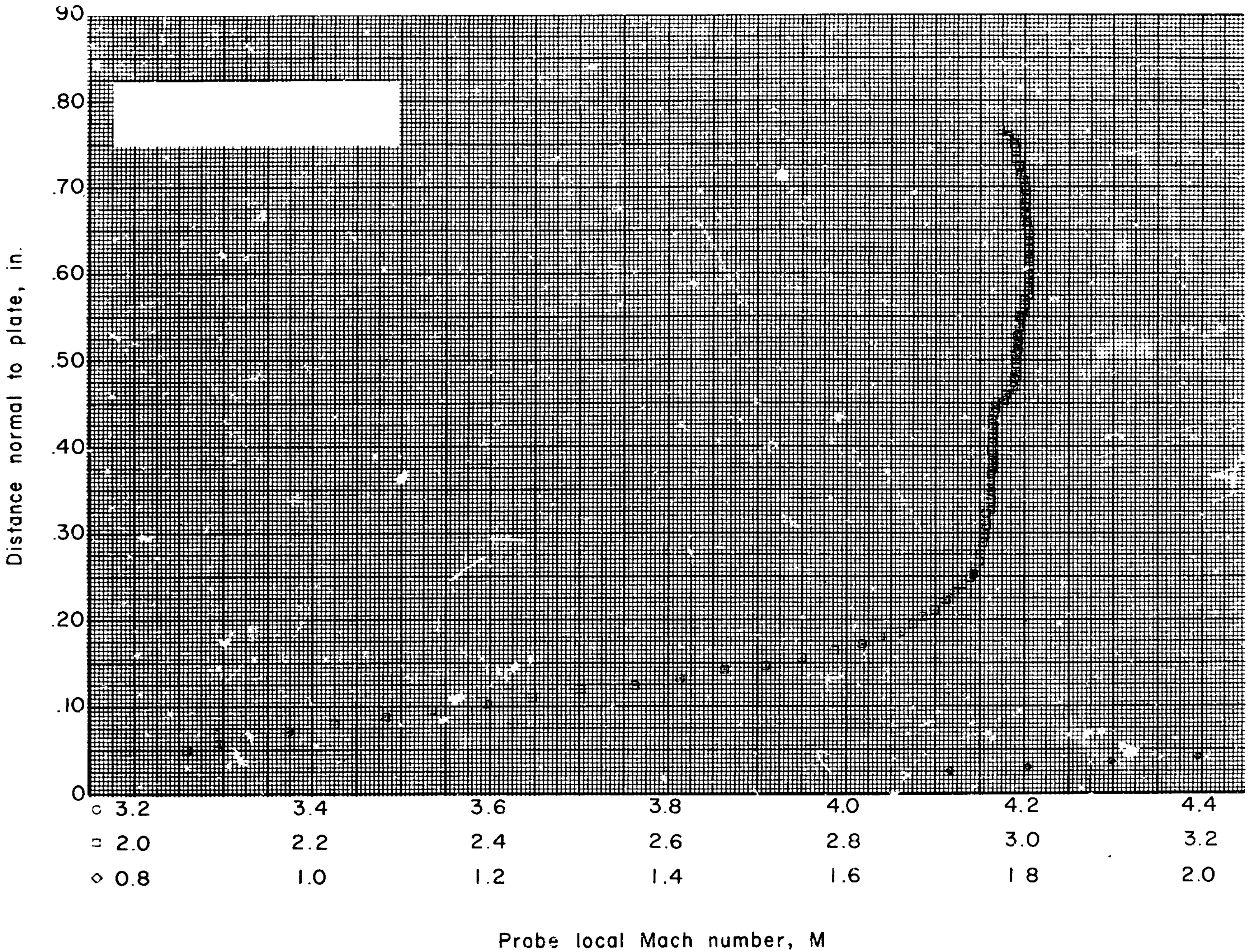

Figure 117.- Boundary-layer Mach number distribution for run 84. All identifying conditions are given in table III.

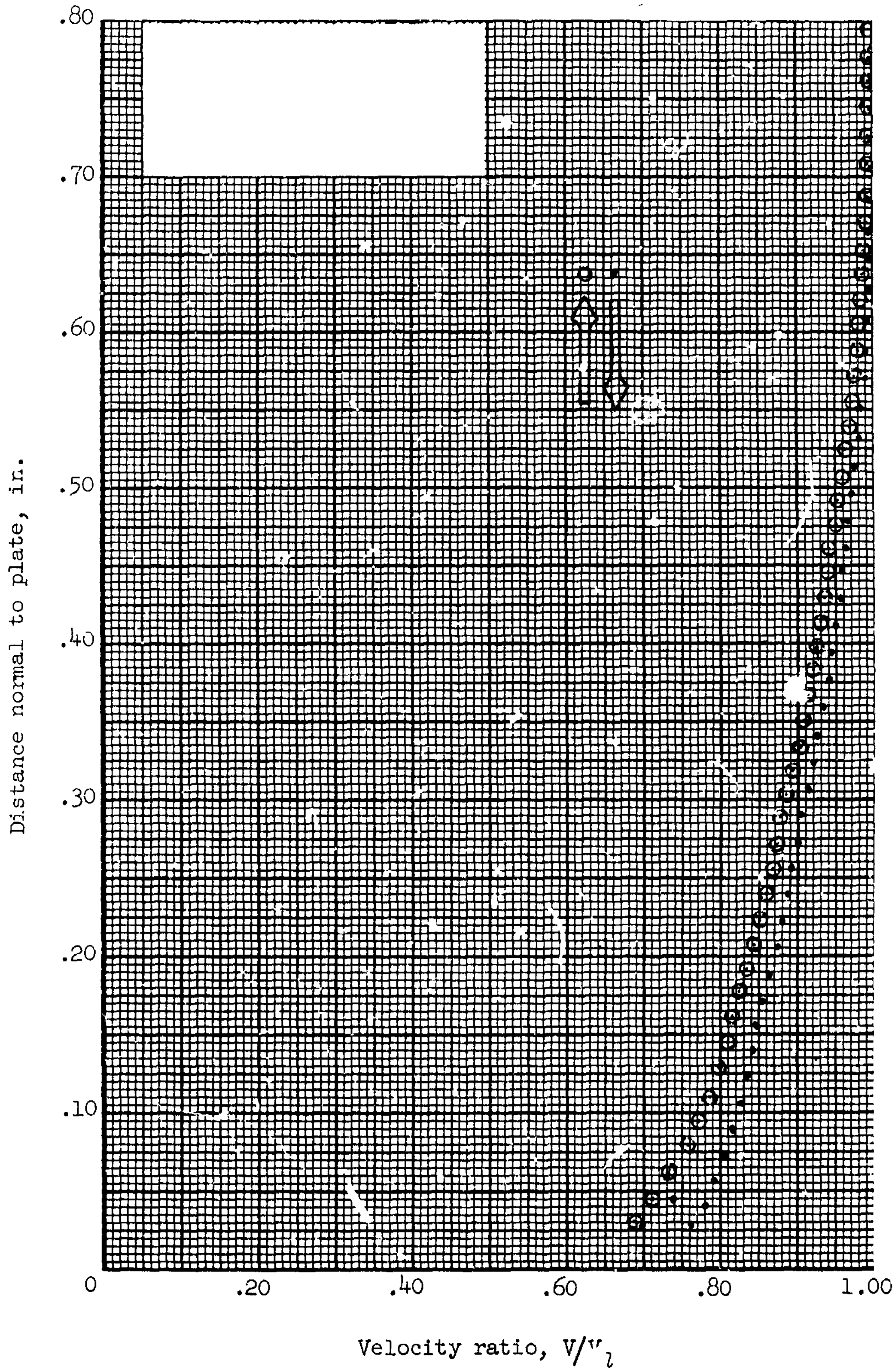

Figure 118.- Boundary-layer velocity distribution for run 2. All identifying conditions are given in table III. Arrows identify direction of probe travel across the boundary layer.

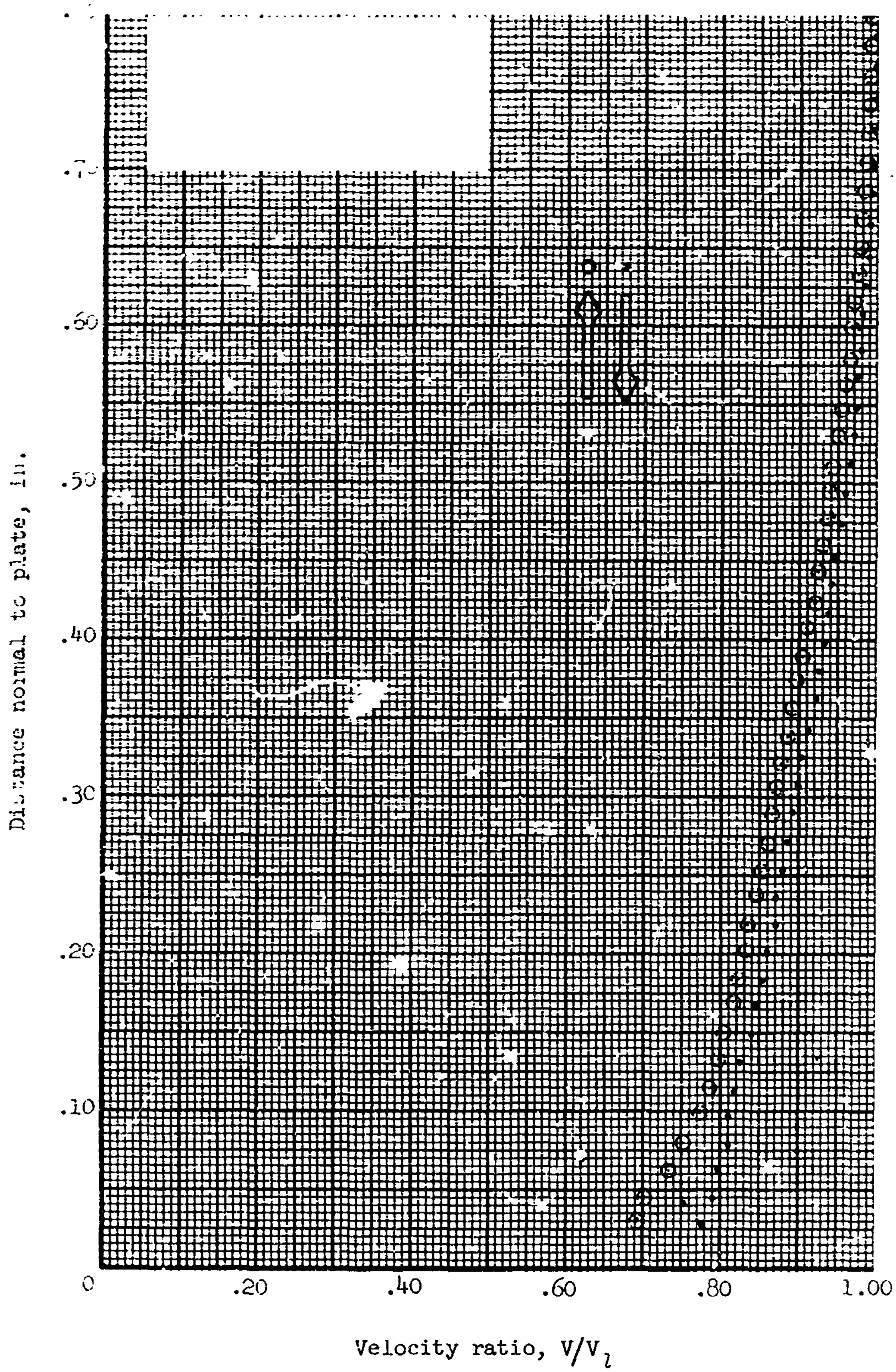

Figure 119.- Boundary-layer velocity distribution for run 3. All identifying conditions are given in table III. Arrows identify direction of probe travel across the boundary layer.

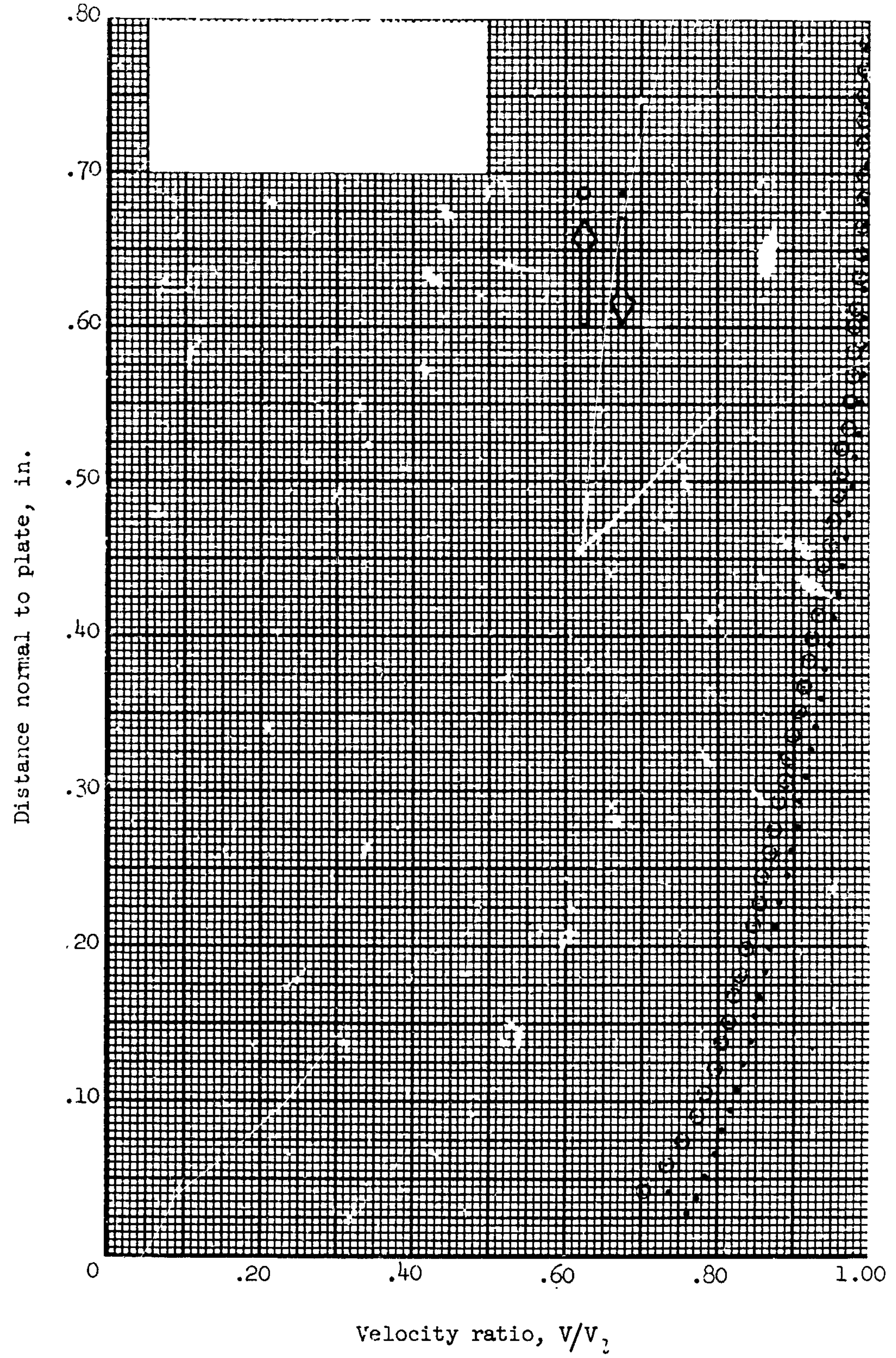

Figure 120.- Boundary-layer velocity distribution for run 4. All identifying conditions are given in table III. Arrows identify direction of probe travel across the boundary layer.

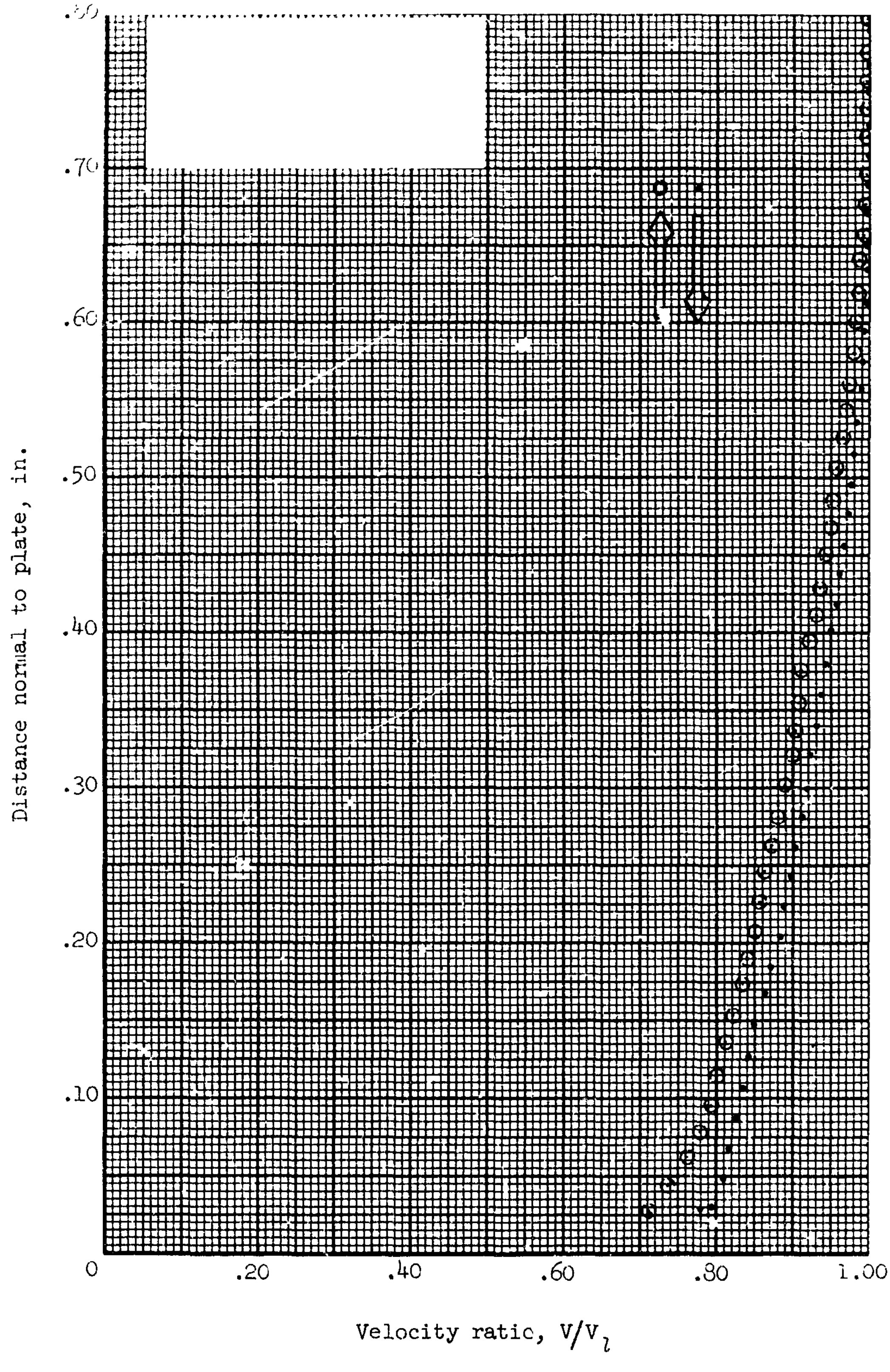

Figure 121.- Boundary-layer velocity distribution for run 5. All identifying conditions are given in table III. Arrows identify direction of probe travel across the boundary layer.

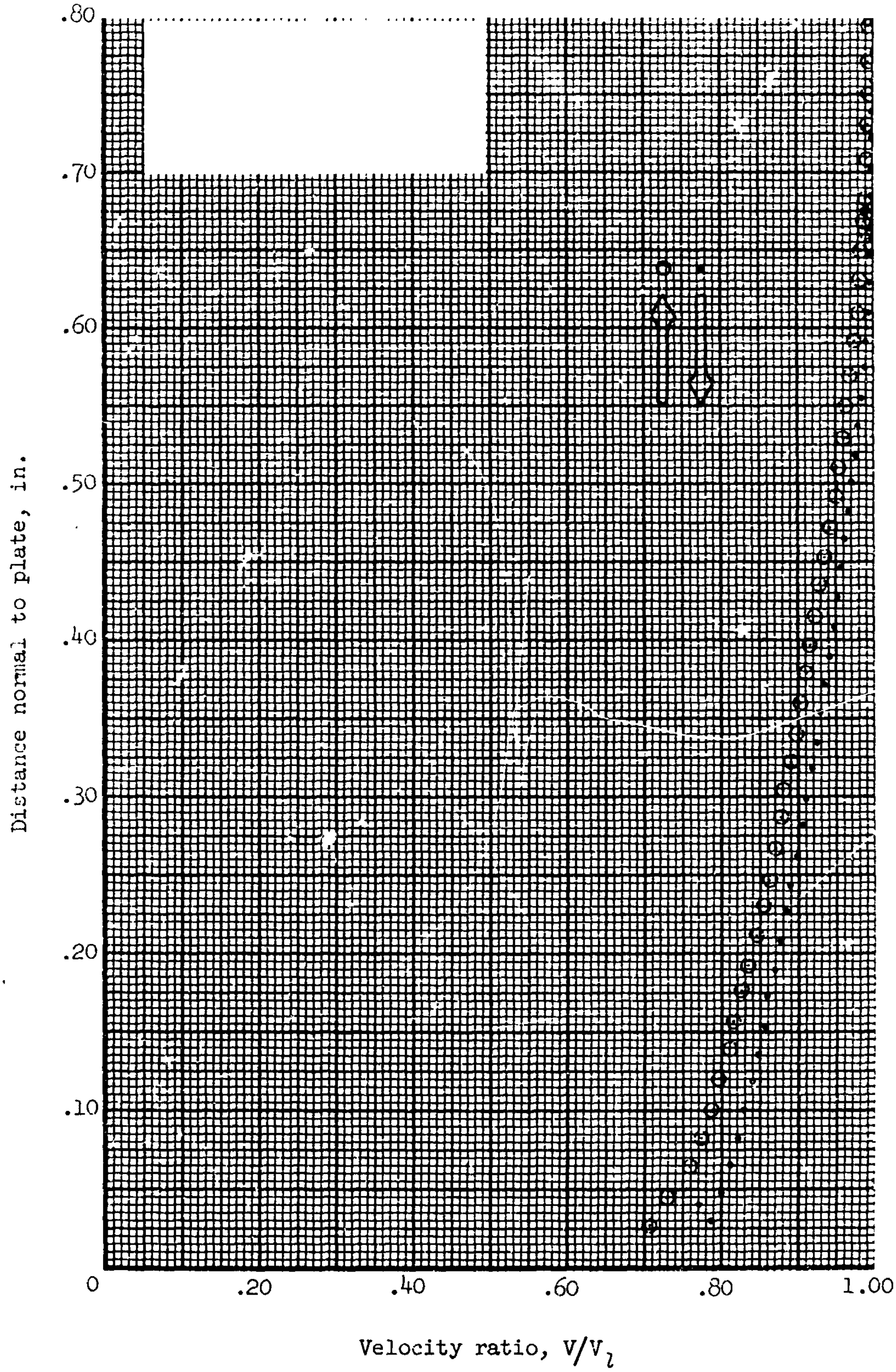

Figure 122.- Boundary-layer velocity distribution for run 6. All identifying conditions are given in table III. Arrows identify direction of probe travel across the boundary layer.

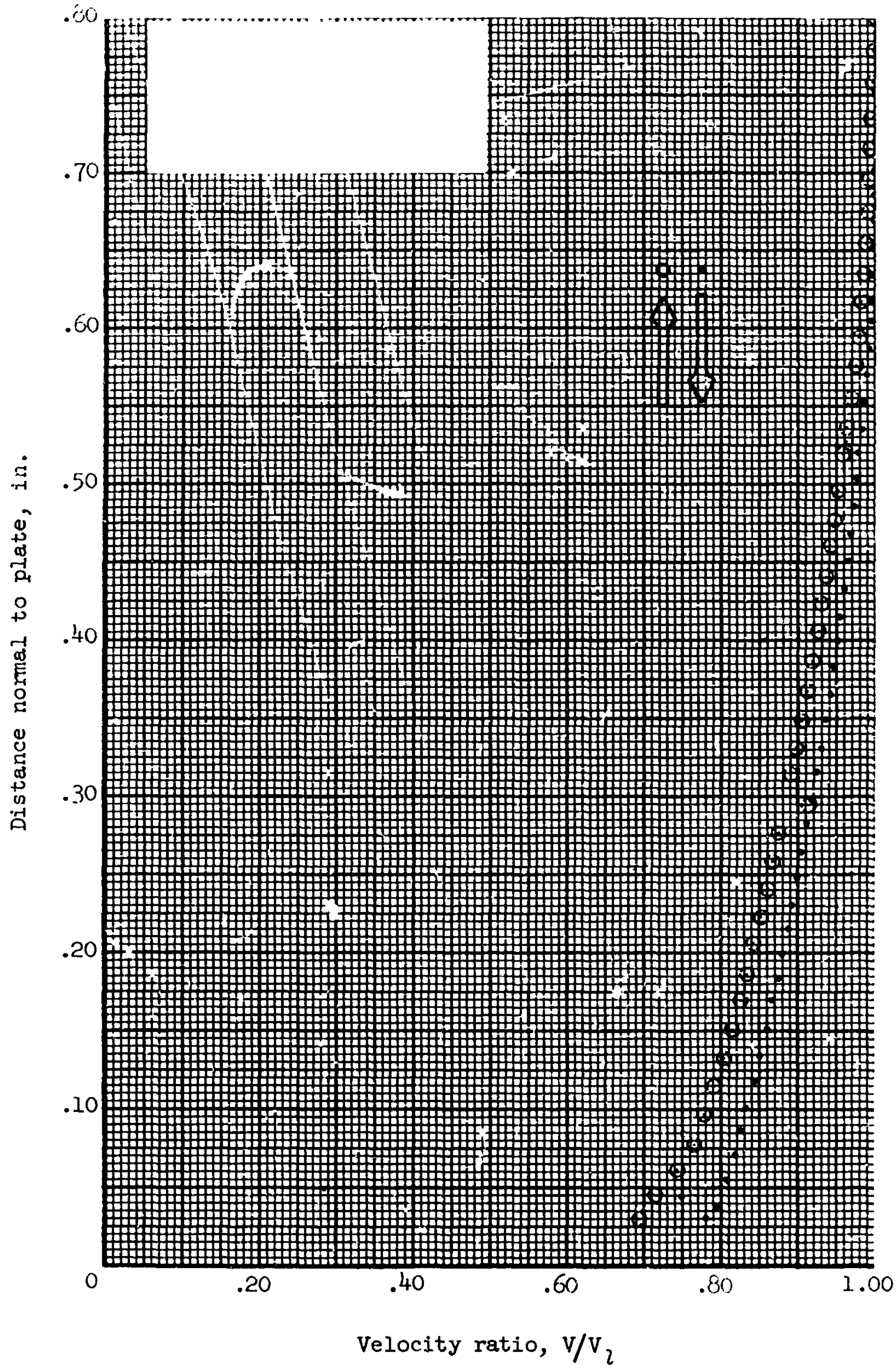

Figure 123.- Boundary-layer velocity distribution for run 7. All identifying conditions are given in table III. Arrows identify direction of probe travel across the boundary layer.

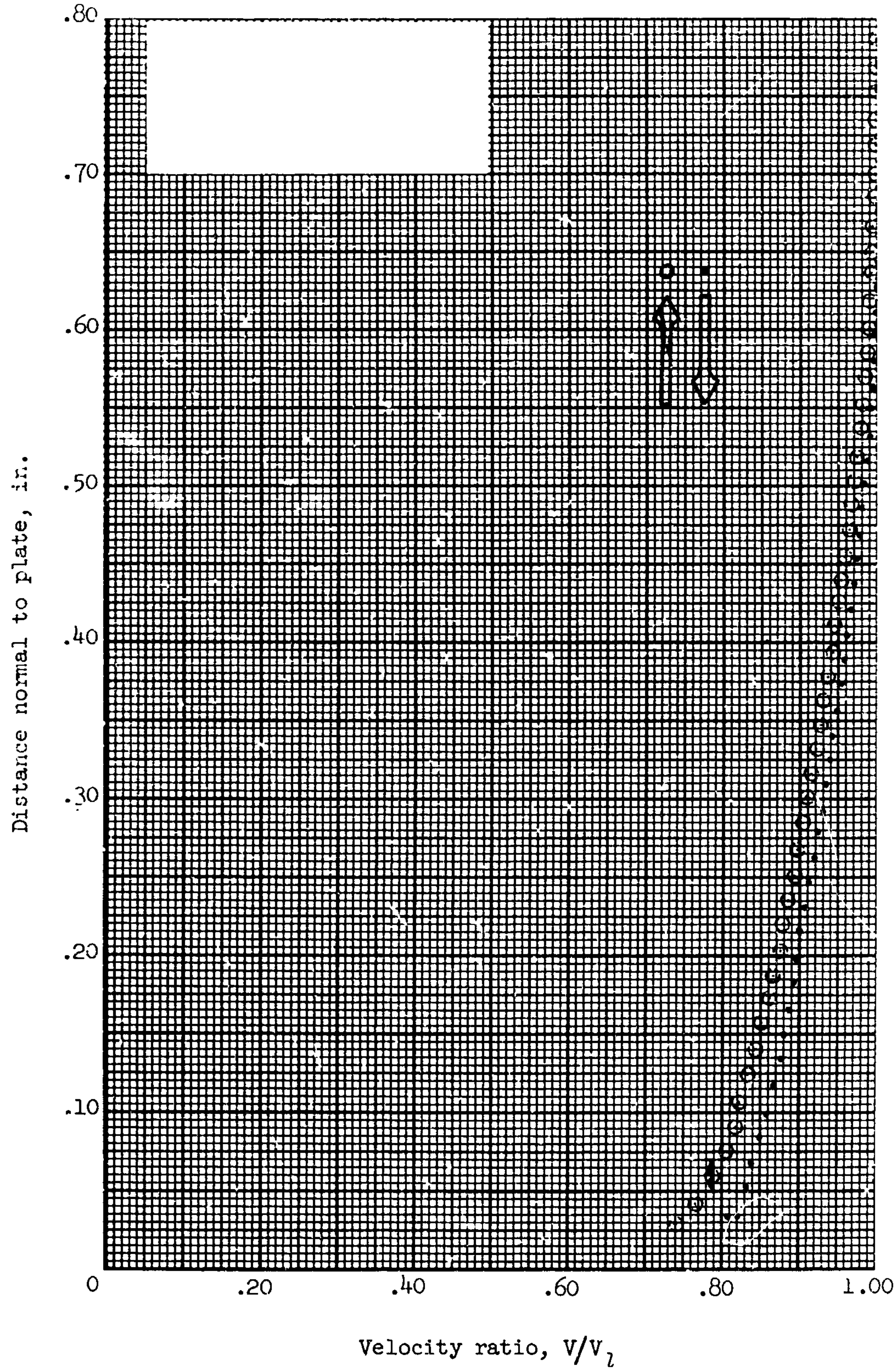

Figure 124.- Boundary-layer velocity distribution for run 8. All identifying conditions are given in table III. Arrows identify direction of probe travel across the boundary layer.

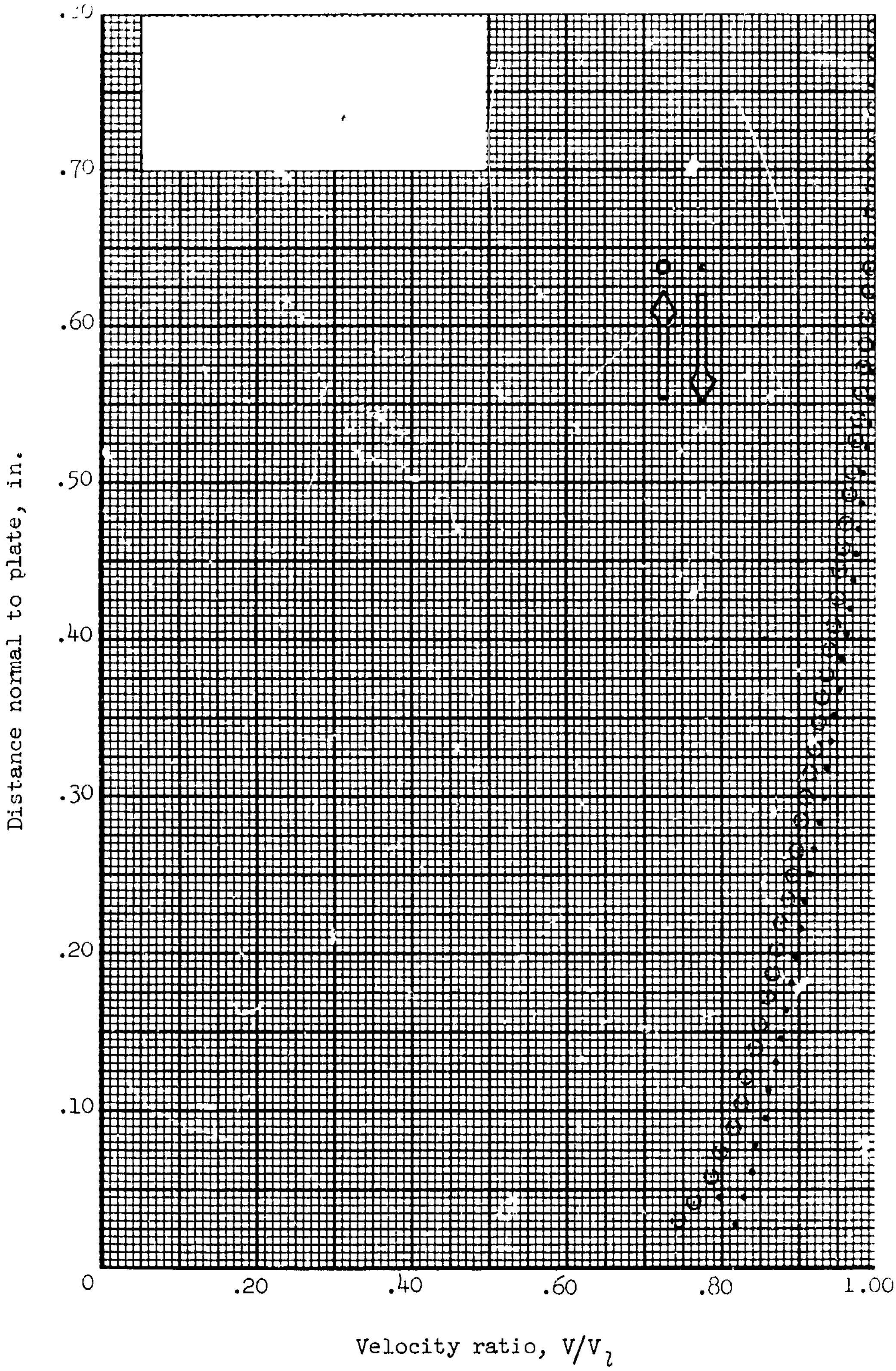

Figure 125.- Boundary-layer velocity distribution for run 9. All identifying conditions are given in table III. Arrows identify direction of probe travel across the boundary layer.

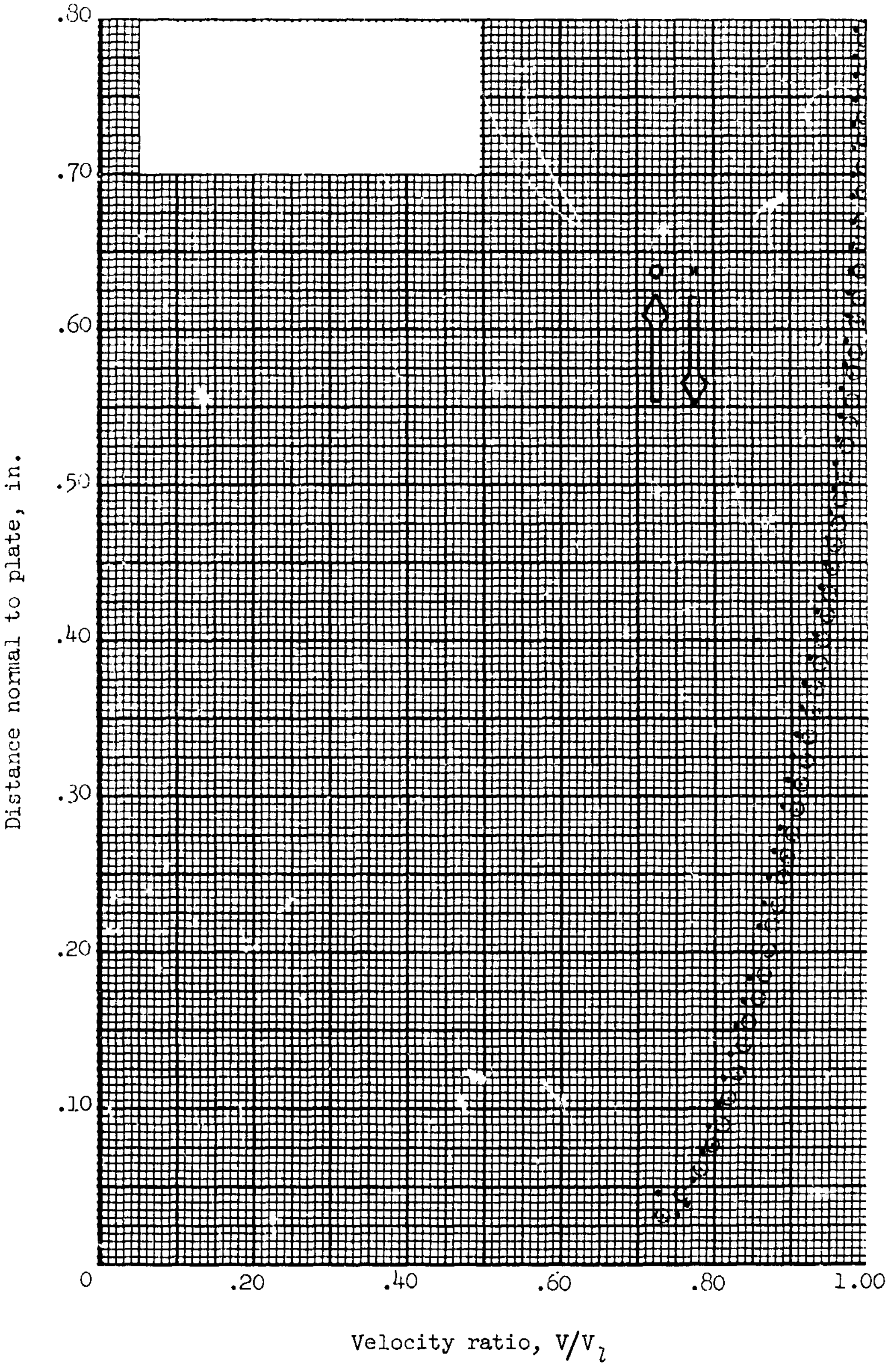

Figure 126.- Boundary-layer velocity distribution for run 10. All identifying conditions are given in table III. Arrows identify direction of probe travel across the boundary layer.

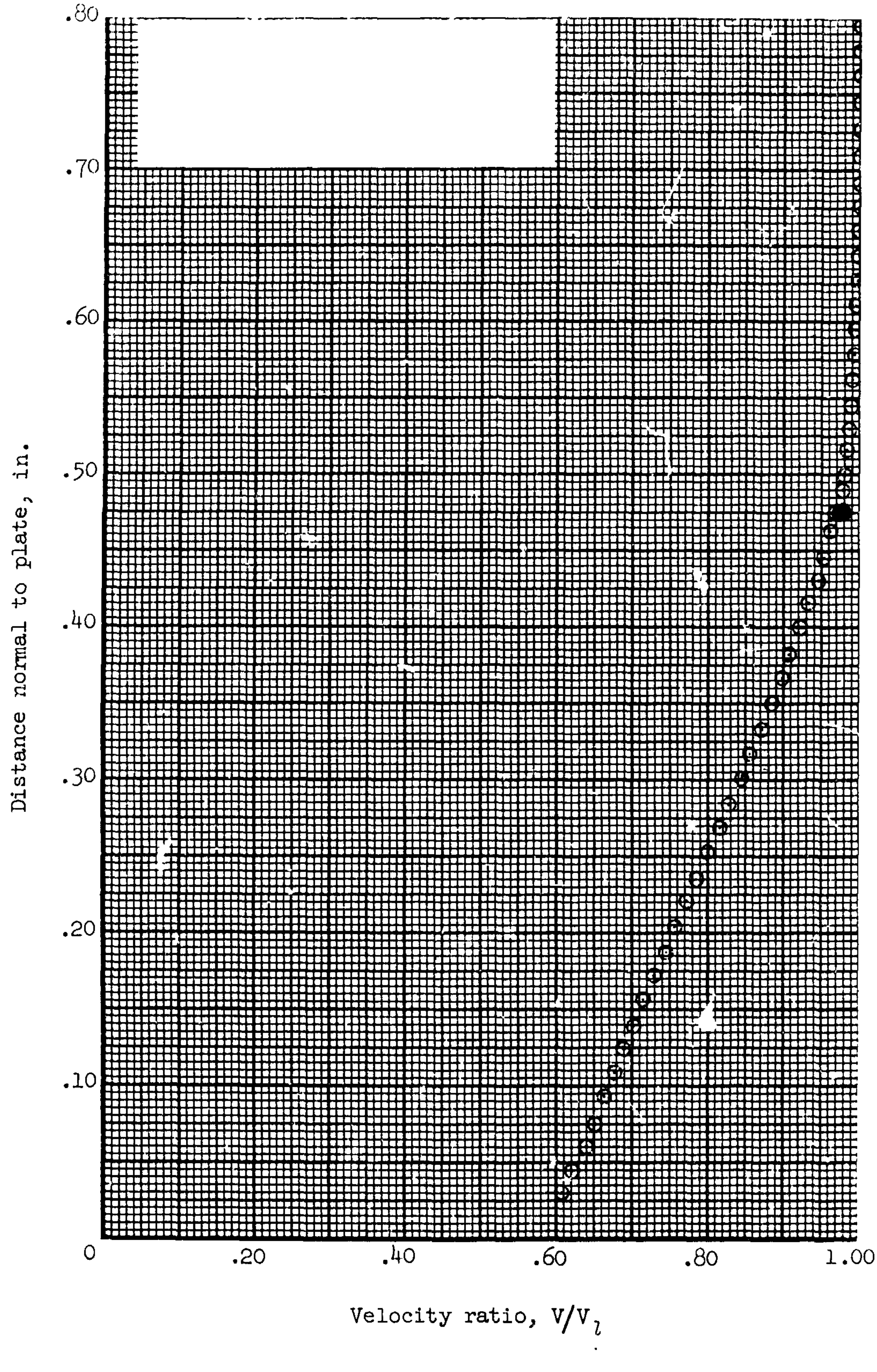

Figure 127.- Boundary-layer velocity distribution for run 11. All identifying conditions are given in table III. Data points at a distance from the plate of 0.475 inch indicate effect of time lag on values of the velocity ratio.

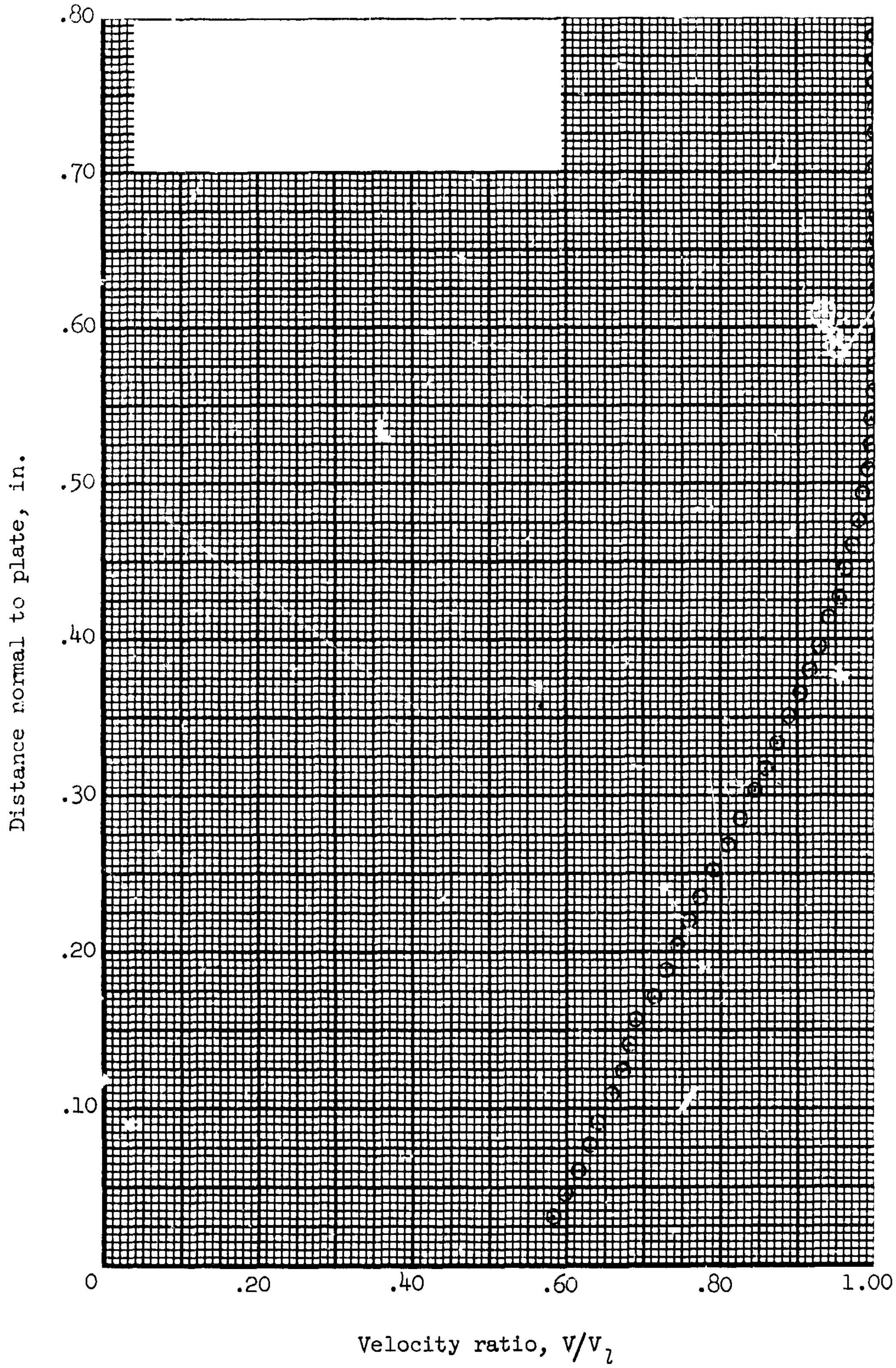

Figure 128.- Boundary-layer velocity distribution for run 12. All identifying conditions are given in table III.

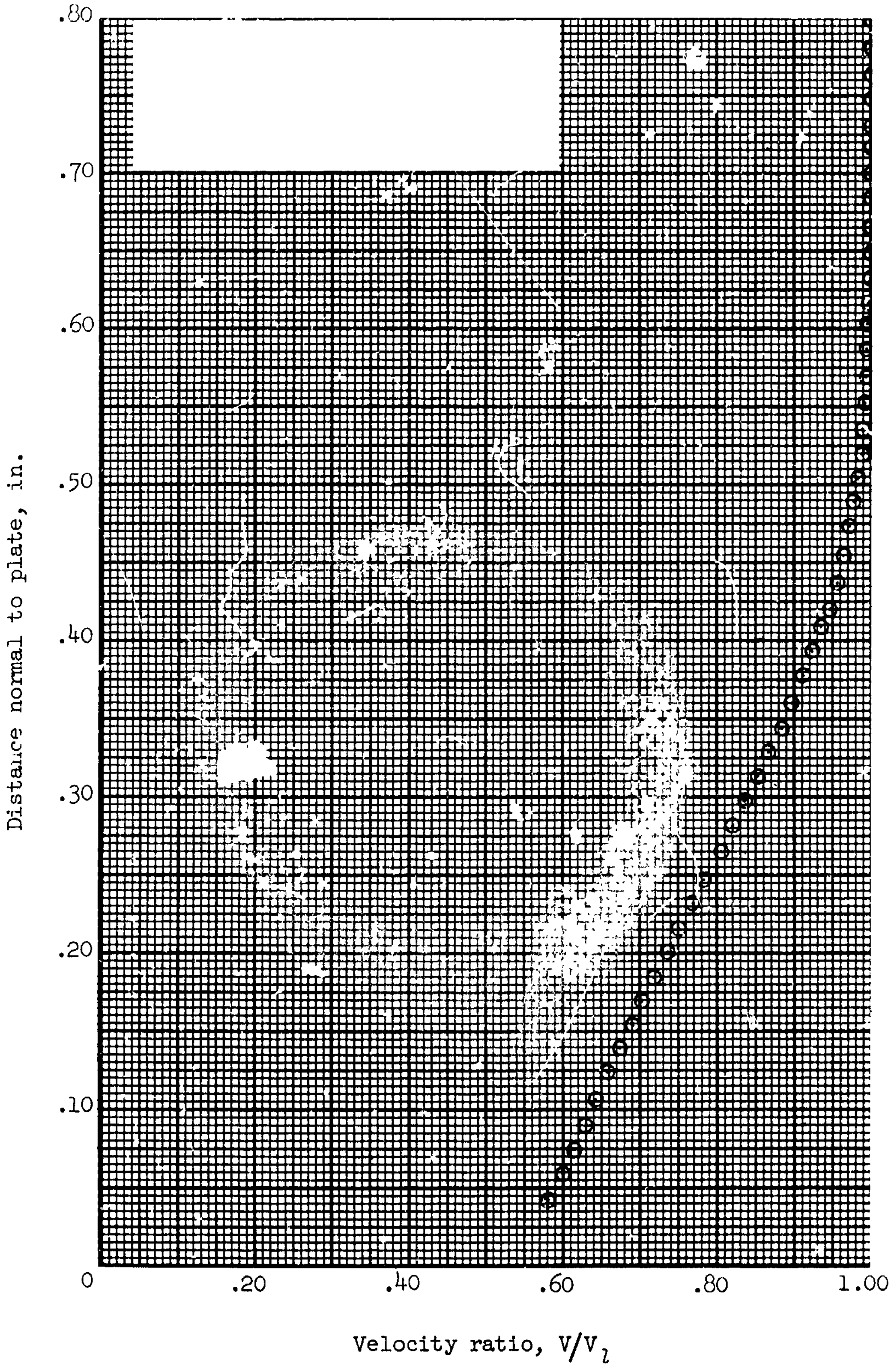

Figure 129.- Boundary-layer velocity distribution for run 13. All identifying conditions are given in table III.

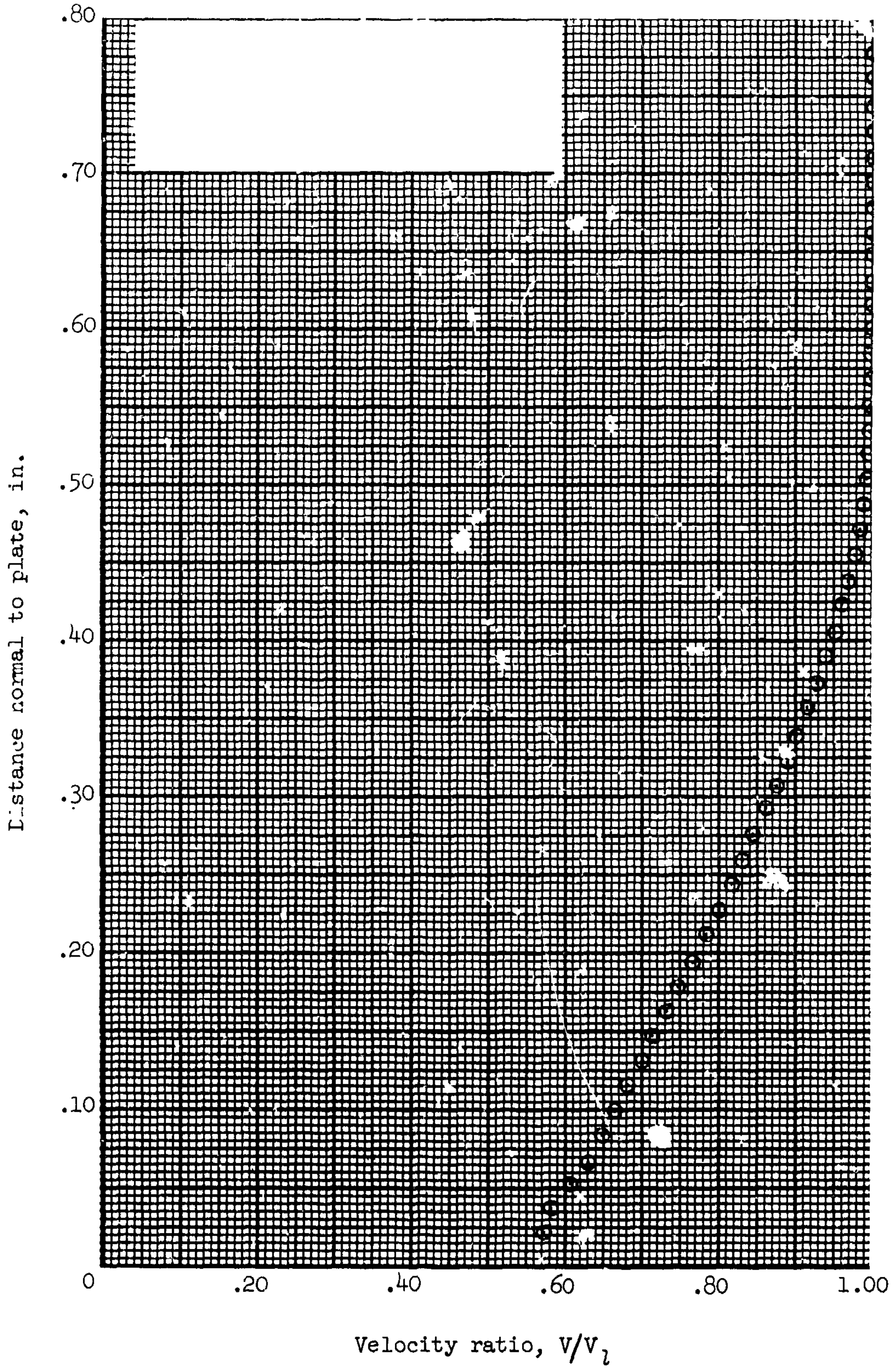

Figure 130.- Boundary-layer velocity distribution for run 14. All identifying conditions are given in table III.

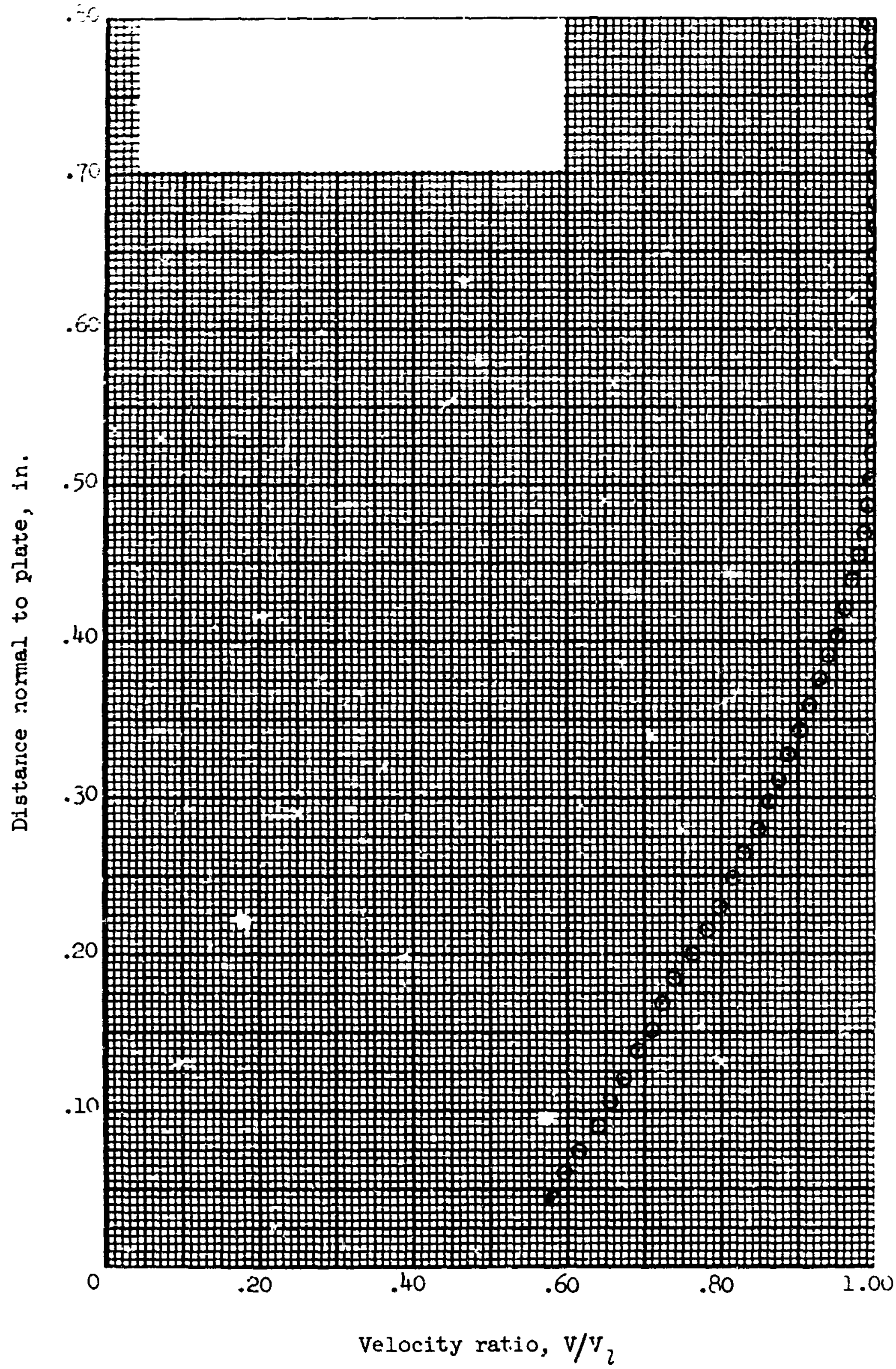

Figure 131.- Boundary-layer velocity distribution for run 15. All identifying conditions are given in table III.

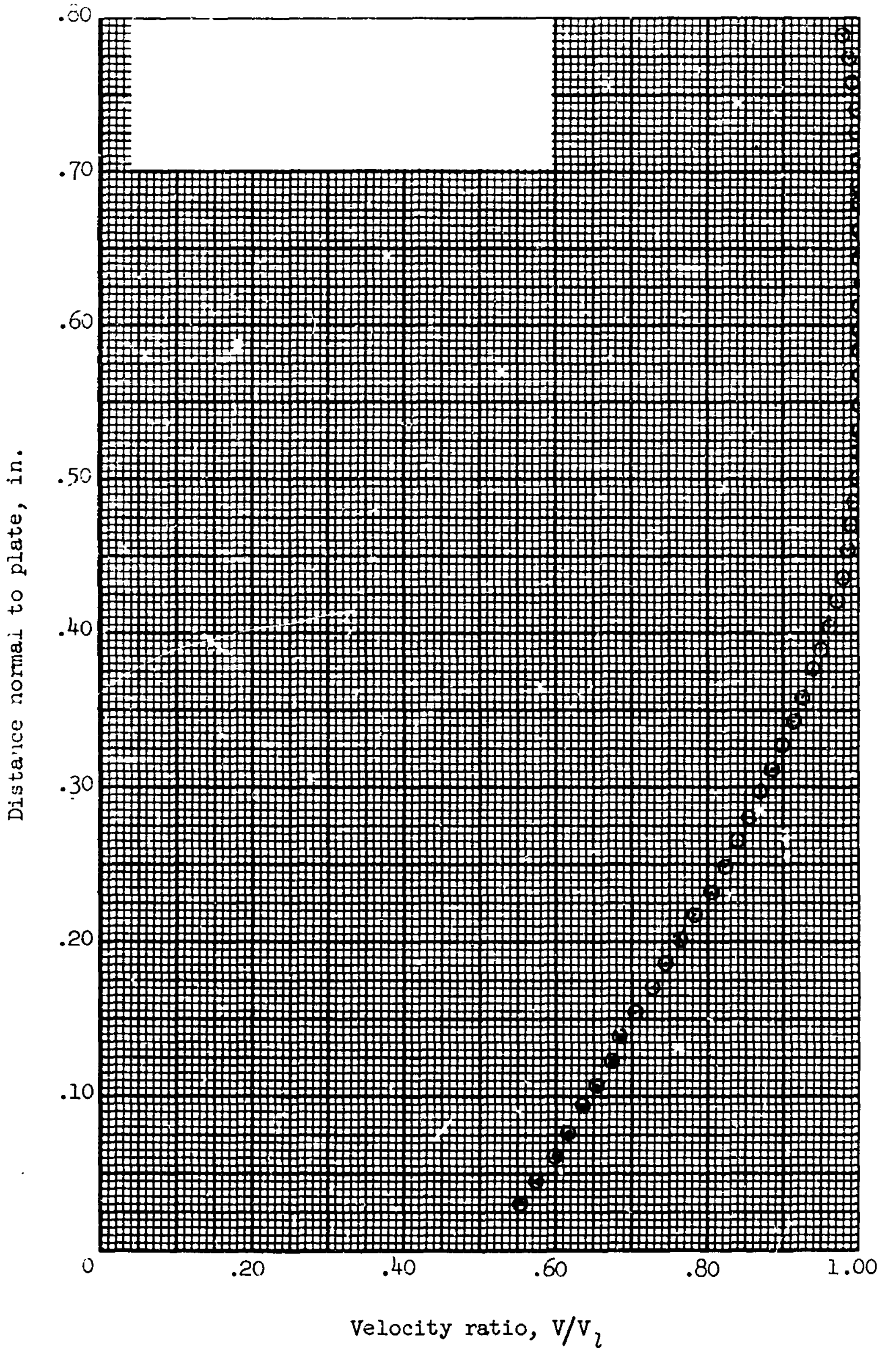

Figure 132.- Boundary-layer velocity distribution for run 16. All identifying conditions are given in table III.

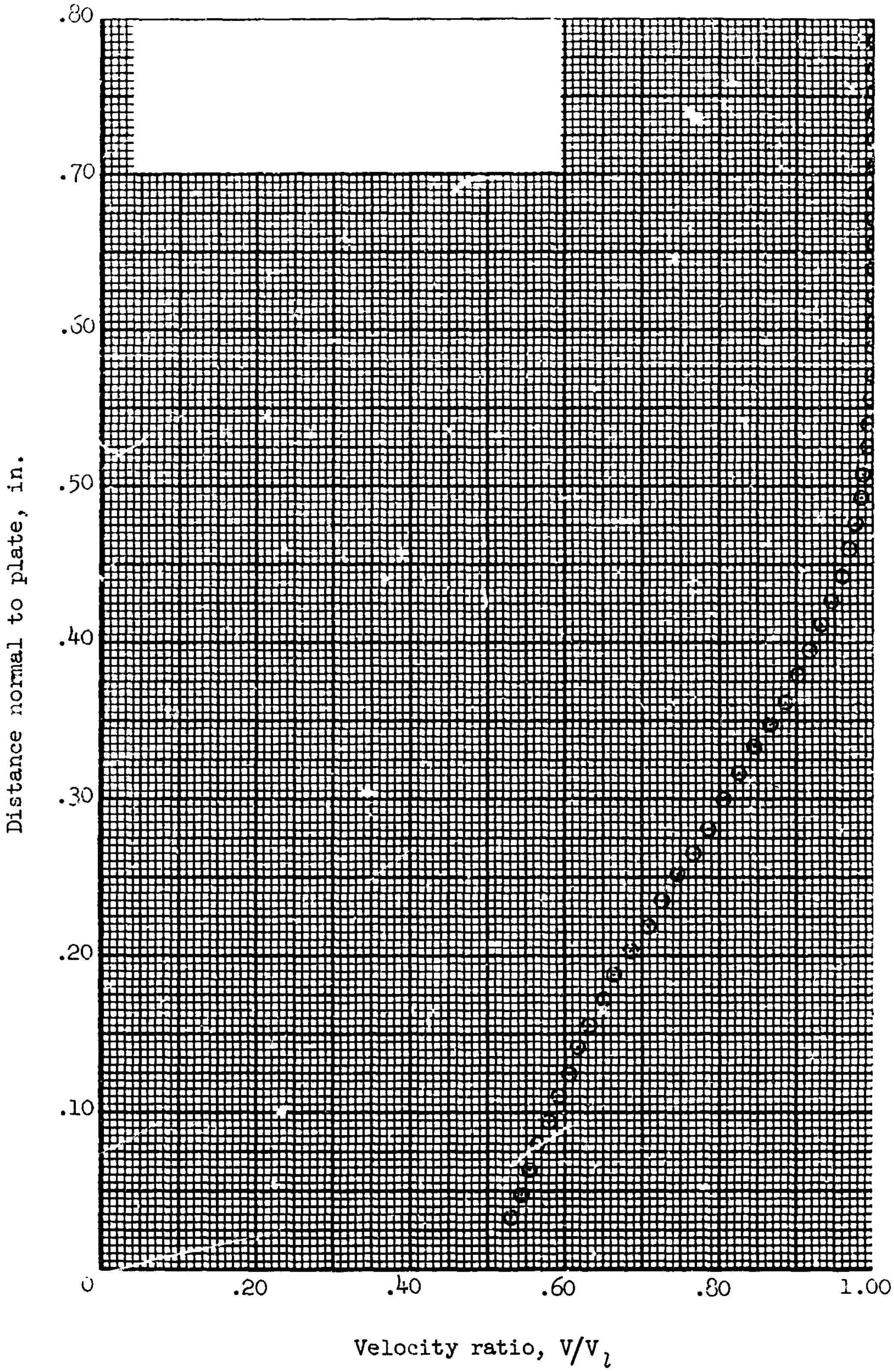

Figure 133.- Boundary-layer velocity distribution for run 17. All identifying conditions are given in table III.

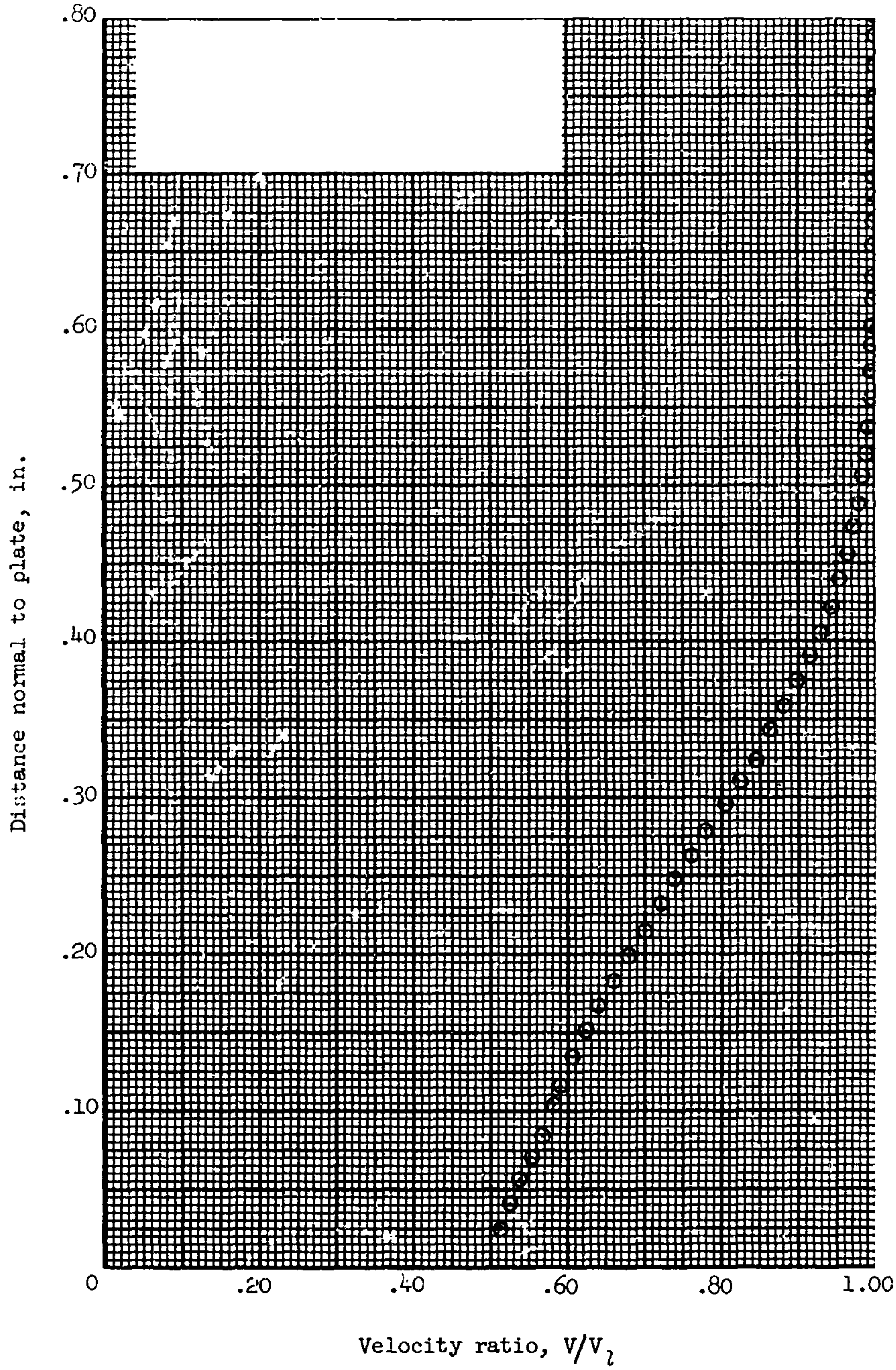

Figure 134.- Boundary-layer velocity distribution for run 18. All identifying conditions are given in table III.

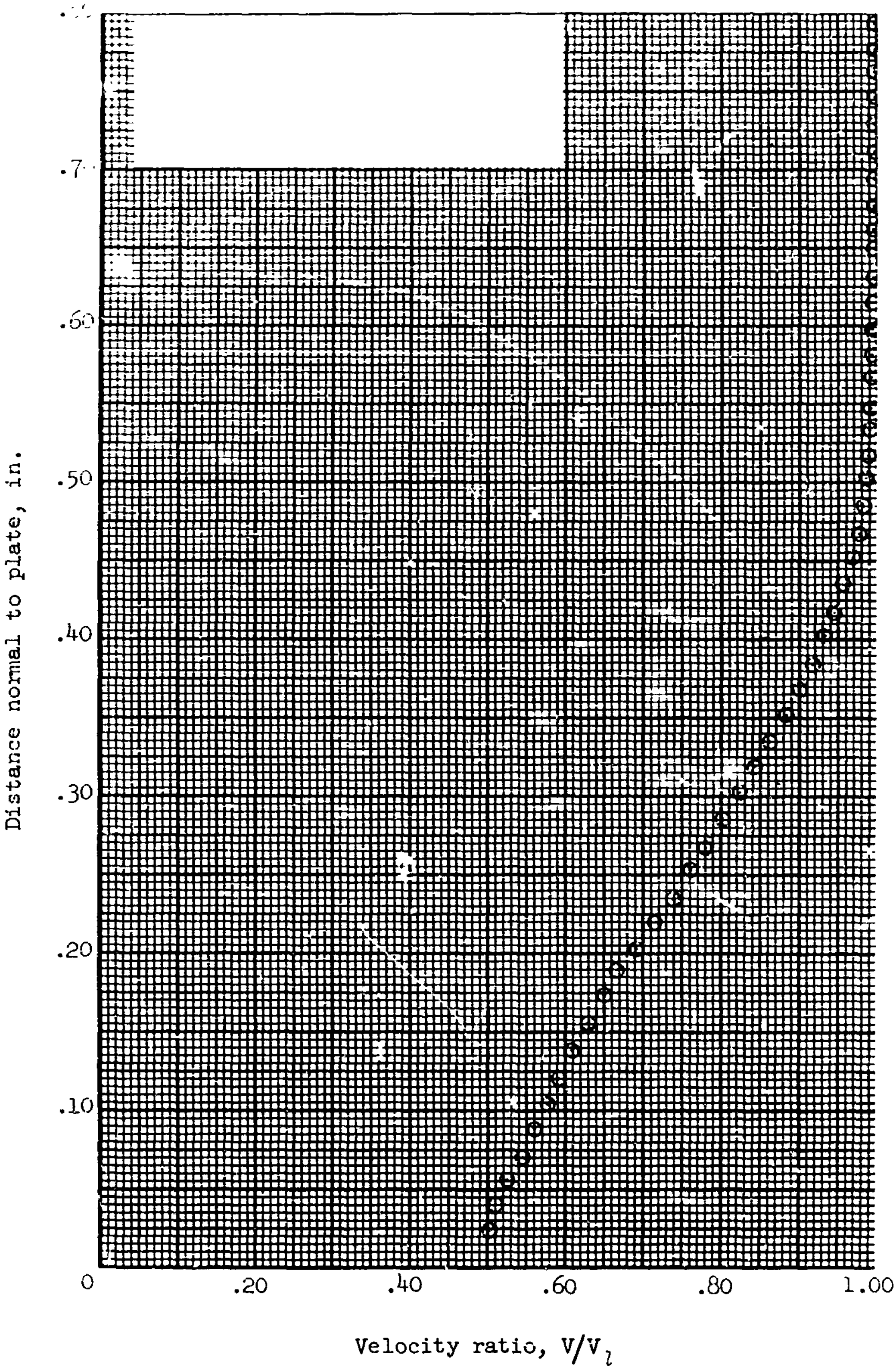

Figure 135.- Boundary-layer velocity distribution for run 19. All identifying conditions are given in table III.

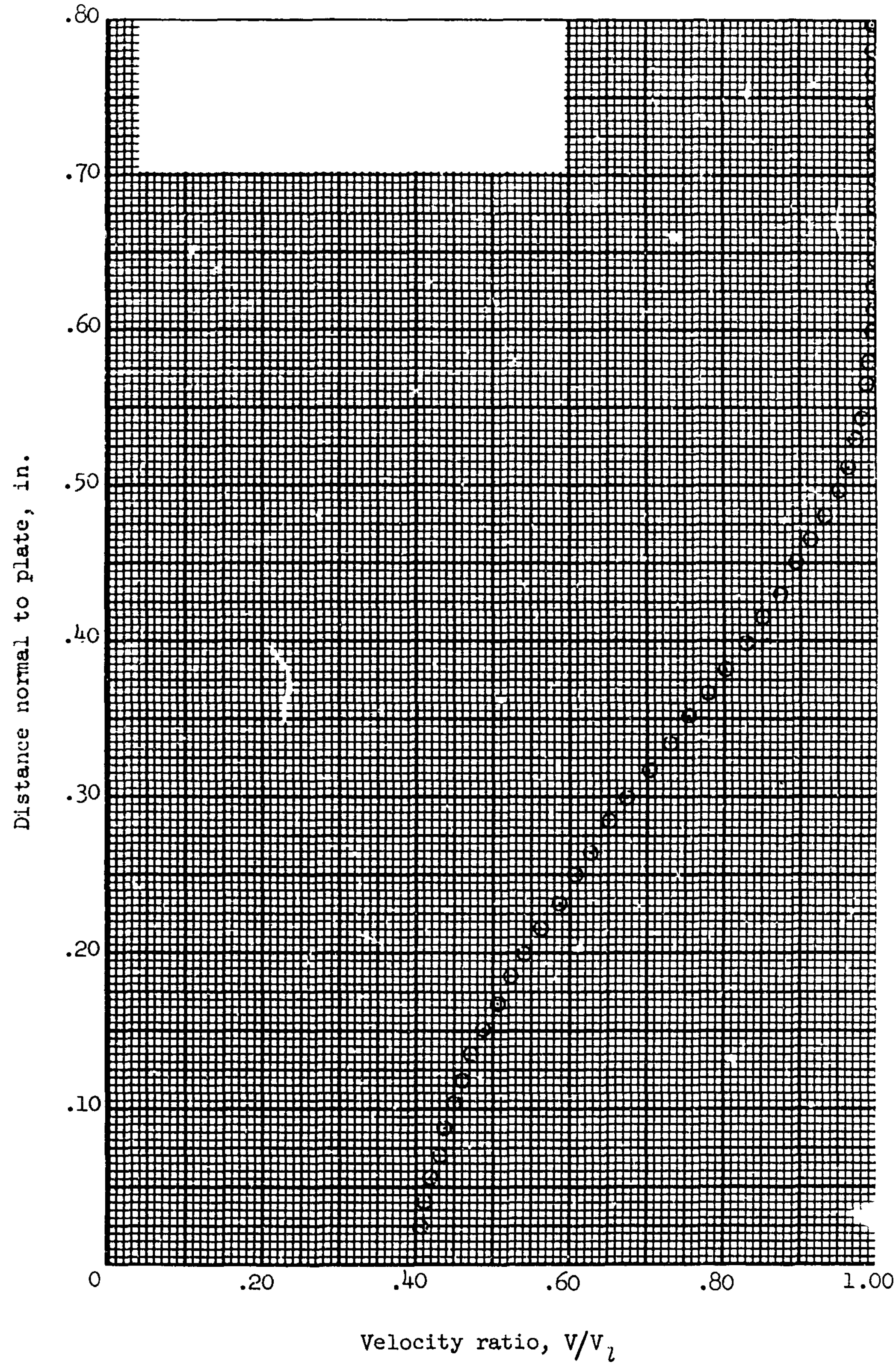

Figure 136.- Boundary-layer velocity distribution for run 20. All identifying conditions are given in table III.

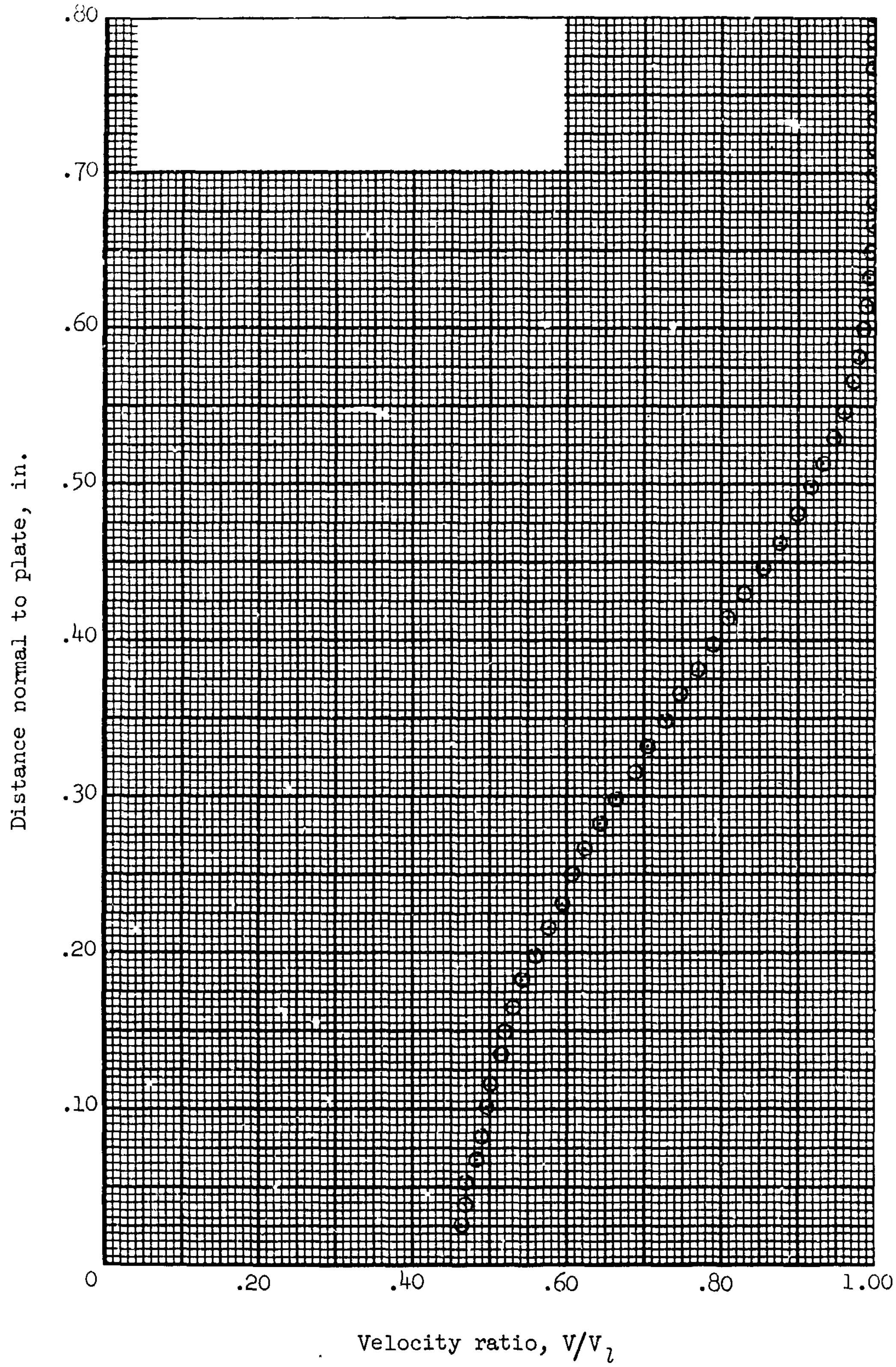

Figure 137.- Boundary-layer velocity distribution for run 21. All identifying conditions are given in table III.

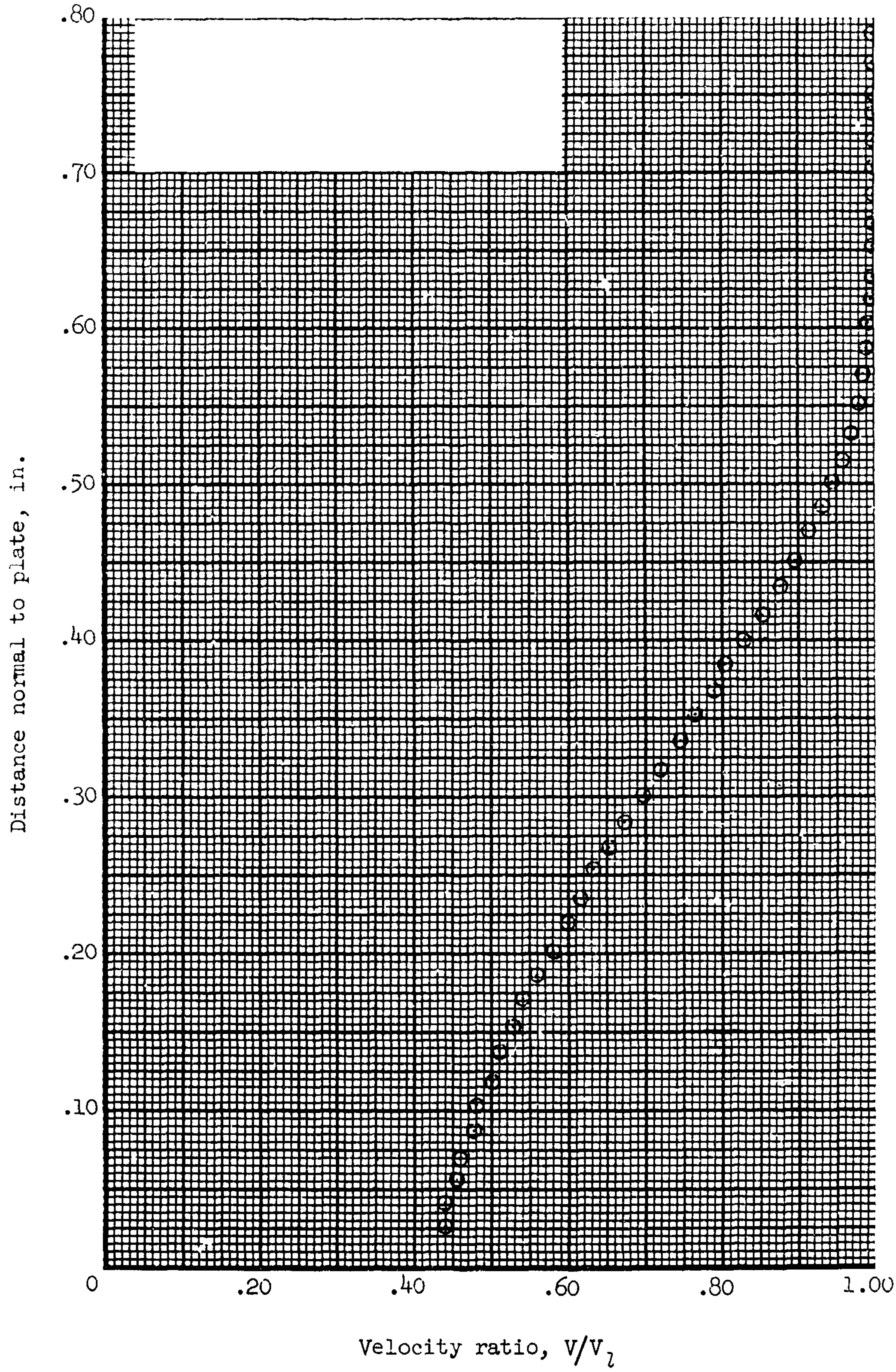

Figure 138.- Boundary-layer velocity distribution for run 22. All identifying conditions are given in table III.

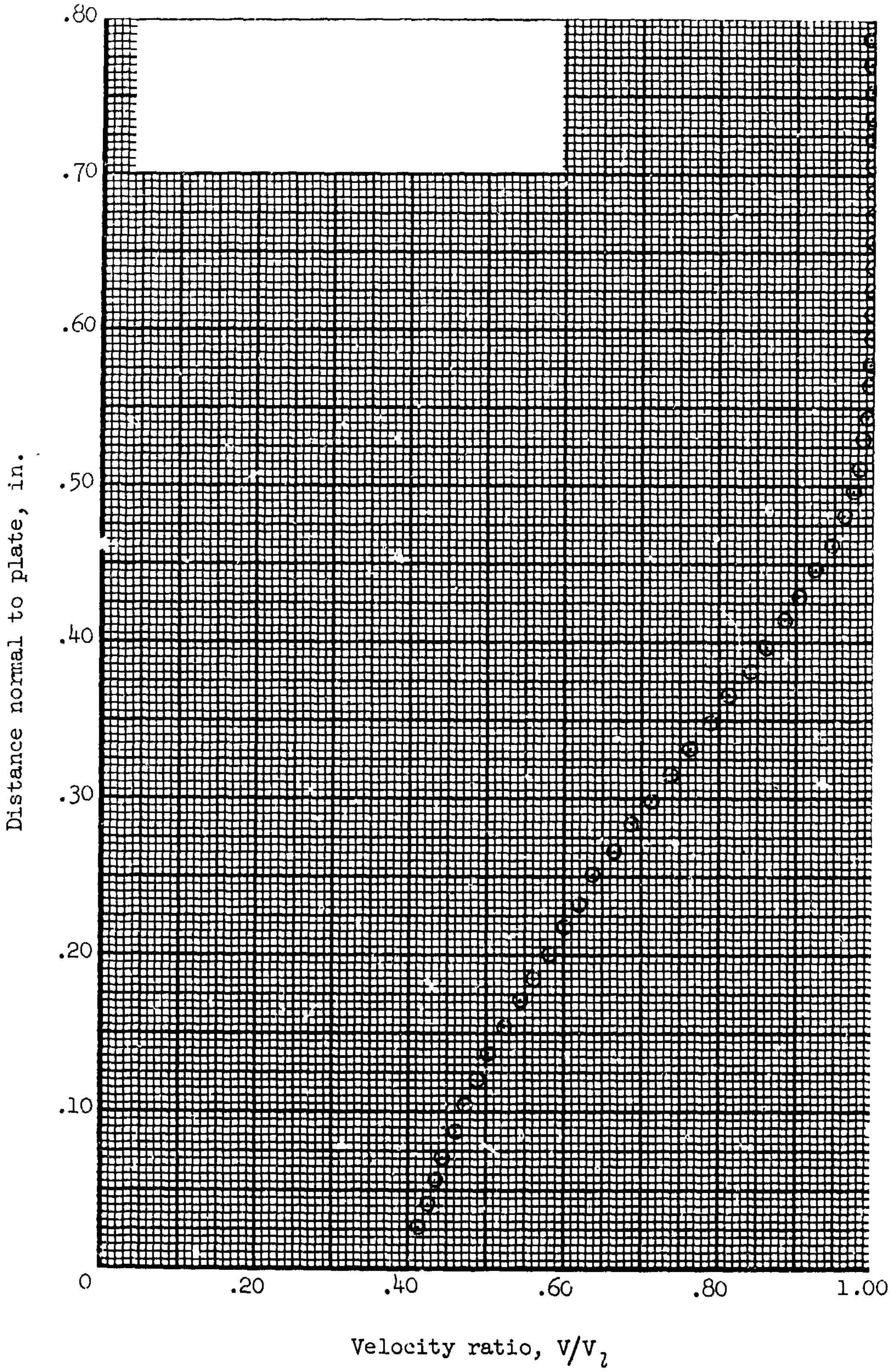

Figure 139.- Boundary-layer velocity distribution for run 23. All identifying conditions are given in table III.

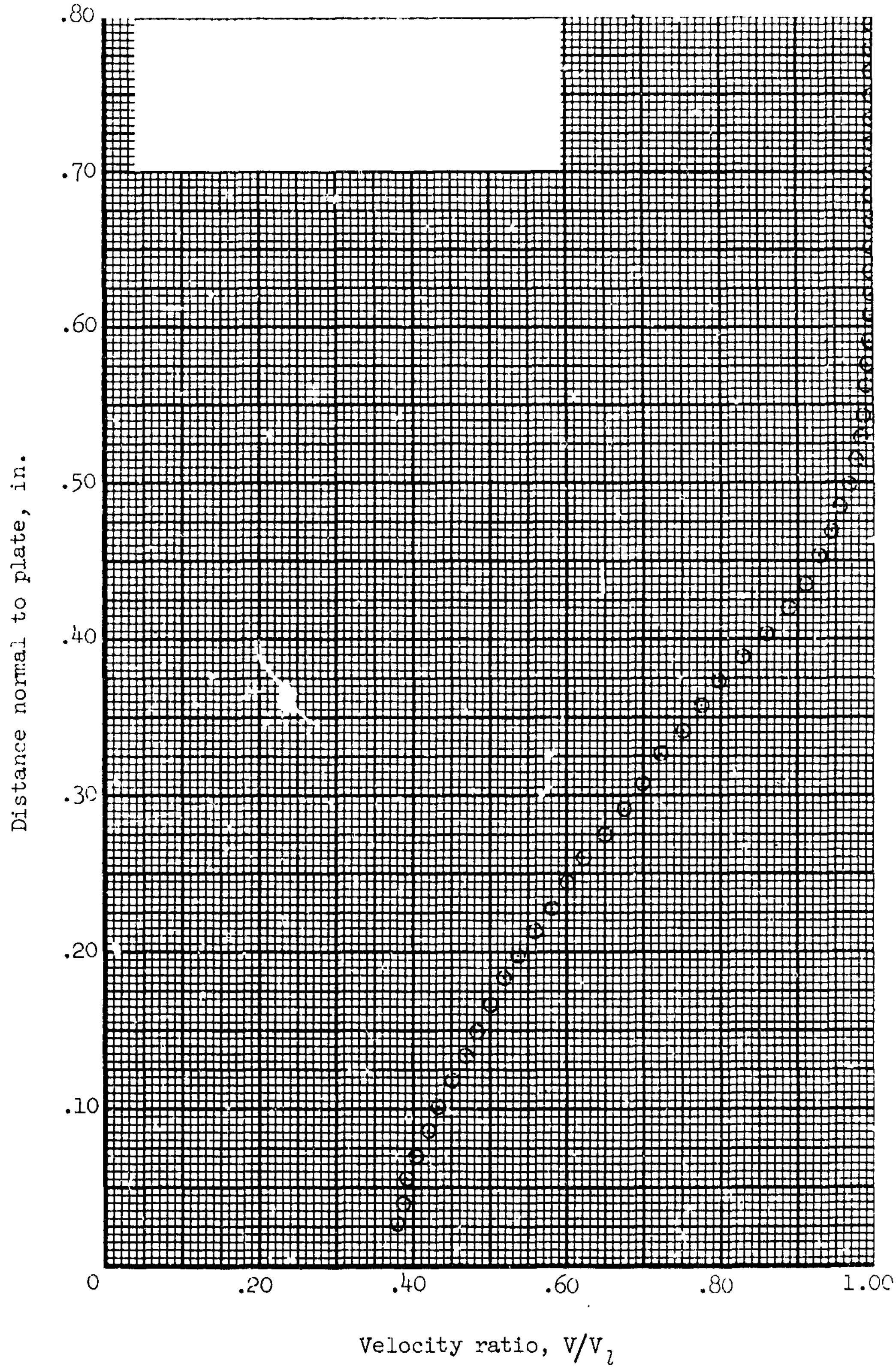

Figure 140.- Boundary-layer velocity distribution for run 24. All identifying conditions are given in table III.

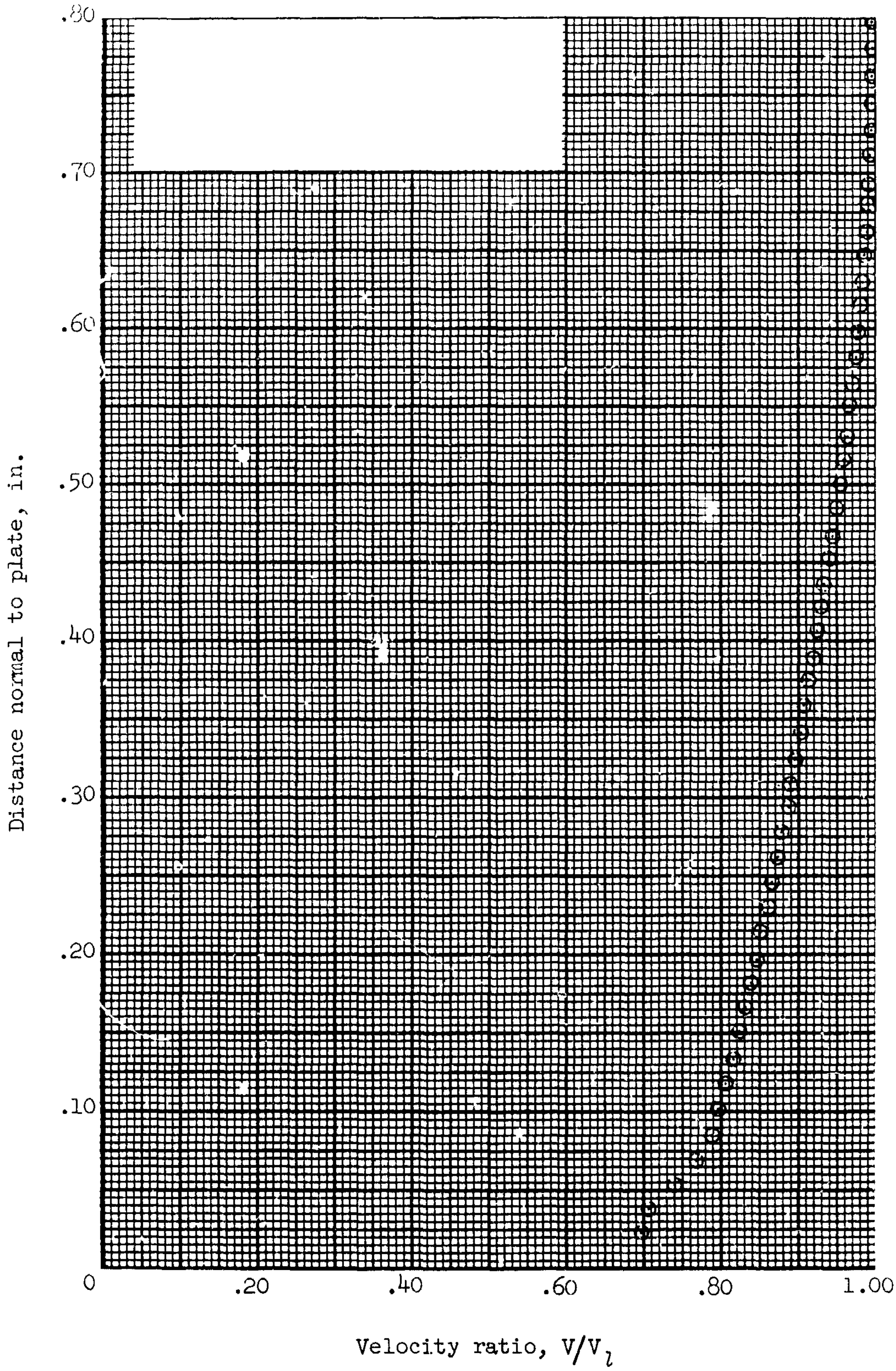

Figure 141.- Boundary-layer velocity distribution for run 25. All identifying conditions are given in table III.

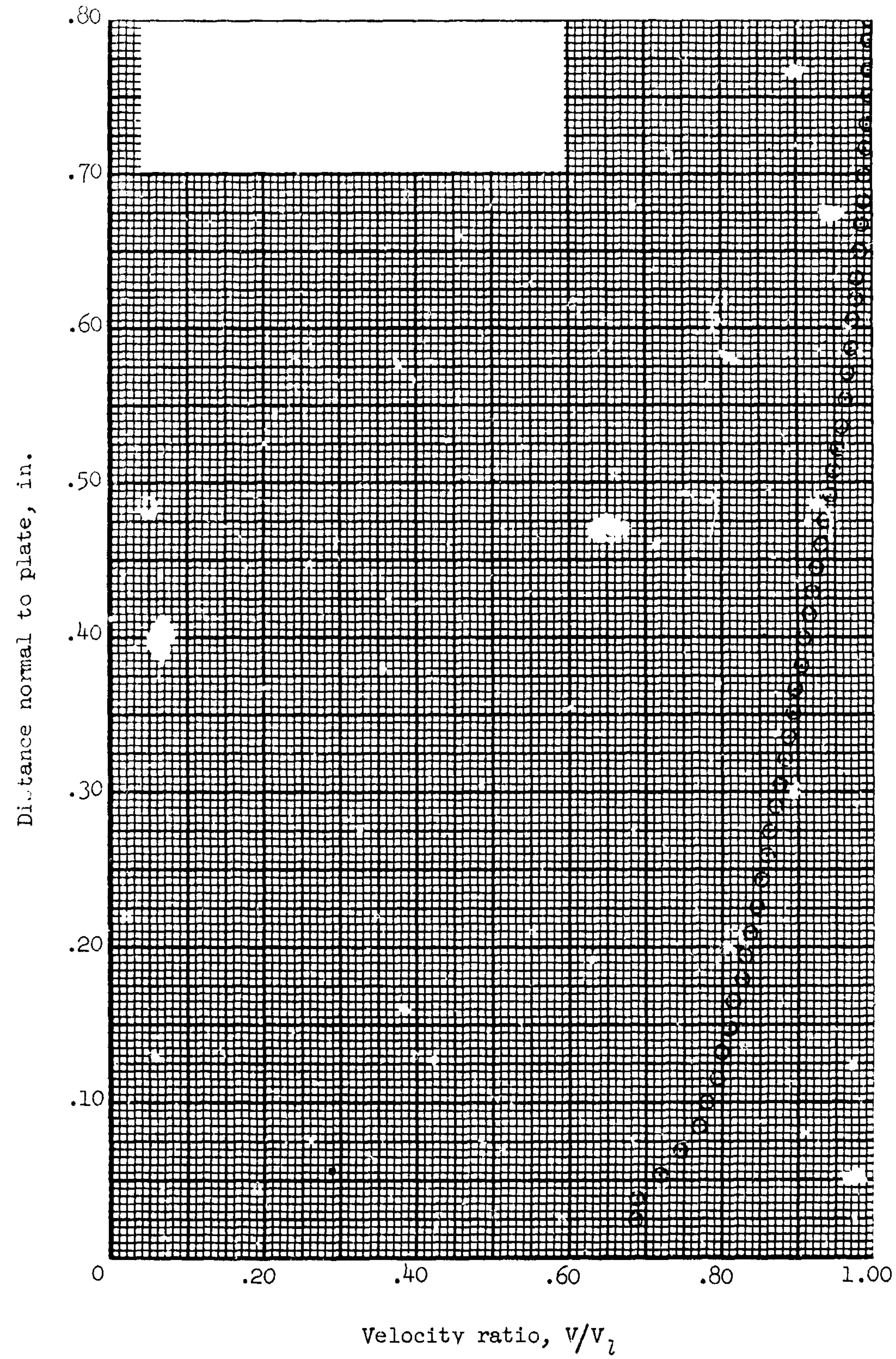

Figure 142.- Boundary-layer velocity distribution for run 26. All identifying conditions are given in table III.

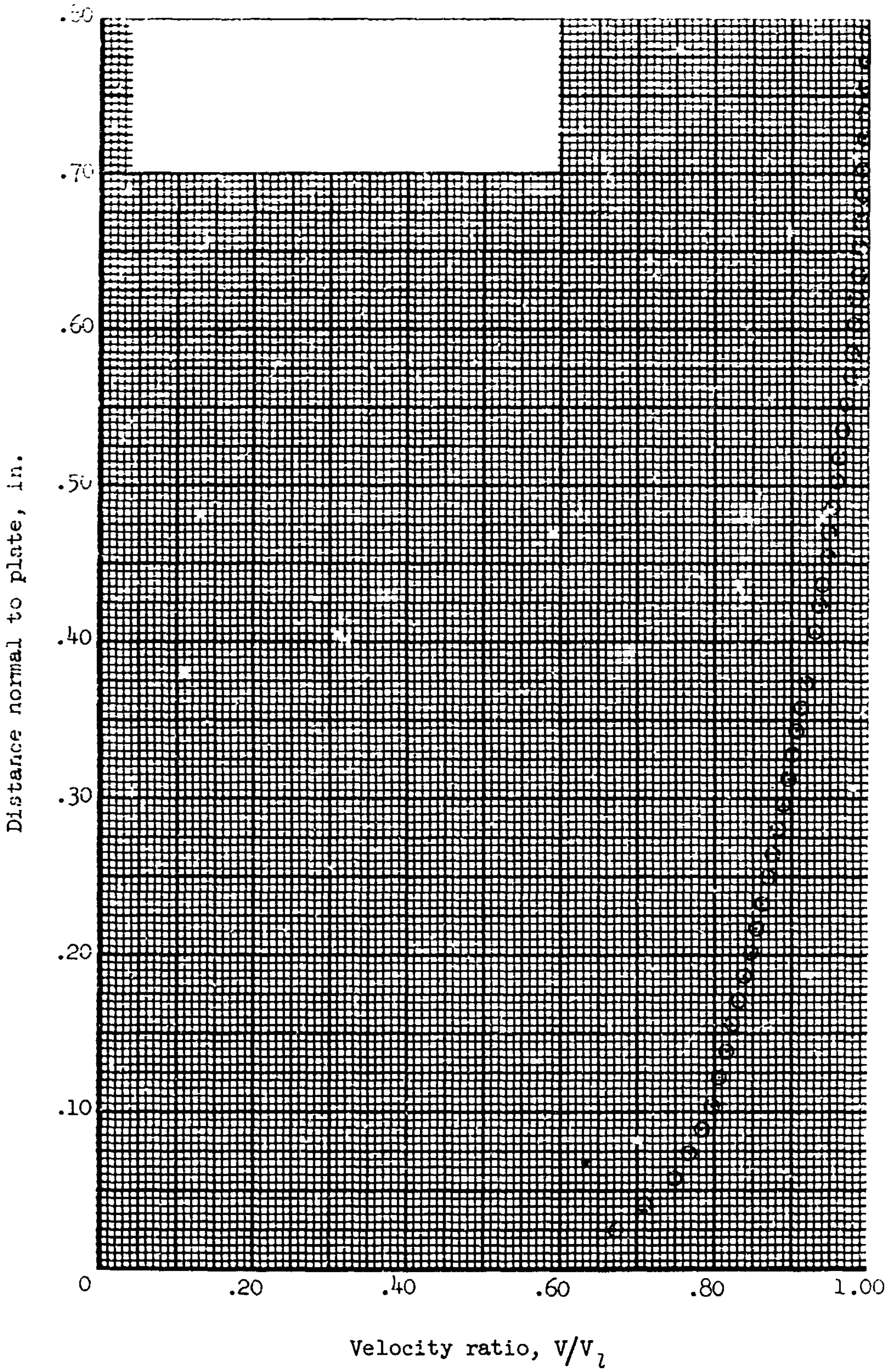

Figure 143.- Boundary-layer velocity distribution for run 27. All identifying conditions are given in table III.

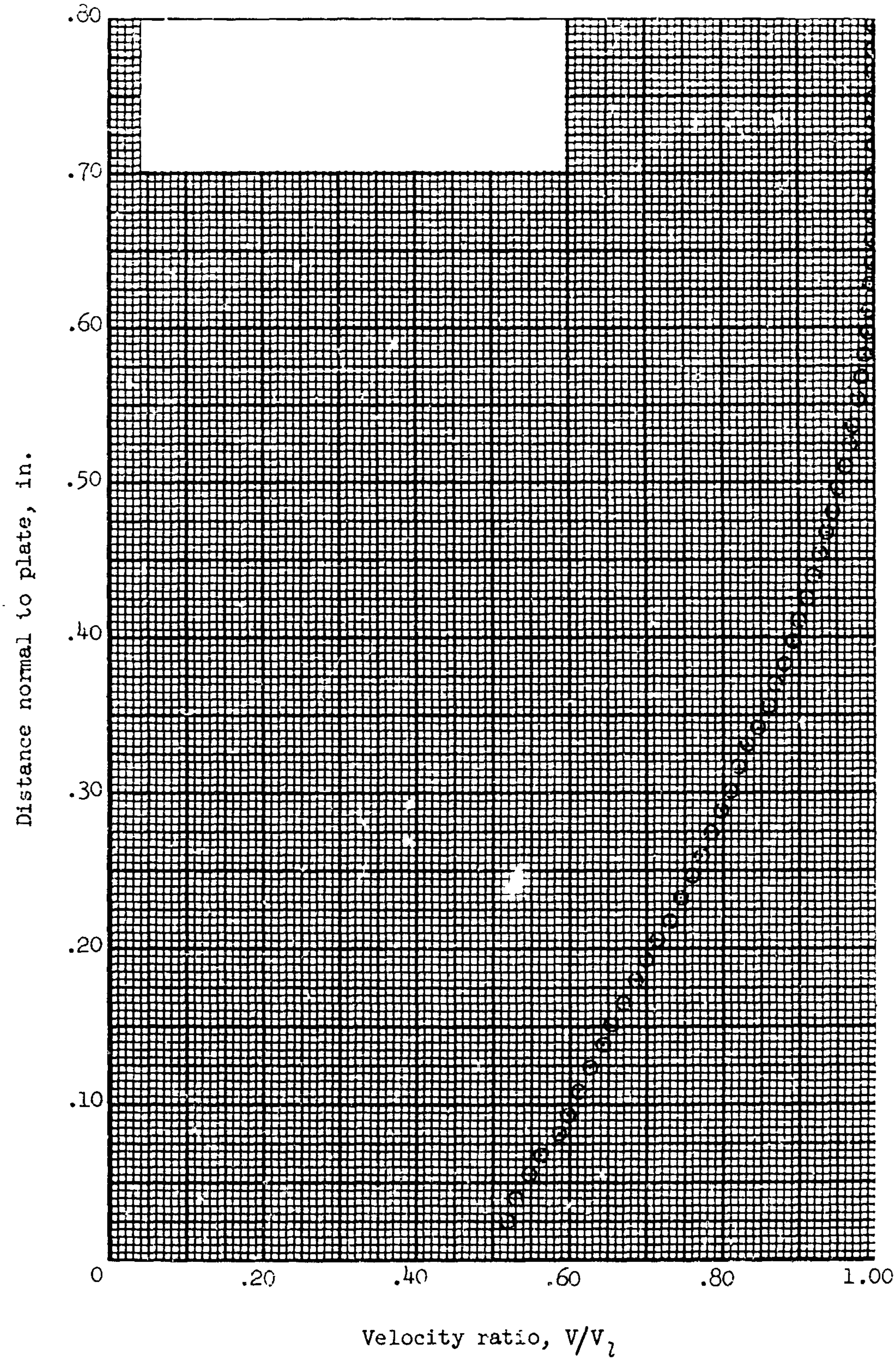

Figure 144.- Boundary-layer velocity distribution for run 28. All identifying conditions are given in table III.

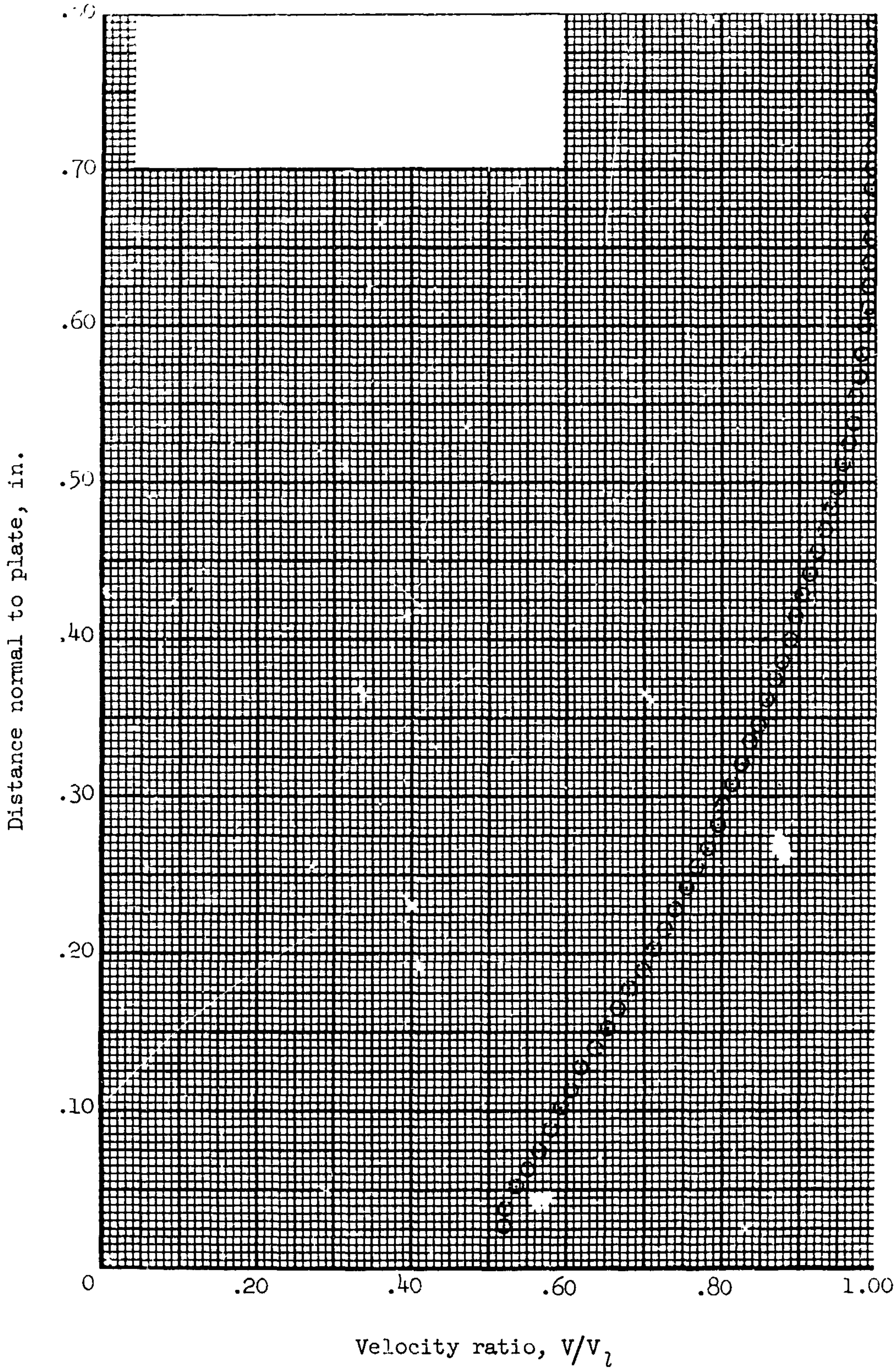

Figure 145.- Boundary-layer velocity distribution for run 29. All identifying conditions are given in table III.

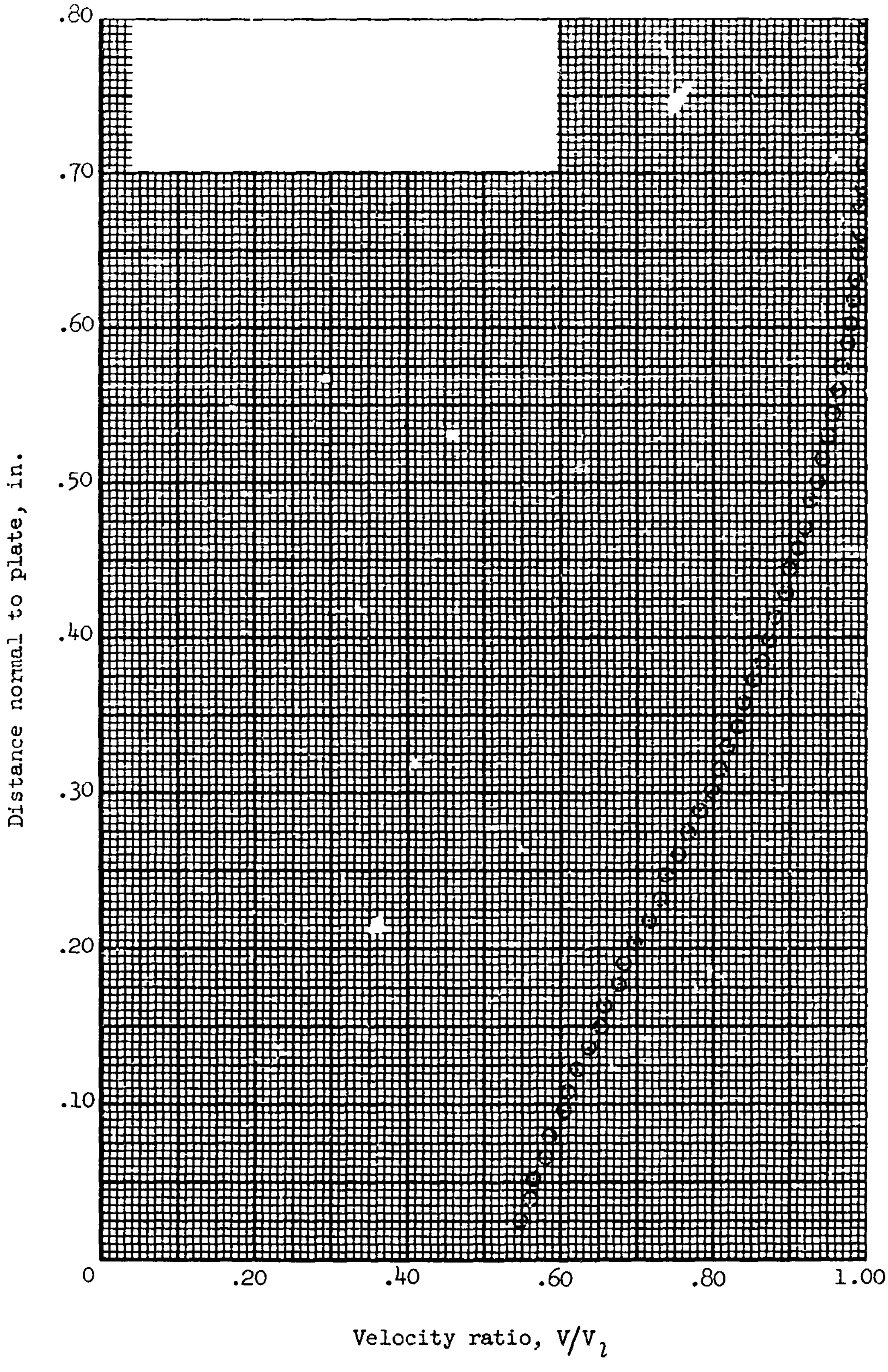

Figure 146.- Boundary-layer velocity distribution for run 30. All identifying conditions are given in table III.

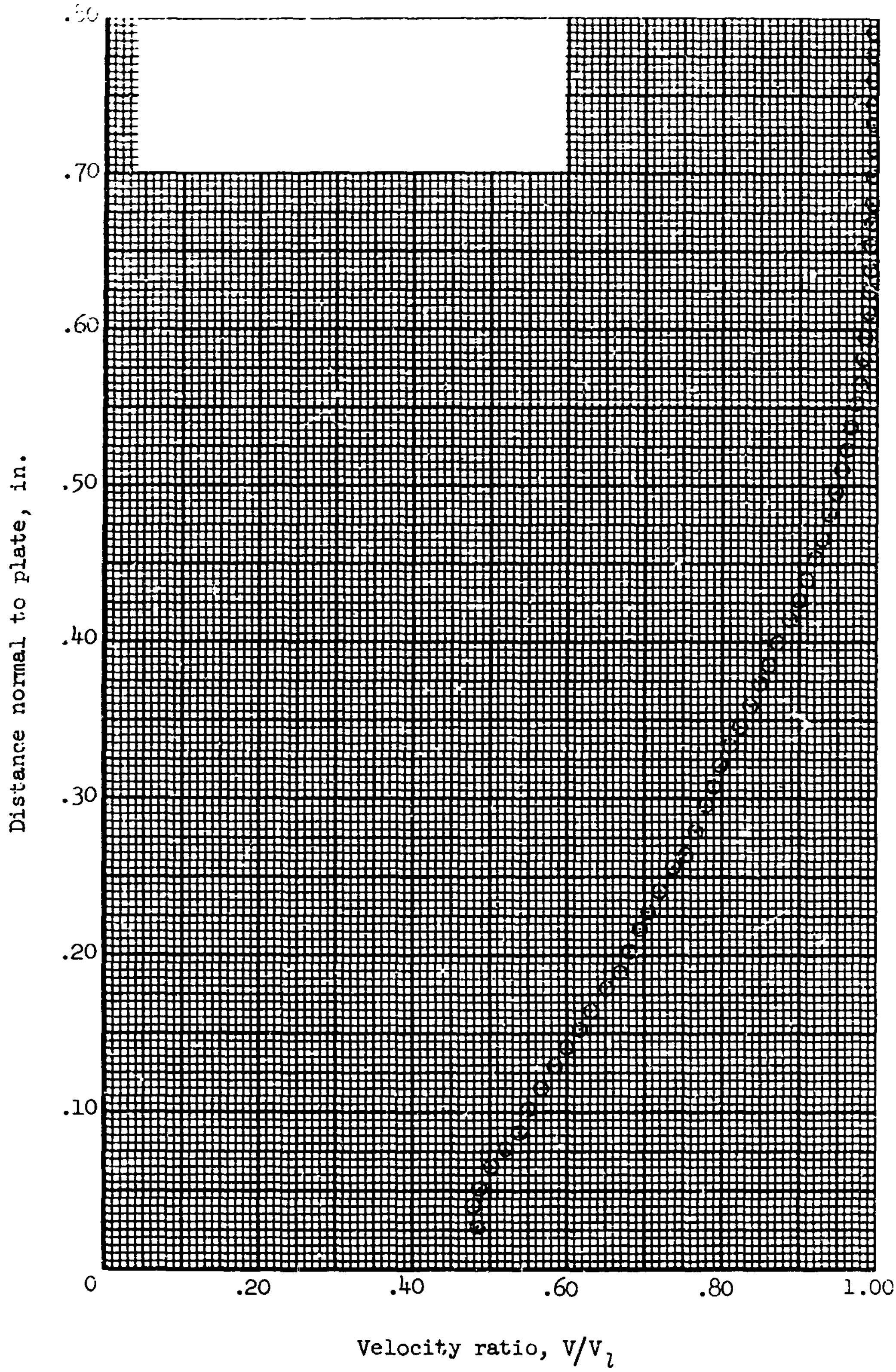

Figure 147.- Boundary-layer velocity distribution for run 31. All identifying conditions are given in table III.

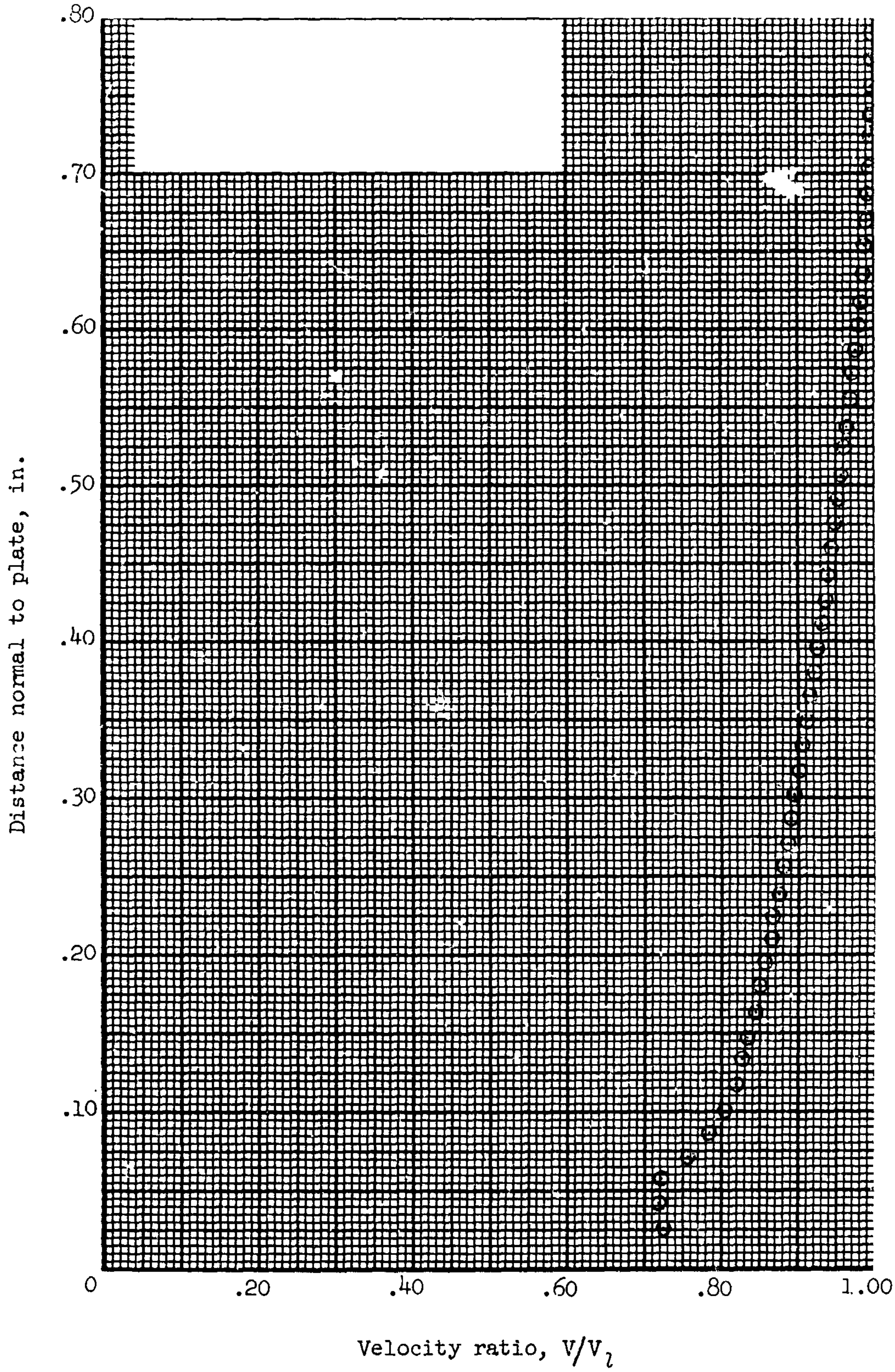

Figure 148.- Boundary-layer velocity distribution for run 42. All identifying conditions are given in table III.

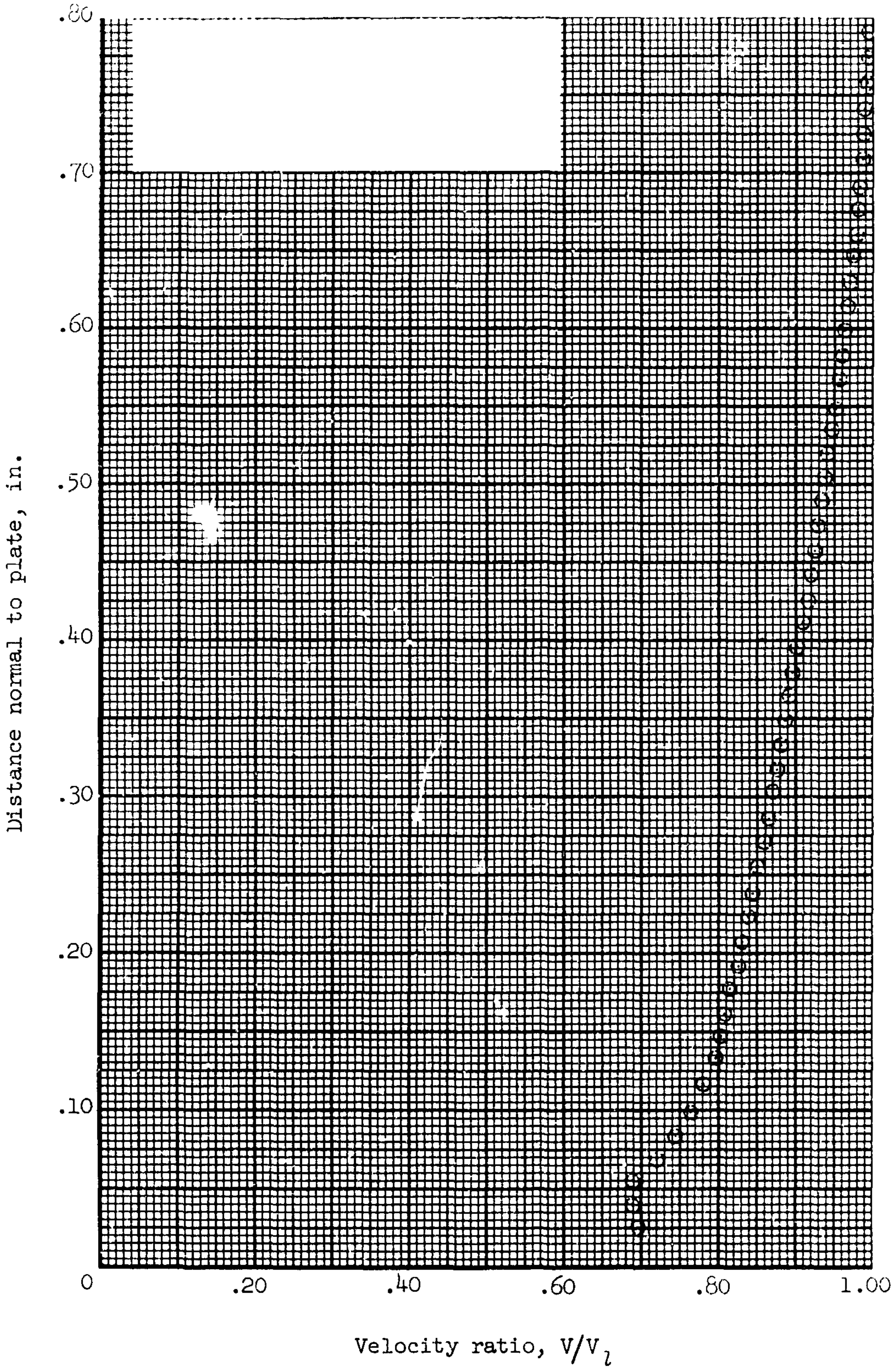

Figure 149.- Boundary-layer velocity distribution for run 43. All identifying conditions are given in table III.

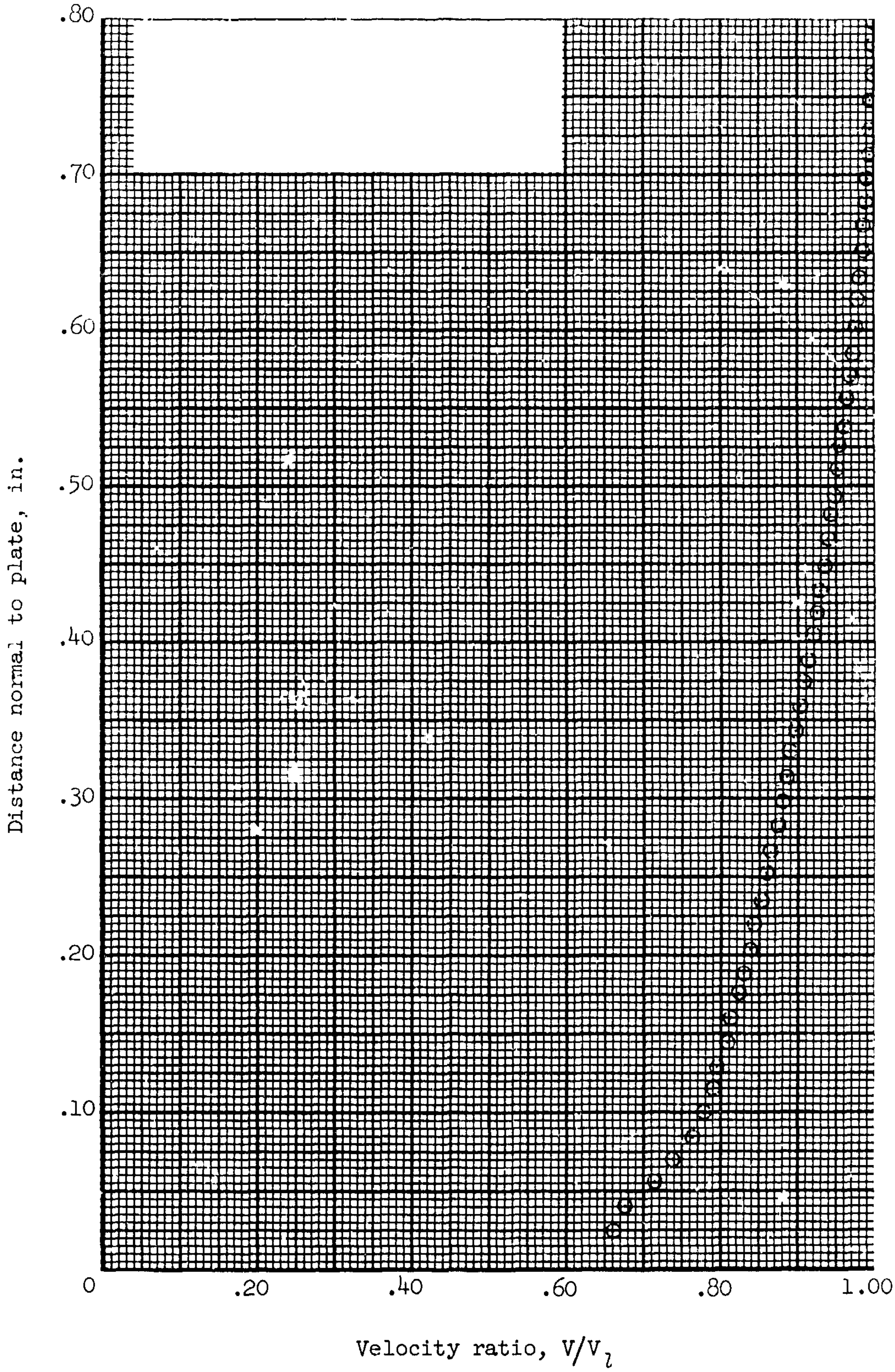

Figure 150.- Boundary-layer velocity distribution for run 44. All identifying conditions are given in table III.

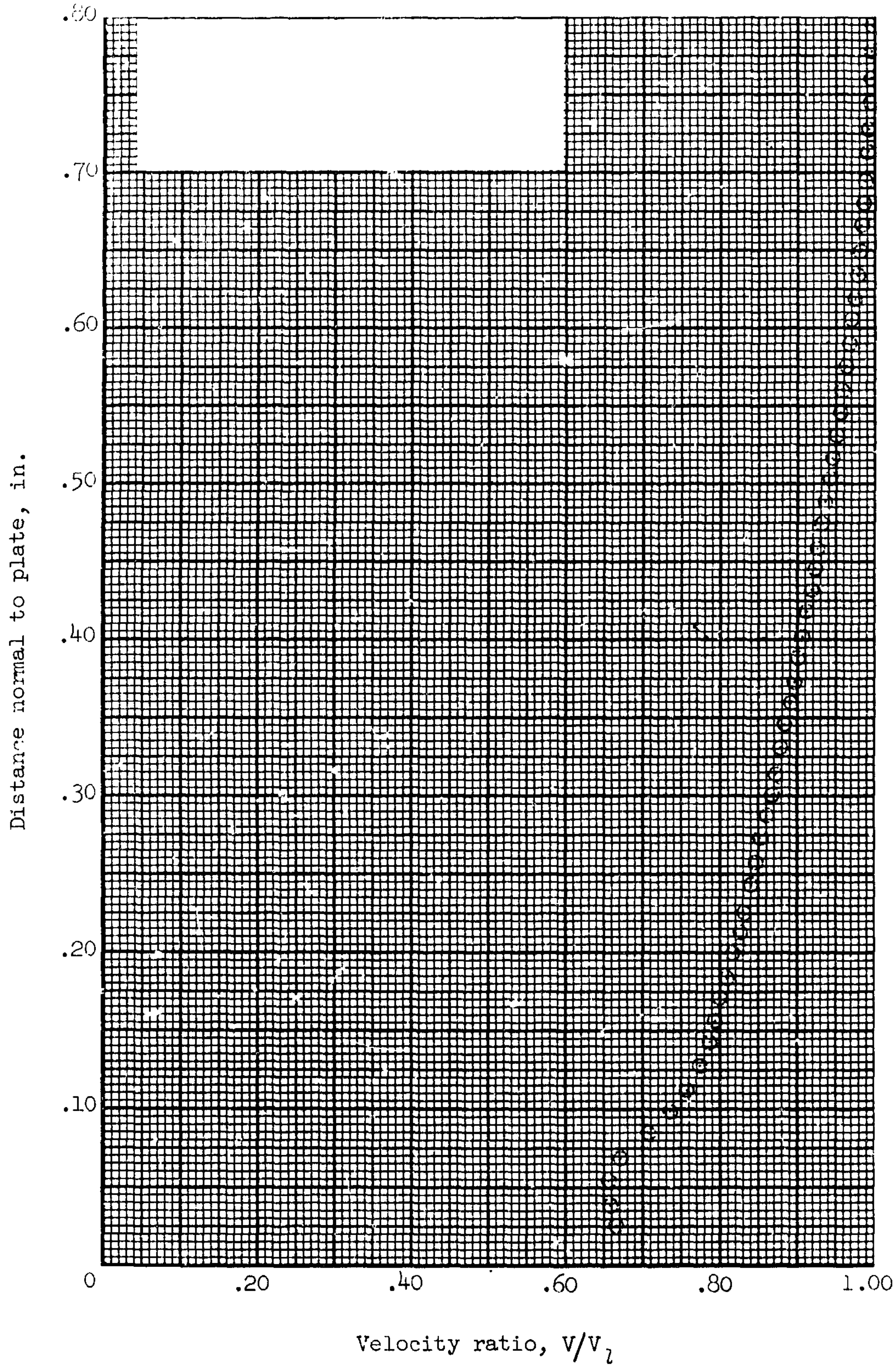

Figure 151.- Boundary-layer velocity distribution for run 45. All identifying conditions are given in table III.

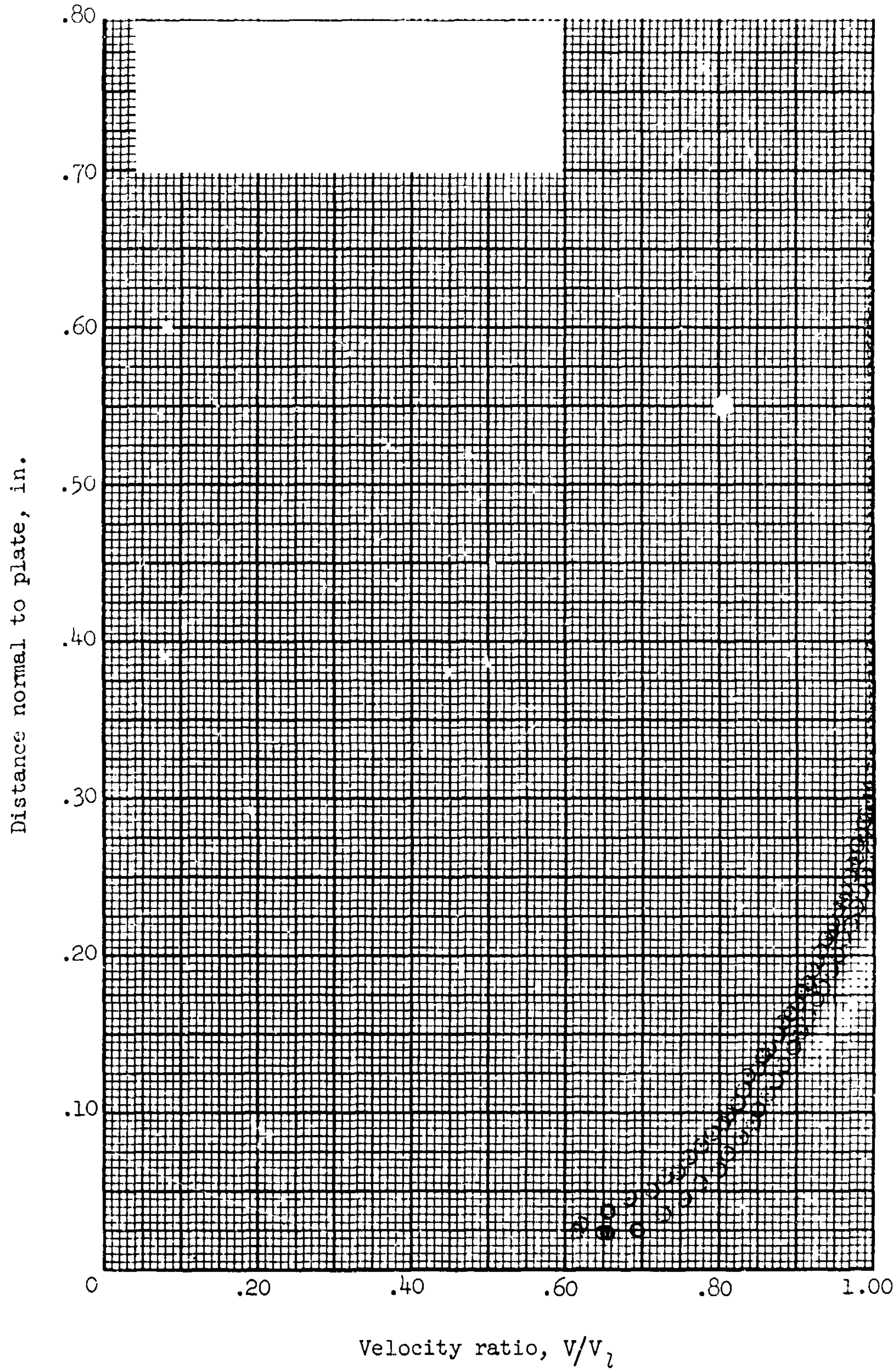

Figure 152.- Boundary-layer velocity distribution for run 46. All identifying conditions are given in table III.

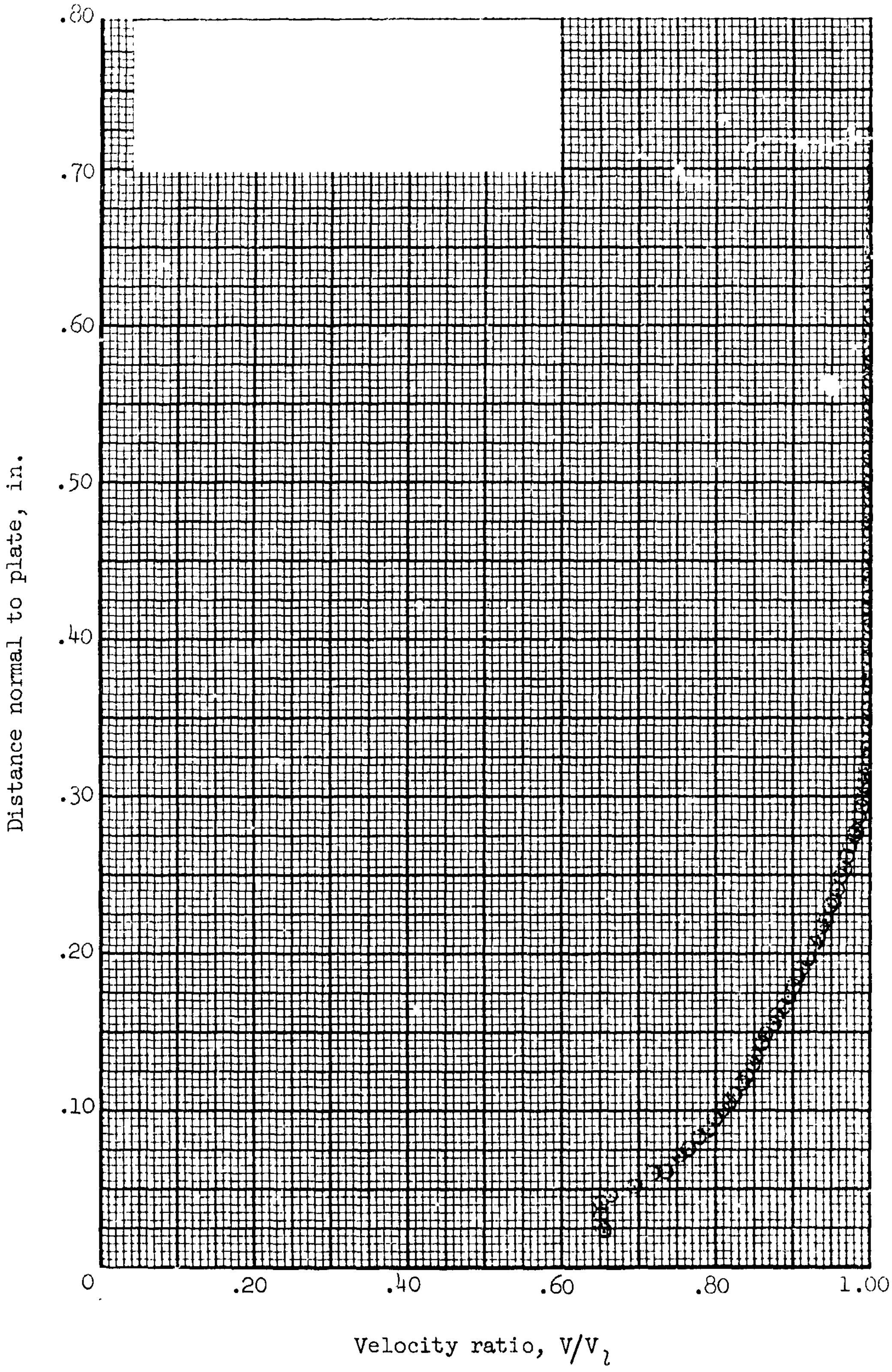

Figure 153.- Boundary-layer velocity distribution for run 47. All identifying conditions are given in table III.

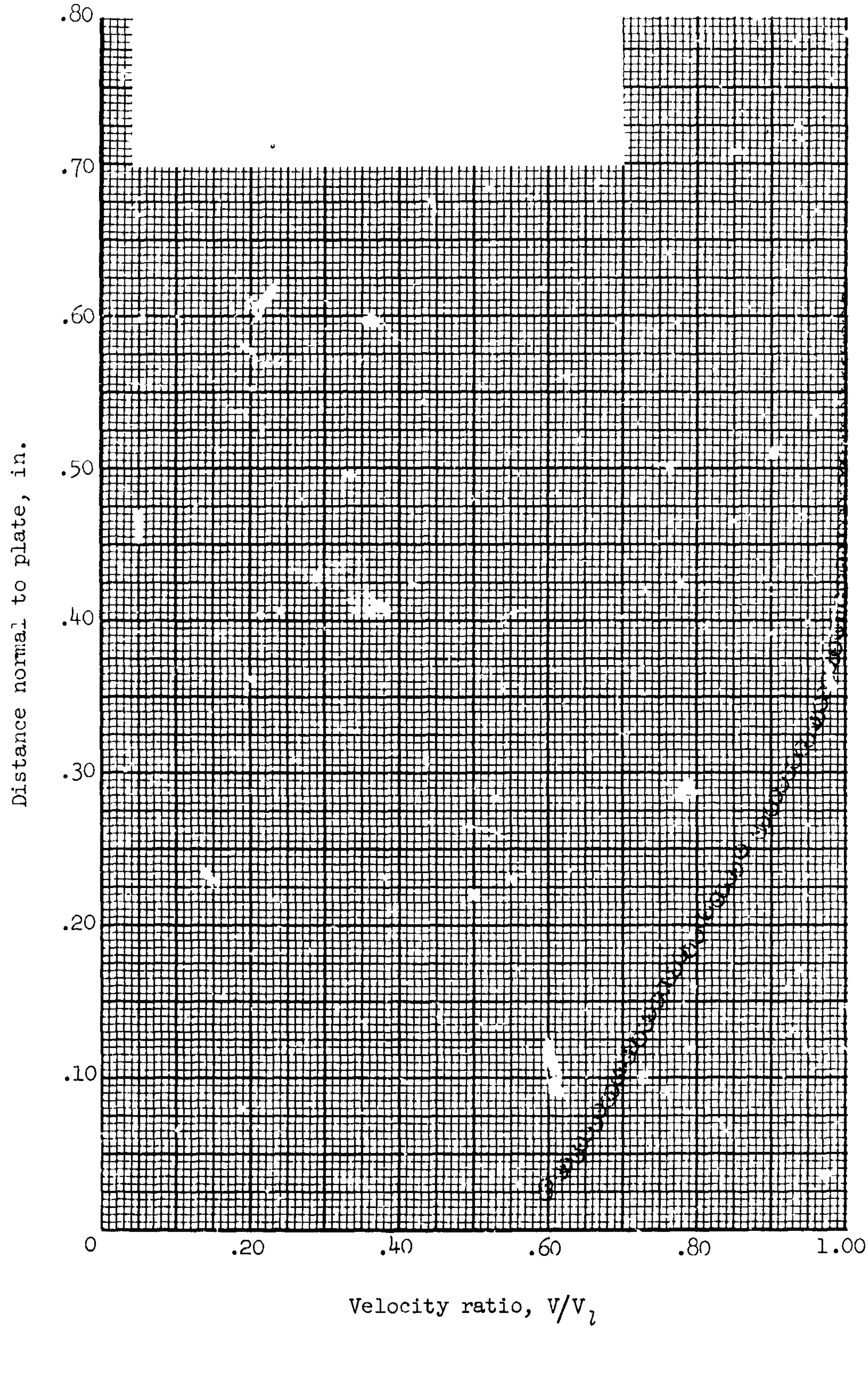

Figure 154.- Boundary-layer velocity distribution for run 48. All identifying conditions are given in table III.

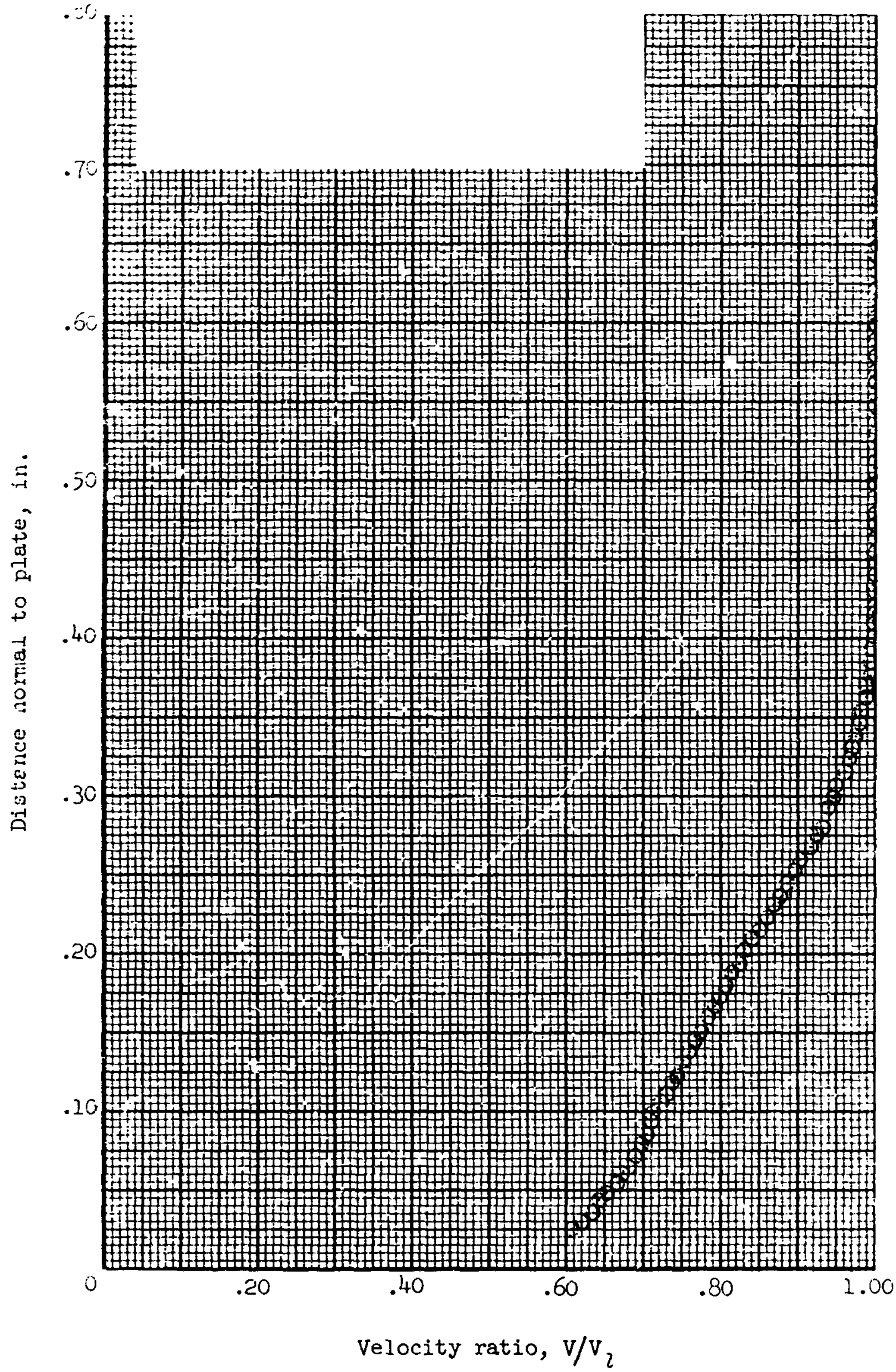

Figure 15[illegible].- Boundary-layer velocity distribution for run 49. All identifying conditions are given in table III.

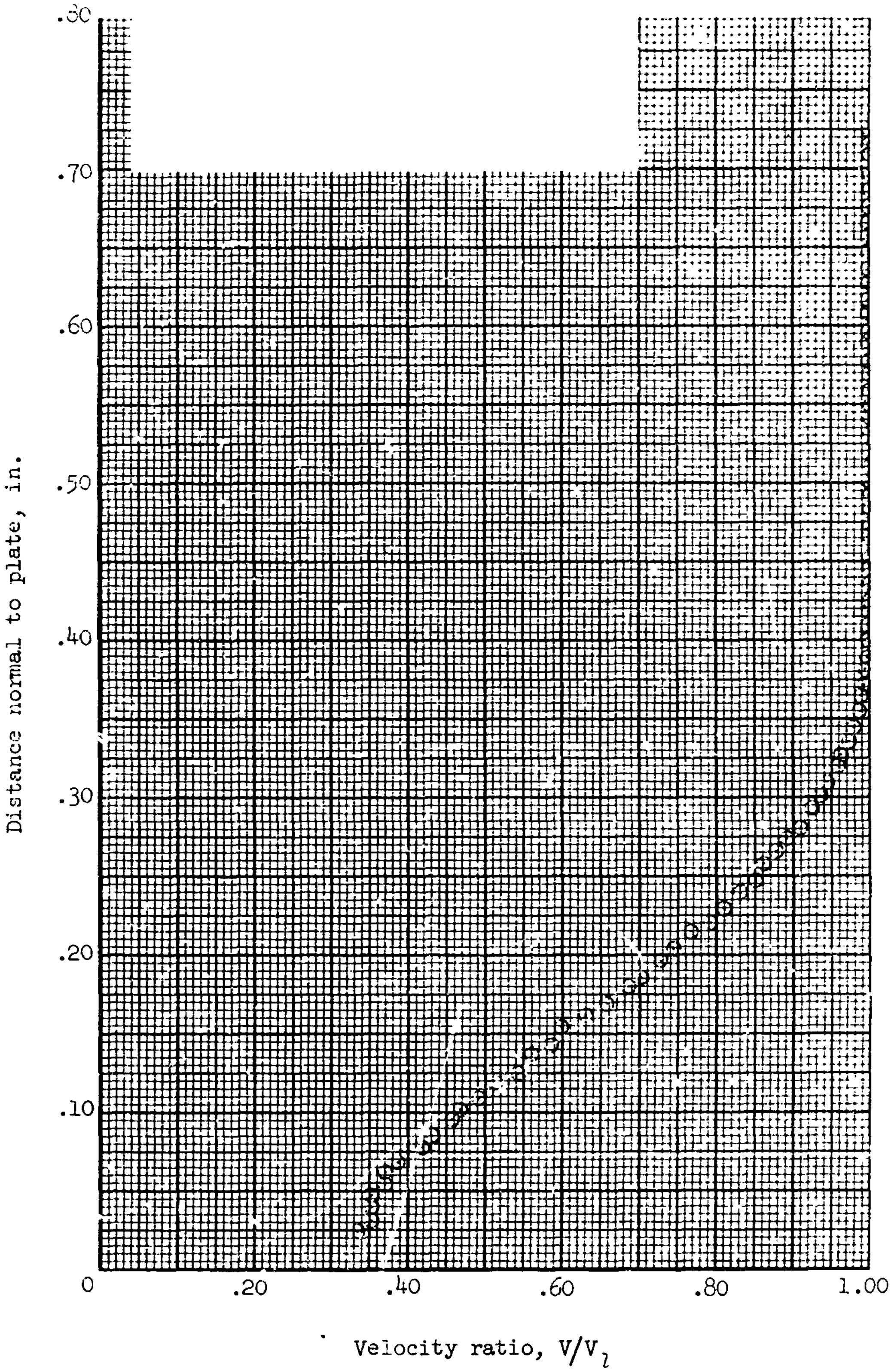

Figure 156.- Boundary-layer velocity distribution for run 50. All identifying conditions are given in table III.

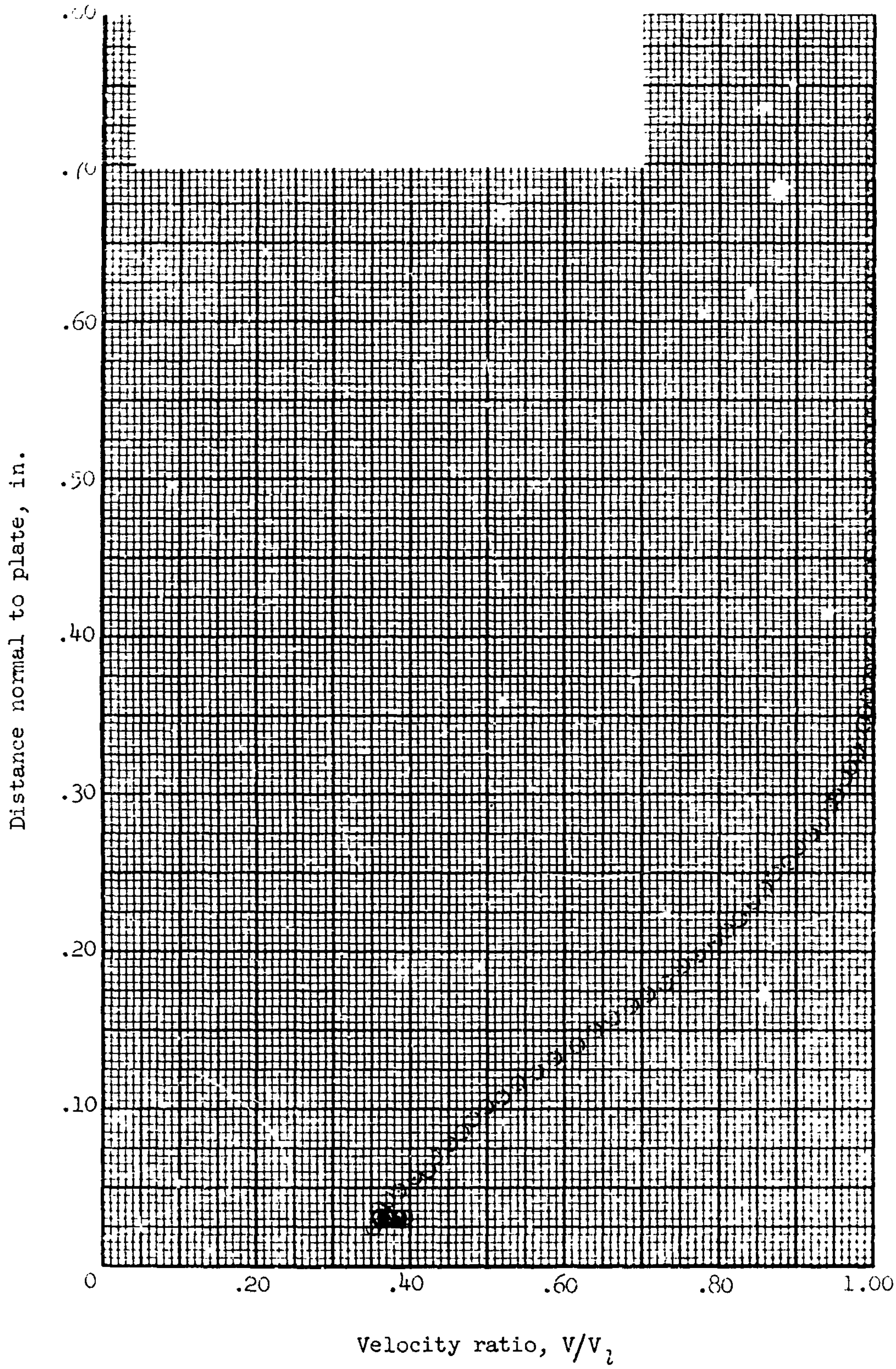

Figure 157.- Boundary-layer velocity distribution for run 51. All identifying conditions are given in table III.

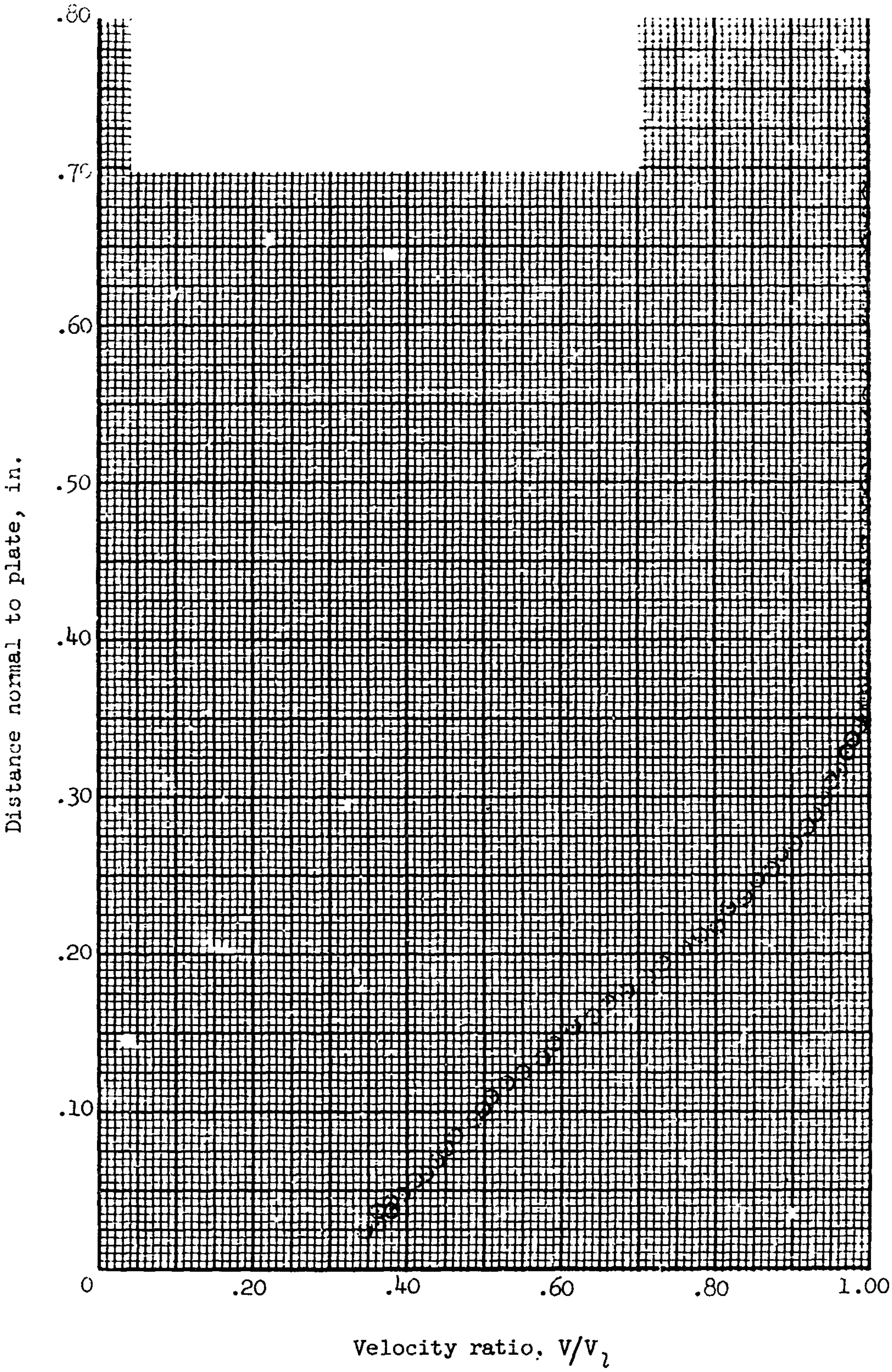

Figure 158.- Boundary-layer velocity distribution for run 52. All identifying conditions are given in table III.

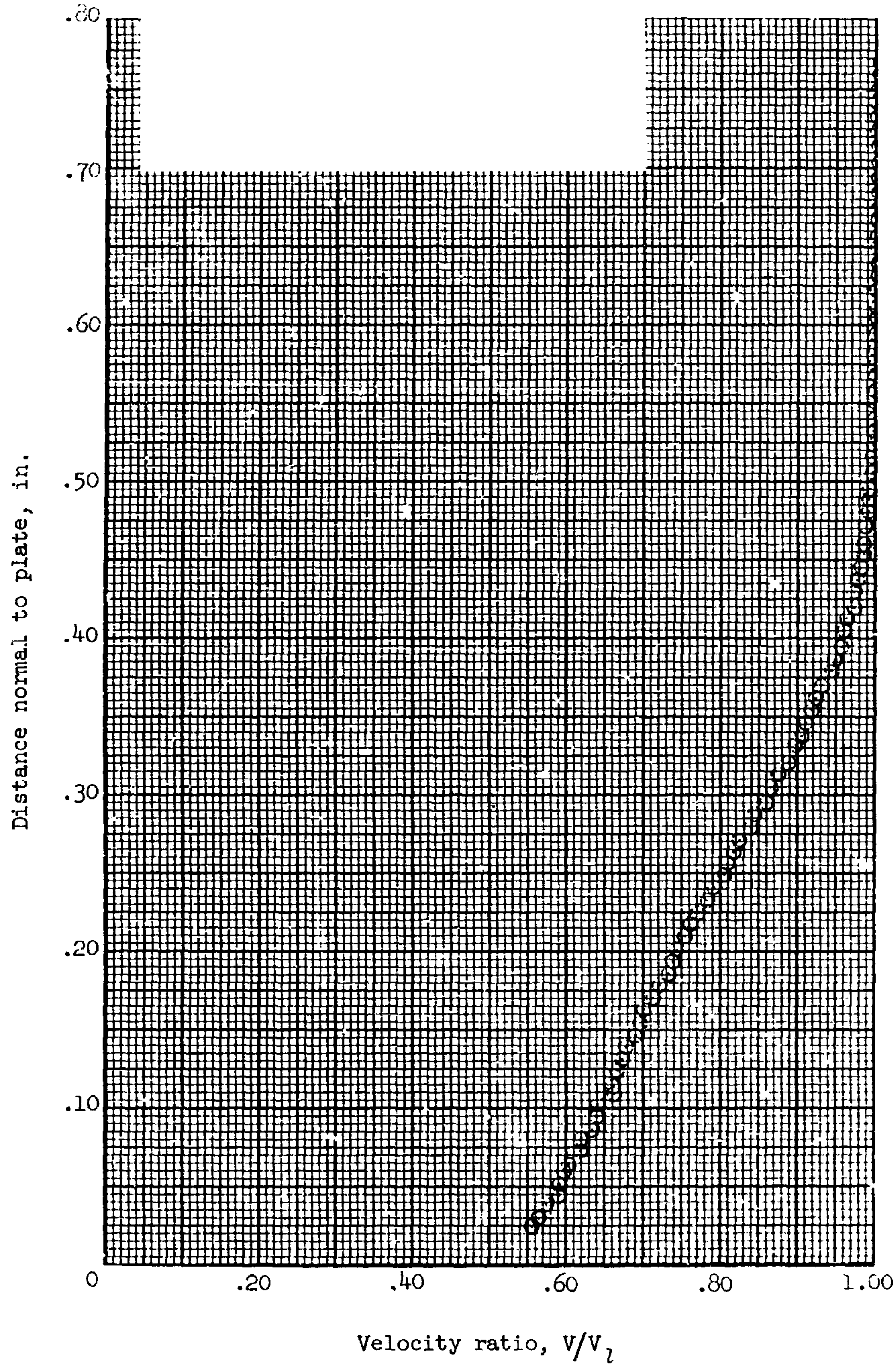

Figure 159.- Boundary-layer velocity distribution for run 53. All identifying conditions are given in table III.

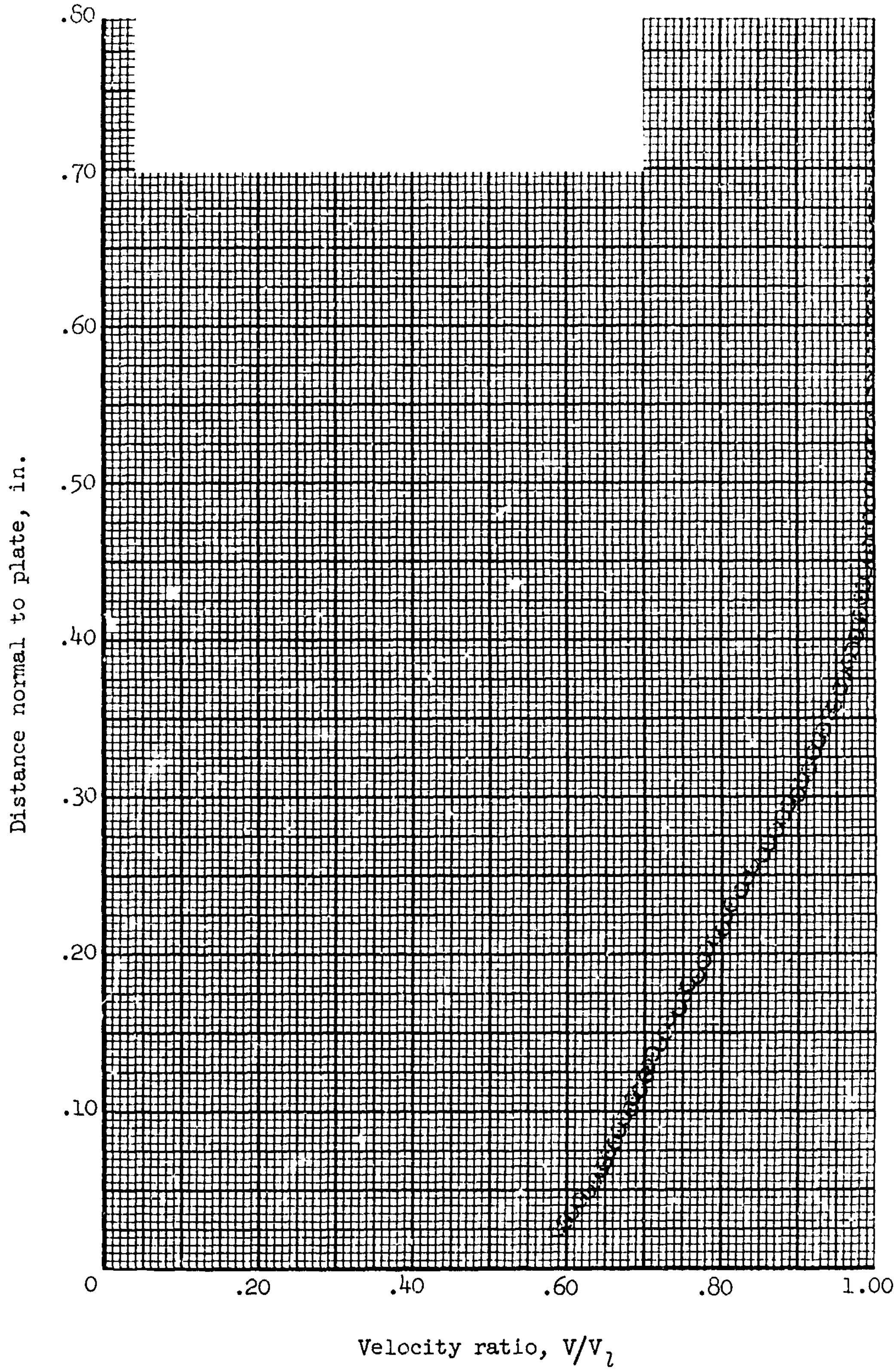

Figure 160.- Boundary-layer velocity distribution for run 54. All identifying conditions are given in table III.

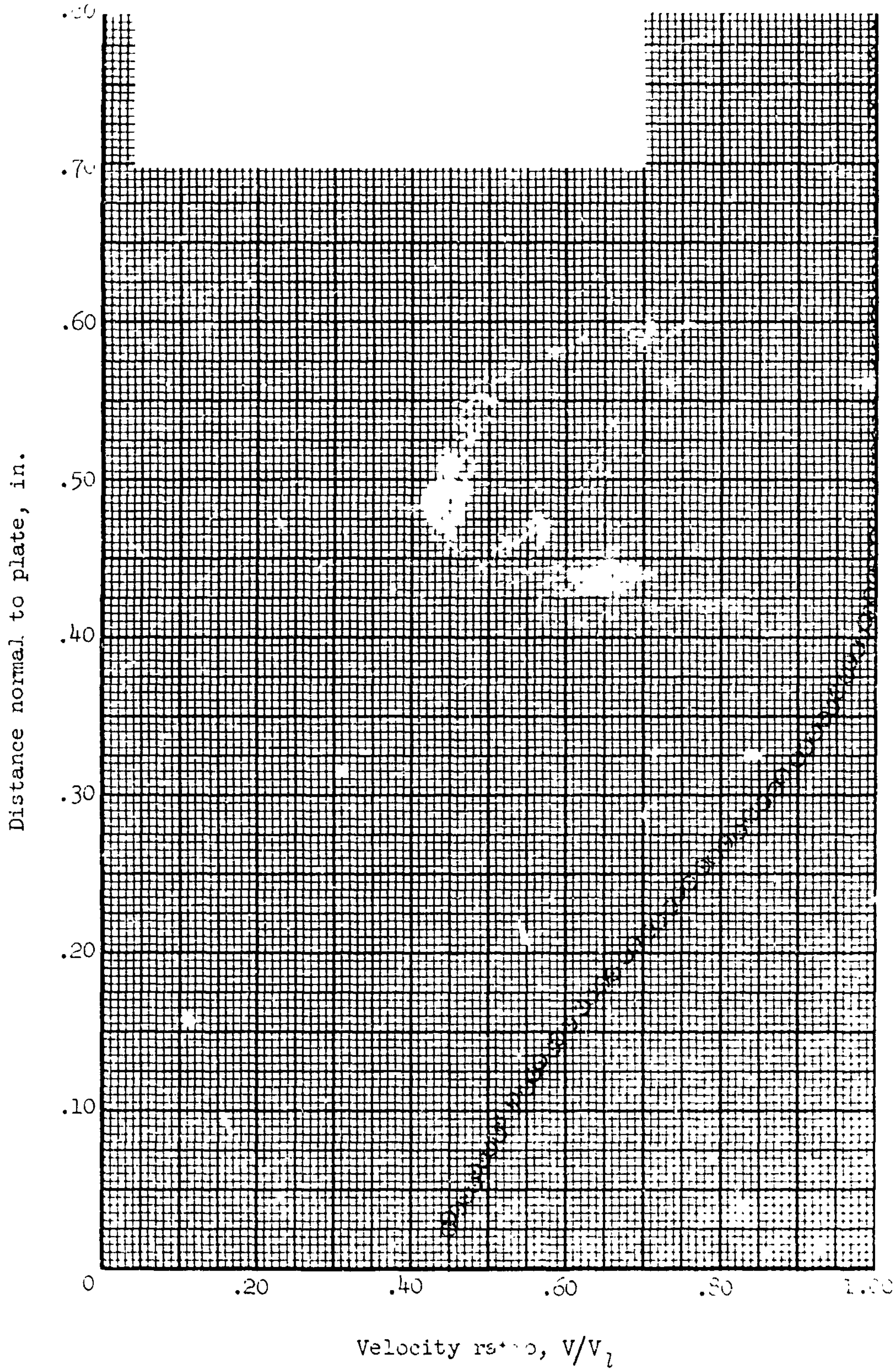

Figure 161.- Boundary-layer velocity distribution for run 55. All identifying conditions are given in table III.

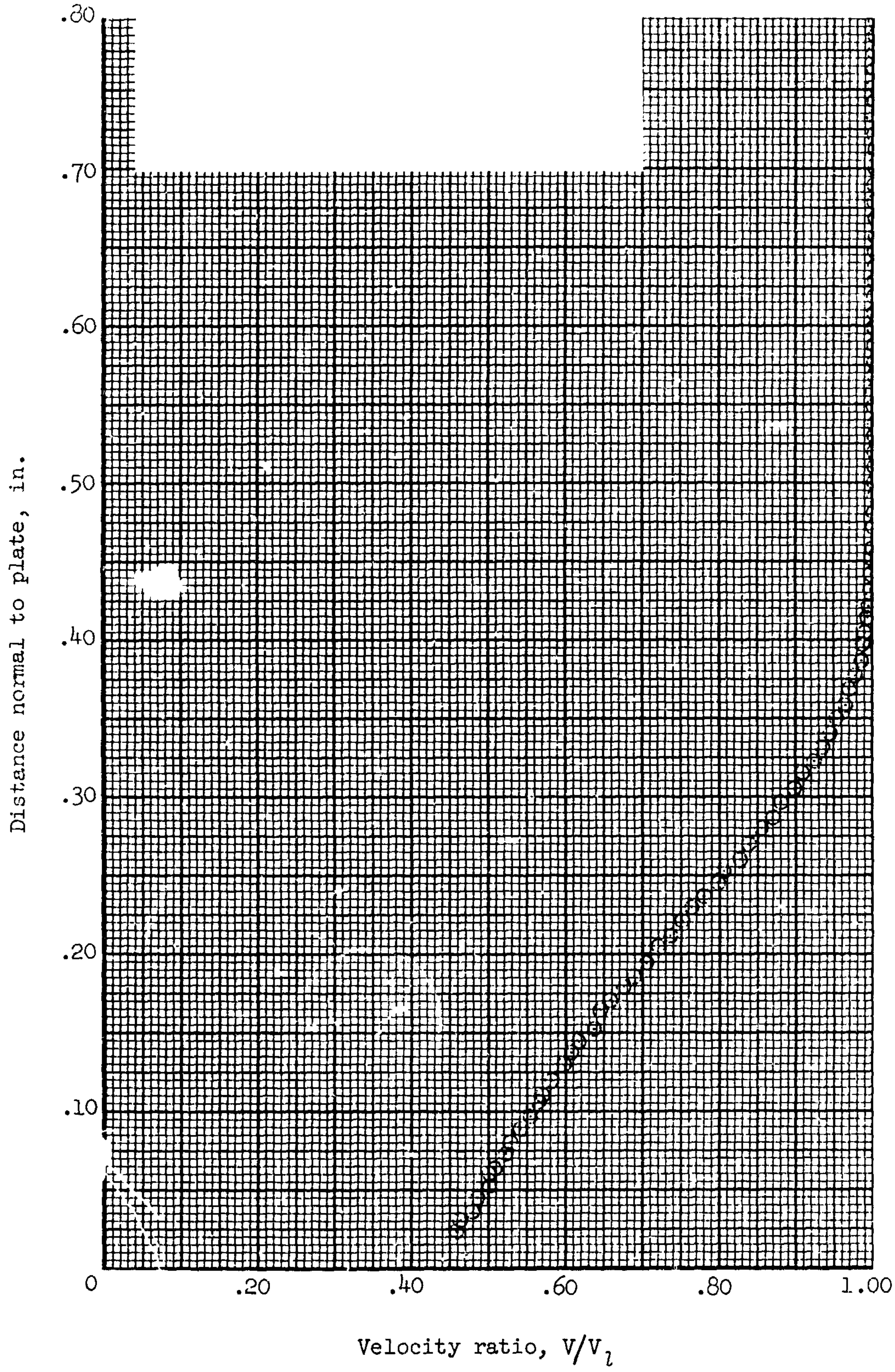

Figure 162.- Boundary-layer velocity distribution for run 56. All identifying conditions are given in table III.

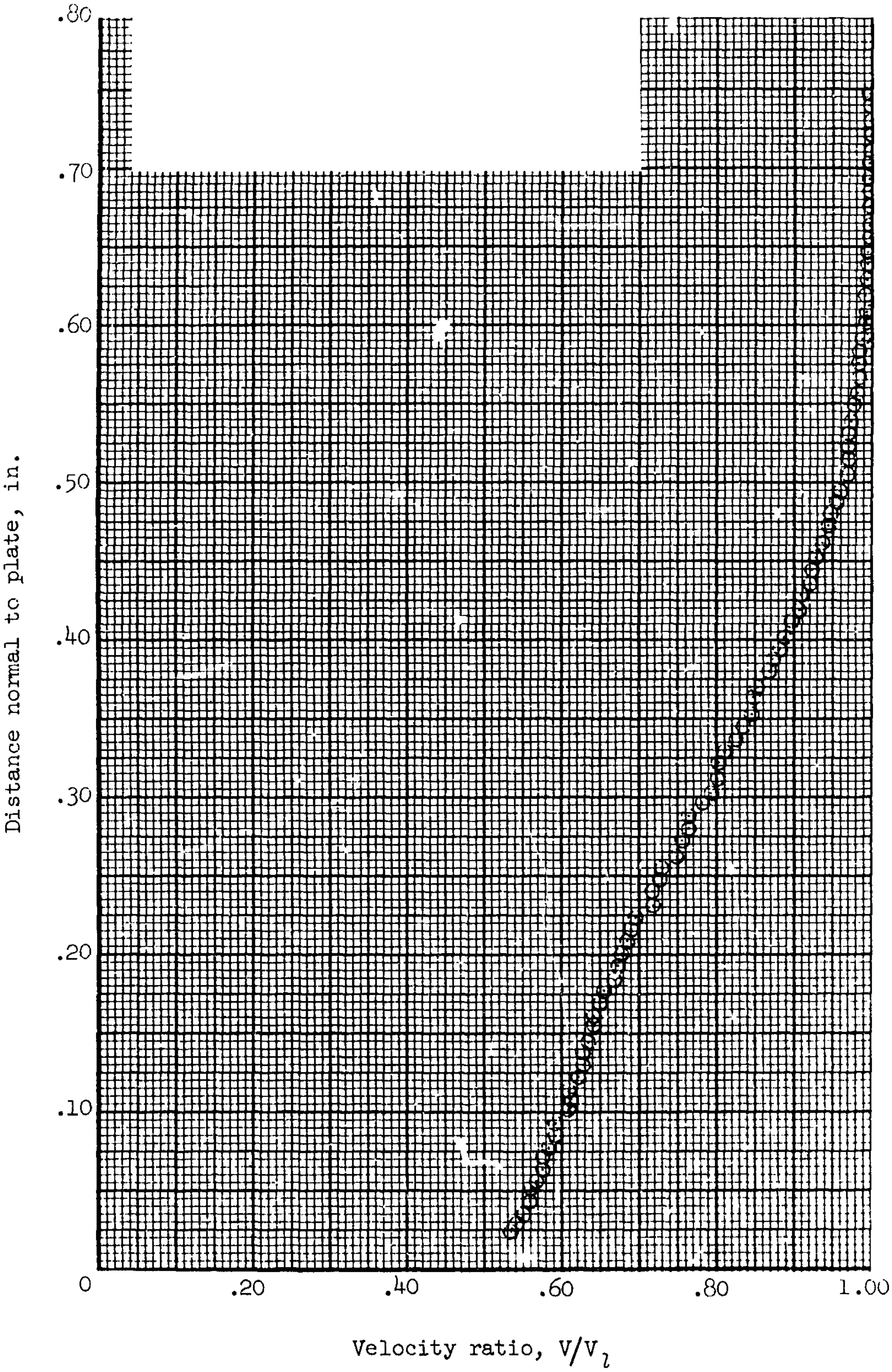

Figure 163.- Boundary-layer velocity distribution for run 57. All identifying conditions are given in table III.

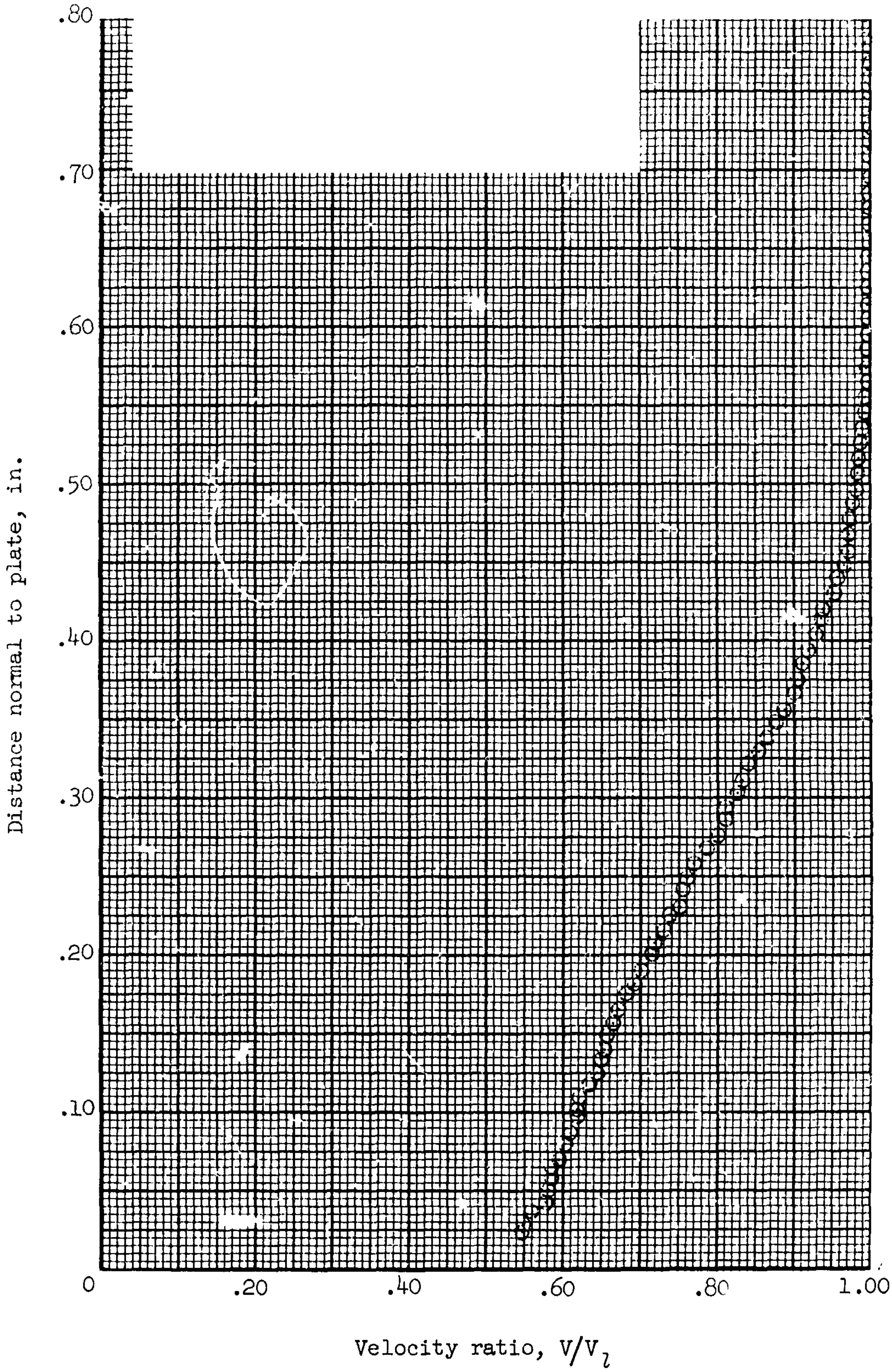

Figure 164.- Boundary-layer velocity distribution for run 58. All identifying conditions are given in table III.

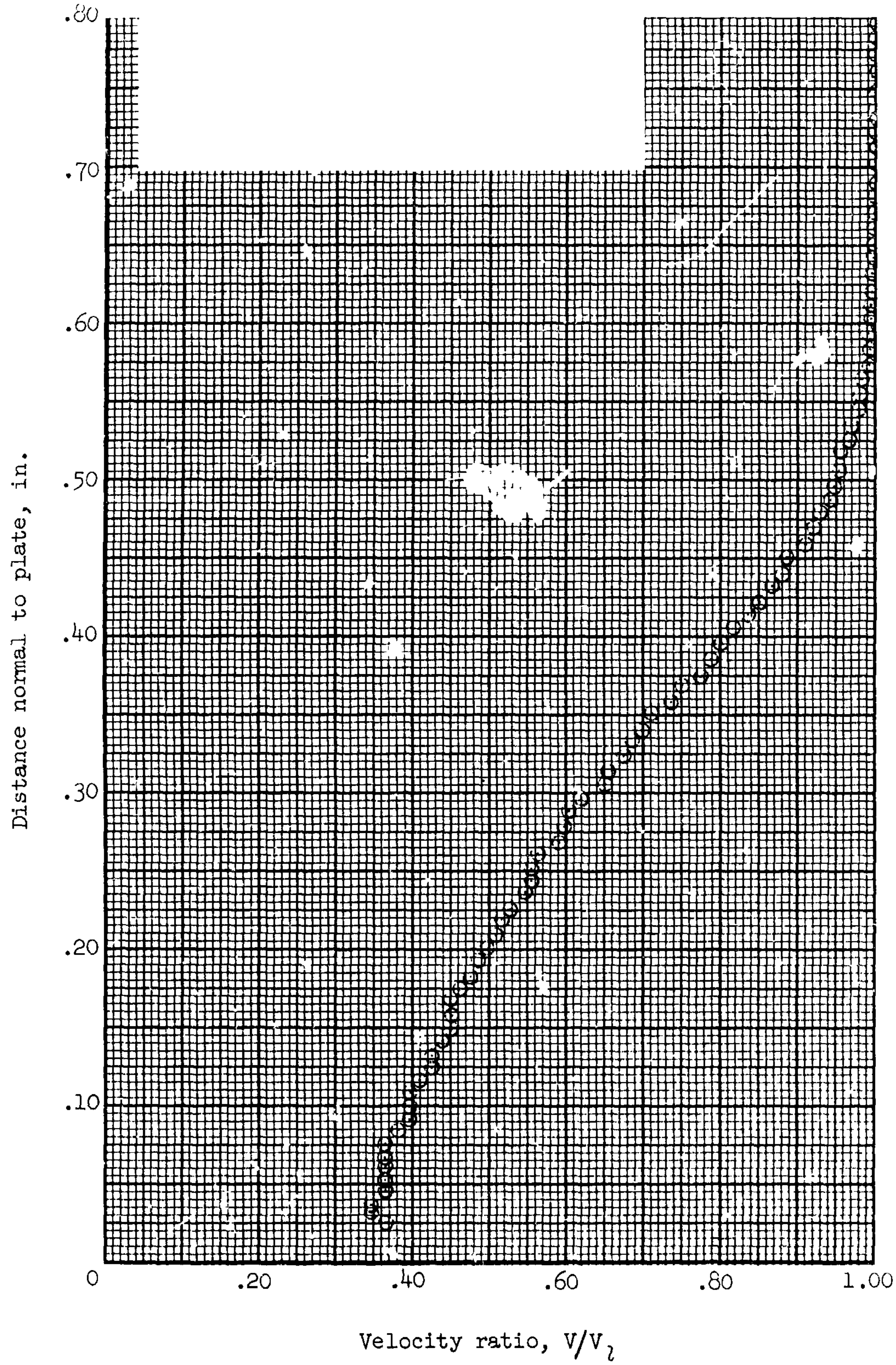

Figure 165.- Boundary-layer velocity distribution for run 59. All identifying conditions are given in table III.

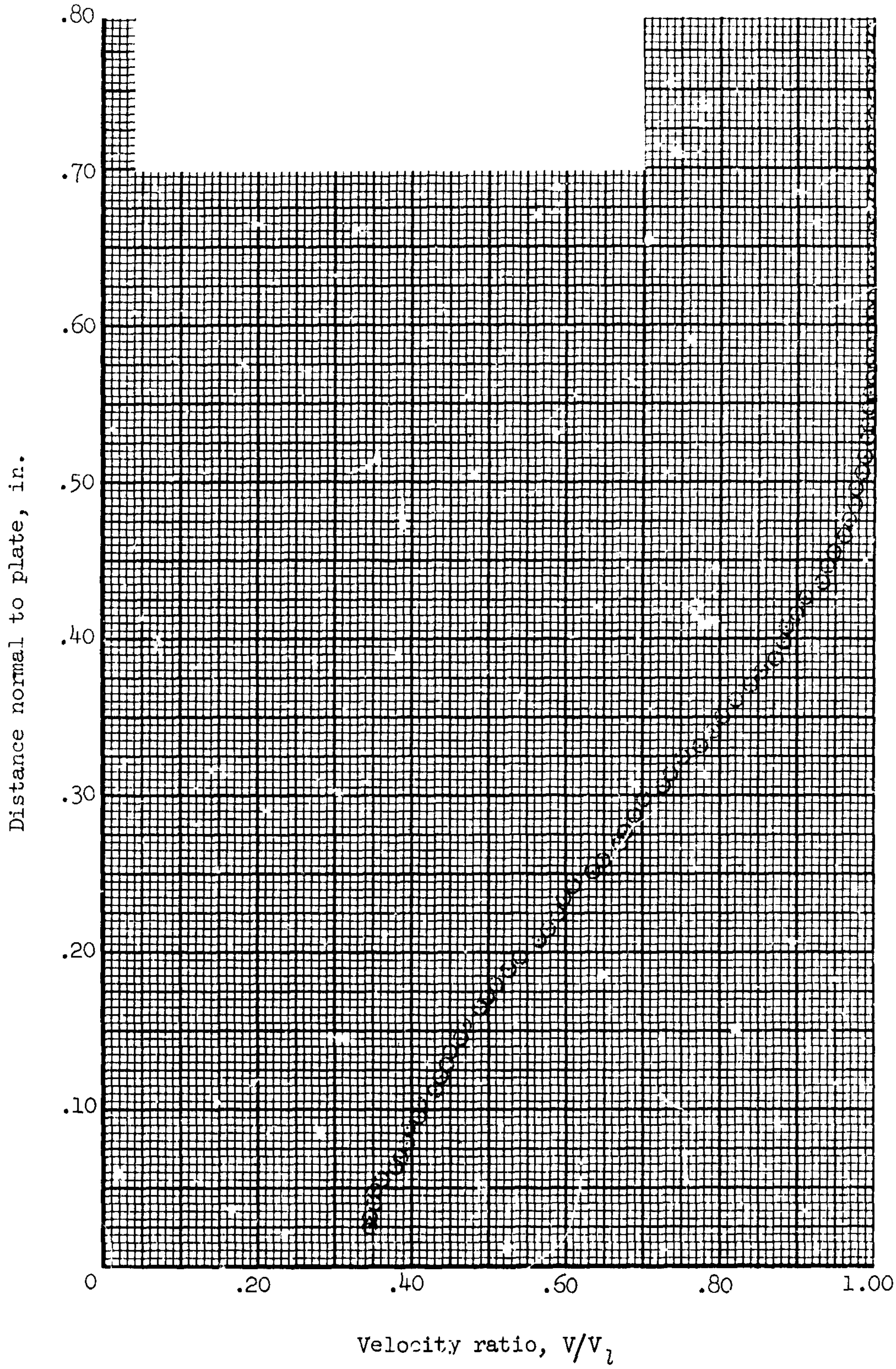

Figure 166.- Boundary-layer velocity distribution for run 60. All identifying conditions are given in ta[illegible]

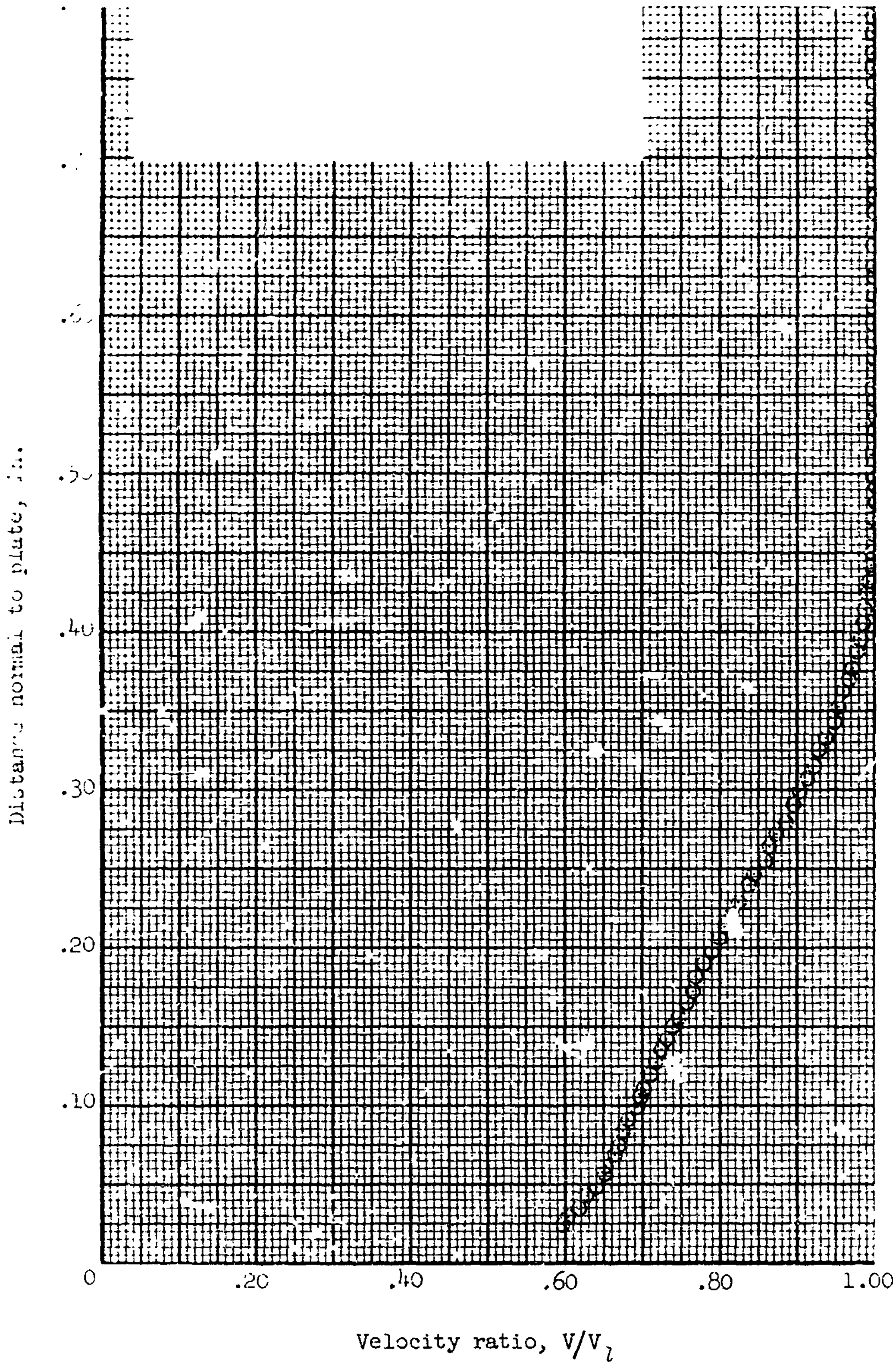

Figure 167.- Boundary-layer velocity distribution for run 61. All identifying conditions are given in table III.

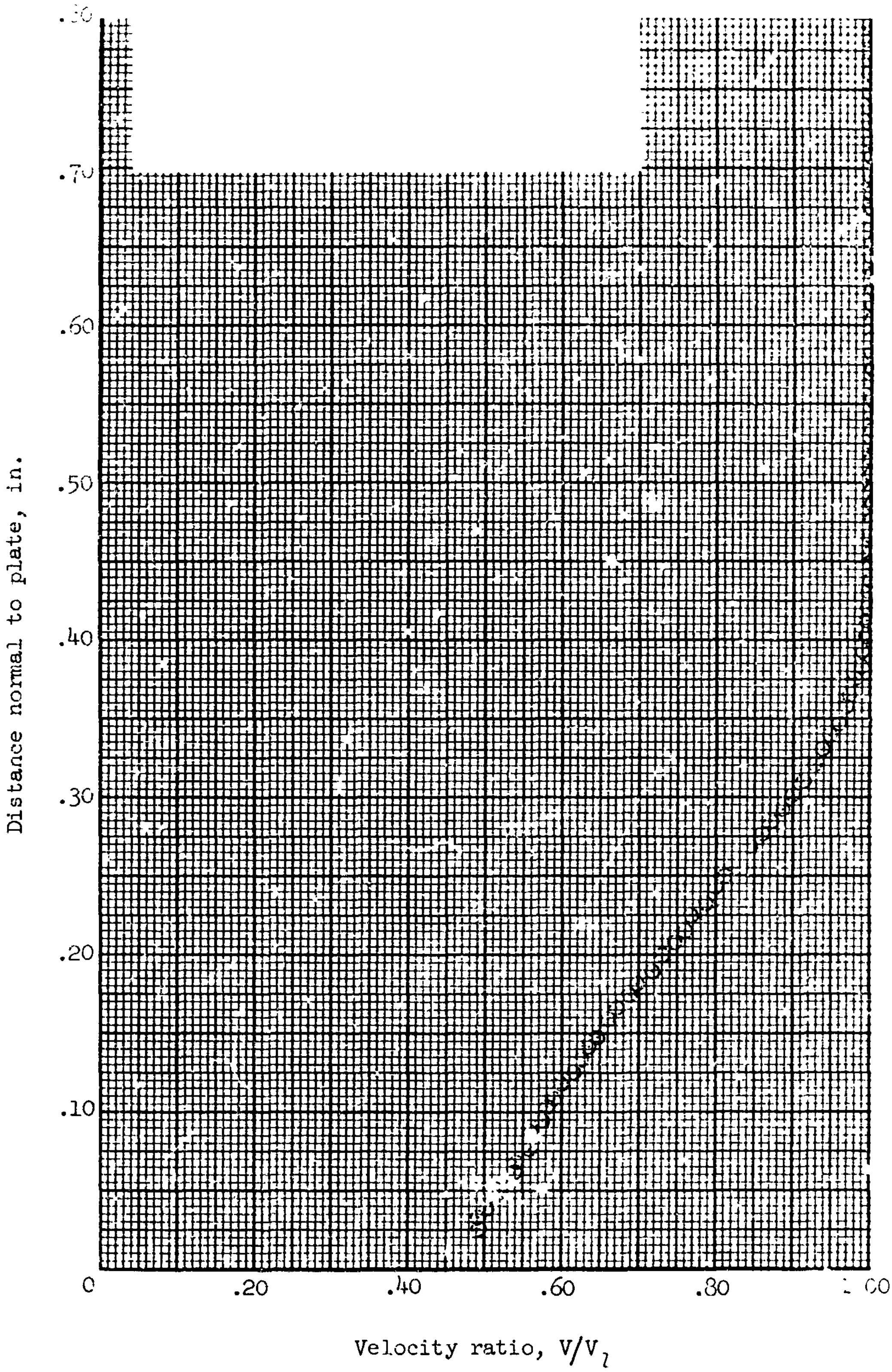

Figure 168.- Boundary-layer velocity distribution for run 62. All identifying conditions are given in table III.

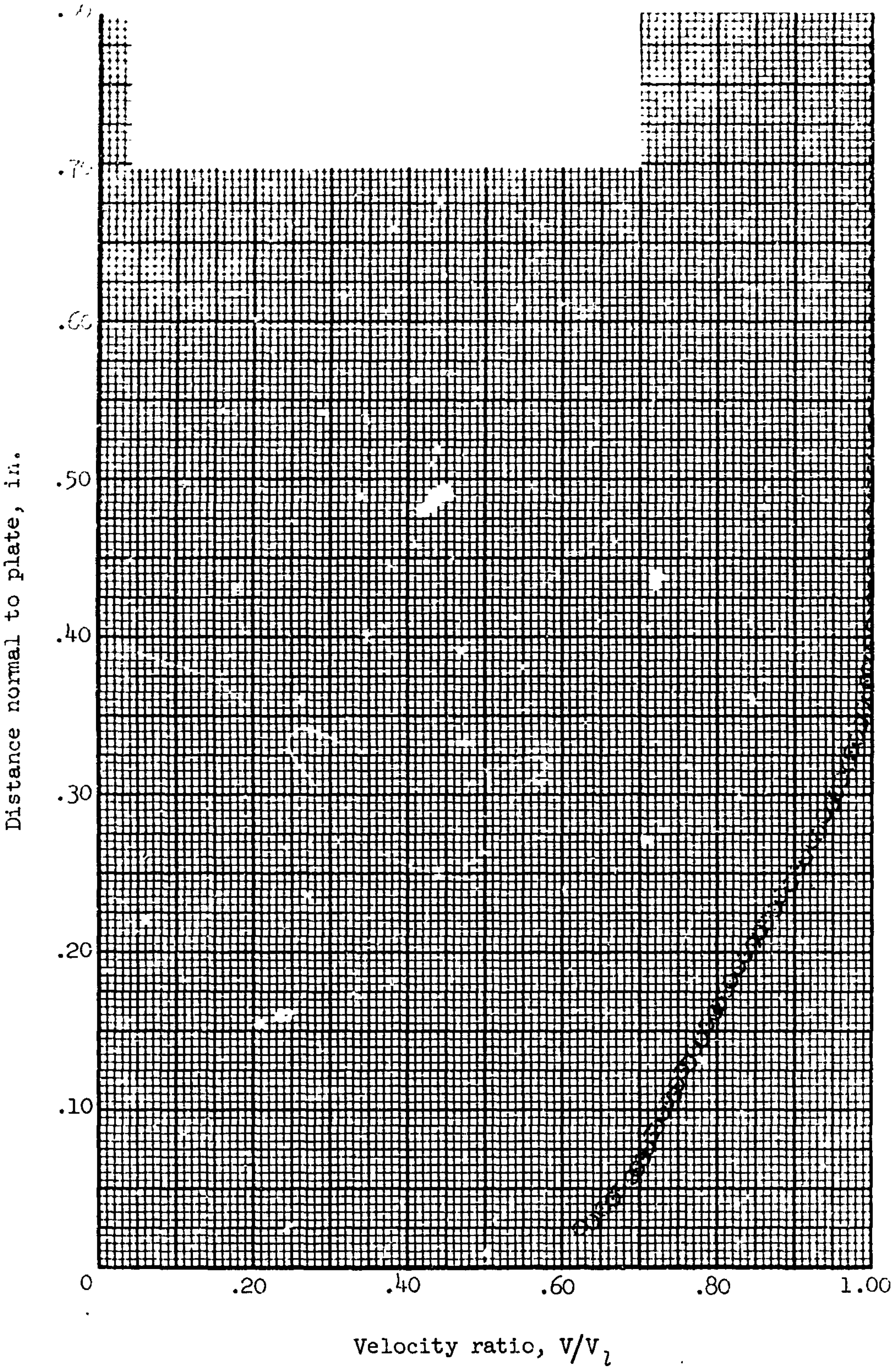

Figure 169.- Boundary-layer velocity distribution for run 63. All identifying conditions are given in table III.

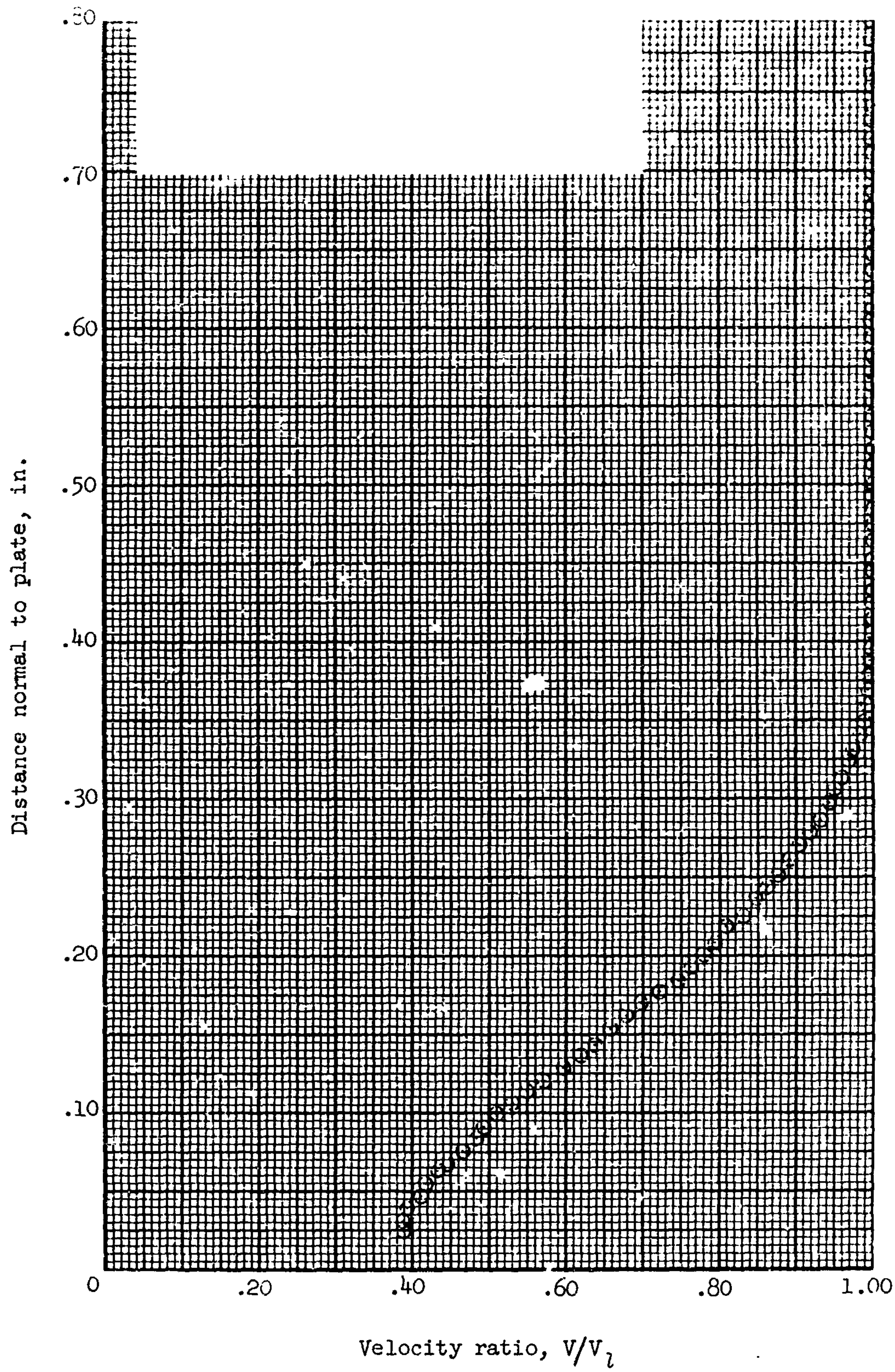

Figure 170.- Boundary-layer velocity distribution for run 64. All identifying conditions are given in table III.

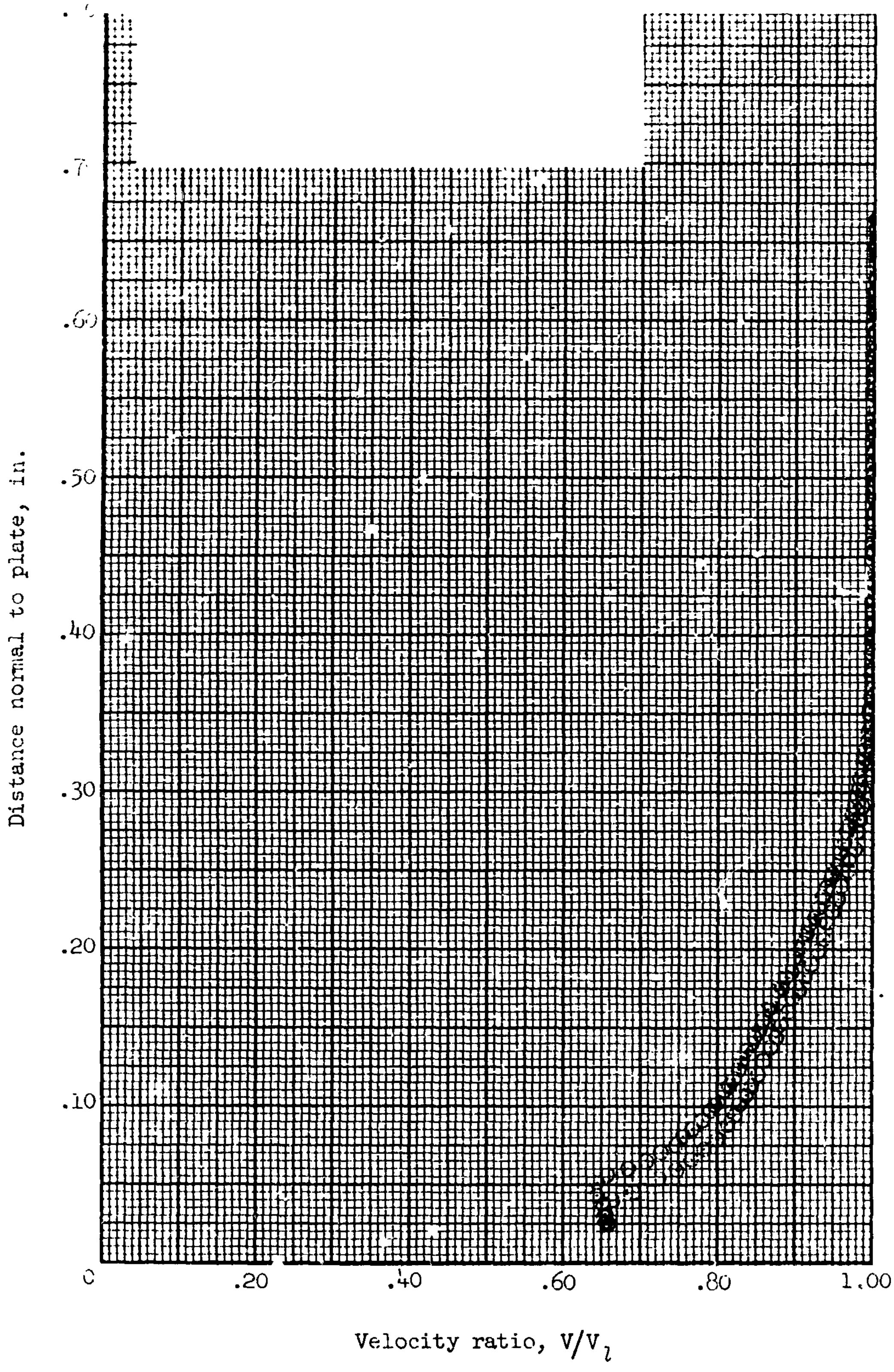

Figure 171.- Boundary-layer velocity distribution for run 65. All identifying conditions are given in table III.

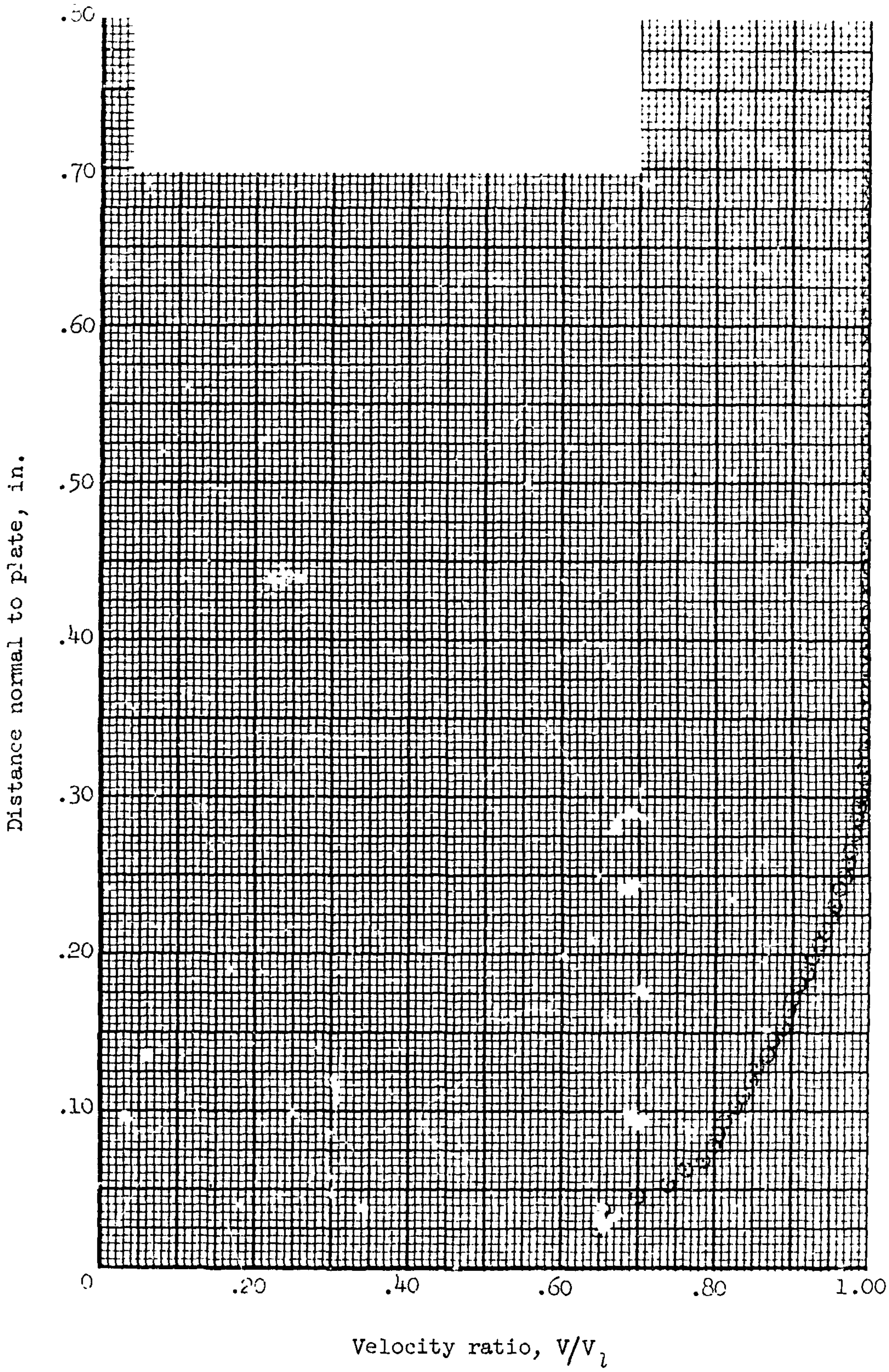

Figure 172.- Boundary-layer velocity distribution for run 66. All identifying conditions are given in table III.

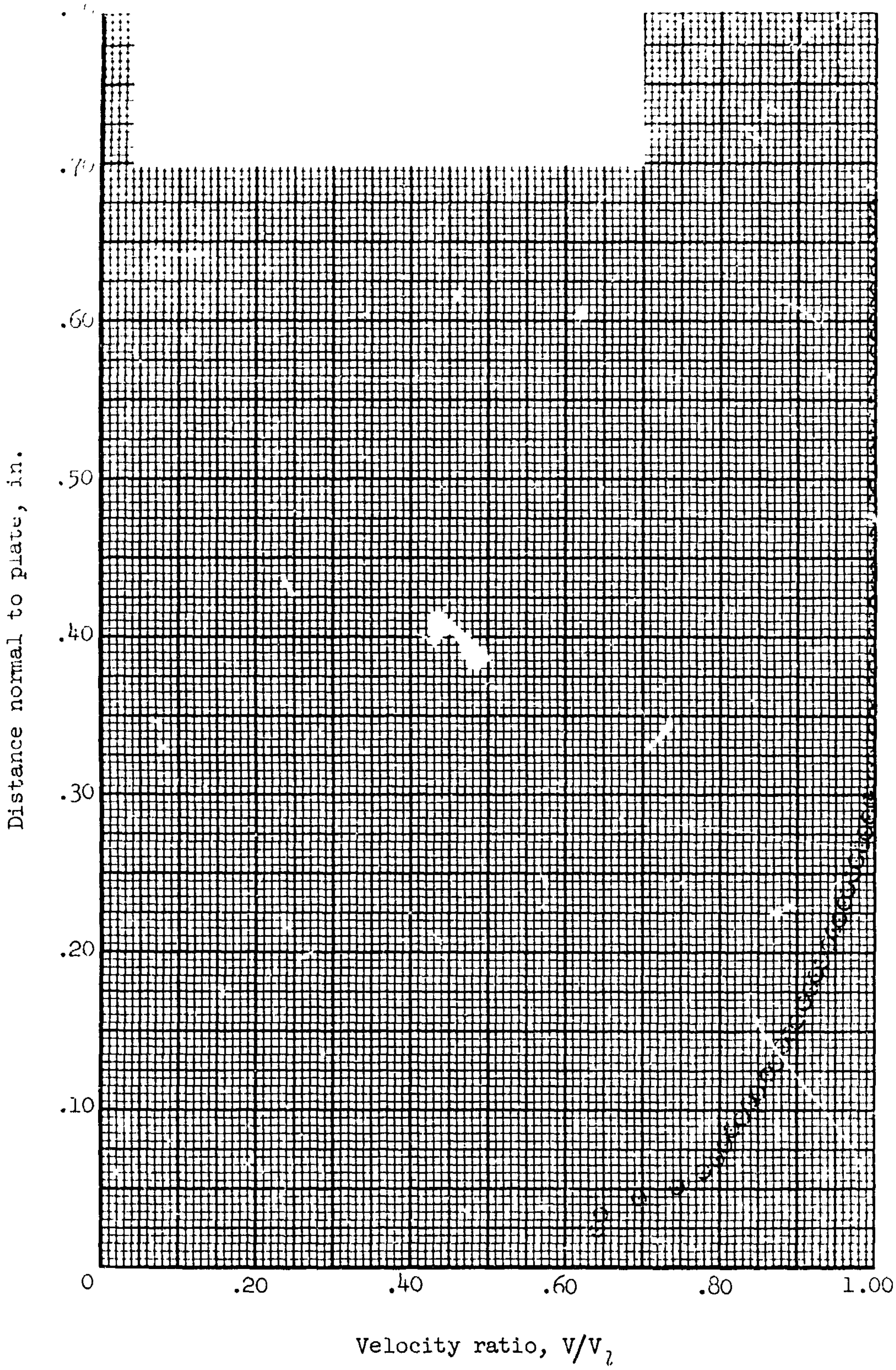

Figure 173.- Boundary-layer velocity distribution for run 67. All identifying conditions are given in table III.

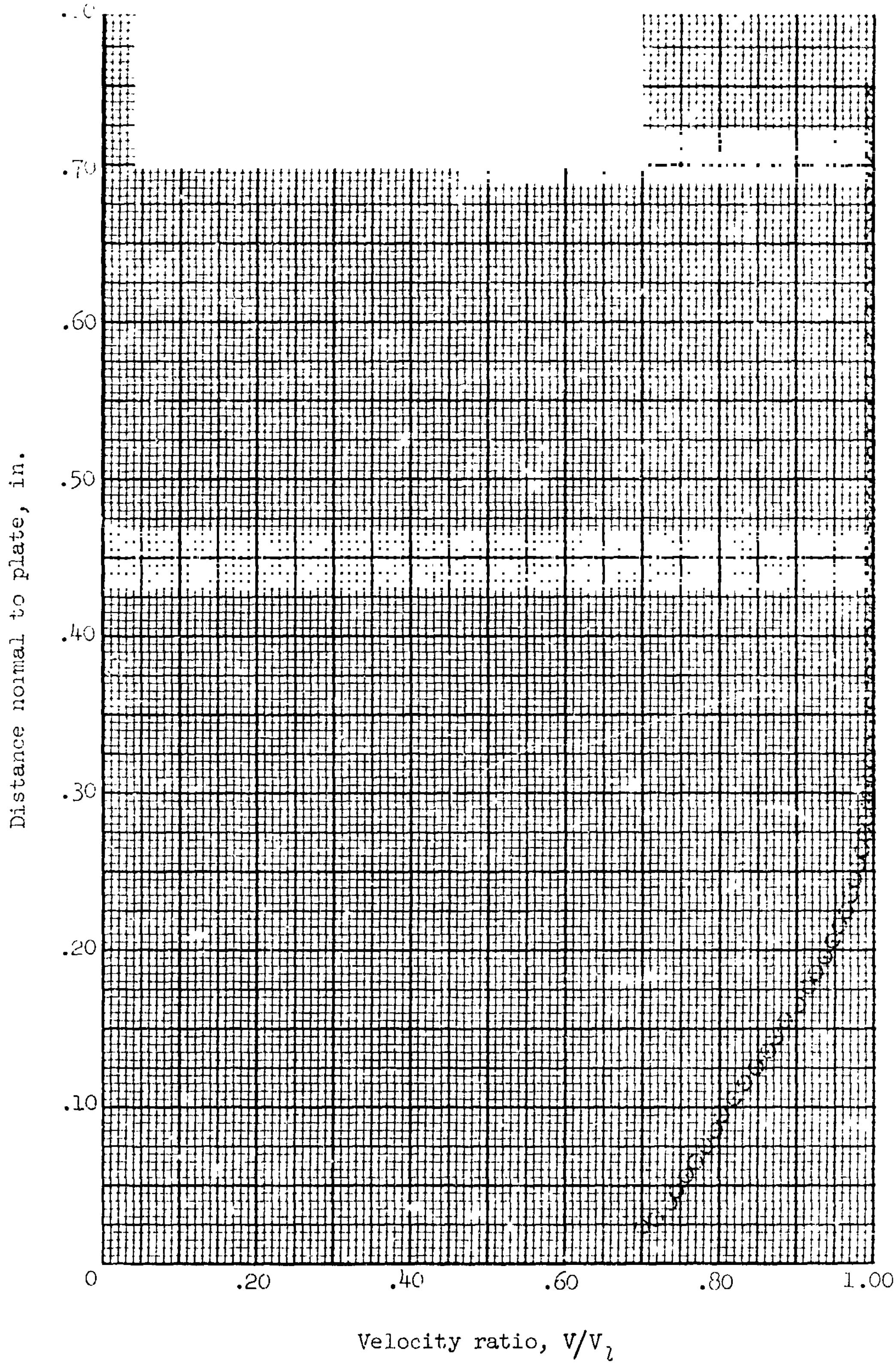

Figure 174.- Boundary-layer velocity distribution for run 69. All identifying conditions are given in table III.

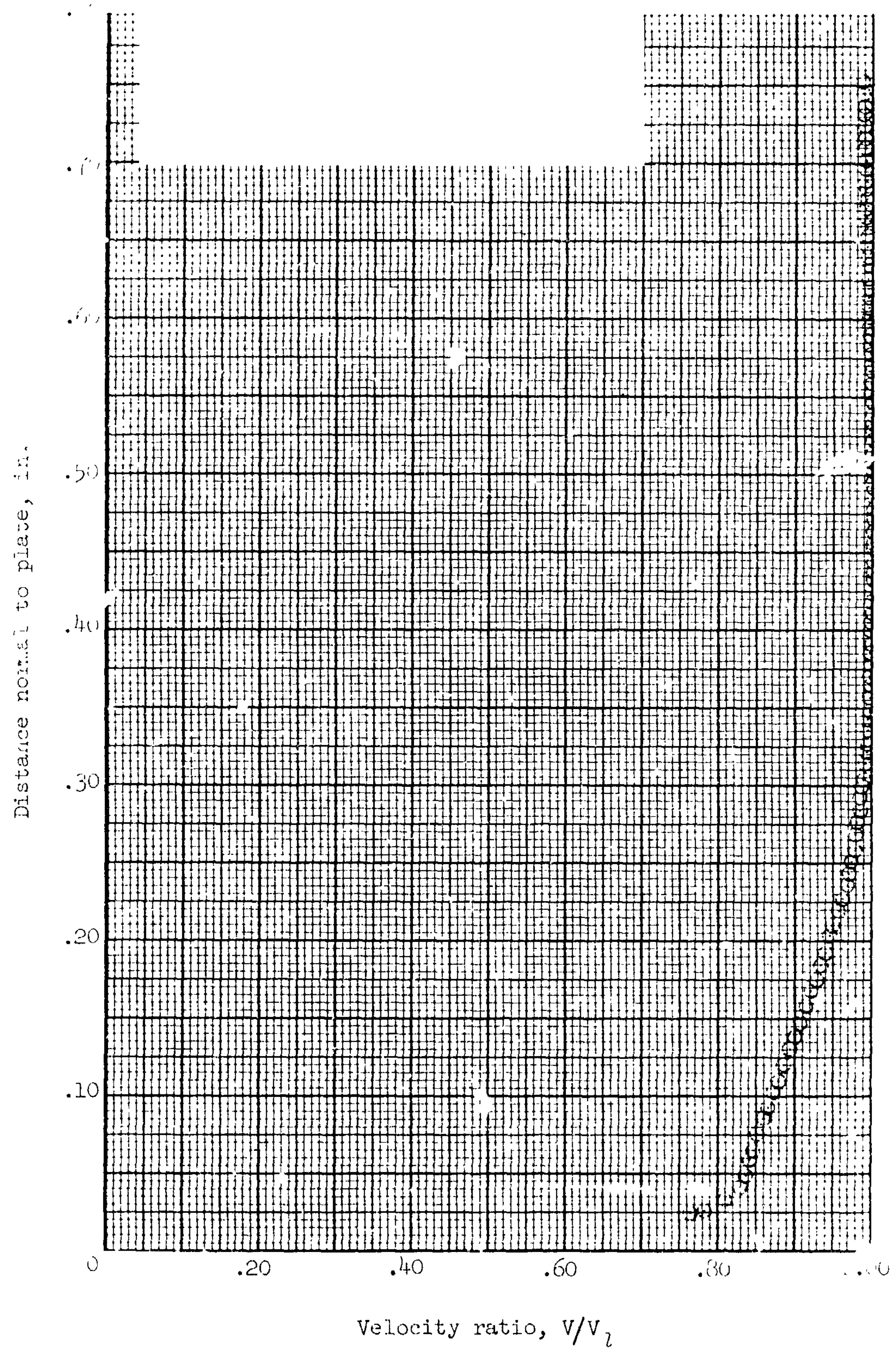

Figure 175.- Boundary-layer velocity distribution for run 70. All identifying conditions are given in table III.

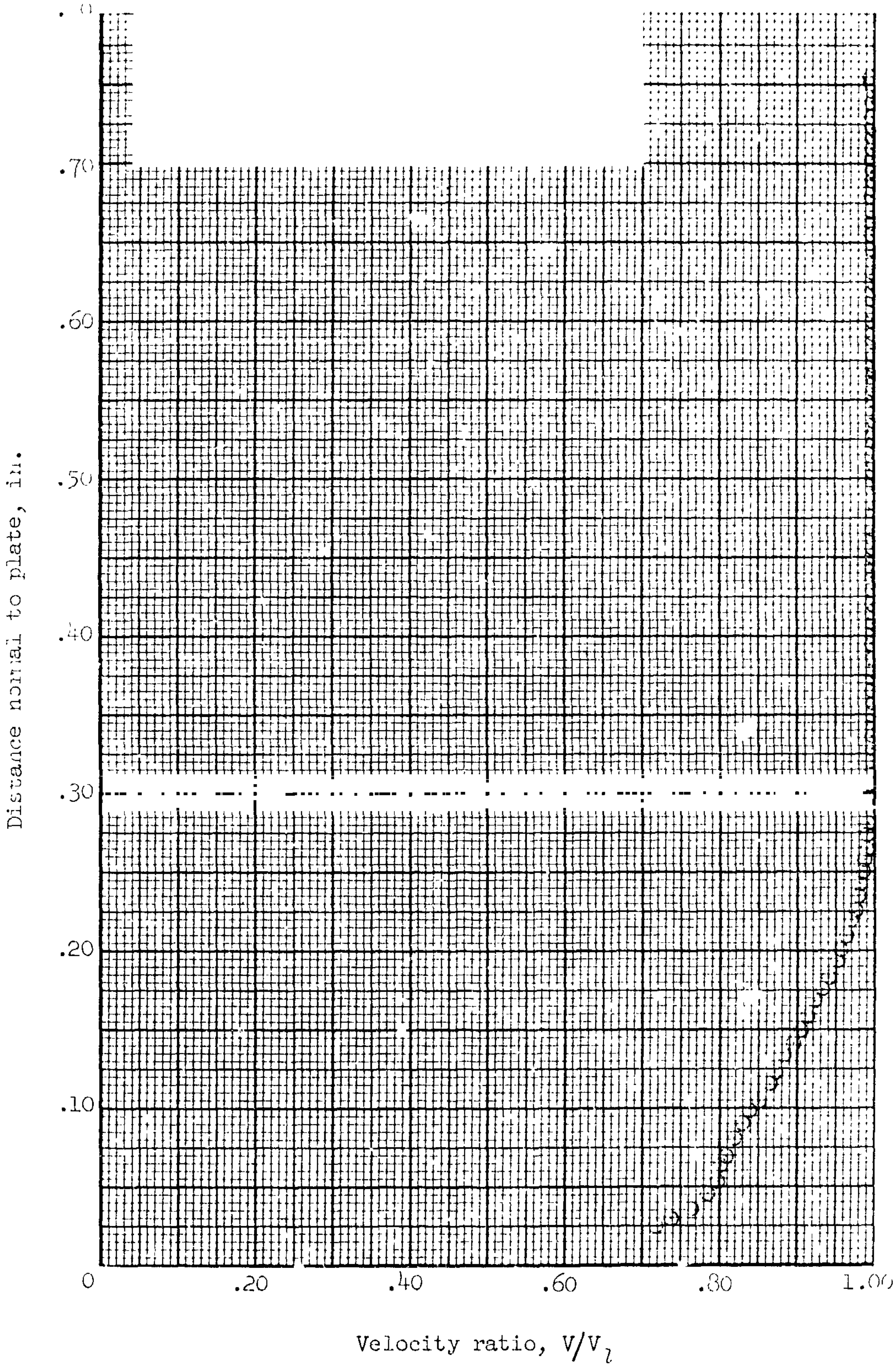

Figure 176.- Boundary-layer velocity distribution for run 71. All identifying conditions are given in table III.

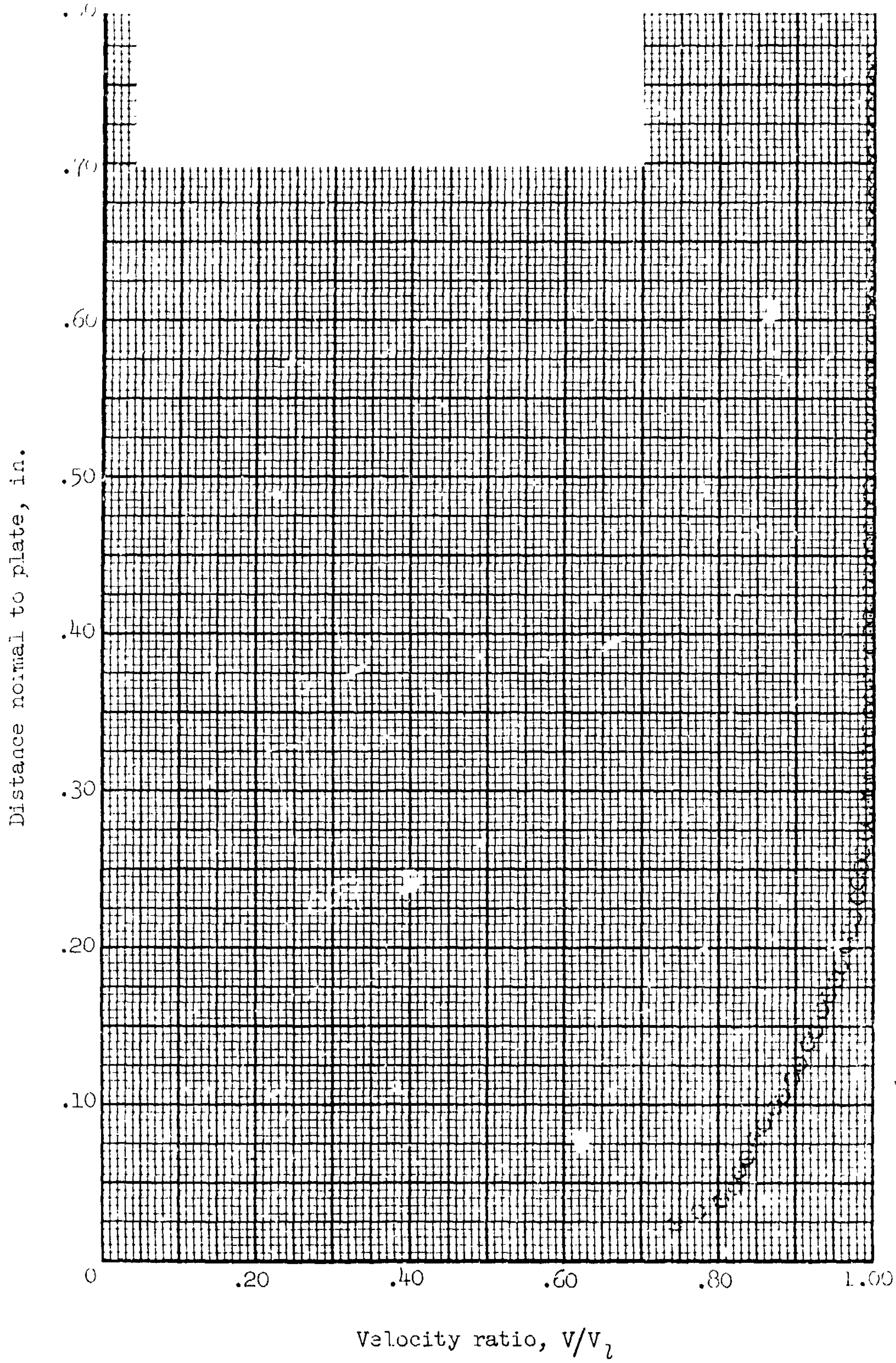

Figure 177.- Boundary-layer velocity distribution for run 72. All identifying conditions are given in table III.

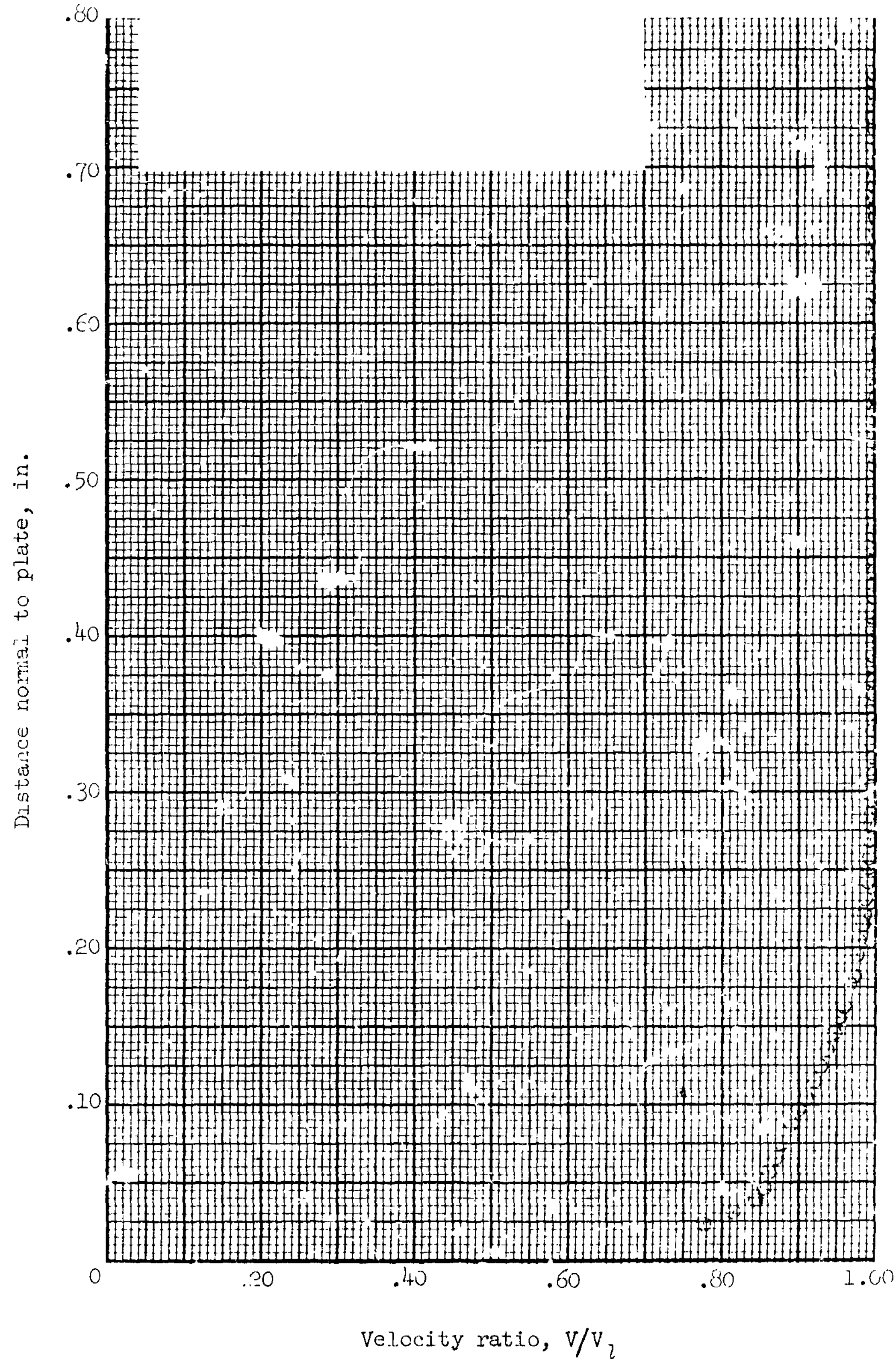

Figure 178.- Boundary-layer velocity distribution for run 73. All identifying conditions are given in table III.

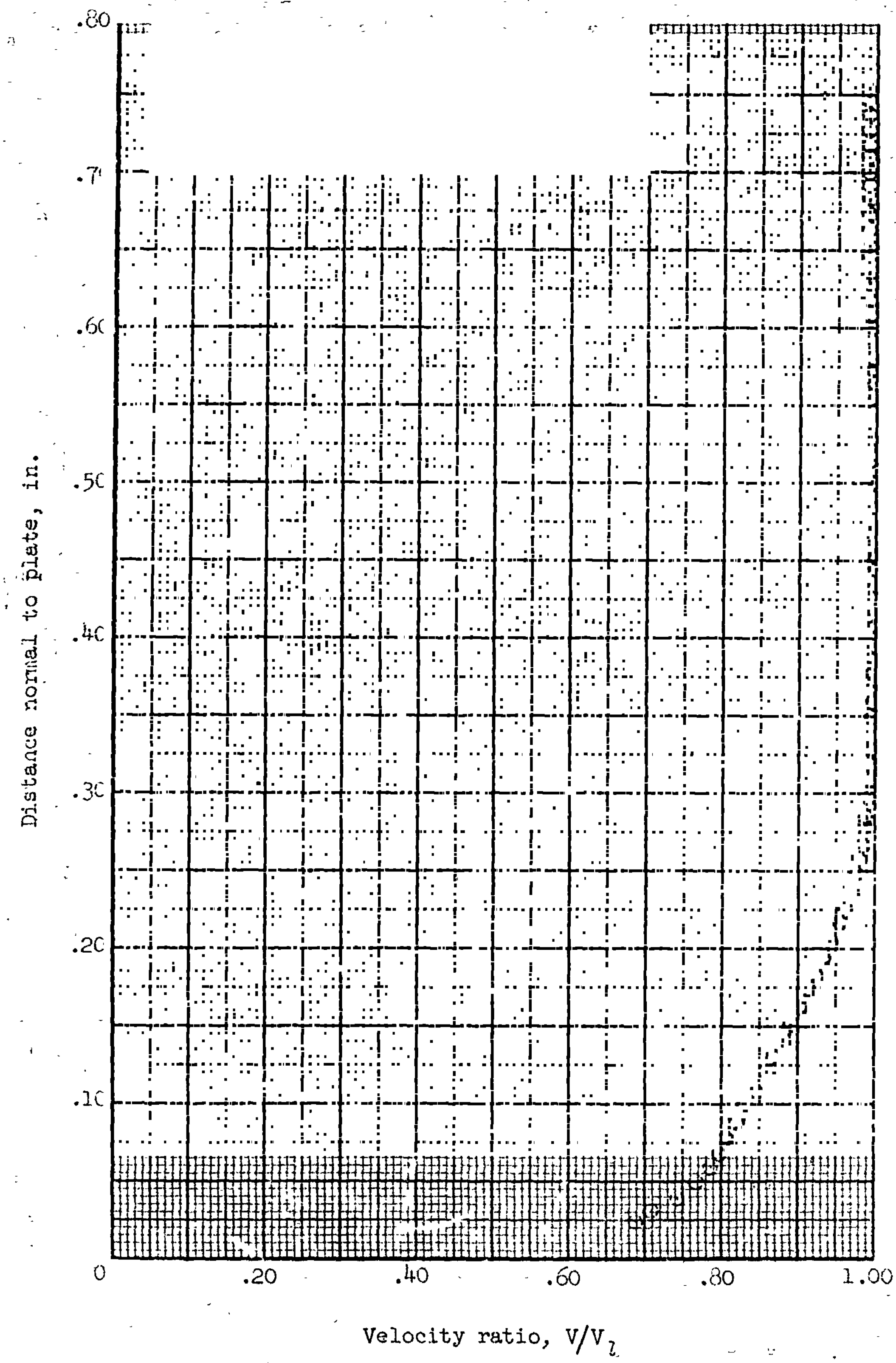

Figure 179.- Boundary-layer velocity distribution for run 76. All identifying conditions are given in table III.

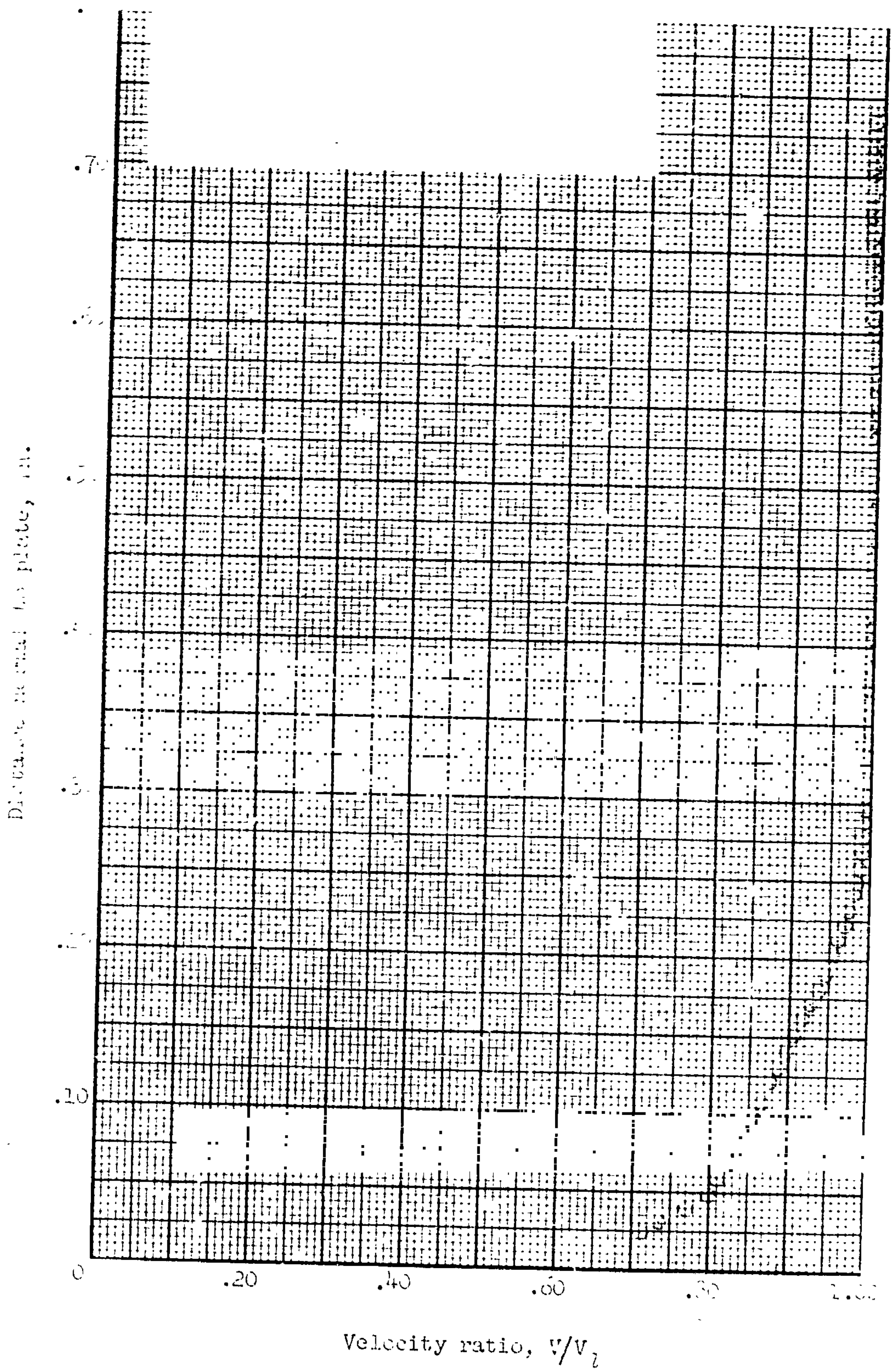

Figure 180.- Boundary-layer velocity distribution for run 77. All identifying conditions are given in table III.

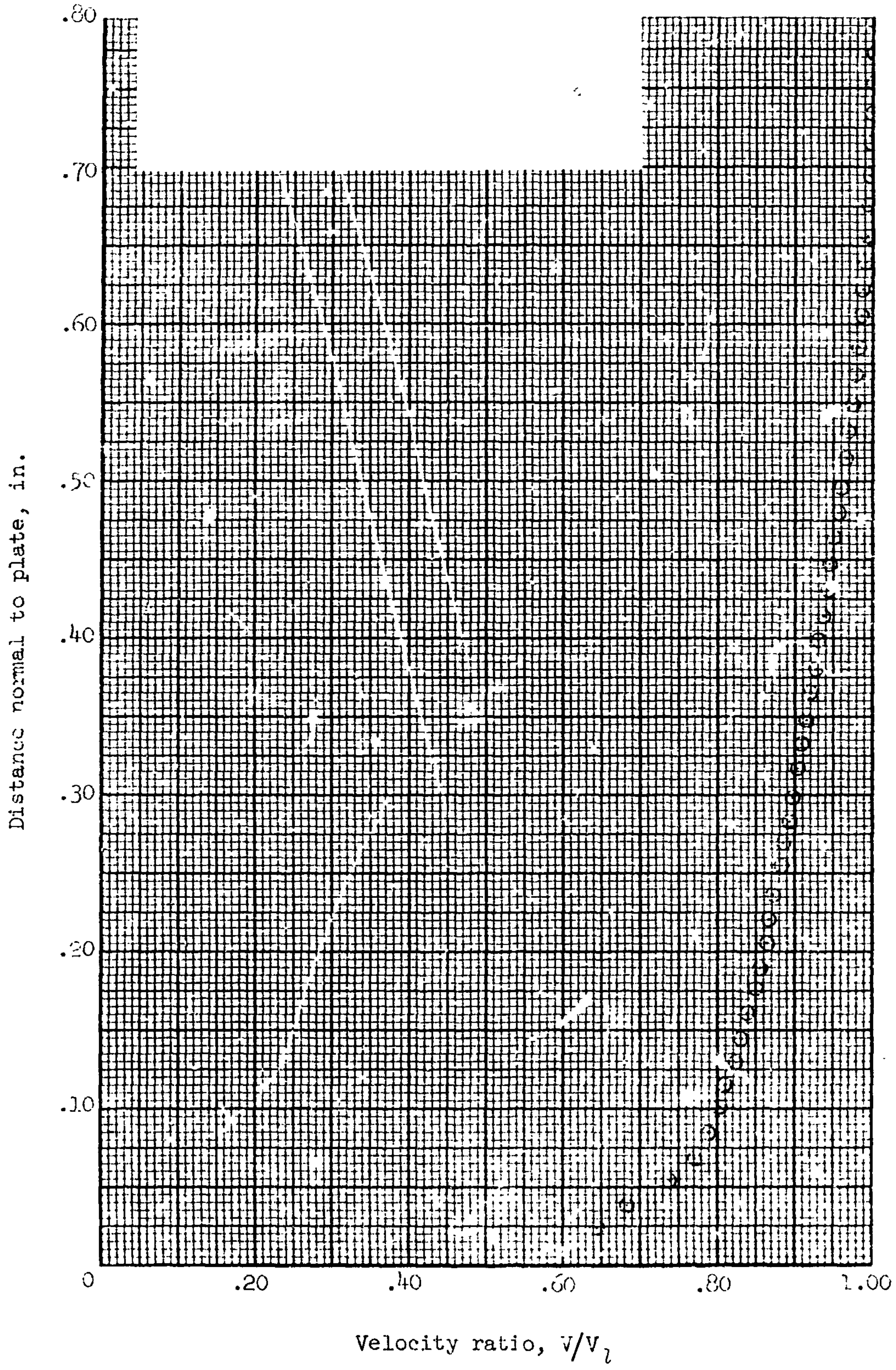

Figure 181.- Boundary-layer velocity distribution for run 80. All identifying conditions are given in table III.

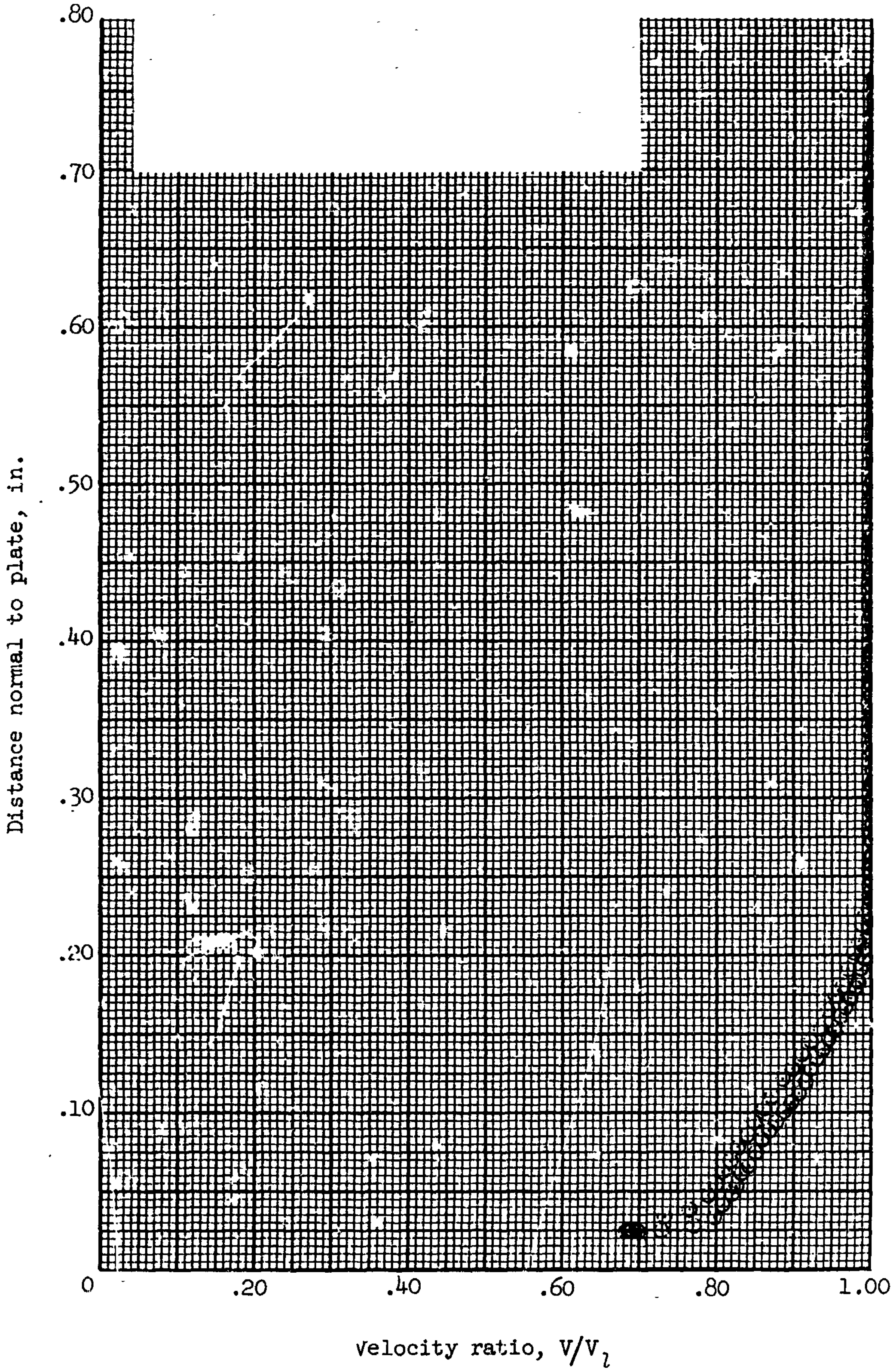

Figure 182.- Boundary-layer velocity distribution for run 81. All identifying conditions are given in table III.

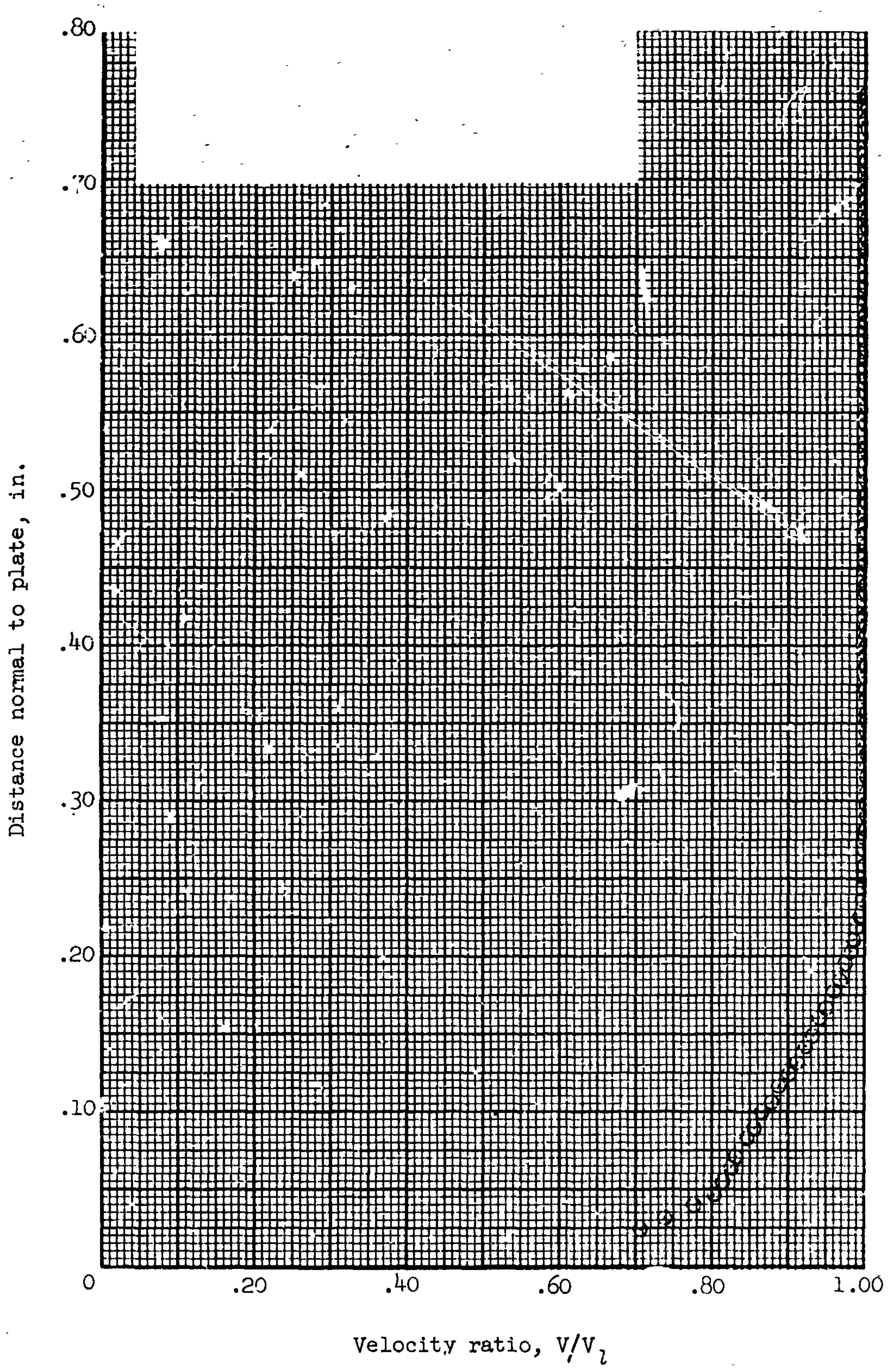

Figure 183.- Boundary-layer velocity distribution for run 82. All identifying conditions are given in table III.

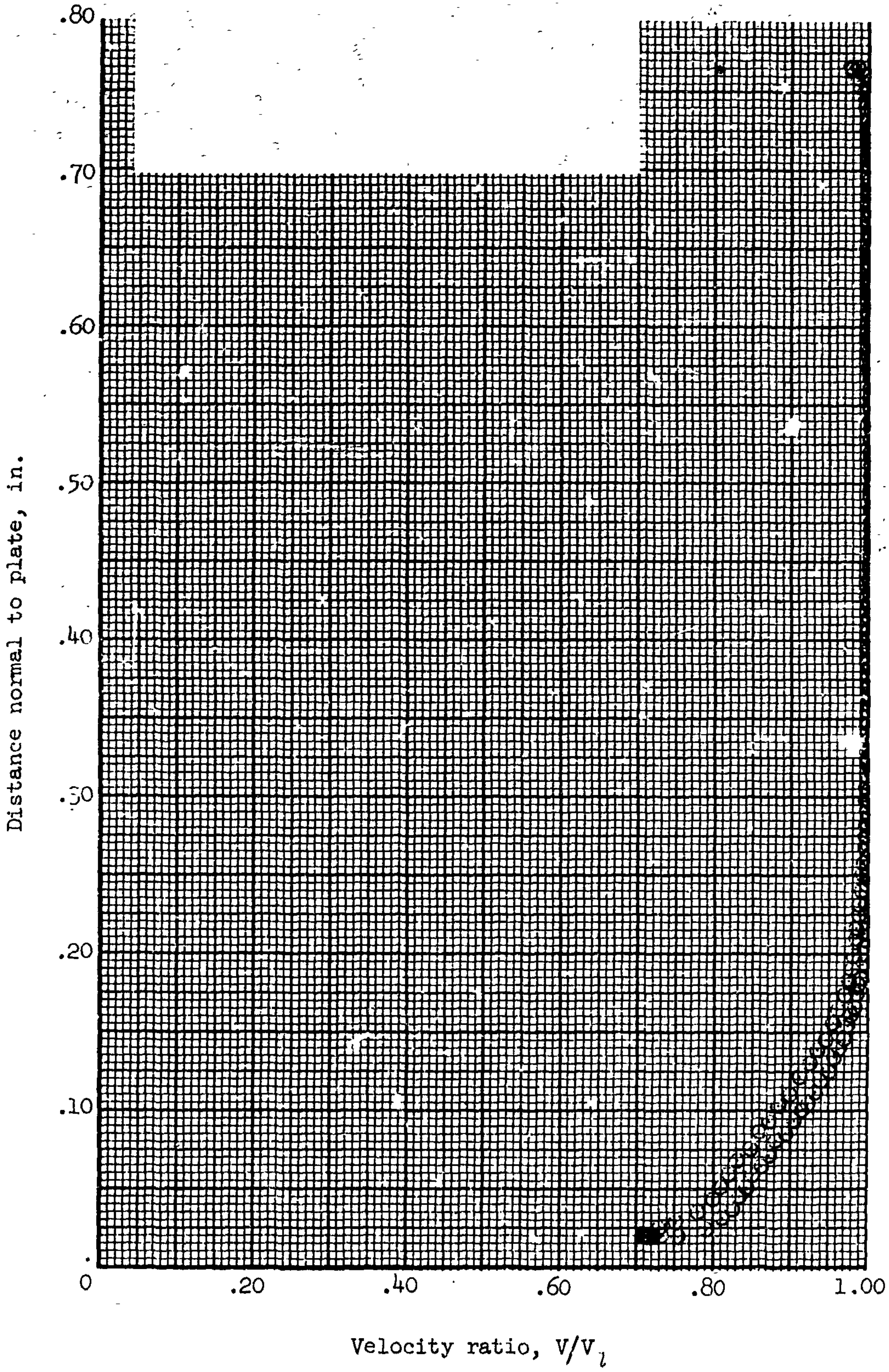

Figure 184.- Boundary-layer velocity distribution for run 83. All identifying conditions are given in table III.

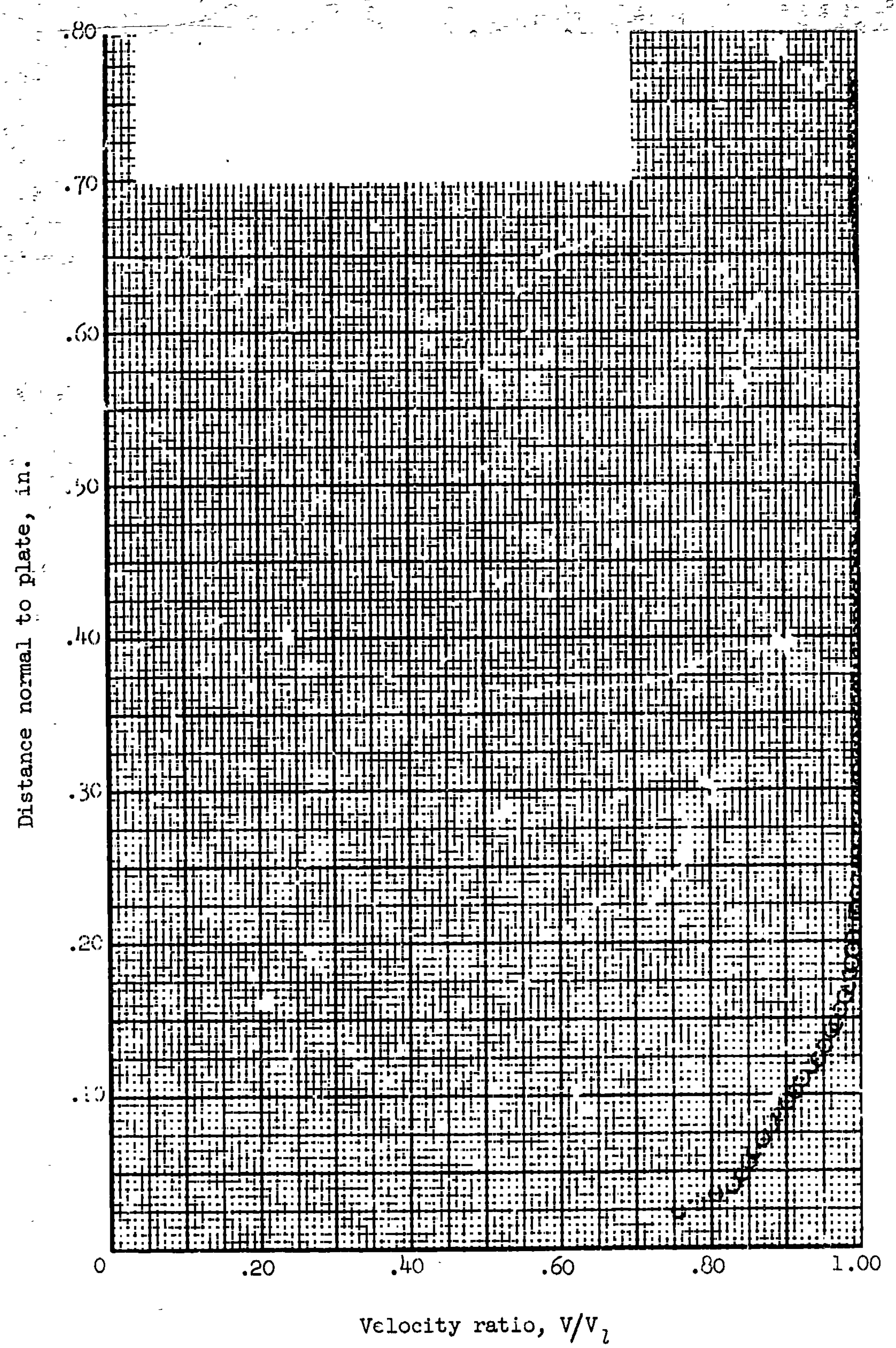

Figure 185.- Boundary-layer velocity distribution for run 84. All identifying conditions are given in table III.

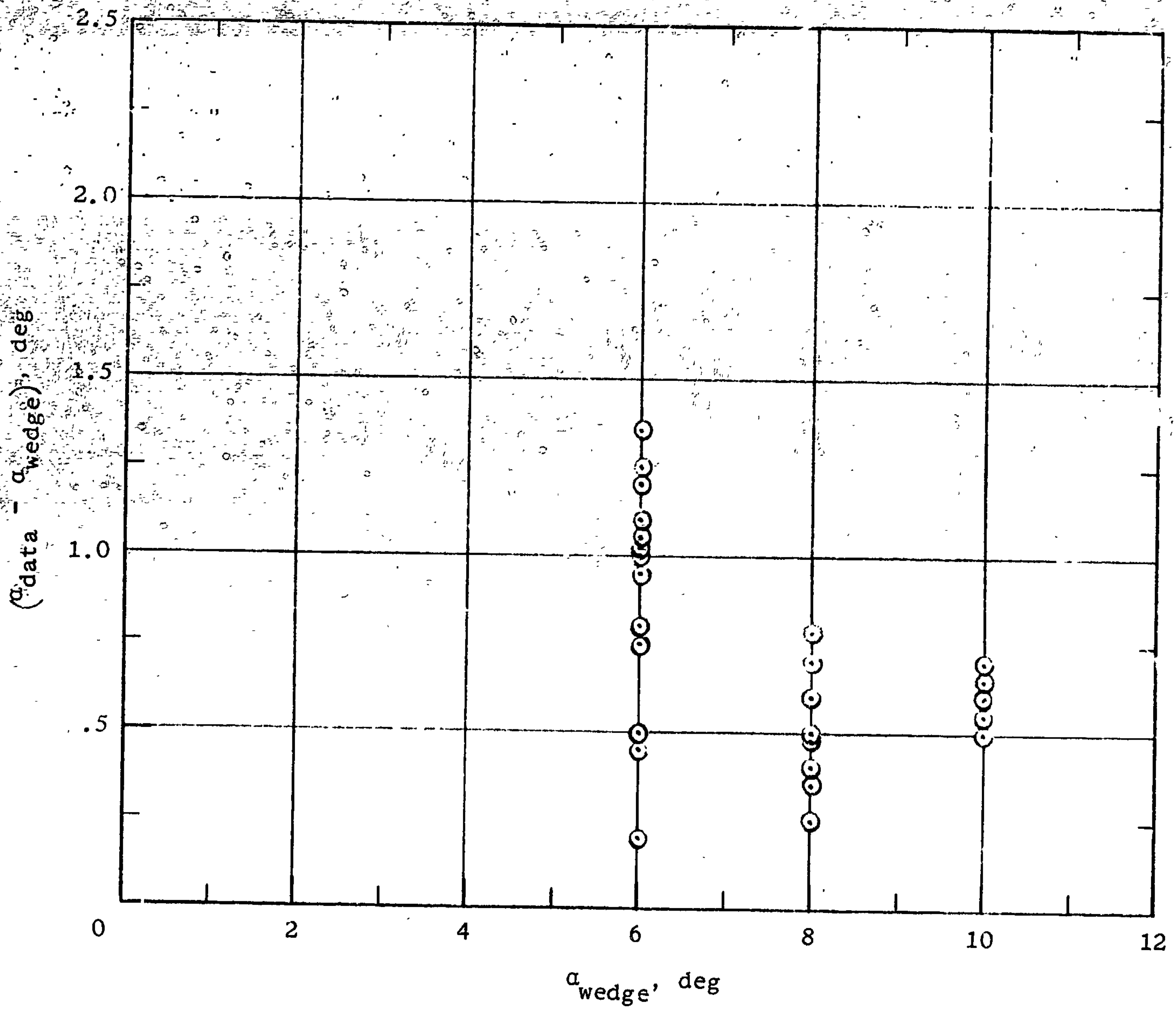

Figure 186.- Increase in shock-turning angle due to boundary-layer buildup on the shock-generator wedge surface.

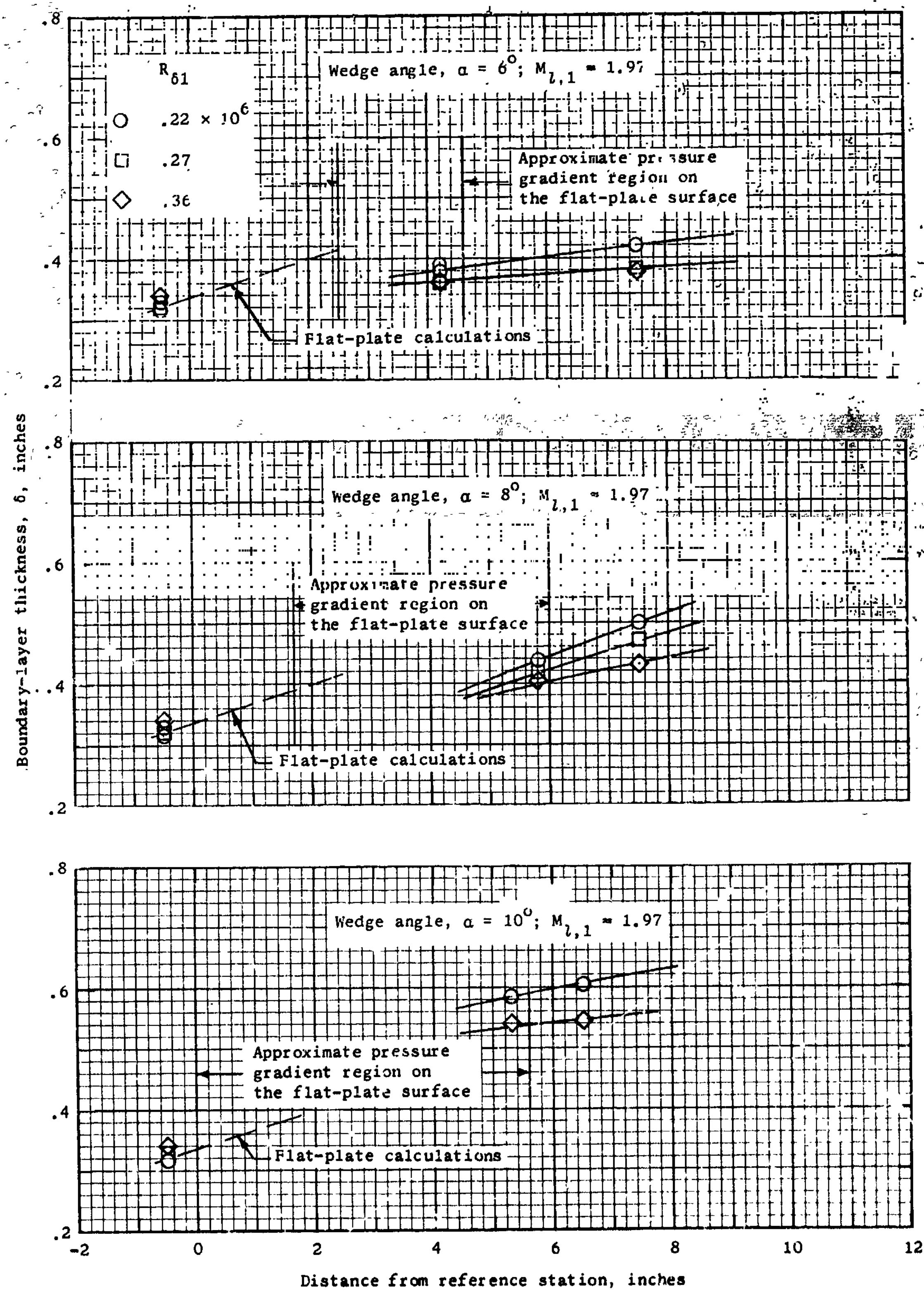

(a) Tunnel Mach number region 2.0.

Figure 187.- Variation of boundary-layer thickness δ along the flat plate.

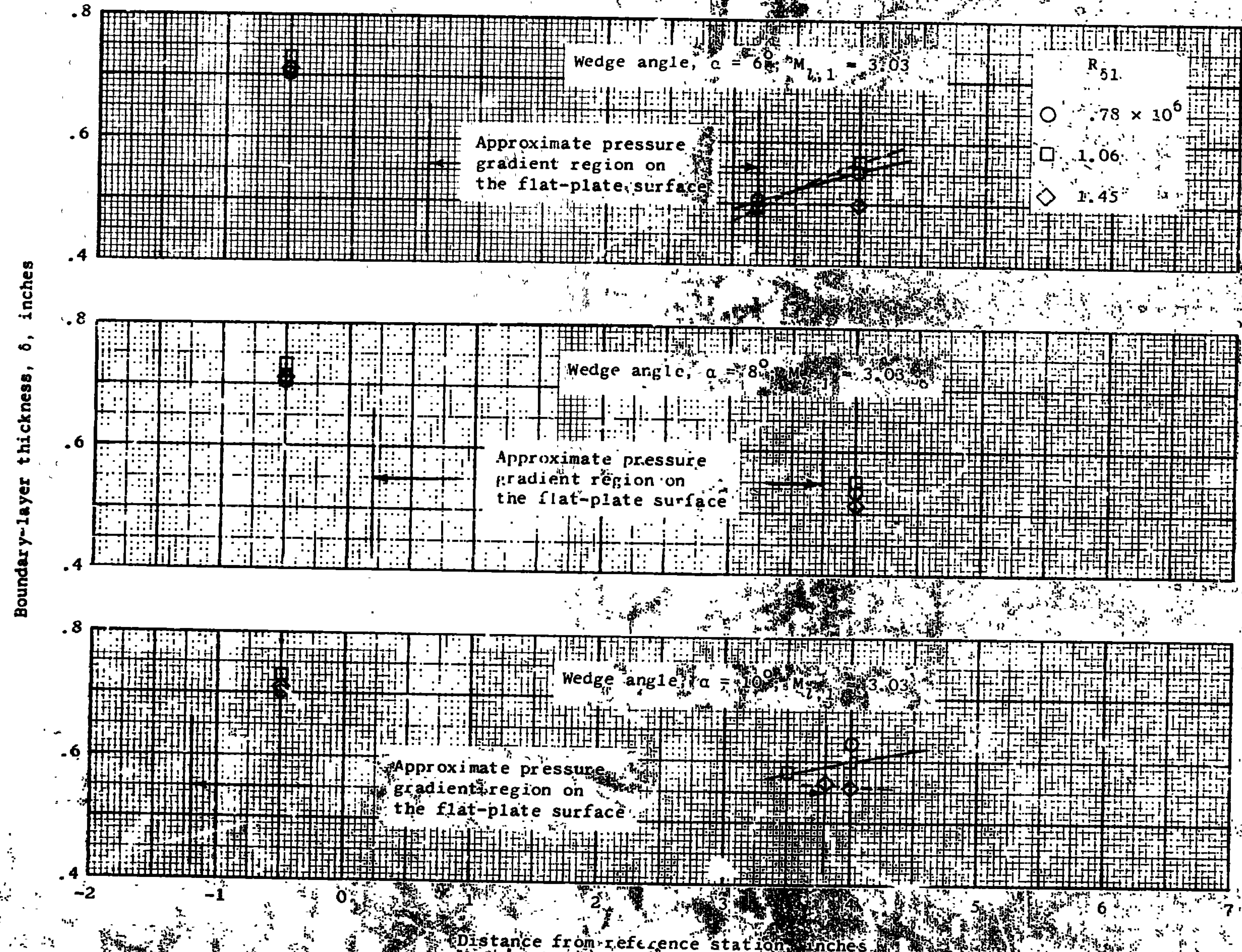

(b) Tunnel Mach number region 3.0

Figure 37.- Continued.

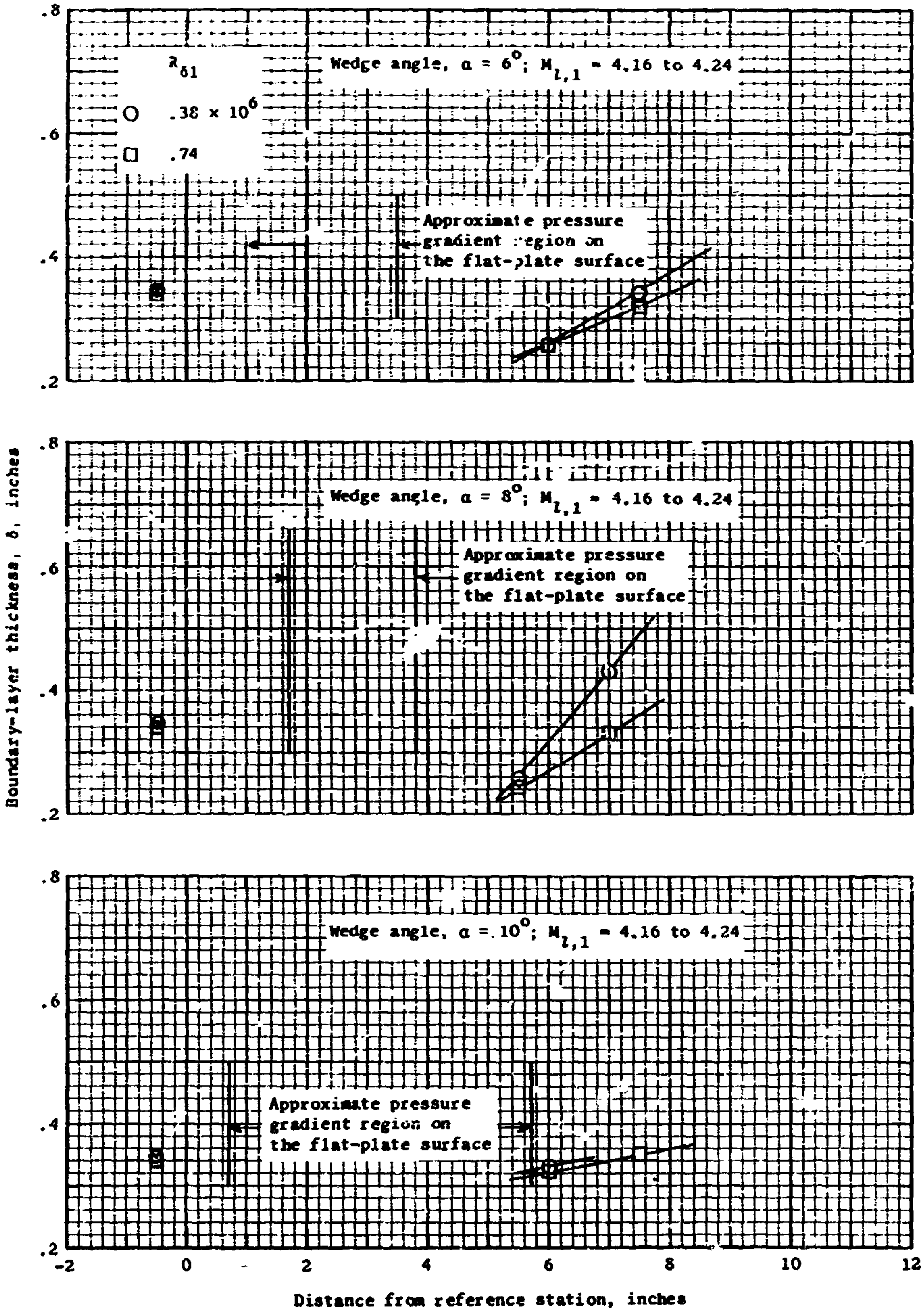

(c) Tunnel Mach number region 4.5.

Figure 187.- Concluded.

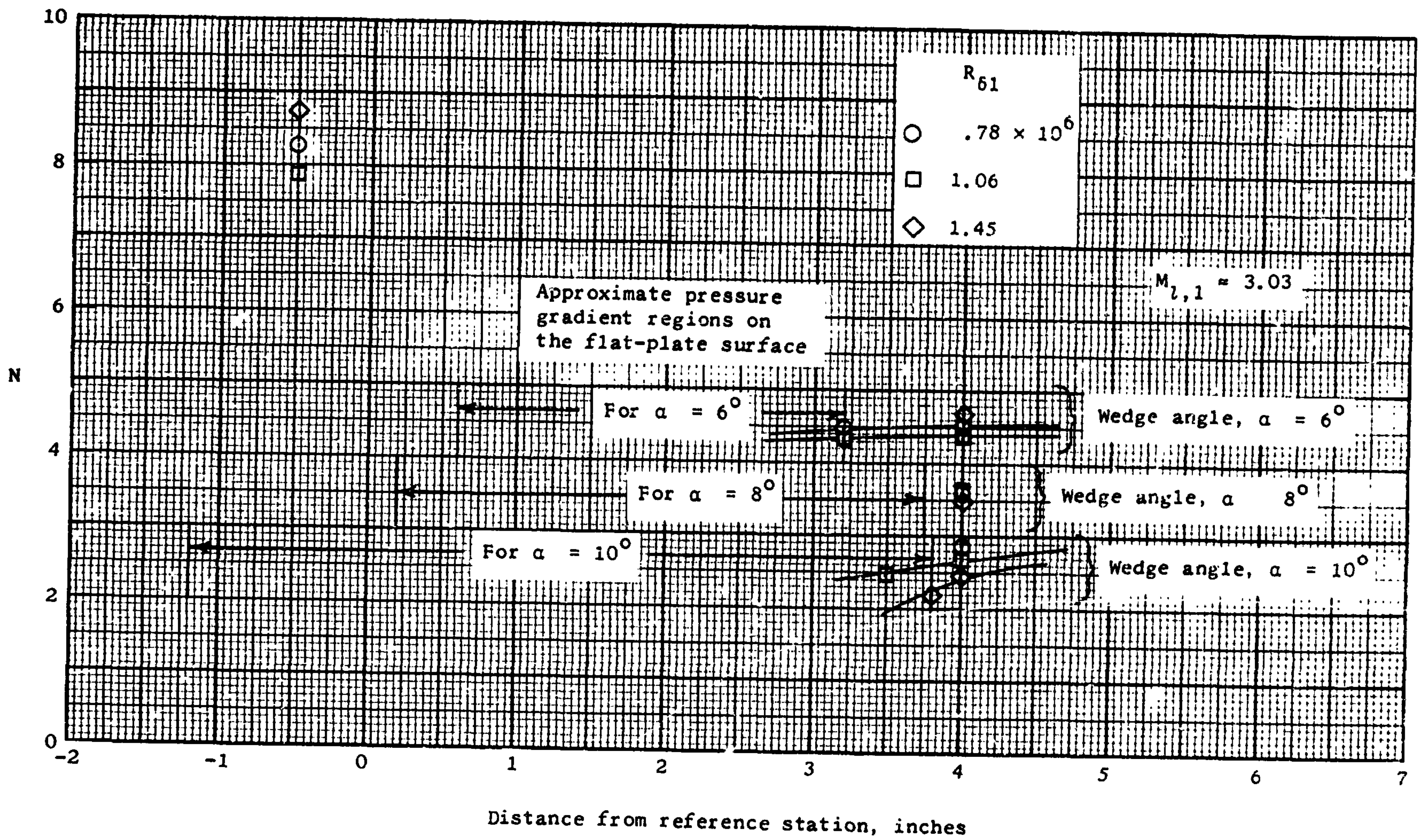

Figure 188.- Effect of incident-reflecting shock interaction on the boundary-layer velocity profile as represented by the variation of the profile index N.